

2D Static Light Scattering for Dairy Based Applications

Jacob Lercke Skytte

DTU



Kongens Lyngby 2014
PhD-2014-333

Technical University of Denmark
Department of Applied Mathematics and Compute Science
Matematiktorvet B322, DK-2800 Kongens Lyngby, Denmark
Phone +45 45253031, Fax +45 45882673
compute@compute.dtu.dk
www.compute.dtu.dk PhD-2014-333

Summary (English)

Throughout this thesis we investigate a recently introduced optical technique denoted 2D static light scattering (2DSLS). The technique is remote sensing, non-invasive, highly flexible, and appears to be well suited for in-line process control. Moreover, the output signal contains contributions from several different optical phenomena, which can be utilised to provide information on chemical composition and underlying microstructure of an investigated sample.

The main goal of this thesis is to provide an exploratory study of the 2DSLS technique in relation to dairy based applications. This includes getting an understanding of the various parameters in the setup as well as understanding the output signal in terms of potential and limitations. Furthermore, suitable ways of quantifying the signal are investigated. Here, both established physical models and statistical descriptions of the signal are evaluated and discussed.

There is a major emphasis on using 2DSLS to discriminate between different protein microstructures in yogurt products. This potentially allows for process control, in relation to microstructure, during yogurt manufacture. As microstructure is critical for consumer acceptability, this specific process control can be highly beneficial. To provide suitable reference measures on the actual microstructure, we investigate how to quantify micrographs of yogurts objectively. We provide a comparative study that includes a broad range of different image texture descriptors.

Summary (Danish)

I denne afhandling undersøger vi en nyligt introduceret optisk teknik, 2D Static Light Scattering (2DSLS). Teknikken er baseret på fjernmålinger, er ikke-invasiv, fleksibel og er potentielt velegnet til in-line proceskontrol. Desuden indeholder 2DSLS signalet informationer fra flere forskellige optiske fænomener, hvilket kan benyttes til at uddrage oplysninger om kemisk sammensætning og underliggende mikrostruktur af den undersøgte prøve.

Hovedformålet med afhandlingen er at undersøge 2DSLS teknikken i forbindelse med mejeri applikationer. Dette omfatter forståelsen af de forskellige parametre i den eksperimentelle opstilling af teknikken, såvel som forståelsen af 2DSLS signalets potentiale og begrænsninger. Desuden undersøges forskellige metoder til at kvantificere signalet. Her bliver både etablerede fysiske modeller såvel som statistiske beskrivelser evalueret og diskuteret.

Der lægges stor vægt på at bruge 2DSLS teknikken til at skelne mellem forskellige protein mikrostrukturer i yoghurt lignende produkter. Potentielt vil dette give mulighed for proceskontrol, i forhold til mikrostruktur, under yoghurt produktion. Da mikrostrukturen er en vigtig parameter for forbrugers accept af yoghurt produkter, kan denne specifikke proceskontrol være særdeles gavnlig. For at få referencemålinger af den faktuelle mikrostruktur, undersøges også hvordan mikroskopi billeder af yoghurt kan kvantificeres objektivt. Vi præsenterer således også et studie der sammenligner en række af forskellige deskriptorer af mikroskopi billedernes tekstur.

Preface

This thesis was prepared at the Image Analysis and Computer Graphics section at the Department of Applied Mathematics and Computer Science at the Technical University of Denmark (DTU). It was done in fulfillment of the requirements for acquiring a doctor of philosophy degree (PhD) within the topic of image analysis.

The presented work was financed by the Centre for Imaging Food Quality project, which is funded by the Danish Council for Strategic Research (contract no. 09-067039) within the Programme Commission on Health, Food and Welfare.

The research presented in the thesis concerns a recently introduced optical technique and its applicability within dairy production. First, the underlying theoretical concepts are introduced alongside the utilised instrumentation, and hereafter an overview of the applied methodologies is provided. Finally, the major findings are covered and discussed, which leads to the conclusion. Following the conclusion are six manuscripts prepared during the course of the PhD study.

The project has been supervised by Professor Rasmus Larsen and co-supervised by Associate Professor Anders B. Dahl. The research has mainly been carried out at DTU but also at Centre for Image Processing & Analysis at Dublin City University during an external stay under supervision of Professor Paul F. Whelan and Ovidiu Ghita.

Lyngby, 14th of March, 2014

A handwritten signature in blue ink, reading "Jacob Lercke Skytte". The signature is written in a cursive style with a large, stylized initial 'J'.

Jacob Lercke Skytte

Acknowledgements

During my three years as a PhD student I have been fortunate to collaborate and share work environment with a lot of dedicated and inspiring people. I would like to thank the colleagues at the Image Analysis and Computer Graphics section at The Technical University of Denmark (DTU) for creating a very pleasant and open work environment, which is both engaging and fun to be a part of. Furthermore, a special thanks goes to my loyal officemates Camilla H. Trinderup, Hildur Einarsdottir, and Otto H. A. Nielsen.

Also, I thank my supervisor Rasmus Larsen and co-supervisor Anders B. Dahl for guidance and encouragement and my industrial collaborators Ulf Andersen from Arla and Flemming Møller from DuPont, for providing insights and knowledge on the dairy industry. Furthermore, I would like to thank people and personnel at the laboratories at Arla, DuPont, and The National Food Institute, DTU, for willingly providing space, time and support for our experiments. And a special thanks to all of my additional collaborators – in no particular order: Otto H. A. Nielsen, Jeppe R. Frisvad, Ovidiu Ghita, Paul F. Whelan, Faisal Kamran, Sara Sharfizadeh, Line K. H. Clemmensen, Jens M. Carstensen, and Bjarne K. Ersbøll. I would further like to thank Paul F. Whelan and his group at Dublin City University, for a very pleasant and fruitful external stay.

Finally, I would like to express my sincere appreciation for the love and support from my family and friends, and a very special thanks to Migle Stasiukelyte for unbounded love, support, and patience.

Contributions

Papers included in this thesis

Paper A. Jacob L. Skytte, Otto H. A. Nielsen, Ulf Andersen, Flemming Møller, Jens M. Carstensen, Anders B. Dahl, Rasmus Larsen, *Monitoring Optical Changes during Milk Acidification using Hyperspectral Diffuse Reflectance Images*, submitted.

Paper B. Jacob L. Skytte, Otto H. A. Nielsen, Ulf Andersen, Jens M. Carstensen, Anders L. Dahl, Rasmus Larsen, Flemming Møller, Faisal Kamran, Jeppe R. Frisvad, *Decomposition of Diffuse Reflectance Images - Features for Monitoring Structure in Turbid Media*, InsideFood Symposium: Book of proceedings. 2013.

Paper C. Sara Sharifzadeh, Jacob L. Skytte, Line K. H. Clemmensen, Bjarne K. Ersbøll, *DCT-Based Characterization of Milk Products Using Diffuse Reflectance Images*, 2013 18th International Conference on Digital Signal Processing (DSP). IEEE, 2013. p. W3C-6.

Paper D. Jacob L. Skytte, Ovidiu Ghita, Paul F. Whelan, Ulf Andersen, Flemming Møller, Anders B. Dahl, Rasmus Larsen, *Evaluation of Confocal Scanning Laser Micrographs of Stirred Yogurts Using Image Analysis*, submitted.

Paper E. Jacob L. Skytte, *Discriminating Yogurt Microstructure Through 2D Static Light Scattering*, technical report.

Paper F Jacob L. Skytte, *Quantification of Multiple Scattered Light, Speckle Patterns, and Scattering Eccentricity in Diffuse Reflectance Images*, technical report.

Not included in this thesis

Jacob L. Skytte, A. L. Dahl, R. Larsen, Lars B. Christensen, Bjarne K. Ersbøll, *Classification Methods for CT-Scanned Carcass Midsections : A Study of Noise Stability*, Scandinavian Workshop on Imaging Food Quality 2011: Ystad, May 27, 2011 - Proceedings. Kgs. Lyngby, Denmark : Technical University of Denmark, 2011. p. 41-46 (IMM-Technical Report-2011; No. 15).

Jacob L. Skytte, Ulf Andersen, Flemming Møller, Otto H. A. Nielsen, Jens M. Carstensen, Anders L. Dahl, Rasmus Larsen, *Monitoring Structure Development in Milk Acidification Using Diffuse Reflectance Profiles*, Proceedings of the 14th Food Colloids Conference 2012. University of Copenhagen, 2012.

Jeppe R. Frisvad, Otto H. A. Nielsen, Jacob L. Skytte, Marek K. Misztal, Anders L. Dahl, *Digital Prototyping of Milk Products*, Proceedings of the 14th Food Colloids Conference 2012. University of Copenhagen, 2012. p. P53.

Sara Sharifzadeh, Jacob L. Skytte, Otto H. A. Nielsen, Bjarne K. Ersbøll, Line K. H. Clemmensen, *Regression and Sparse Regression Methods for Viscosity Estimation of Acid Milk From it's SLS Features*, Proceedings: IWSSIP 2012, 11-13 April 2012, Vienna, Austria. 2012. p. 58-61.

Otto H. A. Nielsen, Arman A. Subash, Frederik D. Nielsen, Anders B. Dahl, Jacob L. Skytte, Stefan Andersson-Engels, Dmitry Khoptyar, *Spectral Characterisation of Dairy Products Using Photon Time-of-Flight Spectroscopy*, Journal of Near Infrared Spectroscopy, 2013, 21(5):375-383.

Philip J. Sassene, Jacob L. Skytte, Sara Sharfizadeh, Line K. H. Clemmensen, Huiling Mu, Thomas Rades, Anette Müllertz, *Evaluation of Off-line Intestinal In Vitro Lipolysis of Lipid-based Drug Delivery Systems (LbDDS) by Diffuse Reflectance Imaging (DRI)*, 9th World Meeting on Pharmaceutics, Biopharmaceutics and Pharmaceutical Technology: Lisbon, March 31, 2014, Accepted.

Otto H. A. Nielsen, Faisal Kamran, Anders B. Dahl, Jacob L. Skytte, Frederik D. Nielsen, Carsten L. Thomsen, Peter E. Andersen, Rasmus Larsen, Jeppe R. Frisvad, *Non-Invasive Assessment of Dairy Products Using Spatially Resolved Diffuse Reflectance Spectroscopy*, submitted.

Contents

Summary (English)	i
Summary (Danish)	iii
Preface	v
Acknowledgements	vii
Contributions	ix
1 Introduction	1
1.1 Objectives	5
1.2 Thesis Overview	6
1.3 Contribution Overview	6
1.4 Abbreviations	8
2 Milk and Fermented Milk Products	9
2.1 Milk	9
2.2 Yogurt	11
2.3 Cheese	14
3 Light Propagation in Milk Products	17
3.1 Light Propagation	17
3.1.1 Physical Models	23
3.1.2 Additional Scattering Types	27
3.1.3 Milk Products	28

4	Instrumentation	31
4.1	Applied Instrumentation	31
4.1.1	CIFQ Workbench	31
4.1.2	Confocal Scanning Laser Microscopy	40
4.1.3	Small Amplitude Oscillatory Rheology	42
4.2	Related Instrumentation	45
4.2.1	Optical Methods	47
4.2.2	Comparison Between 2DSLS and Related Optical Methods	51
5	Data	53
5.1	2 ³ Fermentation Processes	53
5.2	Milk Products	57
5.3	Intralipid Series	57
5.4	2 ⁴ Stirred Yogurts	59
5.5	Repeated Fermentation Processes	62
6	Methods	65
6.1	2D Static Light Scattering	65
6.1.1	Oblique Model Based Characterisation	67
6.1.2	Intensity Based Characterisation	71
6.1.3	Scattering Eccentricity Characterisation	74
6.1.4	Speckle Size Characterisation	75
6.1.5	Discrete Cosine Transform	76
6.2	Confocal Scanning Laser Microscopy	79
6.2.1	Image Textures	81
6.2.2	Multiscale Representation and Filter Banks	82
6.2.3	Textons	90
6.3	Data Transformation	92
6.3.1	Principal Component Analysis	92
6.3.2	Distance Matrix	94
6.3.3	Multidimensional Scaling	94
6.4	Clustering	96
6.4.1	<i>K</i> -Means Clustering	97
6.4.2	Gaussian Mixture Model	98
6.4.3	Hierarchical Clustering	100
6.5	Classification	101
6.5.1	Cross Validation	102
6.5.2	<i>k</i> -Nearest Neighbour	102
6.5.3	Support Vector Machine	103
6.6	Analysis of Variance in Factorial Designs	105
6.6.1	ANOVA	106
6.6.2	MANOVA	108
6.6.3	NPMANOVA	108

7	Results and Discussion	113
7.1	Paper A - Monitoring Optical Changes during Milk Acidification Using Hyperspectral Diffuse Reflectance Images	113
7.2	Paper B - Decomposition of Diffuse Reflectance Images - Features for Monitoring Structure in Turbid Media	114
7.3	Paper C - DCT-Based Characterization of Milk Products Using Diffuse Reflectance Images	116
7.4	Paper D - Evaluation of Confocal Scanning Laser Micrographs of Stirred Yogurts Using Image Analysis	117
7.5	Paper E - Discriminating Yogurt Microstructure Through 2D Static Light Scattering	118
7.6	Paper F - Quantification of Multiple Scattered Light, Speckle Patterns, and Scattering Eccentricity in Diffuse Reflectance Images	119
8	Conclusion	123
A	Monitoring Optical Changes during Milk Acidification Using Hyperspectral Diffuse Reflectance Images	127
A.1	Introduction	128
A.2	Material and Methods	131
A.2.1	Experimental Design	131
A.2.2	Milk Sample Preparation	132
A.2.3	Milk Temperature Control	132
A.2.4	Hyperspectral Diffuse Reflectance Images	133
A.2.5	Small Amplitude Oscillatory Rheology	135
A.2.6	Analysis of Variance	137
A.2.7	Multivariate Analysis of Variance	137
A.3	Results	138
A.3.1	Hyperspectral Diffuse Reflectance Images	138
A.3.2	Small Amplitude Oscillatory Rheology	141
A.3.3	Analysis of Variance	143
A.3.4	Multivariate Analysis of Variance	144
A.4	Discussion	144
A.5	Conclusion	148
A.6	Acknowledgements	148
B	Decomposition of Diffuse Reflectance Images - Features for Monitoring Structure in Turbid Media	149
B.1	Introduction	150
B.2	Material	151
B.2.1	Diffuse Reflectance Images	151
B.2.2	Intralipid Data Set	153
B.3	Methods	153

B.3.1	Farrell Model Decomposition (FM)	154
B.3.2	Oblique Model Decomposition (OM)	154
B.3.3	Loglog Model Decomposition (LM)	155
B.3.4	Patch Average Decomposition (PA)	155
B.3.5	Intensity Spread Decomposition (IS)	155
B.3.6	Feature Evaluation	156
B.4	Results and Discussion	156
B.5	Conclusions	160
B.6	Acknowledgements	161
C	DCT-Based Characterisation of Milk Products Using Diffuse Reflectance Images	163
C.1	Introduction	164
C.2	Data Description	166
C.3	Characterisation of the Images	167
C.3.1	DCT Transform	167
C.3.2	Entropy	169
C.3.3	Forming the Initial Feature Set	170
C.3.4	Feature Forming Based on log-log Model	170
C.4	Feature Selection and Discrimination	170
C.4.1	Preparation of Training and Test Sets	173
C.4.2	Wavelength Selection	173
C.4.3	Feature Selection for the Selected Band	173
C.4.4	Discrimination	174
C.5	Results and Discussion	175
C.5.1	Characterisation Results in DCT Domain	175
C.5.2	Characterisation Results Using the log-log Model	177
C.5.3	Discussion	177
C.6	Conclusion	179
D	Evaluation of Confocal Laser Scanning Micrographs of Stirred Yogurts Using Image Analysis	181
D.1	Introduction	182
D.2	Materials and Methods	185
D.2.1	Experimental Design	185
D.2.2	Confocal Laser Scanning Microscopy	185
D.2.3	Image Pre-Processing	187
D.2.4	Image Descriptors	189
D.2.5	Method Evaluation	198
D.3	Results	200
D.3.1	Gel Segmentation	200
D.3.2	Parameter Selection	200
D.3.3	Nearest Neighbour Classification	204
D.3.4	Non-Parametric Multivariate Analysis of Variance	207

D.3.5 Hierarchical Clustering	209
D.4 Discussion	209
D.5 Conclusion	211
D.6 Acknowledgements	212
E Discriminating Yogurt Microstructure Through 2D Static Light Scattering	213
E.1 Introduction	214
E.2 Materials and Methods	215
E.2.1 Experimental Design	216
E.2.2 2D Static Light Scattering	216
E.2.3 CSLM Image Descriptor	219
E.2.4 Multidimensional Scaling	219
E.2.5 Statistical Analysis	221
E.3 Results	221
E.3.1 Multidimensional Scaling	221
E.3.2 Statistical Analysis	222
E.4 Discussion and Conclusion	229
F Quantification of Multiple Scattered Light, Speckle Patterns, and Scattering Eccentricity in Diffuse Reflectance Images	231
F.1 Introduction	232
F.2 Materials and Methods	235
F.2.1 2D Static Light Scattering	235
F.2.2 Data	240
F.3 Results	242
F.3.1 Dairy Products	242
F.3.2 Milk Fermentation Data	249
F.4 Discussion and Conclusion	253
Bibliography	255

CHAPTER 1

Introduction

Milk has been a food source for humans since prehistoric times. While the primary natural function of milk is nutrition for the young, it has also been a general steady food source ever since the first domestication of animals. Fermentation of milk was initially used to conserve the nutrients of milk, which would otherwise deteriorate rapidly, especially in hot climates. Fermentation added safety and portability to milk as well as novelty for the consumer due to the viscous consistency with unique texture and flavour (Chandan and Kilara, 2013).

The consumption of milk is very geographically dependent, with the highest milk consumed per capita in North America, Australia, and Northern Europe. Africa, South America, and Asia are amongst areas with the lowest consumption per capita, which can be due to a high percentage of the population being lactose intolerant as well as a limited availability of refrigeration. However, during production of fermented milk products, lactose is broken down, making products easier to digest for lactose intolerants and non-intolerants alike. Combined with the increased shelf life, fermented milk products are more attractive to these markets.

Almost every part of the world has its own regional variants of fermented milk products (Chandan and Kilara, 2013). This is partly due to tradition, where each region developed its own approach to fermentation, and partly due to

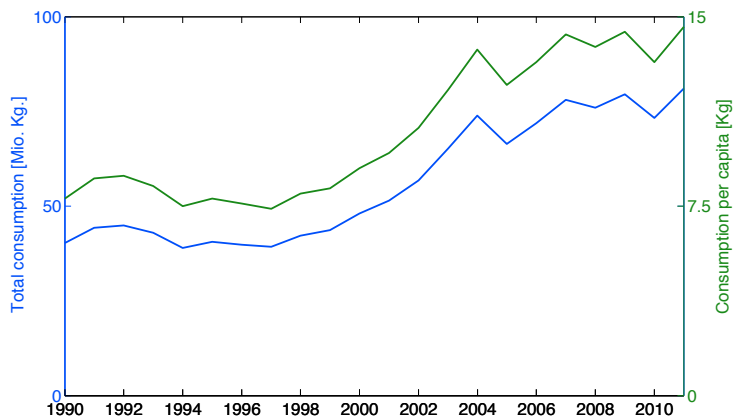


Figure 1.1: Yogurt consumption in Denmark in the period 1990-2011. Data is from Statistics Denmark (www.dst.dk).

market preference in terms of flavour, appearance, and texture. In Denmark there is currently an increasing trend in the demand for products with high protein and low fat contents. Throughout the thesis we will primarily consider acid fermented milk products and we will in broad terms refer to these products as yogurt.

Following a recent business reports by PM Food & Dairy Consulting (2012) and Research and Markets (2012), the yogurt demand is growing globally. In 2000 the global production of yogurt reached 20 million tonnes, and by 2010 the production reached nearly 30 million tonnes. By 2015 it is expected that the production will exceed 40 million tonnes, which corresponds to a revenue of 70 billion US dollars. These significant increases in demand have especially been attributed recent trends in Asia, as well as dietary and health benefits, that are continuously discovered (Van de Water et al., 1999; Desobry-Banon et al., 1999; Larsson et al., 2008; Mozaffarian et al., 2011). In Denmark the yogurt consumption has increased almost consistently since the late 90's as can be seen in Figure 1.1.

Comparable to any other product, consumer acceptability is a critical parameter. Muir and Hunter (1992) investigated sensory properties of fermented milk products and found that consumer acceptability was positively affected by the following sensory properties: *Creamy flavour*, *creamy texture*, and *viscosity*. While flavour relates to the taste and smell of the product, texture and viscosity are related to mouthfeel and the general physical properties, and are defined by the ingredient composition and microstructure of the product (Folkenberg et al., 2005).

Fat positively affects the perceived creaminess of a product (Janhøj et al., 2006), and as a result the recent demand for yogurts products with low fat content and high protein content, has provided the industry with additional challenges. This has lead to increased activity in finding ways to replace fat, either by special processing of the milk protein or adding different ingredients as fat replacers to attain the same type of creaminess (Sandoval-Castilla et al., 2004; Paseephol et al., 2008; Torres et al., 2012).

Thereby, texture can partly be related to the product composition. Lucey (2004) also lists a broad range of production parameters that can result in texture defects if not carefully considered. These texture defects includes a weak body, graininess, and wheying-off where water is wrongfully expelled from the yogurt. Figure 1.2 gives a schematic overview of the production steps involved in the making of stirred yogurt, which is the most common yogurt product in Denmark. Following Lucey (2004) the majority of these production steps, as well as the handling of the bulk between the production steps (typically transportation through pipes), can result in texture defects of the final product if not considered carefully. In order to maintain a consistent product quality in a yogurt production line, it can therefore be beneficial to monitor the microstructure within and between the different production steps.

Process control can hereby be applied in several areas of the yogurt production. It can be used to monitor different processing steps such as the incubation, where the yogurt structure is formed, or it could be used to pinpoint critical production steps where unwanted structural changes might occur, e.g. due to wear and tear of the processing equipment or maladjusted processing parameters. Related to a slightly different topic, an optical technique sensitive to microstructure could potentially aid in screening process parameters during development of new products.

Process control sensors can be divided into three different categories, and throughout this thesis we will adopt the following terminology:

- **In-line.** The sensor can be mounted directly in the on-going process flow.
- **On-line.** Some of the process flow is diverted in order to reach the sensor.
- **At-line.** Sample has to be extracted from the process flow in order to be measured.

In relation to acidified milk products, such as yogurts, the pH value is often monitored during manufacture to ensure the correct acidity of the products.

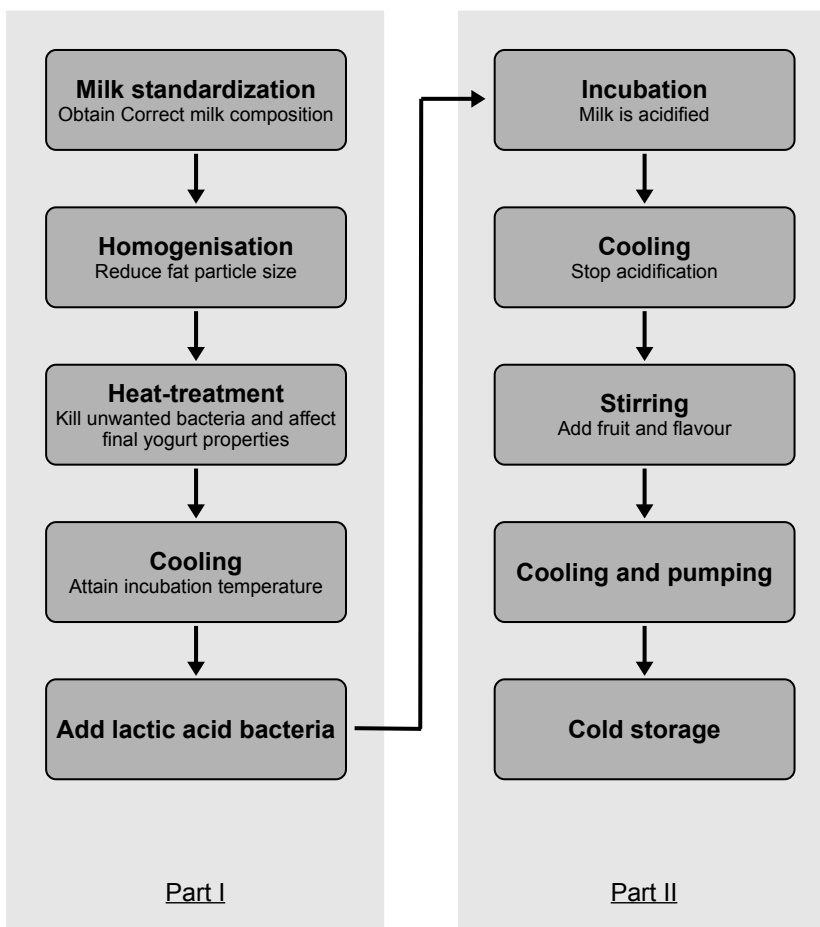


Figure 1.2: Simplified flow chart of the production of stirred yogurts. In part I the milk is still in its liquid state, and in Part II the characteristic yogurt texture is attained. The incubation step in Part II is where the initial yogurt structure is formed. The flow chart is adopted from Lee and Lucey (2010).

However, to the best of our knowledge process control in relation to microstructure in yogurt production remains a rather untouched subject in the literature as well as in the real world. However, sensors sensitive to microstructure applied in the making of hard cheese has been covered to a great extent, and several review papers can be found (Lucey, 2002; O’Callaghan et al., 2002; Castillo, 2006). Here, a broad selection of methodologies is covered ranging from mechanical testing to thermal conductivity, and optical methods. Especially, the optical methods have always been of great interest in regards to quality inspection and process control in general due to their non-invasive nature (Chen and Sun, 1991). Lucey (2002) notes that while a lot of different methods for process control techniques exist for cheese making no standard approach is commonly used in modern dairy production. Among other things Lucey attributes this to problems such as the sensors not being suitable for in-line implementation, difficulty in meeting hygienic standards, and the lack of robustness of the sensors in a commercial setting.

Throughout this thesis 2D Static Light Scattering (2DSLS), a novel optical technique, is investigated. The technique is remote, flexible in terms of setup, and provides a signal that has not been investigated previously for dairy applications. We hypothesise that the technique potentially can alleviate some of the above mentioned implementation issues. However, preliminary studies have to be conducted in order to verify the potential of the technique as a new sensor technology. For process control it is required that the sensor is sensitive to the particular factor being evaluated (here the yogurt microstructure), the sensor output should be reproducible, and the signal-to-noise ratio (SNR) should be appropriate (Chen and Sun, 1991; MacGregor and Kourti, 1995).

1.1 Objectives

The main objective of this thesis is to provide an exploratory study of the 2DSLS technique within the confines of dairy products. This includes both understanding the 2DSLS signal itself to determine the potential and limitations of the novel modality, as well as determining appropriate ways to parameterise the output signal.

Interpretation of the signals is another important aspect of the investigation, for which well established reference methods should also be applied. This can aid in determining what kind of chemical or microstructural phenomena that can be detected using the 2DSLS.

Additionally, the work of this thesis was carried out in parallel to another PhD

project, within the Centre for Imaging Food Quality (CIFQ), by Otto H. A. Nielsen (Nielsen, 2014). In his project the actual 2DSLS system setup was continuously developed. Thus, another important part of this project was to provide feedback whenever the system was used in practice, to aid in the continuous development of the 2DSLS platform.

1.2 Thesis Overview

The thesis is structured with two introductory chapters, which first gives a brief overview of milk, yogurt and the production of yogurt (Chapter 2). Hereafter, an introduction to the relevant concepts of light scattering is provided, which additionally is put into context of dairy products (Chapter 3).

Based on these chapters descriptions of reference instrumentation is provided, as well as details on the 2DSLS platform and its related methods (Chapter 4). Next, the data sets used throughout the included contributions are presented (Chapter 5), and in Chapter 6 most of the methodologies applied during the analysis of the data sets are described.

Chapter 7 highlights and discusses the major findings for each of the included contributions found in Appendix A through F. The results alongside the actual contributions should preferably be read before the conclusion in Chapter 8.

It should be noted that the layout of the contributions in Appendix A through F has been adapted to be consistent with the thesis layout.

1.3 Contribution Overview

The major contributions of this thesis cover an explorative study of the applicability of the 2DSLS modality. This includes a validation of the method, in light of existing technologies and established light scattering theory, as well as an exploration of the different pieces of information available in the 2DSLS signal. The majority of the presented work has been carried out within the confines of dairy products.

Additionally, a significant amount of work has been put into quantifying micrographs of protein microstructure in yogurts in an objective manner. This area has previously been investigated, but no standard approach has been suggested, thus we provide a comparative study that considers a broad range of

methods. The objective description of the actual microstructure has allowed for direct comparisons between 2DSLS and the actual microstructure of a yogurt. This was necessary in order to verify the sensitivity of 2DSLS toward changes in protein microstructure.

1.4 Abbreviations

2DSLS	- 2D Static Light Scattering
ANOVA	- Analysis Of Variance
AOTF	- Acousto-Optical Tuneable Filter
BIF	- Basic Image Features
CCD	- Charge Coupled Device
CIFQ	- Centre for Imaging Food Quality
DLS	- Dynamic Light Scattering
DWS	- Diffusing Wave Spectroscopy
FWHM	- Full Width at Half Maximum
GDL	- Glucono- δ -Lactone
GLCM	- Grey Level Co-occurrence Matrix
GMM	- Gaussian Mixture Model
HDR	- High Dynamic Range
IR	- Infrared
LED	- Light Emitting Diode
LOOCV	- Leave-One-Out Cross Validation
MANOVA	- Multivariate Analysis Of Variance
MDS	- Multidimensional Scaling
MFP	- Mean Free Path
NPMANOVA	- Non Parametric Multivariate Analysis Of Variance
NIR	- Near Infrared
RTE	- Radiative Transfer Equation
SAOR	- Small Amplitude Oscillatory Rheology
SIFT	- Scale Invariant Feature Transform
SMP	- Skimmed Milk Powder
SNR	- Signal-to-Noise Ratio
SS	- Sum of Squares
SVM	- Support Vector Machine
UV	- Ultra Violet
VIS	- Visible

CHAPTER 2

Milk and Fermented Milk Products

This chapter gives an introduction to bovine milk and the production of related fermented milk products. While the main focus of this thesis is on fermented milk products such as yogurt, a lot of the previous process control techniques have been introduced in the context of cheese making. Therefore, a brief section on cheese making is also included in order to provide the necessary foundation for Chapter 4, where applied and related instrumentation is introduced.

2.1 Milk

Milk is a complex food with more than 100000 different molecular variations, based on different species, in-species variations, seasonal variations, geographic variations, etc. The average constituents of cows milk are (Walstra et al., 2010):

- **Water (87.1%)**. Acts as the host medium.
- **Lactose (4.6%)**. Milk sugar solubilised in the host medium.
- **Fat (4.0%)**. Exist as fat globules.

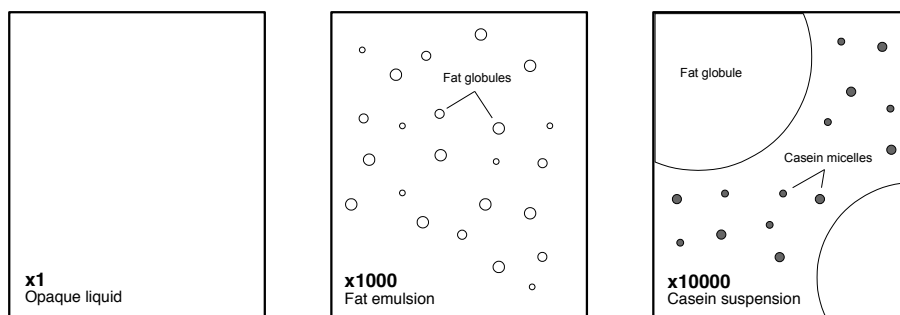


Figure 2.1: Milk illustrated at different scales.

- **Protein (3.3%).** 80% of the protein is casein which exists as micellar structures and 20% is whey protein, which is solubilised in the host medium.
- **Other (1%)** - minerals, enzymes, and vitamins.

Milk is a turbid liquid, made up by an emulsion of fat globules, and a suspension of casein micelles. This is illustrated in Figure 2.1, where milk is sketched at different scales.

Fat globules are droplets, and their size range is between 100-10000nm. Casein micelles are significantly smaller, 20 – 400nm, but the structure of these is not yet agreed upon in the literature, and several review papers have been published within the last decade (Dalglish and Corredig, 2012).

The dry matter content of the casein micelle in bovine milk consists of approximately 94% protein, divided between four different types of casein (α_{s1} -, α_{s2} -, β -, and κ), and 6% calcium phosphate. A recent study by Dalglish (2011) suggests that the most probable structure of the casein micelle is a "coated sphere model", where most of the κ -casein is present on the surface of the micelle, providing a steric stabilisation that prevents aggregation with other micelles.

The internal structure of the casein micelle is quite irregular. At neutral pH (6.7), the micelle structure is held together by a balance of attractive hydrophobic forces and electrostatic repulsion between caseins. The structure is further stabilised by calcium phosphate, which is bound to α_s - and β -casein. The micelles are very porous, and thereby highly hydrated, thus while they constitute

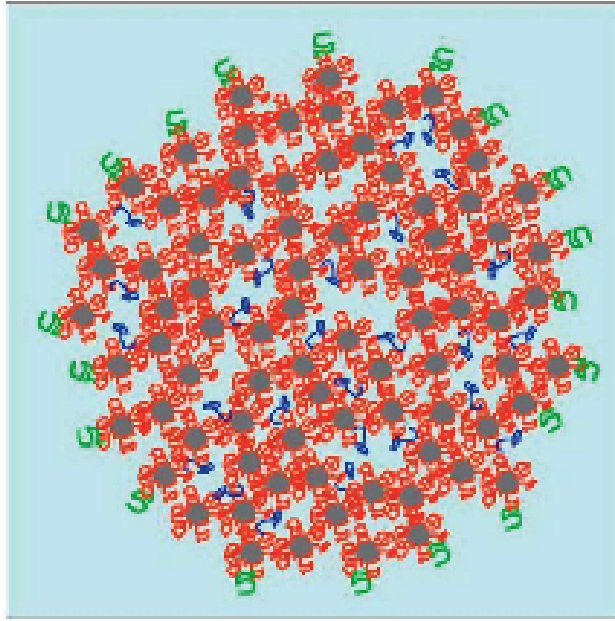


Figure 2.2: Probable structure of the casein micelle. The surface is covered by κ -casein (green), and the inside consists of α_s - and β -casein (red) bound by calcium phosphate. Some casein is bound by hydrophobic attraction (blue). Image from Dalgleish (2011).

a relative small part of the total weight of milk, they occupy approximately 10% of the total volume. The probable structure of the casein micelle is illustrated in Figure 2.2.

2.2 Yogurt

Yogurt is a fermented milk product made by adding lactic acid bacteria to the milk. The bacteria convert lactose into lactate, which lowers the pH value. This change in environment destabilises the casein micelle, which eventually leads an aggregation of the micelles resulting in the formation of a protein network. We will use the terms casein network and protein network interchangeably through-

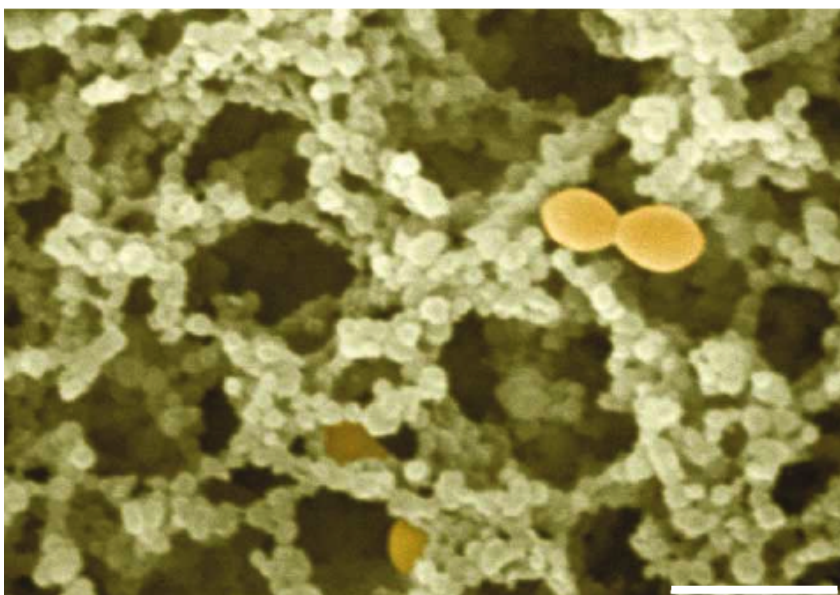


Figure 2.3: The protein network of a milk gel along with lactic acid bacteria (yellow) observed through an electron microscope. The scale bar is $2\mu\text{m}$. Image from Kalab (2010).

out the thesis. As seen in Figure 2.3, the network consists of clusters and chains of casein and constitutes a weak gel with some resistance to deformation. The strength of the gel is defined by the total solid content in the base milk as well as the density and amount of cross-linking in the network.

Even though lactic acid bacteria are used for most commercial products, as bacteria are living organisms there is a natural variability in the activity, and processes can be hard to reproduce. Glucono- δ -lactone (GDL) is a food additive that acts as acidifier when it hydrolyses in water, and is commonly used to mimic bacteria fermentations. However it has been shown that the physical properties of the protein networks created from lactic acid bacteria and GDL differ (Lucey et al., 1998a). Based on these results it was concluded that model studies performed with GDL should be verified using lactic acid bacteria as well.

The fermentation process can be roughly divided into three different pH intervals (Lee and Lucey, 2010):

- **pH 6.7 to 6.0.** Small amount of calcium phosphate is solubilised. Overall structure of the casein micelle is unchanged.
- **pH 6.0 to 5.0.** Calcium phosphate is continuously being solubilised, and complete "gone" when pH reaches 5.0. The outer layer of κ -casein shrinks, and the internal stability is weakened.
- **pH \leq 5.0.** Getting closer to the isoelectric point of casein (pH 4.6), the electrostatic repulsion diminishes and hydrophobic casein-casein attraction predominates. This eventually leads to aggregation of the entire system (the gelation point). After the gelation point additional cross-linking of micelles continues, which strengthens the gel further.

It is important to note that two similar pH developments do not imply similar physical properties of the protein network (Haque et al., 2001). Referring to Figure 1.2, a lot of process parameters exist for the production of fermented milk products that change the fermentation kinetics as well as the final product. Throughout the thesis we are mainly making investigations based on the process parameters leading up to the fermentation: Milk standardisation, homogenisation, heat treatment, and incubation temperature.

Milk standardisation is the first step in yogurt production, in which the composition of the base milk is adjusted to ensure the desired fat content. This is typically done using skimmed milk and cream. Additionally, milk powders can be used to adjust the protein content, which is often the case with low-fat yogurts. This is needed as the final strength of the protein network also relies on the total milk solid content. In general the total milk solid content for yogurt ranges between 9% to 20% for certain concentrated yogurts (Lee and Lucey, 2010).

In homogenisation the size of the fat globules is reduced ($\approx 2\mu\text{m}$) through high-pressure treatment. This produces a more stable emulsion, and a new surface layer of casein and whey is formed on the fat globules (Lee and Lucey, 2010; Yildiz, 2010). This allows for fat globules to be embedded in the protein network and thereby increases the strength of the network. The casein micelles are not affected by homogenisation.

Heat treatment has two major purposes. It is used to eliminate unwanted microorganisms, which would otherwise provide "competition" when using lactic acid bacteria. Furthermore, the denatured whey proteins interact with κ -casein on the micelle surface. This allows for more casein cross-linking and thereby more dense gels (Anema and Li, 2003).

Fermentation temperature greatly affects the speed at which GDL hydrolyses,

and the activity of the lactic acid bacteria. As a result this affects the speed at which the fermentation process occurs. Higher temperatures tend to result in a faster fermentation process, where a lot of rearrangements are made during the casein aggregation. This results in a more loose gel. At lower temperature fewer rearrangements are made during the aggregation, and denser gels are produced (Lee and Lucey, 2010).

When the pH reaches a certain value (often pH 4.6, but can be different depending on the product), the fermentation process is typically stopped by rapid cooling. This ensures the right acidity of the yogurt. While this can give a yogurt the right flavour, changing the parameters of the different processing steps can lead to very different structural developments and end results in terms of structure (Lee and Lucey, 2010).

2.3 Cheese

In cheese making the fermentation is mainly carried out by adding rennet to milk. Rennet is an enzyme and contrary to the acid fermentation described previously, enzyme fermentation does not destabilise the internal structure of the casein micelles. Instead the enzymes only break down parts of the κ -casein on the surface, which reduces the steric stability of the colloidal system, and the entire micelles eventually aggregate and form a gel network (the curd) (Dalglish and Corredig, 2012). Again, after aggregation additional cross-linking of micelles further strengthens the gel and increases the curd firmness.

When the curd has reached a suitable firmness, the cheese curd has to be cut into smaller cubes in order draw out the water (the whey). The cutting increases the gel surface to volume ratio, allowing whey to be easier separated. The time of cutting greatly affects the final product. If the curd is cut when the firmness is too low the cheese yield is reduced, or if the curd firmness is too high when the curd is cut in results it a quality reduction (Castillo, 2006). Thus, there is an incentive to be able to consistently determine a cutting point that gives the biggest yield while retaining the desired quality.

Additionally, the coagulation speed has been of interest to determine how rapidly the milk system starts to aggregate after rennet addition, which can affect the throughput in a production line. This is of course very dependent on the process parameters. Thus, in application and research related studies four parameters are typically of interest in relation to cheese making:

- **Coagulation speed.** The rate at which at aggregation starts to occur

after rennet addition.

- **Gelation point.** The point at which all the casein aggregates.
- **Curd firming.** How fast is the curd firming after the gelation point.
- **Cutting time.** The time when the curd is cut.

As will be seen in Chapter 4, a lot of process control methods have previously been investigated for monitoring or estimating these specific parameters.

CHAPTER 3

Light Propagation in Milk Products

In this chapter a brief introduction to light propagation in diffusive materials is provided, and the chapter will act as theoretical foundation for parts of Chapters 4 and 6. Initially, basic concepts of light and light scattering are introduced, and hereafter few physical models will be described. Finally, the presented topics will be put into context of Chapter 2.

3.1 Light Propagation

Light is electromagnetic radiation, which can be described as a duality between waves and particles (Jonasz and Fournier, 2011). Thereby it can be thought of as a collection of one or more photons propagating through space as electromagnetic waves. In broad terms light covers the wavelength spectrum from 10 to 10000nm, where the ultraviolet (UV) regime covers 10-400nm, the visible (VIS) regime covers 400-700nm, and the infrared (IR) regime covers 700-10000nm as shown in Figure 3.1. Often a sub category to IR, near infrared (NIR), is defined to cover 700-2500nm (Young and Freedman, 2008).

Interaction between light and matter can be observed at different scales. On

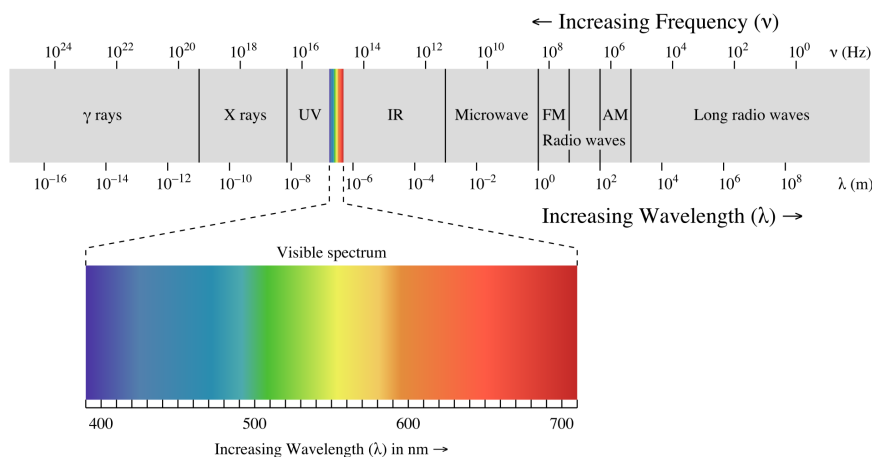
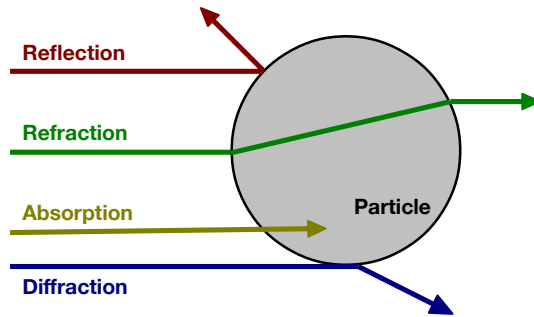


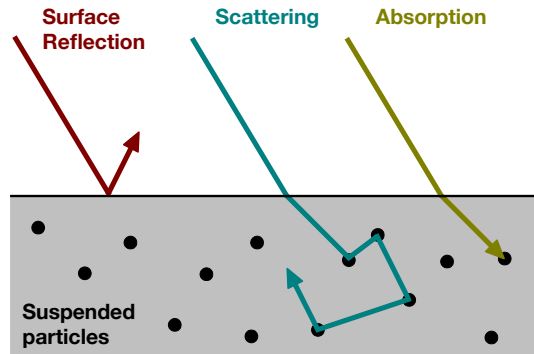
Figure 3.1: The spectrum for electromagnetic radiation. Graphics by Philip Ronan.

a microscopic scale, when a photon interacts with a particle it can either be diffracted or absorbed by the particle, or experience a change in direction (denoted scattering) due to reflection or refraction (Martelli et al., 2010). These different phenomena are illustrated in Figure 3.2(a). For simplicity we assume that scattering is elastic, meaning that the photon experience no difference in energy before and after a change in direction. Other types of scattering will be discussed in Section 3.1.2. On a macroscopic scale, light-matter interaction is typically described through absorption, reflection, refraction, or scattering, as illustrated in Figure 3.2(b).

The specific phenomenon exhibited between light and matter is dependent on both wavelength and the composition of the material. Materials can e.g. be classified as transparent, translucent, turbid, or reflective, due to chemical composition or specific spatial arrangement of the particles in the material. In this way, optical properties often attest to the properties of the material itself. The chemical composition of a material can be investigated through its absorption properties. Chemical compounds absorb at different wavelengths, characterised by their absorption spectra, which often contains a unique combination of absorption peaks. Thus, the absorption spectra are sometimes denoted as spectral fingerprints (Siesler et al., 2008). Absorption spectra are commonly investigated through near-infrared spectroscopy, which is a family of methods that have been widely applied in pharmaceutical and agricultural applications (Roggo et al., 2007; Huang et al., 2008). Scattering is dependent on the microstructure of the sample, and is e.g. affected by the density of the material,



(a) Microscopic scale.



(b) Macroscopic scale.

Figure 3.2: Light-matter interaction on different levels of scale.

the spatial distribution of the scattering particles (homogeneous, heterogenous, etc.) as well as the particle sizes in the material, which will be discussed later in this section. Scattering is also dependent on the wavelength of the light. However, contrary to the spectral fingerprints in the absorption spectra, scattering decreases monotonically as a function of the wavelength (Jonasz and Fournier, 2011). Investigating the absorption and scattering properties of a material can hereby be used to probe information on both the chemical and micro structural properties of the material.

A group of materials that has been thoroughly investigated in regard to both medical and agricultural applications is biological tissues (Martelli et al., 2010).

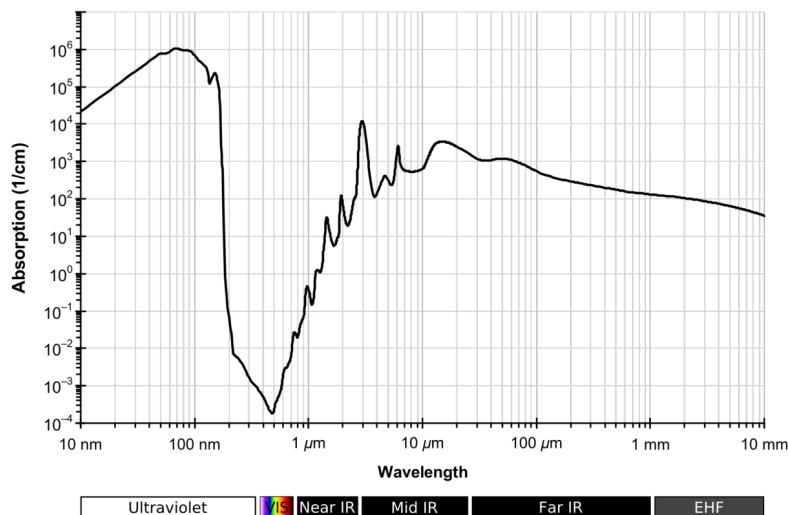


Figure 3.3: Water absorption spectrum. Image by Palosirkka.

Generally biological tissues are turbid materials, in which light exhibits diffusive behaviour, meaning that the scattering properties dominate the absorption properties within the VIS regime. Biological tissue often contains a considerable amount of water, and thereby it is important to pay attention to the absorption spectrum of water. From Figure 3.3 it can be seen that water is transparent for the entire VIS spectrum, however it significantly absorbs light when stepping into the UV or NIR regimes. The effects of the scattering properties can thereby be hard to detect in these areas. This makes the VIS regime particularly well suited for investigating the scattering properties of biological tissue (Jonasz and Fournier, 2011).

Thus, when shining visible light into biological tissue most of the light penetrates the surface of the material, where it is initially refracted (described by the refractive index) and hereafter scattered beneath the surface of the tissue (Martelli et al., 2010). After a number of scattering events, some of the light eventually exits the tissue. This exiting light is denoted as diffuse reflectance or diffuse transmittance depending on which side of the tissue it is observed at, as illustrated in Figure 3.4.

If a narrow light beam is used, a decay of the diffuse reflectance can be observed emanating from the incident point of the light. The light close to the point of incidence has typically undergone single or few scattering events, whereas light further away from the point of incidence has typically been scattered multiple

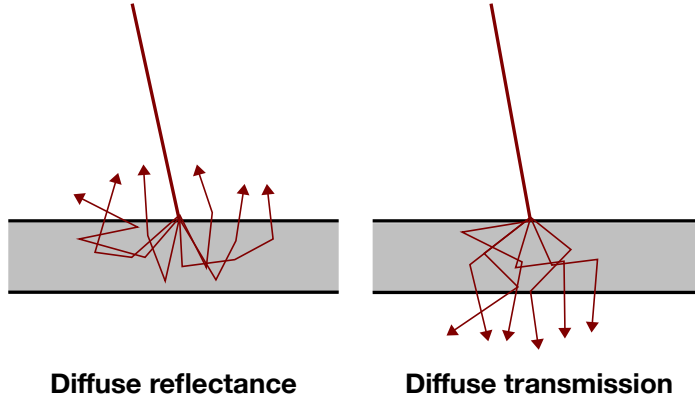


Figure 3.4: Examples of diffuse reflectance and diffuse transmission when a material is illuminated by a light beam.

times. Likewise for the diffuse transmittance a decay can be observed, although it is a simpler signal as mainly light that has been scattered multiple times. These decays are highly dependent on the underlying particle size distribution as illustrated in Figure 3.5. Here it can be seen how the decay depends on particle size and particle concentration when a narrow light beam is shone orthogonally into the material.

Increasing the particle concentrations results in more scattering, but larger particles also increases the scattering. Furthermore, increased scattering results in higher intensities near the light incident points. In general, large particles scatter light more efficiently, and more precisely the scattering efficiency is proportional to the *size parameter*. Assuming the scattering particle is spherical, the dimensionless size parameter is defined as (Martelli et al., 2010):

$$s = \frac{2\pi r}{\lambda}, \quad (3.1)$$

where r is the radius of the particle and λ is the wavelength of the light. From the equation it can be seen that both larger particles and lower wavelengths increase the scattering efficiency.

Light scattering is generally described by Mie scattering theory (Mie, 1908), with the special case of very small particles, denoted Rayleigh scattering theory

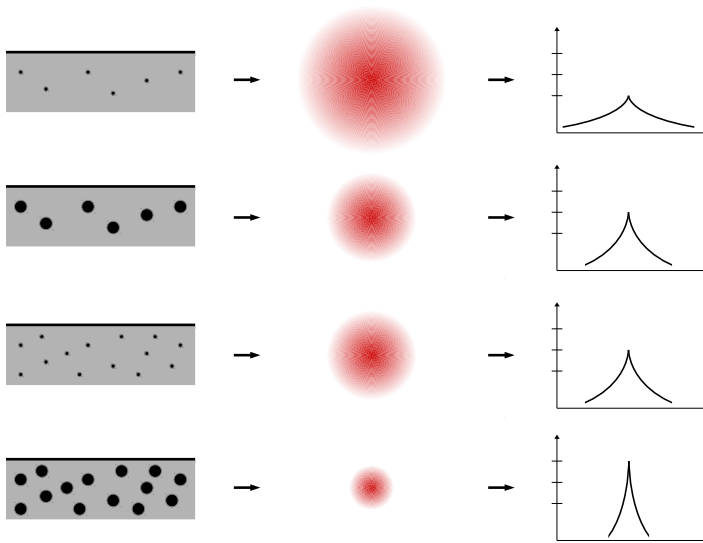


Figure 3.5: The decay of the diffuse reflectance illustrated for materials with different density and size distribution of the suspended particles. The first column depicts the different materials, the second column depicts the spatial distribution of the diffuse reflectance, and the third row shows an intensity profile through the centre of the signal.

Table 3.1: Naming convention for scattering in terms of the size parameter, s , from Equation 3.1, as well as the corresponding scattering decays across wavelength.

Scattering name	Size parameter	Scattering decay rate
Rayleigh	$s \ll 1$	λ^{-4}
Mie	$s \approx 1$	λ^{-1}

(Rayleigh, 1899). In terms of the size parameter in Equation (3.1), we consider Mie scattering when the wavelength is proportional to the particle size ($s \approx 1$) and Rayleigh scattering when the wavelength is much larger than the particle size ($s \ll 1$). A major difference between the two types of scattering is that Rayleigh scattering is more wavelength dependent, and decays faster across wavelengths (Jonasz and Fournier, 2011). The decay rates are summarised in Table 3.1.

Thus, the size of the particles affects both the scattering efficiency and the decay rate of the scattering efficiency across wavelengths. Finally, the particle size is also related to the *phase function*; a probability density function that determines the direction of the light after it has been scattered by a particle. The phase function is also dependent on the size parameter in Equation (3.1), and when particles are small compared to the wavelength of the light, scattering is isotropic. If the particles are large compared to the wavelength of the light, the direction of scattering typically becomes elongated. An example of a forward lobed phase function is given in Figure 3.6. The effects of a forward lobed probability density function are most prominent when considering single or few scattering events. For multiple scattered light, the ensemble of scattering events eventually becomes completely random and thereby isotropic.

3.1.1 Physical Models

Following the notation by Frisvad et al. (2007), macroscopic light transport in diffusive media can be described through the *Radiative Transfer Equation* (RTE)(Chandrasekhar, 1960):

$$(\vec{\omega} \cdot \nabla)L(\mathbf{x}, \vec{\omega}) = -\mu_t L(\mathbf{x}, \vec{\omega}) + \mu_s \int_{4\pi} p(\vec{\omega}', \vec{\omega})L(\mathbf{x}, \vec{\omega}')d\omega', \quad (3.2)$$

where $L(\mathbf{x}, \vec{\omega})$ is the radiance at point \mathbf{x} in direction $\vec{\omega}$. Radiance (or light) is measured in energy flux per solid angle per projected area. μ_t , μ_s , and $\mu_a =$

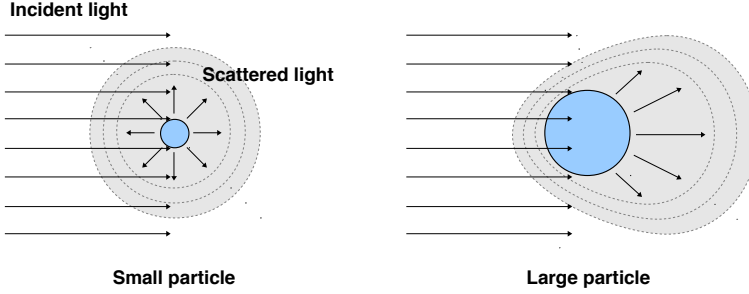


Figure 3.6: Illustration of how particle size can affect the phase function (depicted in gray).

$\mu_t - \mu_s$ are the extinction, scattering, and absorption coefficients respectively. p denotes the phase function, which is defined by a probability density function for the outgoing direction of the scattered light. The left hand side of the equation is the change of light along a ray, which is explained by two terms on the right hand side: the attenuation and the incoming scattering from all directions.

When multiple scattered light is considered in practice, the Henyey Greenstein model (Henyey and Greenstein, 1941) is commonly considered as a single number parameterisation of the phase function in 3.2. It is represented by the asymmetry factor g , which is a measure of the asymmetry in the single scatter pattern

$$p(\theta) = \frac{1}{4\pi} \frac{1 - g^2}{[1 + g^2 - 2g \cos(\theta)]^{3/2}}, \quad (3.3)$$

Here, $-1 < g < 1$, $g = 0$ denotes isotropic scattering, and negative and positive values of g denote backward and forward scattering respectively. Figure 3.7 shows the single scatter patterns for different values of g as well as different inclination angles of the incident light beam. From here it is clear that an oblique incident angle of the light can provide significantly more information on g compared to an orthogonal light beam.

While Equation (3.2) provides a good description of light diffusion in diffusive media, no practical analytical solutions are available (Martelli et al., 2010). It can be solved numerically through Monte Carlo simulations, but this is inefficient for real-time computations, which are required for process control ap-

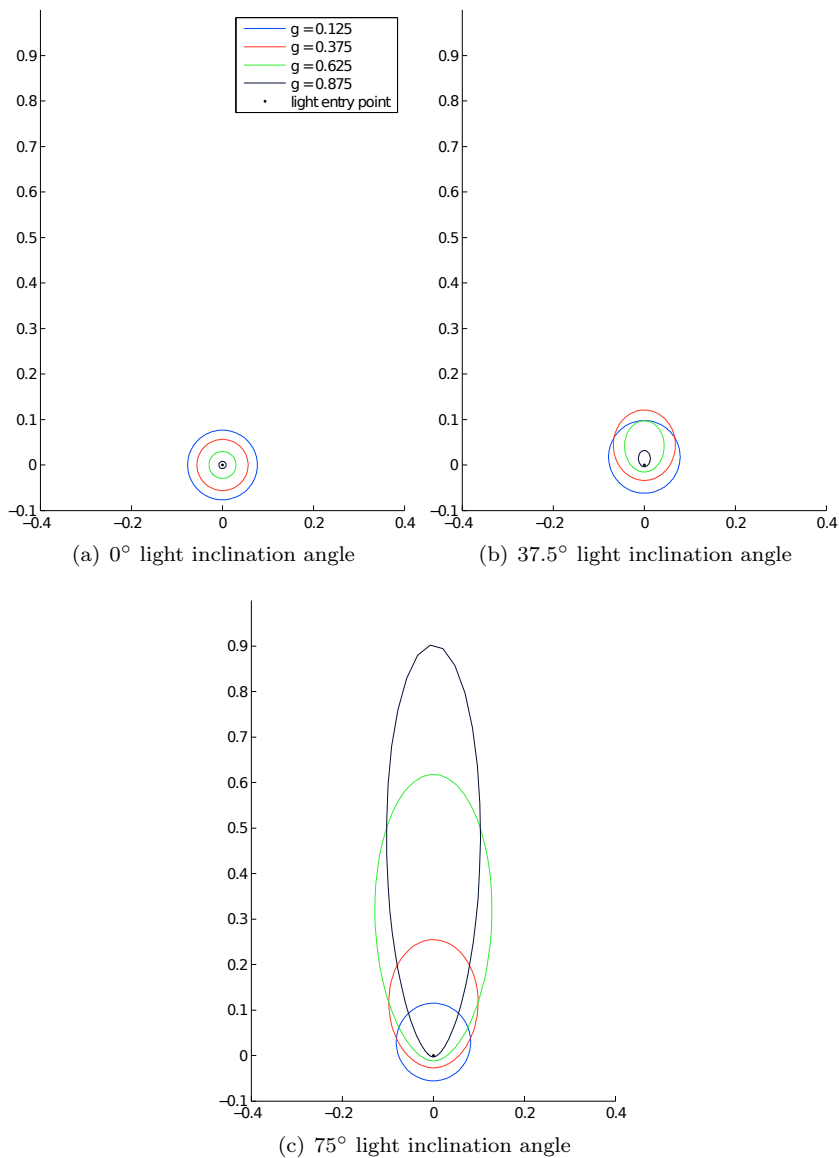


Figure 3.7: The single scattering patterns visualised for positive values of g and different light inclination angles. The shown curves are derived from the Henyey Greenstein model. At 0° the incident light is orthogonal to the illuminated surface, and for inclination angles $> 0^\circ$, the light comes from the bottom side of the plot.

plications. However, various approximations to the RTE have been suggested and a common variant is the diffusion approximation. Here it is assumed that all light has been scattered multiple times (thus, single scattering is neglected), and the scattering coefficient of (3.2) is replaced by the reduced scattering coefficient $\mu'_s = \mu_s(1 - g)$. By using μ'_s instead of μ_s , direct measures of g are avoided. Based on the diffusion approximation, Farrell et al. (1992) derived a (calculation wise) simplified analytical expression for semi-infinite diffusive media illuminated orthogonally by a narrow light beam. The diffuse reflectance of multiple scattered light, R , is described as a function of the distance, r , to the point of incidence:

$$R(r) = \frac{a'}{4\pi} \left[\frac{1}{\mu'_t} \left(\sqrt{3\mu_a\mu'_t} + \frac{1}{\rho_1} \right) \frac{\exp(-\sqrt{3\mu_a\mu'_t} \rho_1)}{\rho_1^2} + \left(\frac{1}{\mu'_t} + \frac{4A}{3\mu'_t} \right) \left(\sqrt{3\mu_a\mu'_t} + \frac{1}{\rho_2} \right) \frac{\exp(-\sqrt{3\mu_a\mu'_t} \rho_2)}{\rho_2^2} \right], \quad (3.4)$$

where $a' = \mu'_s/(\mu_a + \mu'_s)$ is the transport albedo, i.e. the proportion of light reflected by the surface, and $\mu'_t = \mu_a + \mu'_s$ is the extinction coefficient. A is defined as the mismatch in refractive index between air and the diffusive media, and can be calculated by the empirical formula originally given by Groenhuis et al. (1983). ρ_1 and ρ_2 are quantities introduced as boundary conditions in the derivation of the analytical expression and given by:

$$\rho_1 = \left[\left(\frac{1}{\mu'_t} \right)^2 + r^2 \right]^{1/2}, \quad (3.5)$$

$$\rho_2 = \left[\left(\frac{1}{\mu'_t} + \frac{4A}{3\mu'_t} \right)^2 + r^2 \right]^{1/2}. \quad (3.6)$$

From the above it can be seen that the entire expression in (3.4) can be described entirely through μ_a and μ'_s . Graaff et al. (1992) further makes an approximation to the wavelength dependency of μ'_s through a power function, in order to obtain more information on the particle size distribution:

$$\mu'_s = \alpha\lambda^{-\beta}. \quad (3.7)$$

Here, α is the signal amplitude, and related to particle density, and β is related to the ratio between wavelength and particle radius and can thereby provide information on the particle sizes. Following the notation of Table 3.1 $\beta = 4$ corresponds to Rayleigh scattering and $\beta \approx 1$ corresponds to Mie scattering. A final important quantity to consider is the mean free path (MFP), which is based on both the absorption and scattering coefficients (Martelli et al., 2010):

$$\text{MFP} = \frac{1}{\mu'_t} = \frac{1}{(\mu_a + \mu'_s)}. \quad (3.8)$$

MFP describes the average path length a photon travels into a given material before it is scattered for the first time. In Chapter 6 this property will be considered further in an extension to Equation 3.4.

3.1.2 Additional Scattering Types

In the previous sections we assumed that scattering was an elastic process. However, scattering can be divided into three groups:

- **Elastic scattering.** Assumes no change in energy between scattering events. This is what has been considered until now in this chapter, and the majority of optical methods in Chapter 4 rely on this kind of scattering. Typically, elastic scattering can be quantified by four parameters: μ_a , μ'_s , g , and the refractive index.
- **Inelastic scattering.** There is a change in energy between scattering events. This energy can partly be attributed to fluorescence, in which the wavelength of the incident light is different from the scattered light (Young and Freedman, 2008). This phenomena is exploited in Confocal Scanning Laser Microscopy, see Section 4.1.2
- **Quasi-elastic scattering.** Assumes no change in energy between scattering events. However, the wavelength of the scattered light shifts due to Doppler shifts caused by moving particles. This can be used to get information on the mobility of the scattering particles (Alexander and Dagleish, 2006).

While the concept of inelastic scattering is straightforward, quasi-elastic scattering requires a brief introduction. This phenomenon can only be observed when using a coherent light source, such as a laser. A laser is monochromatic coherent

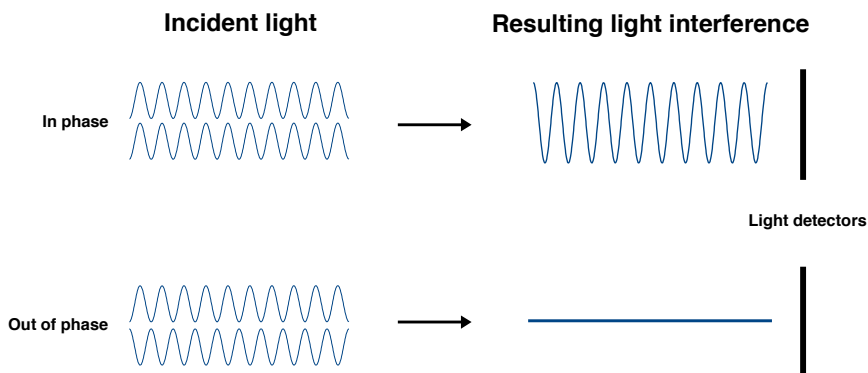


Figure 3.8: Examples of light interference effects. Light in phase experiences constructive interference, resulting in a high intensity being captured by the detector. For light out of phase the deconstructive interference results in a low intensity being captured by the detector. In our case the change in phase is caused by Doppler Shifts due to moving particles.

light, meaning that the light waves are in phase at every point in space. This property allows for indirect observation of Brownian motion, which is random motion of particles suspended in a host medium, e.g. a fluid. The motion is due to the particles colliding with the molecules of the host medium, and the speed of this motion is highly dependent on the size of the suspended particles (Alexander and Dagleish, 2006). Thus, the Brownian motion can be indirectly observed as intensity fluctuations (denoted speckle) in scattered laser light, due to destructive or constructive interference caused by Doppler shifts. The interference effects causing speckle is illustrated in Figure 3.8. This type of speckle is exploited by a family of methods presented in Section 4.2.1.3.

3.1.3 Milk Products

Milk and fermented milk products are diffusive materials (Martelli et al., 2010), and thereby light interaction is dominated by scattering in the VIS regime. The main scatterers in milk are the fat globules and the casein micelles. As mentioned in the previous chapter, the fat globules are significantly larger than the

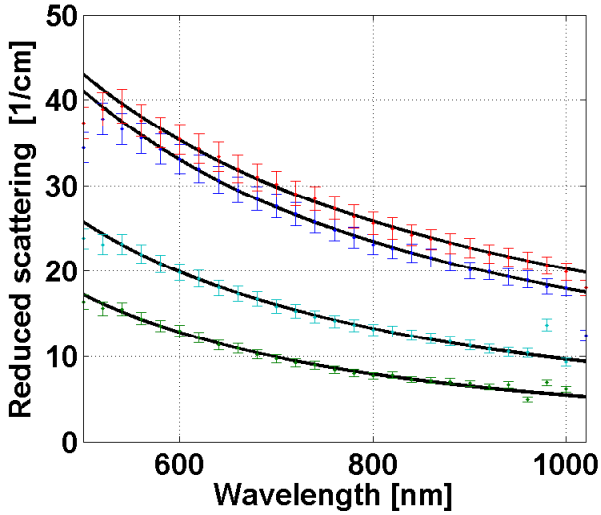
casein micelles, and following Equation (3.1) they scatter light more efficiently. In fact, the globules are close to Mie scattering, whereas the casein micelles are closer to the Rayleigh scattering.

Combining the low absorption properties and the wavelength dependent scattering decays of Table 3.1, this explains why full-fat milk appears white, as all wavelengths are scattered almost equally by the fat globules. However, for low-fat milk the scattering contribution from the casein micelles becomes significant, meaning that the scattering becomes more wavelength dependent. Shorter wavelengths are hereby scattered more than the longer wavelengths, explaining why low-fat milk tends to have a blue tint.

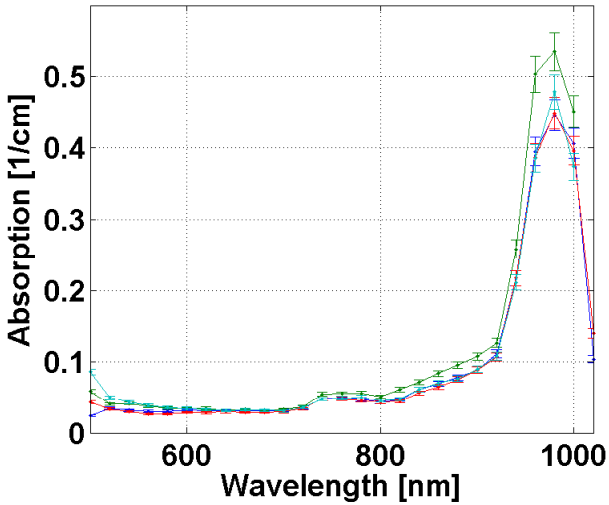
During milk fermentation the particle size distribution naturally changes due to the aggregation of the casein micelles. While the final protein network does not have an inherent particle size, the scattering properties change (Claesson and Nitschmann, 1957). Thereby, the scattering properties are of great interest for fermented milks as some of the scattering can be attributed to the aggregated casein micelles. In terms of quasi-elastic scattering, the aggregation of the casein micelle will greatly affect the particle mobility and thereby the observed speckle (Alexander and Dagleish, 2004).

In Nielsen et al. (2013) we used Photon Time-of-Flight Spectroscopy to investigate the absorption and scattering properties from 550-1000nm for several commercially available milk products. Some of the results are presented in Figure 3.9. The green and cyan curves are milk with 0.5% and 1.5% fat respectively and 3.5% protein. The Blue and red curves are yogurts with 0.5% and 1.5% fat and 4.5% and 4.0% protein respectively. It can be seen that both fat content and the fermentation changes the scattering properties of the products. This is despite the small differences in protein content. The small differences in protein content of the fermented products can be observed at the smaller wavelengths, where protein contributes most to scattering, and the blue curve is steeper due to Rayleigh scattering. Also it can be seen that $\mu_a \ll \mu'_s$ as expected, and water absorption peaks can be observed around 750nm and 970nm as previously noted by (Palmer and Williams, 1974).

Moreover, from μ_a and μ'_s the MFP can be calculated. For the least scattering product (0.5% milk) the MFP approximately ranges from 0.6mm to 2mm in the shown wavelength interval, and for the most scattering product (1.5% yogurt) the MFP approximately range from 0.3mm to 0.5mm. This also gives an idea about the penetration depth of the technique in relation to milk and yogurt products.



(a)



(b)

Figure 3.9: Reduced scattering and absorption properties for different dairy products. The green and cyan curves are milk with 0.5% and 1.5% fat respectively and 3.5% protein. The Blue and red curves are yogurts with 0.5% and 1.5% fat and 4.5% and 4.0% protein respectively.

Instrumentation

This chapter introduces the instrumentation that has been used for data acquisition during the work resulting in this thesis, including a thorough introduction to the CIFQ workbench. Also provided, is a brief overview of previous and existing methods that have been used to monitor milk fermentations, with a strong emphasis on the optical methods. Although the main focus of this thesis is yogurt, related work will be presented in the context of cheese making. Finally, similarities and differences between the CIFQ workbench and related optical methods will be pointed out.

4.1 Applied Instrumentation

4.1.1 CIFQ Workbench

In this section we present the CIFQ workbench, which is the primary instrument used during the work of this thesis. As mentioned in Chapter 1, the instrument has been developed parallel to this project, and the author of this thesis has aided in the continuous development of the system through direct hands on experience with the system. It is a novel imaging modality in relation to dairy process control, and from here on the modality will be referred to as 2D Static

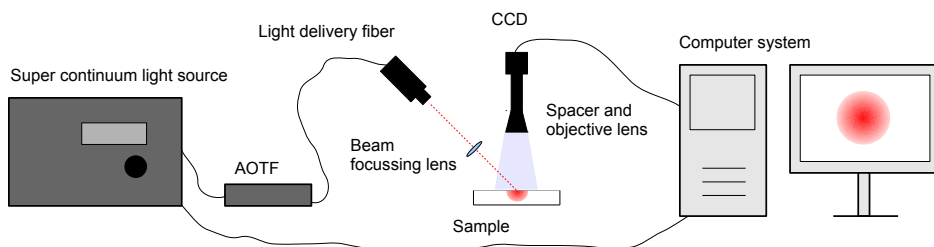


Figure 4.1: A schematic view of the hyperspectral vision system. Additionally two lenses were installed, one in front of the laser beam and one in front of the camera.

Light Scattering (or 2DSLS). The system is a generalisation of the commercial product VideometerSLS (*Videometer A/S, Hørsholm, Denmark*), and was introduced in (Nielsen et al., 2011b,a). Following its introduction, several evolutionary upgrades have been performed as knowledge on the system as well as data sets have been gathered. A schematic of the setup is presented in Figure 4.1

It consists of two major parts: A light delivery system, and a detector system. The light delivery system consists of a super continuum light source (*SuperK Extreme EXW-12, NKT Photonics, Birkerød, Denmark*), which produces a broad white lightband (400-2400nm).

The light is filtered by an acousto-optic tunable filter (AOTF) (*SuperK SELECT, NKT Photonics, Birkerød, Denmark*), and the combined system produces a Gaussian shaped polarised laser beam, in the range 465-1030nm, at high spectral resolution (approximate $\pm 5\text{nm}$). The system can hereby be considered hyperspectral. Furthermore, the laser beam is focused down using a beam-focusing lens (focal length = 40mm), which gives a wavelength dependent beam waist ranging from 100-200 μm in the wavelength interval. The laser is focused on the surface of the investigated sample at an oblique incident angle ($\approx 45^\circ$).

The resulting spatial distribution of diffuse reflectance is captured using a CCD camera with an objective lens. A spacer tube is installed in between camera and lens to enhance the level of zoom. Throughout the work of this thesis, two different detector systems have been used, which are summarised in Table 4.1. The main difference between the two capturing systems is the increased field of view of the most recent detector system. With the increased field of view of

Table 4.1: The two different CCD and objective lens setups used throughout the thesis.

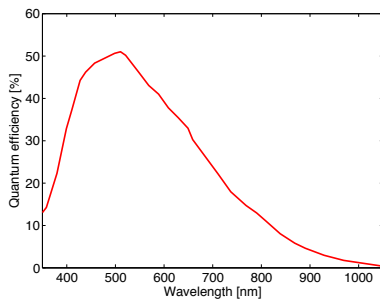
Camera	Spacer	Objective lens	Pixel resolution	Spatial resolution
Grasshopper CCD, Point Grey Research, Richmond, Canada	6.5cm	23FM50L, Tamron Co. Ltd. Saitama, Japan	1200 × 1600	(3.2 μ m) ²
AM-800GE CCD, JAI, Yokohama, Japan	8.5cm	LM50XC, Kowa Co. Ltd., Nagoya, Japan	2472 × 3296	(3.2 μ m) ²

most dynamics of the diffuse reflectance can be captured better. The working distance is ≈ 5 cm in both setups, thus data is captured remotely. The acquisition time has changed throughout the work of this thesis. At its current state the system captures a set of high dynamic range (HDR) images at approximately 2 seconds/wavelength.

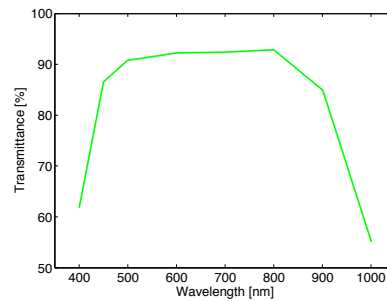
Figure 4.2 presents the quantum efficiency of the CCD, the transmission spectrum of the objective lens, and the output power of the laser. While the wavelength range spanned by the AOTF can be changed via add-ons, it can be seen that the detector setup has to be changed entirely if wavelengths outside the visible regime should be explored. Images of the setup can be found in Figure 4.3.

Cf. Figure 4.2 the image intensities are different between wavelengths, due to a wavelength dependent combined system response. In general, the entire dynamic range of the light intensities cannot be spanned by a single exposure time. Thus, high dynamic range (HDR) imaging is required to avoid saturated areas or areas with low SNR (Mann and Picard, 1994). This is done by capturing layers of the same image at different exposure times (exposure times range between 160 μ s and 1.6s). For each pixel in the image, the layer with the longest possible exposure time, without saturation, is selected. The final pixel value in the HDR image is obtained by normalising with the corresponding exposure time.

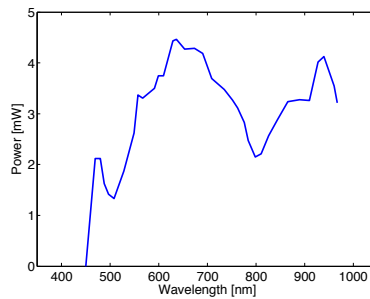
A conceptual view of the 2DSLS signal (or diffuse reflectance image) is shown in Figure 4.4, which illustrates the incident light beam in relation to the sample surface. Furthermore, it can be seen that the signal is symmetrically elongated along the light direction. The presented colourmap convention will be used for all diffuse reflectance images throughout the thesis. We will use the terms 2DSLS signal and diffuse reflectance image interchangeably throughout the thesis.



(a) CCD quantum efficiency



(b) Objective lens transmission spectrum

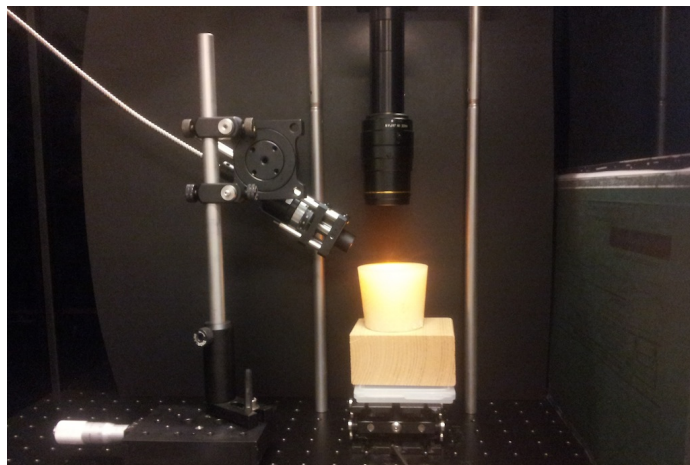


(c) Laser output power

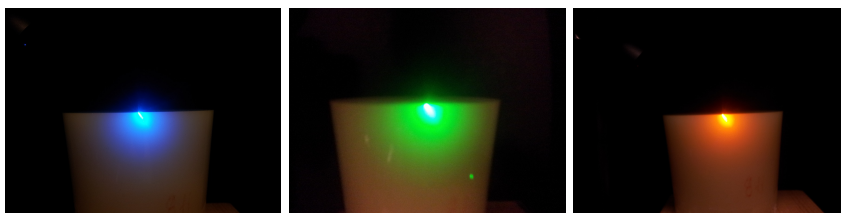
Figure 4.2: CCD quantum efficiency, objective lens transmission spectrum, and the output power of the laser. Combined, these components define the amplitude of the system response.



(a) The entire 2DSLS setup



(b) Light delivery fibre and objective lens



(c) 470nm

(d) 510nm

(e) 600nm

Figure 4.3: (a) shows the native 2DSLS setup, where the parts of the light delivery system is highlighted. The black box on the righthand side contains the light delivery fibre and CCD detector system as shown in (b). (c) through (e) show different wavelengths illuminating a solid epoxy optical phantom.

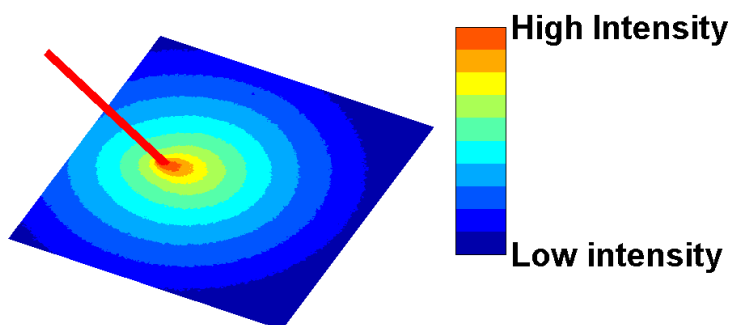
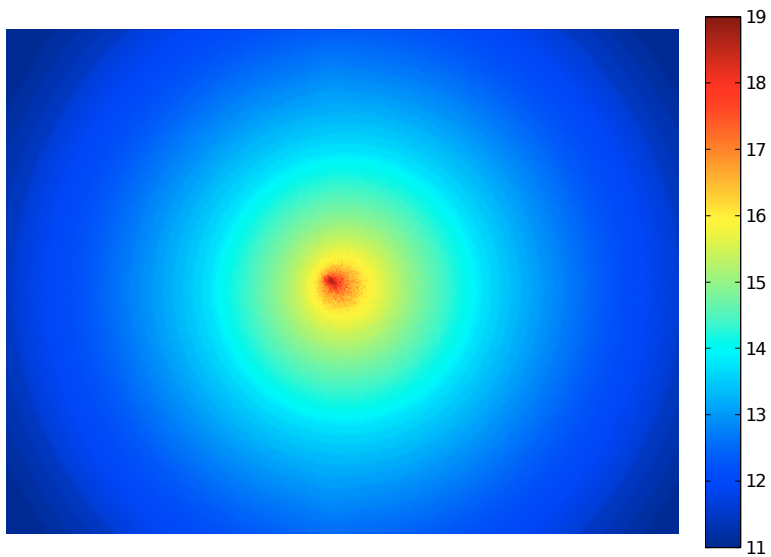


Figure 4.4: Conceptual view of the 2DSLS signal. The presented colourmap convention will be used throughout the thesis.

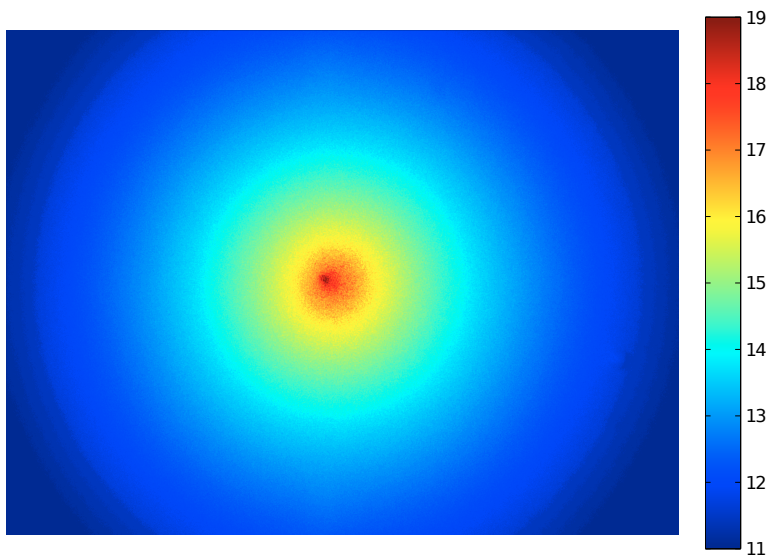
Concrete data examples of milk and fermented milk illuminated at different wavelengths are shown in Figure 4.5 and 4.6. It can be seen that the diffuse reflectance images consist of the incidence point of the light (highest intensity) and hereafter a diffusion of the light. Close to the point of incidence, light has undergone few scattering events as can be seen by the elongated isocontour in which effects of the phase function, Equation (3.2), can be observed. Moving away from the point of incidence, multiple scattering eventually predominates as can be seen as the isocontours becoming isotropic. This is due to multiple scattered light being completely random. Also considering Figure 4.5 and 4.6, a wavelength dependency can be observed. The shorter wavelengths are scattered more and therefore reaches isotropic scattering closer to the point of incidence, whereas elongation effects from single scattering are more prominent for the longer wavelengths.

In addition to the light diffusion, a speckle interference pattern can be observed as an underlying high frequency pattern. Looking at Figure 4.5 and 4.6 the speckle can be seen quite clearly near the point of incidence. Additionally, for Figure 4.6 the speckle can vaguely be seen further away (at log-intensity values 12-13) especially for the fermented milk samples.

The speckle is due to the coherency of the light source, which can get out of phase due to the Doppler effect, as described in Section 3.1.2, or simply by differences in the path length travelled of the diffuse reflected light. This has been studied previously in relation to several phenomena such as: Brownian motion (quasi elastic scattering), flow (Briers and Webster, 1996), surface irregularities (Chandley, 1976), and scattering in turbid media in general (Piederrière et al., 2004b). In some applications it is simply considered noise (Goodman, 1976).

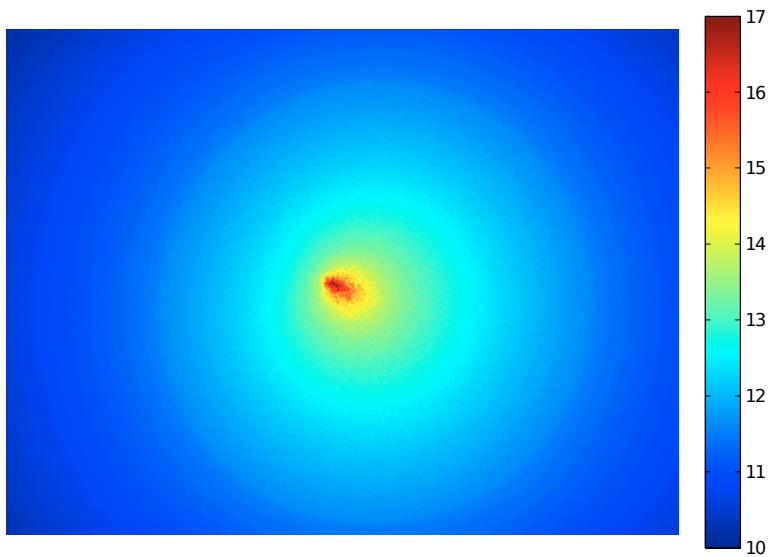


(a) Milk (1.5% fat), 500nm

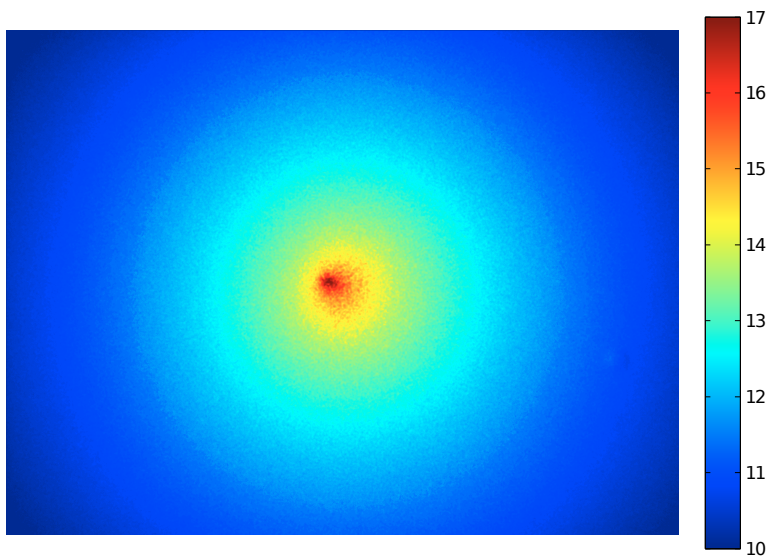


(b) Yogurt (1.5% fat), 500nm

Figure 4.5: Log-transformed diffuse reflectance images at 500nm. The incident light comes from the top left corner of the image.



(a) Milk (1.5% fat), 900nm



(b) Yogurt (1.5% fat), 900nm

Figure 4.6: Log-transformed diffuse reflectance images at 900nm. The incident light comes from the top left corner of the image.

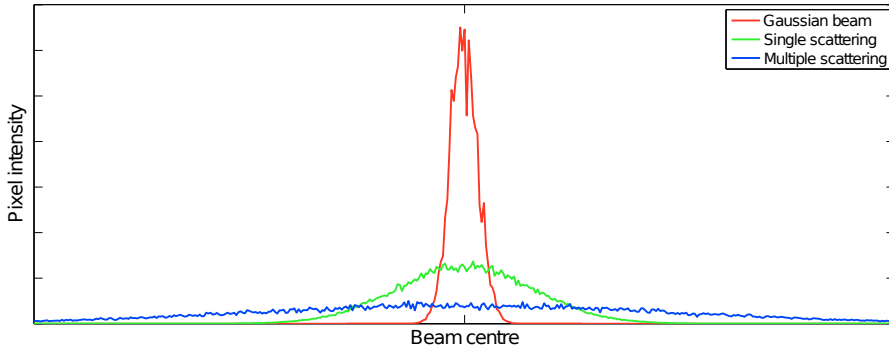


Figure 4.7: A one-dimensional view of the different contributions in the 2DSLS signal. The highest amplitude corresponds to the reflection of the incident Gaussian beam. The light intensity decays rapidly hereafter, and close to the beam centre the single scattering contribution predominates. Moving further away from the beam centre, only effects from multiple scattered light can be seen. Additionally, all three contributions are affected by speckle due to the coherency of the light.

Spatial speckle effects, as seen in the diffuse reflectance images, typically arise from surface irregularities and scattering in turbid media, and the effects can be confounded (Guyot et al., 2004). Additionally, the spatial speckle size increases as the wavelength of the light increases (Viasnoff et al., 2002). Dynamic speckle effects (intensity fluctuations) arise from flow or Brownian motion, and are typically analysed using time resolved measurements, as will be presented in Section 4.2.1.3. Thus, in order to avoid the spatial speckle effects becoming "blurred" due to dynamic speckle, the exposure time must be short relative to the correlation time of the dynamic speckle (Piederrière et al., 2005). However, as the diffuse reflectance images are created from multiple HDR layers with different exposure times, different areas of the images will be affected differently by the dynamic speckle effect. Thus, according to the spatial location in the diffuse reflectance images there may be contributions from three different speckle phenomena. The speckle part of the diffuse reflectance images is investigated further in Paper F.

In summary the 2DSLS signal is complex and consists of contributions from several phenomena, as illustrated in Figure 4.7. In Section 6.1 different ways to quantifying these phenomena, both independently and combined, are considered.

Similar 2D imaging modalities have previously been applied, and very much in

relation to predicting quality parameters of apples (Cho and Han, 1999; Lu, 2004; Peng and Lu, 2007; Qing et al., 2008; Romano et al., 2011). There are four major additions to the systems used in these studies and our 2DSLS setup:

- **Hyperspectral.** The increased spectral resolution allow for easier investigation of wavelength dependent phenomena.
- **Coherent light.** Interference effects in form of speckle can be observed.
- **Oblique incident angle of the light.** Cf. Figure 3.7, information from single scattering effects, and thereby effects of the phase function, can be investigated.
- **Higher spatial resolution.** Small areas can be observed, which e.g. allows for measuring the mean free path and asymmetry related parameters in the single scattered light.

As mentioned in Chapter 1, the presented system can be considered a laboratory workbench. Through the flexibility of the setup, a broad range of parameters such as spatial setup, wavelengths, and signal quantification can be investigated. From these investigations more focused and cost-efficient systems can be designed, e.g. using only the "necessary" wavelengths in form of laser LEDs or specific camera setups.

4.1.2 Confocal Scanning Laser Microscopy

Microscopy has been widely used in order to study the microstructure of fermented milk products (Kalab, 1981; Skriver, 1995; Sandoval-Castilla et al., 2004; Folkenberg et al., 2005). Especially Confocal Scanning Laser Microscopy (CSLM) has become popular within the last two decades (Lucey and Singh, 1997; Lucey et al., 1998b,a). This microscopy modality is well suited for studying the microstructure of milk gels as it requires little sample preparation. By relying on observing inelastic scattering, specific compounds can be targeted using fluorescent stains. These stains can target specific molecules such as fat and protein.

One way to apply the fluorescent stain to a sample is through an acetone solution of the stain. The solution is applied to a microscopy slide, and when the acetone has fully evaporated the sample is applied on top of the fluorescent stain. When the sample has rested for a couple of minutes it is ready for measurements. A stained sample is illuminated by a certain wavelength, and the fluorescent

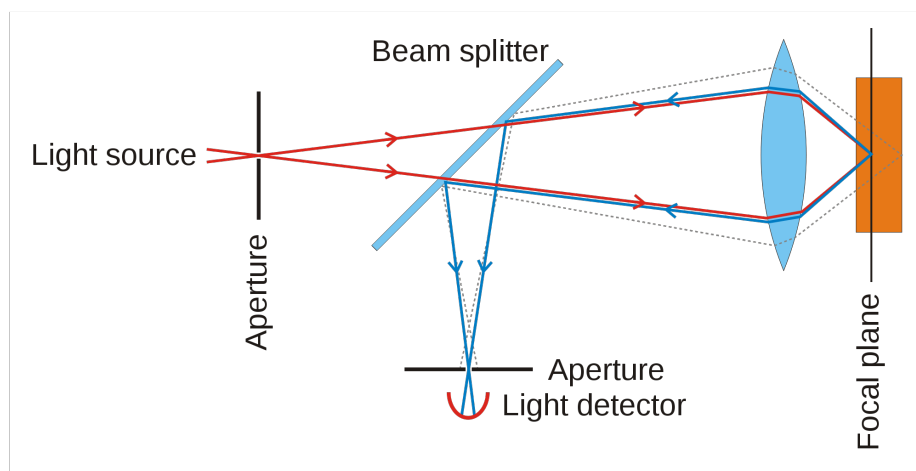


Figure 4.8: The principle of confocal laser scanning microscopy. The red lines denote the light which hits the sample of interest in the focal plane. The blue lines denote the emitted light from the fluorescent dye in the focal plane, which is captured by the detector. The dashed black lines are emitted light, which is out of focus, and does not hit the detector. Graphics by Magnus Manske.

stained molecules excite another wavelength, which is captured by a detector. The confocal principle of CSLM is illustrated in Figure 4.8. By using a point light source and pinholes in a confocal setup, the optical resolution and contrast can be increased. The point light is scanned across the stained sample, and primarily light in the focal plane is captured.

As light is mainly collected from a single plane is captured, CSLM can be used to perform optical sectioning and thereby create 3D views of the investigated sample. However, depending on the task, it can be more relevant to randomly sample 2D slices at the same depth to ensure a more representative view of the gel network. Figure 4.9 shows examples of three different stirred yogurts. The pixel intensities correspond to a combination of the focus and the amount of protein present at the given pixel. Bright pixels denote high protein content, as this was the chosen stain, whereas dark pixels typically denote the pores containing the continuous phase such as whey.

From the example images, it can be seen that the amount of protein appears to increase both when fat and protein are added to the base yogurt. While this change in total intensity is straightforward when the protein content is increased, the change in total intensity when the fat content is increased can be attributed

to the homogenisation of the milk, cf. Chapter 2. In homogenised milk the fat globules are covered with a protein layer, thus the amount of visible protein changes in the CSLM images.

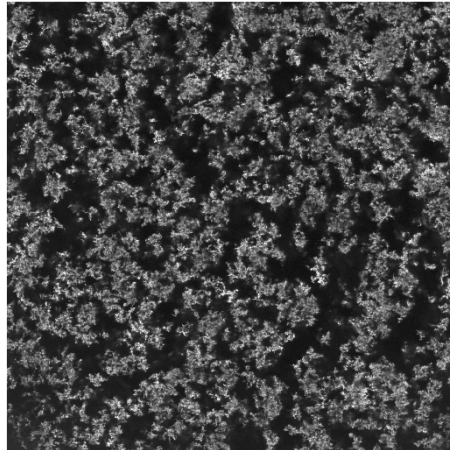
4.1.3 Small Amplitude Oscillatory Rheology

Rheology is the study of deformation and flow of matter, often in form of viscous fluids. Rheology is performed by quantifying the sample response to physical force or movement and can be measured in multiple ways, but can be generalised into two major categories: Large deformation and small deformation rheology. Both categories have found their place within the field of food science (Steffe, 1996). Large deformation rheology is destructive, however in terms of milk gels it has been found to correlate well with the oral perception of viscosity, due to the similarities to mastication. Small deformation rheology is non-destructive and correlates well with non-oral perception of viscosity, e.g. stirring a yogurt with spoon (Skriver et al., 1999). A major advantage of small deformation rheology is that it can be used to continuously monitor a developing system such as milk fermentations.

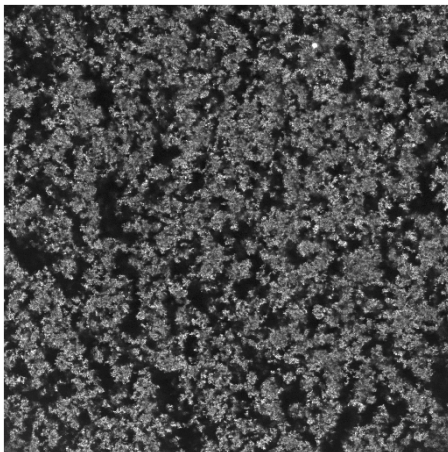
The variant of rheology applied in this thesis is the Small Amplitude Oscillatory Rheology (SAOR) (Bohlin et al., 1984). It has become a popular method for studying milk fermentation in general, and is furthermore often used as reference when studying optical methods. In SAOR a small sinusoidal deformation is applied, in which small deformation is defined as a relative deformation, which does not disrupt the development of the network structure (Lee and Lucey, 2010). Fermented milks are viscoelastic, meaning that they express both ideal elastic and ideal viscous behaviour. These behaviours can be described by the storage (elastic) modulus (G'), which is the amount of energy stored per deformation cycle, and the loss (viscous) modulus (G''), which is the amount of energy lost as dissipation per deformation. Throughout the thesis, we will only report the storage modulus (G') when rheological measurements are presented.

Different geometries can be used in SAOR. However, the most commonly used geometry, in relation to milk gels, is the double gap concentric cylinder. This measuring geometry has a large interface between sample and geometry, which is ideal for weak gels such as fermented milk products. The measuring geometry is shown both separately and installed in a rheometer in Figure 4.10.

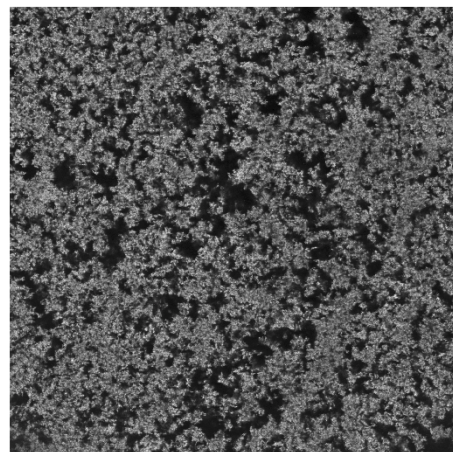
The typical rheological behaviour of a GDL milk fermentation can be seen in Figure 4.11 in relation to time and pH value. It can be seen the storage modulus has a zero baseline until the point where casein micelles start to aggregate, which is \approx pH 5 cf. Section 2. Hereafter a sigmoidal behaviour can be observed (Lee



(a) Base yogurt



(b) Base yogurt with additional fat



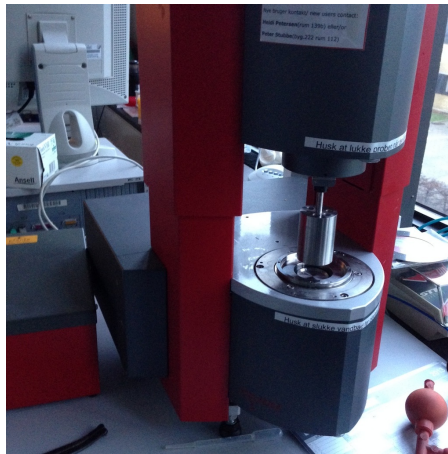
(c) Base yogurt with additional protein

Figure 4.9: Confocal laser scanning microscopy images of stirred yogurts with different compositions. The resolution of the images is 1024×1024 pixels, and each images covers an area of $375 \times 375 \mu\text{m}$.



(a) The separate parts of the geometry.

(b) The geometry in measuring position.



(c) The geometry installed in a rheometer, where it can be lowered to measuring position.

Figure 4.10: The double gap concentric cylinder geometry used in SAOR (small amplitude oscillatory rheology). As the name implies measurements are performed by small circular oscillatory motions of the geometry.

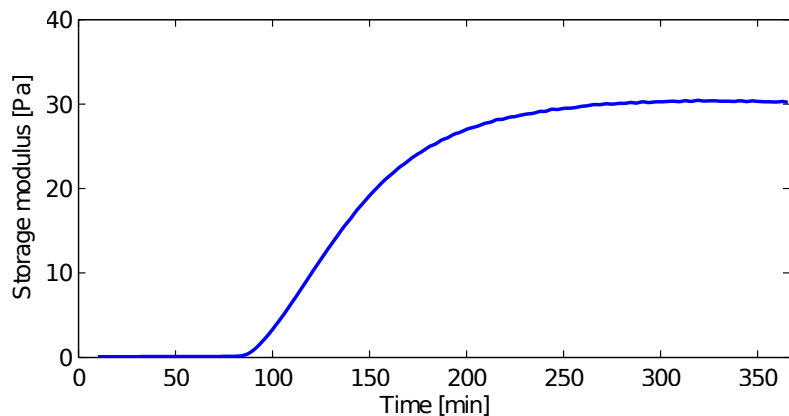
and Lucey, 2010).

4.2 Related Instrumentation

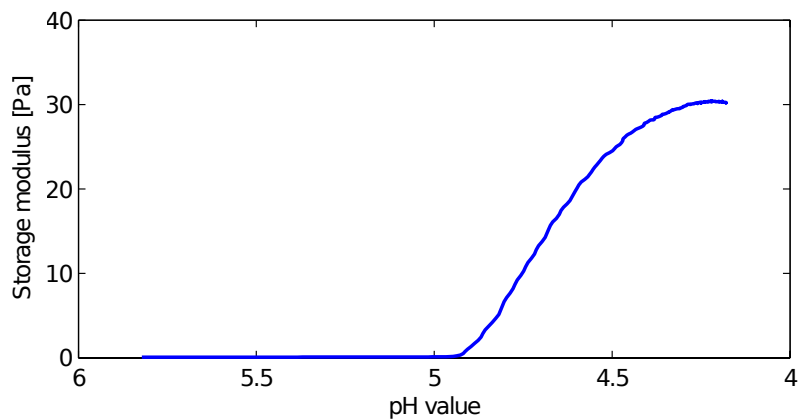
Comprehensive overviews of measuring techniques that previously have been used to monitor milk fermentation are by Lucey (2002); O'Callaghan et al. (2002); Castillo (2006). These methods have mainly been presented in relation to estimating the optimal cutting time in cheese making. A lot of the early methods involves observing a milk sample extracted from the bulk or direct destructive contact with the bulk:

- **Visual methods.** A popular method was proposed by Berridge (1952) to determine the point of gelation. It is based on visually detecting the first signs of graininess of the milk clinging to the inside surface of an inclined, revolving bottle.
- **Penetrometers.** To measure the curd firmness, the force or depth penetration of the curd is measured using various probes (knife, sieve, etc.).
- **Suspended bodies.** A geometry (ball, cone, plate, etc.) is suspended in the curd. The curd firmness is then determined by the drag exerted by the curd when slowly lifting the geometry.
- **Rheological methods.** This family of methods is less empirical than the previously described. Controlled levels of strain are applied to the curd to measure the absolute viscosity. As mentioned in Section 4.1.3, the large deformation rheology was introduced, and later the non-destructive small deformation methods were introduced. While large deformation methods could determine the curd firmness in a destructive manner, small deformation allows for continuous nondestructive measurements. This way both the gelation point and curd firming can be observed (Bohlin et al., 1984).

Generally, any interaction with the milk gel during fermentation is preferably avoided during production, due to risk of contaminating or damaging the milk gel. Thus, more recent methods have had a stronger emphasis on limited interaction with the milk gel when the measurements are made. As a result a lot of these methods can perform measurements continuously and are potentially easier to implement in-line for modern dairy processing environments. Castillo (2006) divides these nondestructive methods into three categories:



(a) Time vs. rheology curve



(b) pH vs. rheology curve

Figure 4.11: The typical rheological behaviour during a milk fermentation measured by small amplitude oscillatory rheometry. The gelation point is where the baseline for the storage modulus is broken, i.e. around 85min in (a) and just below pH 5 in (b). This corresponds well to the pH intervals presented in Section 2.2.

- **Thermal methods.** Thermal conductivity sensors are used to measure changes in heat transfer from a heat source (typically a wire) to the surrounding milk. The heat transfer changes according to viscosity and O'Callaghan et al. (2002) found that the measured signal was very suitable for estimating the gelation point, but not particularly suited for following the curd firming.
- **Ultrasonic methods.** Through an ultrasound transmitter and a receiver, changes in attenuation and velocity are measured. During coagulation it has been seen that the attenuation decreases as the gel is formed, due to the lower loss of energy in an elastic medium. Features, from a polynomial fit to the measured signal, were found to correlate well with the gelation point and the coagulation speed (Gunasekaran and Ay, 1994)
- **Optical methods.** Light is shined into the milk at one point, and the scattered light is typically measured at another point. Multiple modalities have been suggested, and different types of signals have been reported in the literature with different applications in mind.

The upcoming section gives a short summary of previously investigated optical methods. Furthermore, descriptions are provided for the most applied optical methods, and finally the major similarities and differences between the presented optical methods and the CIFQ workbench are pointed out.

4.2.1 Optical Methods

There has always been great interest in optical methods in regard to quality inspection and process control, due to their noninvasive and nondestructive nature, which makes them ideal for process control of agricultural products (Chen and Sun, 1991).

Optical methods are applied in transmission, sidescatter, or backscatter mode, and recent methods often utilise fibre optic probe setups as illustrated in Figure 4.12. Various light sources and photodetectors are used. In relation to milk fermentation transmission and backscattering modes have typically been applied. Transmission measurements are typically performed through a glass cuvette or similar geometry (potentially on-line or at-line, cf. Chapter 1), while backscattering can be performed both in a geometry or directly on the milk bulk (potentially in-line or on-line, cf. Chapter 1).

While transmission mode requires a more powerful light source and a suitably sized transmission geometry (in regards to the turbidity of the investigated sam-

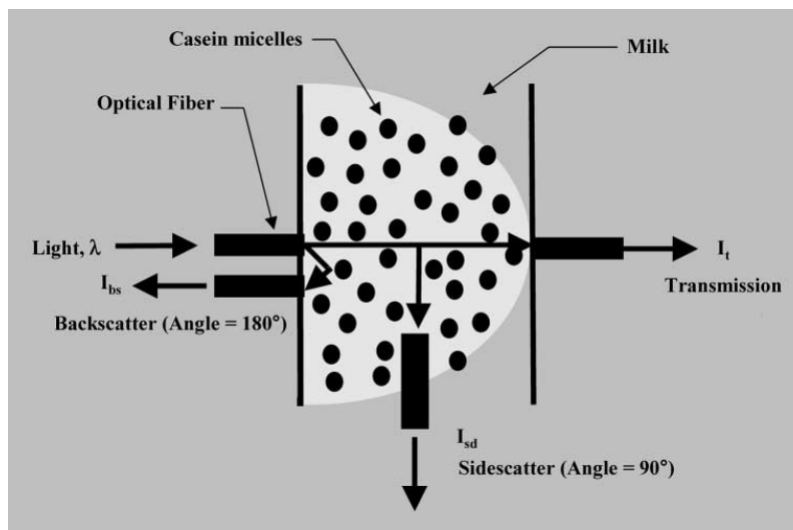


Figure 4.12: Different variations of optical measurements using a fibre optic probe setup. Backscatter mode and transmission mode have most commonly been used in relation to milk fermentations continuously. Image is from Castillo (2006).

ple), the measured signal is simpler as it potentially only consists of light that has been scattered multiple times. Contrary, the measured signal from backscatter mode is a combination of single scattered and multiple scattered light. However, backscatter mode is arguably better suited for process control as it has no requirements but an optically unobstructed view of the sample of interest, whereas transmission often relies on sample extraction. This potentially makes methods based on backscattering easier to implement for real world applications in the dairy production.

When compared to the SAOR measurements seen in Figure 4.11, all optical methods have one thing in common: They are not measuring the same kinetics as SAOR, and they show a clear developing signal before the gelation point. This is most likely due to the early rearrangements and aggregations of casein micelles before the final aggregation, which do not affect the viscosity (Alexander and Dagleish, 2004; Alexander et al., 2006). Consequently, optical signals have typically not been used directly to determine gelation point or the cutting time for cheese making. Instead there has been an emphasis on extracting features from the optical signals, and hereafter application of statistical modelling to predict gelation point or cutting time (O'Callaghan et al., 2002). However, optical methods are not only used in application studies. They are also used to great extent in research based studies, often to investigate how different

treatments affect the coagulation kinetics and generally extend the knowledge of milk coagulation.

4.2.1.1 Turbidity

Turbidity is measured by the fraction of light being transmitted through a geometry as seen in Figure 4.12. In relation to studies on milk fermentation, the first turbidity measurements date back as early as the late 20's where a rennet coagulation was followed, and small turbidity changes were detected (Schneck, 1928). Claesson and Nitschmann (1957) measured turbidity during rennet coagulation at multiple wavelengths (500-900nm) and found that 900nm best suited to follow the rennet coagulation. While 500nm are more scattering according to theory, they found that 900nm showed the percentage wise biggest difference between the initial condition and the end condition.

Turbidity measurements are still used today, and commercial NIR based instruments, such as the Optigraph (*Ysebaert Inc., Frepillon, France*), are available. These instruments are commonly used to investigate the coagulation speed for different process parameters, enzymes, or milk types (McMahon et al., 1984; Serra et al., 2007; Vallas et al., 2010).

4.2.1.2 Diffuse Reflectance

More than five decades after the first paper on turbidity measurements, optical changes were measured by diffuse reflectance in backscatter mode using colour difference meters (Hardy and Fanni, 1981). Here it was seen that the lightness and the blue-yellow parameter (L^* and b^* respectively) in the Lab colour space changed significantly during milk coagulation. In more recent approaches diffuse reflectance is measured using fibre optic probe in backscatter mode with a setup similar to that of Figure 4.12 (Payne et al., 1990). CoAguLite (*Reflectronics, Lexington, KY 40502, USA*) is a commercially available NIR based (880nm) version of the technique, which has been used in application studies on cutting time estimation for on different products (Castillo et al., 2000, 2005; Abdelgawad et al., 2014)

Figure 4.13 presents an example of the signal output from the CoAguLite sensor as a function of time during cheese making. Time is divided into three phases, similar to pH intervals for yogurt fermentation in Section 2.2. In Phase I, enzymatic reactions dominate and it can be seen that the measured signal does not change considerably. In Phase II, aggregation starts to occur, which affects

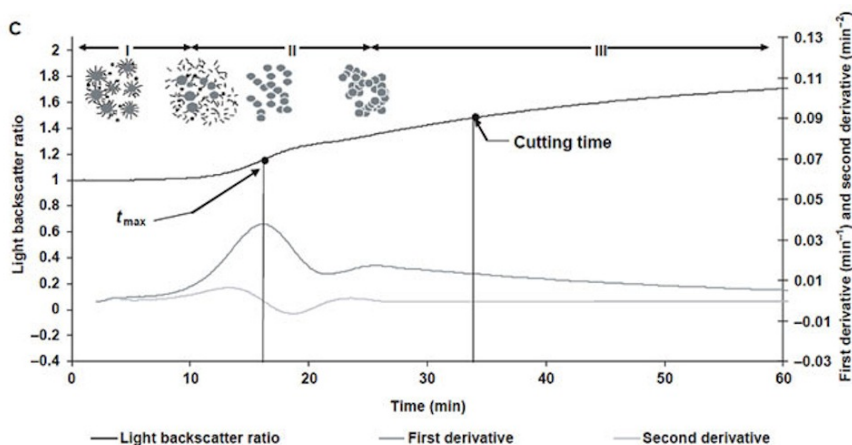


Figure 4.13: The diffuse reflectance (or light backscatter) ratio and its derivatives as a function of time during cheese making. The cutting time is determined by experienced cheese makers. Image is from Payne and Castillo (2007).

the measured signal due to changes in particle sizes. The signal continuously develops throughout the entire phase. The gelation point is located at the end Phase II. Hereafter additional cross-linking proceeds during the curd firming in Phase III.

From the signal derivatives the inflection point (t_{\max}) can be found, which have shown strong correlation to the coagulation speed. Further, under the right circumstances t_{\max} can be used to predict the point of gelation and cutting time (Payne and Castillo, 2007).

4.2.1.3 Dynamic Light Scattering and Diffusing Wave Spectroscopy

While both the previous methods relied on the amount of light being diffusely reflected or transmitted, Dynamic Light Scattering (DLS) relies on using laser light to observe quasi-elastic scattering (see Section 3.1.2) (Berne, 1976). The speckle, due to Brownian motion, is measured through a pinhole using a photomultiplier tube in sidescattering mode. The measured signal is quantified through the temporal autocorrelation function, from which various algorithms can be applied to quantify the particle size distribution of the investigated sample. A significant drawback to DLS is that it only works for single scattered light. This means that highly scattering samples, such as milk, has to be di-

luted. This makes it infeasible for real world applications, as the dilution can damage the weak gel systems of fermented milks.

However, extensions to both the data acquisition and the data analysis technique have been developed to increase the applicability for highly scattering media (Pusey, 1999). A widely used extension is Diffusing Wave Spectroscopy (DWS) (Pine et al., 1988). Contrary to DLS, DWS operates in backscatter or transmission mode, and the algorithms applied to the temporal autocorrelation function assume that all light has been scattered multiple times. Using DWS, the average particle size of the sample and the mean free path of the light can be estimated.

DWS can be measured using a photomultiplier tube or a CCD as detector. A photomultiplier tube is typically used to monitor fast developing speckle patterns due to high temporal resolution, whereas a CCD is used to monitor slowly developing speckle patterns, and the pixels on the CCD are considered as an ensemble of individual detectors (Viasnoff et al., 2002). Additionally, if a CCD is used as detector, the laser beam is expanded before reaching the investigated sample, to get a sufficiently large area of speckles to measure.

DWS has been widely applied as a research tool in relation to milk and other colloidal food systems. Specifically in relation to milk fermentation, DWS has mainly been used to extend the current knowledge of milk coagulation (Alexander and Dalgleish, 2006). However, according to Castillo (2006) NIZO Food Research has used the commercially available system, Rheolight (*Optel, NL-6546 Nijmegen, Netherlands*), in-line to follow the curd firming progress during cheese making.

4.2.2 Comparison Between 2DSLS and Related Optical Methods

Obviously there is a major difference between the setup for the Optigraph (turbidity measurements) and the 2DSLS setup, as they rely on diffuse transmission and diffuse reflectance respectively. However, the Optigraph, CoAguLite, and 2DSLS observe effects of elastic scattering. CoAguLite and 2DSLS are more related as they both rely on diffuse reflectance measurements. Nevertheless, there are still some major differences between the two setups. CoAguLite uses the optic probe setup seen in Figure 4.12, in which light is shined orthogonally into the sample using a fibre, and the diffuse reflectance and captured some distance away by another fibre.

2DSLS uses oblique incident light, which can probe information on the phase

function cf. Figure 3.7, and the diffuse reflectance is captured remotely using a CCD. The CCD allows for not only quantifying the signal in terms of intensity but also in terms of signal shape. A CCD can also be seen as a 2D array of detectors with a narrow field of view, where an optical fibre can be seen as a single detector with a larger field of view. Thus, the diffuse reflectance images could potentially approximate the CoAguLite signal by selecting an area in the diffuse reflectance images.

Contrary to the Optigraph and CoAguLite, both DWS and 2DSLS use a coherent light source. While 2DSLS uses a narrow light beam, DWS expands the beam before illuminating the sample, and quasi-elastic scattering is investigated in the illuminated area. This implies that quasi-elastic scattering is only observable in a narrow area in the 2DSLS signals. Another important difference to DWS is that the measured signal is time resolved and analysed through its temporal autocorrelation function, whereas the signals from the Optigraph, CoAguLite, and 2DSLS are static measures.

In terms of wavelengths most commercial products, based on turbidity or diffuse reflectance, apply a NIR light source. This was justified early on by Claesson and Nitschmann (1957) who observed that longer wavelengths spanned a greater dynamic range when considering the relative increases in the scattering properties during the fermentation in cheese making. This is also verified by the absolute scattering properties for milk and yogurt presented in Figure 3.9. In terms of wavelength DWS just requires a coherent light source, and often a helium-neon laser is used (632.8nm). The above-mentioned spectral ranges are covered entirely by the current 2DSLS setup.

In summary 2DSLS can potentially be considered a combined sensor technology, that holds some of the information that potentially combines features from both CoAguLite and DWS, and additionally contains effects of the phase function. Thus, the 2DSLS signal is a lot more complex compared to the related methods. While this allows for a lot of information being stored in the 2D signals, it also introduces the problem of isolating the different types of information. In Section 6.1 different methods for quantifying the diffuse reflectance images will be introduced.

The aim of this chapter is to provide a brief overview of the types of data investigated throughout this thesis. Each data set is briefly motivated, described, and followed up with clarifying images of the applied experimental setup and data examples if relevant. For the specific details on the actual data acquisition, we refer to the papers, in which the data sets have been utilised. The data sets are presented in chronological order.

For all the presented data sets, the 2DSLS system has been used for data acquisition. However, two different detector systems have been applied throughout the work of this thesis as summarised in Table 4.1. Unless stated otherwise, the *Grasshopper* CCD detector system has been used in the data acquisition.

Table 5.1 provides an overview of the data sets and in which of the included papers they have been used.

5.1 2^3 Fermentation Processes

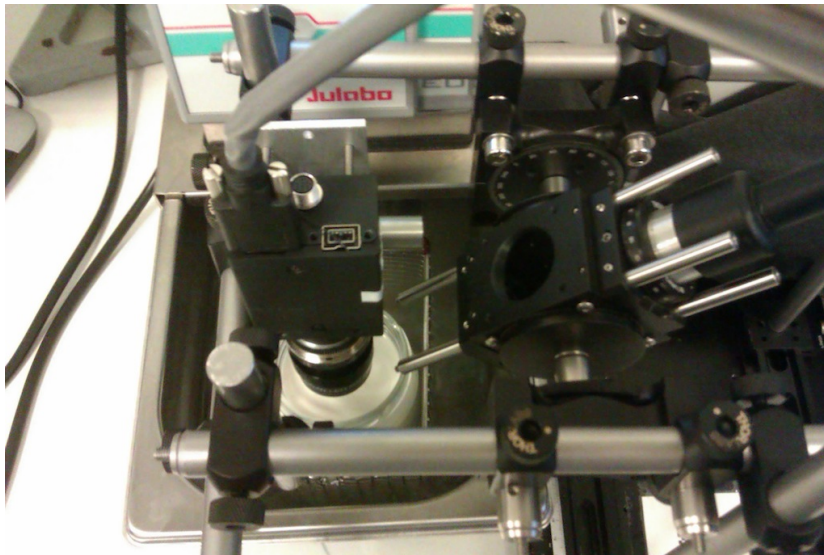
This data set was created to investigate the generalisability of the 2DSLS technique toward common process parameters in the production of fermented milks. Through a 2^3 factorial design, fat content, protein content, and fermentation

Table 5.1: Overview of the data sets, and in which of the included papers they have been used.

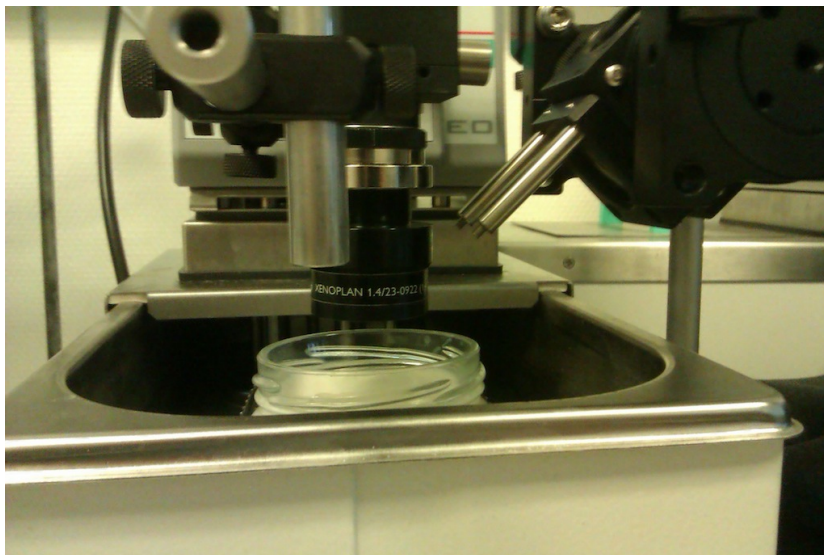
Data set	Paper
2 ³ fermentation processes	A
Milk products	C + F
Intralipid series	B
2 ⁴ stirred yogurts	D + E
Repeated fermentation process	F

temperature was changed systematically between a low and a high level. The factorial design allows for screening factor significance with a small amount of data points (Montgomery, 2005), and additional repeated centre points (average level of all factors) were added to the factorial design to assess the experimental error directly. The fermentations were carried out using GDL.

The fat content was controlled using homogenised UHT semi-skimmed and whole milk for the low and high level respectively. Protein content was changed by adding skimmed milk powder. 2DSLs and SAOR measurements (*Stresstech HR* with temperature cell $\pm 0.1^\circ\text{C}$, *Reologica Instruments AB, Lund, Sweden*) were performed during the fermentation. To ensure the correct temperature for the 2DSLs measurements, the setup was installed around a water bath (*SW2* $\pm 0.2^\circ\text{C}$, *Julabo Labortechnik GmbH, Seelback, Germany*). Figure 4.10 shows images of the applied rheometer and Figure 5.1 shows images of the 2DSLs setup for an early iteration of the experiment. Data examples are shown in Figure 5.2.



(a) Top view



(b) Side view

Figure 5.1: The 2DSLS setup installed around a water bath during on-line measurements of a milk fermentation.

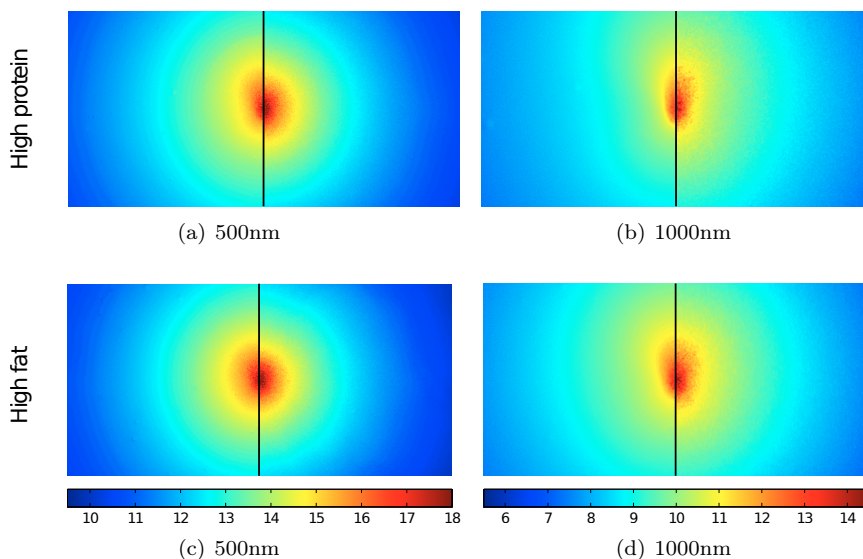


Figure 5.2: Logarithmically transformed diffuse reflectance images from two sample points in the fermentation experiment at different wavelengths. The lefthand side of each image shows the signal before the fermentation, while the righthand side shows the signal after the fermentation. The top row shows examples from the sample with low protein and high fat, while the lower row shows examples from the sample with high protein and low fat.



Figure 5.3: Some of the commercial products used for the milk product data sets.

5.2 Milk Products

Based on 2DSLS measurements of commercial milk products, this data set provides an easy and relevant way of assessing the different types of information available in the 2DSLS signal. By selecting both non-fermented and fermented products with different ingredient compositions the discriminating properties of multiple scattered light, single scattered light, and speckle from the diffuse reflectance images can be related to either ingredient composition or microstructure.

Two slightly different versions of this data set have been produced. The first data set was created using the *Grasshopper* CCD detector system in the 2DSLS setup, and the second set was created using the *AM-800GE* CCD detector system. The details on the different detector setups are summarised in Table 4.1. A subset of the commercial products used for the two data sets is shown in Figure 5.3.

5.3 Intralipid Series

This data set consists of 21 graduated water dilutions of Intralipid (*Intralipid 20%*, *Fresenius Kabi, Bad Homburg, Germany*). Intralipid is a highly stable and standardised fat emulsion, which has been found well suited for simulating the optical properties of biological material. The dilutions were made to have linearly increasing scattering properties encompassing the range of common milk and yogurt products. Each dilution was measured at three different wavelengths (500, 700, and 900nm) using the 2DSLS technique. It should be noted that while Intralipid can be used to change the scattering properties in a controlled manner, the scattering properties are only affected due to the changes in particle density.

This data set was used in Paper B to evaluate the different methods of Section 6.1.1 and 6.1.2, used to quantify the multiple scattered light in the 2DSLS signal. By spanning a broad, yet highly resolved, range of scattering properties, the discriminating properties, as well as the limitations when dealing with very low or high scattering samples, can be evaluated. Figure 5.4 gives examples of the extrema 2DSLS signals in the data set.

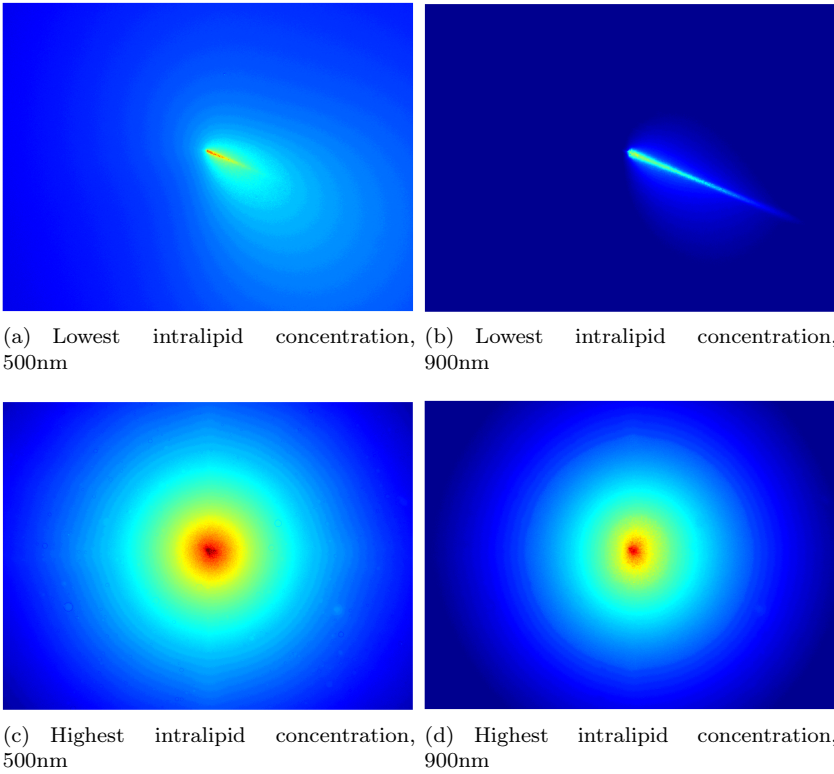


Figure 5.4: Logarithmically transformed diffuse reflectance images of the extremum sample points from the intralipid data set. The colormap is consistent across columns.

5.4 2^4 Stirred Yogurts

The main goal of this data set was to determine how changes to either chemical composition or microstructure affects the diffuse reflectance images of the 2DSLS technique. For this purpose a triple replicated 2^4 factorial design was used to systematically create different types of stirred yogurts. The four factors spanned fat content, protein content, pre-heat treatment, and incubation temperature. The two first mentioned factors changes the chemical composition of the yogurt, while two latter only affects the formation of the microstructure. Thus, all factors are expected to change the final microstructure.

The fat content was controlled using homogenised UHT semi-skimmed and whole milk for the low and high level respectively. Protein content was changed by adding skimmed milk powder. Pre-heat treatment was performed using an autoclave (Systec V-Series, Holm & Halby, Brøndby, Denmark) and the incubation temperature was controlled using water baths (*Lauda Ecoline E100*, *Lauda Dr. R. Wobser Gmbh & Co. Kg*, *Lauda-Königshofen*, *Germany*).

For the milk fermentation lactic acid bacteria was used, and the pH development (*CINAC pH Controller*, *Ysebaert Dairy Division*, *Frepillon*, *France*) was monitored throughout the fermentation. When a sample reached pH 4.6, it was stirred and stored in a refrigerator (5°C) for a week prior to measurements. The final products were measured using both 2DSLS and CSLM (*Leica DM IRE2*, *Leica Microsystems*, *Heidelberg*, *Germany*). Images from the experiments are provided in Figure 5.5, and data examples are given in Figure 5.6.

In Paper D different ways of describing the CSLM image objectively are investigated, and in Paper E comparisons are made between CSLM and the 2DSLS.



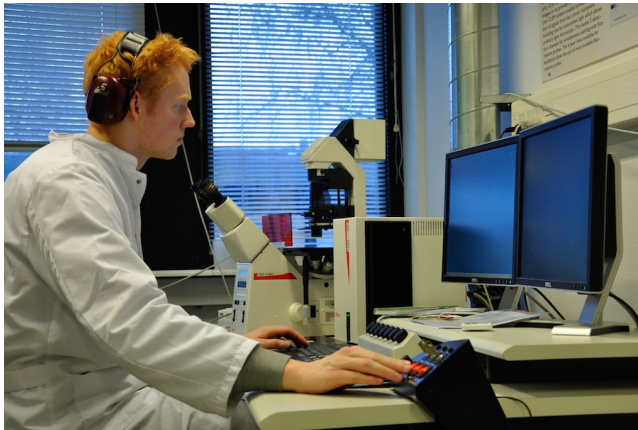
(a) Monitoring the pH development during milk fermentation in two water baths



(b) Autoclave used for pre-heat treatment



(c) Half a batch of yogurt samples



(d) Using the Leica CSLM

Figure 5.5: Images from the sample production and measurements for the 2^4 stirred yogurts data set.

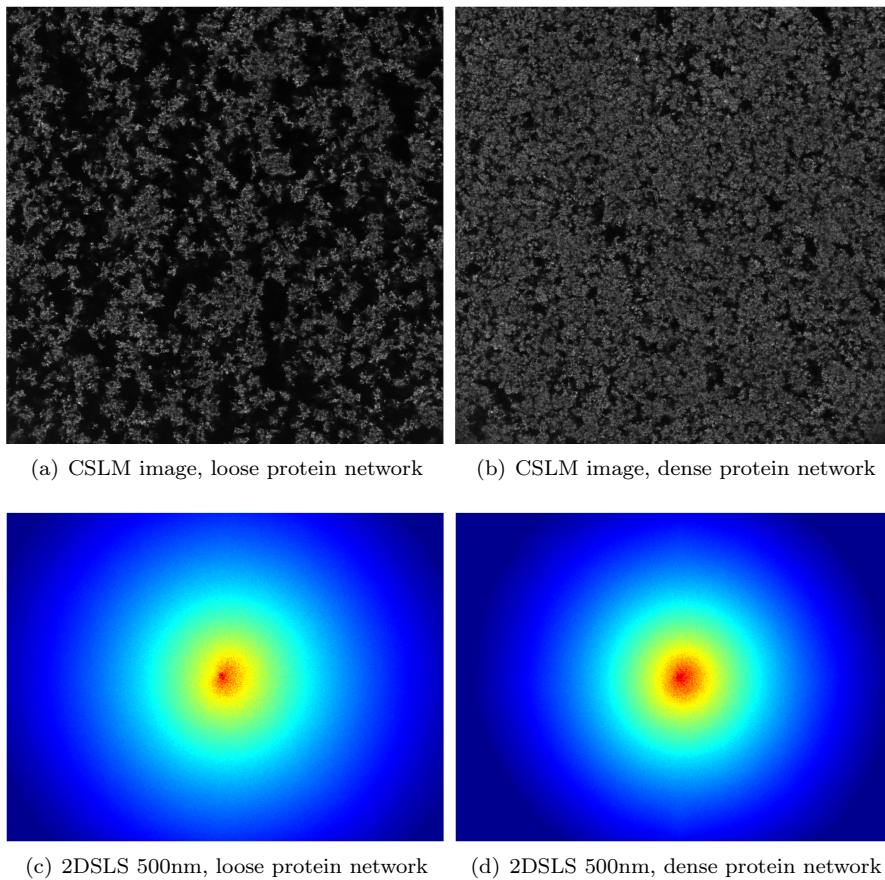


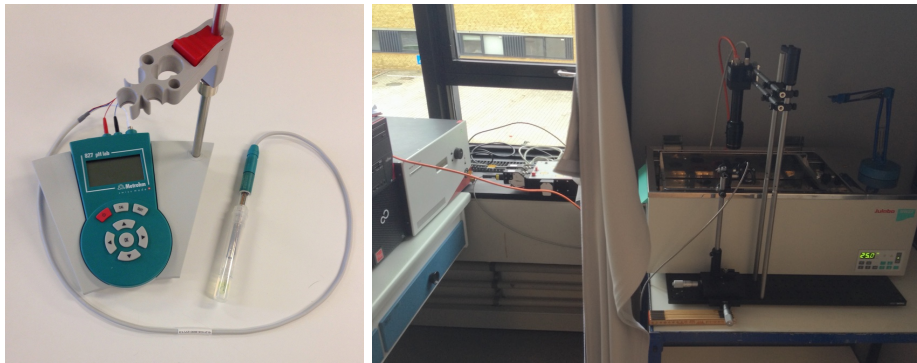
Figure 5.6: Data examples from the 2^4 stirred yogurt experiment. The shown data examples are from the loosest and densest protein networks in the data set. The CSLM images have a spatial resolution of 0.375×0.375 mm and for the 2DSLS images it is approximately 8×10.5 mm.

5.5 Repeated Fermentation Processes

In this data set a single GDL milk fermentation was repeated multiple times. The main idea was to assess the response and reproducibility of the different methods applied to quantifying the 2DSLS signal (see Section 6.1).

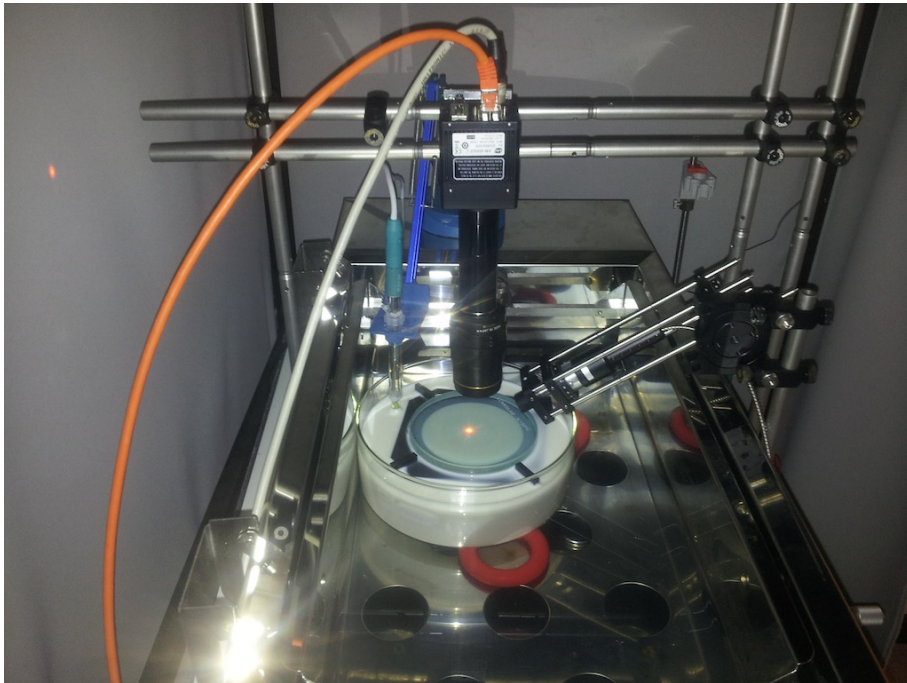
Throughout the milk fermentation pH measurements (*827 pH Lab, Metrohm, Herisau, Switzerland*) and rheological measurements (*Stresstech HR* with temperature cell $\pm 0.1^\circ\text{C}$, *Reologica Instruments AB, Lund, Sweden*) were carried out. For the 2DSLS measurements the *AM-800GE* CCD detector system was used. Additionally, the 2DSLS measurements were performed through a 1.5cm soda lime sight glass (*Lumiglas, F.H.Papenmeier GmbH & Co., Schwerte, Germany*). Similar to Section 5.1 the 2DSLS was installed around a water bath (*SW2 $\pm 0.2^\circ\text{C}$, Julabo Labortechnik GmbH, Seelback, Germany*) in order to maintain a constant temperature throughout the fermentation. Images of the experimental setup are provided in Figure 5.7.

In total seven repeated milk fermentations were carried out, however the data set was found to contain perturbations and low reproducibility, which we at the time of writing have not resolved. Especially the lower wavelengths appear to be significantly different from what was seen in the experiment in Section 5.1. As a consequence, only the measurements for a single milk fermentation are presented in Paper F.



(a) pH meter

(b) 2DSLS setup



(c) 2DSLS setup (close-up)

Figure 5.7: (a) shows the applied pH meter. (b) shows the entire 2DSLS setup installed around a water bath, while (c) shows a close-up view of the 2DSLS system measuring through the sight glass. Additionally the pH probe is also visible in the lefthand side of the glass container.

A broad range of methods has been used to produce the contributions of this thesis. This chapter gives brief introductions to some of the topics and utilised methods, as well as the context in which they have been applied. The aim of this chapter is to facilitate the reading of the contributions. First, different approaches to quantifying the 2DSLS signal are introduced, and hereafter the CSLM images, of the protein network microstructure, are discussed within the scope of image texture analysis. Hereafter, more general methodologies are introduced covering data transformation, clustering, classification, and analysis of variance.

6.1 2D Static Light Scattering

Figure 6.1 shows a diffuse reflectance image captured by the 2DSLS technique. As described in Section 4.1.1, the images are complex signals containing several types of information. In this section we consider three major elements of the images, cf. Figure 4.7:

- **Multiple scattered light.** Observed as the isotropic light diffusion far from the light incident point.

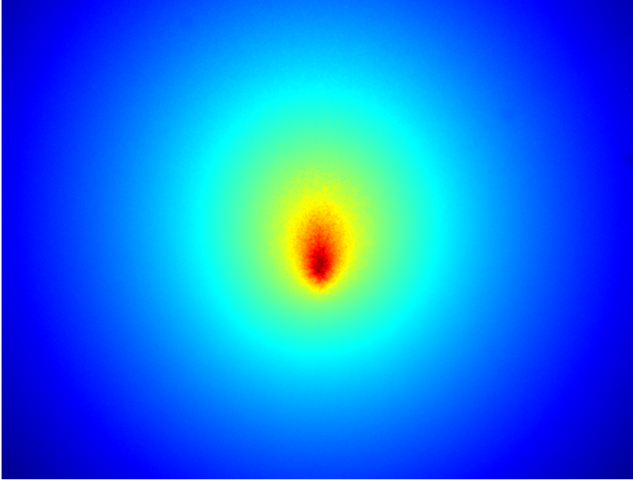


Figure 6.1: 2DSLS image of yogurt (1.5% fat) at 900nm.

- **Single scattered light.** Observed as the anisotropic light diffusion close to light incident point.
- **Speckle.** Observed as the underlying interference pattern (most pronounced near the light incident point).

Following Chapter 3 all three elements can be related to the particle size distribution of the investigated sample. In this section different approaches to quantifying the above-mentioned features are presented. The characterisation methods range from physical models, to empirically verified methods that have been found to work well for specific types of data. The data used in each of the methods will be visualised in relation to Figure 6.1.

Section 6.1.1 and 6.1.2 mainly cover quantification of the multiple scattering effects. In Section 6.1.1 physical modelling is applied in order to estimate the absorption (μ_a) and reduced scattering (μ'_s) coefficients, whereas Section 6.1.2 applies statistical measures to the image intensities in order to derive a response of the combined absorption and scattering properties. While the statistical measures may seem less interpretable, Figure 3.9 verifies that milk products indeed are diffusive media ($\mu_a \ll \mu'_s$), and can be characterised almost exclusively by their scattering properties in the investigated wavelength range. Thus, the combined response of the statistical approaches will mainly describe the scattering properties. Paper B covers a comparative study between the methods in Section 6.1.1 and 6.1.2.

In practice there is an inherent problem with the methods in Section 6.1.2 as they quantify the images based on the image intensities. The image intensities are highly dependent on variations in the system response, which is defined by the light delivery system and detector system for the 2DSLS technique. As discussed in Chapter 1 this can potentially be problematic in relation to process control, where a reasonable SNR must be established before it is meaningful (MacGregor and Kourti, 1995). Thereby, applying intensity-based characterisation may enforce strict stability requirements on both the light delivery system and the detector system, which can be a problem in practice.

Instead of considering image intensities, the characterisation techniques in Section 6.1.1, 6.1.3, and 6.1.4 consider distances and shapes, which are not dependent on image intensities. This alleviates the stability requirements for both light delivery and detector system. However, different requirements are imposed on the detector system like spatial resolution and field of view. Shape characterisation is primarily covered in Paper F.

Finally, the approach in Section 6.1.5 investigates the diffuse reflectance images to the frequency domain, which is investigated further in Paper C. Additionally, for each of the introduced methods, the advantages and limitations will be mentioned briefly.

6.1.1 Oblique Model Based Characterisation

As described in section 3.1.1, Farrell et al. (1992) derived the analytical expression in Equation (3.4) for semi-infinite diffusive media illuminated orthogonally by a narrow light beam. In relation to the diffuse reflectance images the expression can be fitted to image profiles extracted orthogonal to the scattering direction, as illustrated in Figure 6.2(b). Equation (3.4) was derived based on the assumption that all light has been scattered multiple times, and must therefore be fitted to the data a suitable distance away from the beam centre.

Previously, similar modalities to 2DSLS have been used to measure similar profiles, and Equation (3.4) has been fitted to the measured data using non-linear least squares fitting procedures (Wright and Nocedal, 1999). From this, the absorption and scattering properties have been investigated for a broad range of food products covering milk, juice, fruits, vegetables, and sugar gels (Qin and Lu, 2007, 2008; Herremans et al., 2013). However, the approach is dependent on the image intensities, which can be problematic for process control as discussed in the previous section. Furthermore the assumptions of Equation (3.4) are not completely in line with the 2DSLS setup, where the incident light is oblique rather than orthogonal.

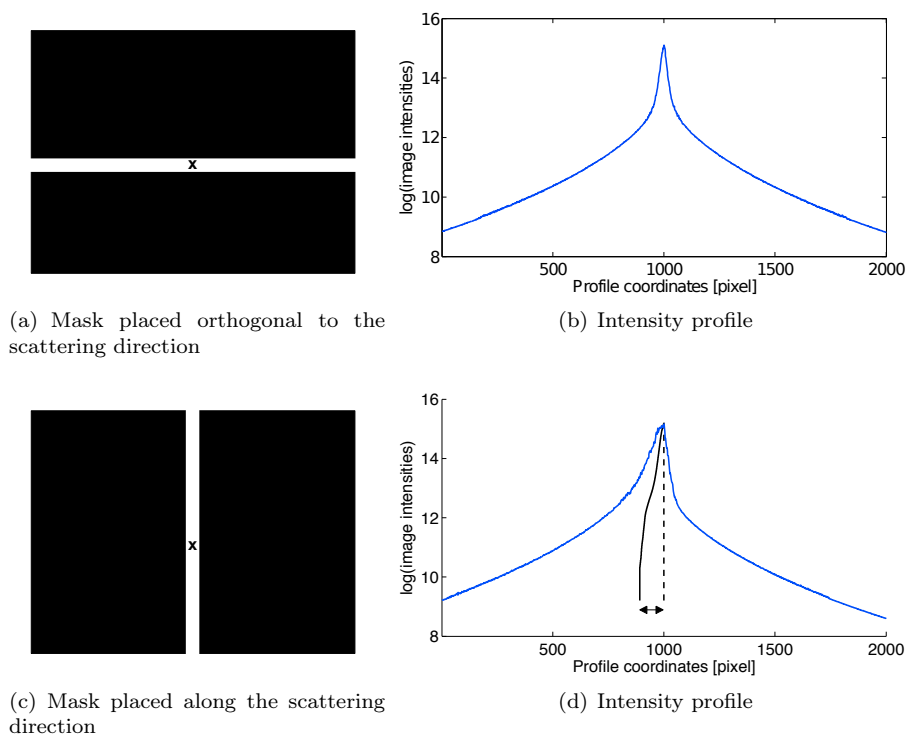


Figure 6.2: The left column presents masks where the white areas illustrate the data, which is extracted from the image in Figure 6.1 and "x" denotes the light incident point. The right column shows the extracted intensity profiles. Additional for (d) the symmetry break due to the oblique incident angle of the light is visualised. Here, the dashed black line corresponds to the coordinate of the light incident point, and the solid black line corresponds to average coordinate position for each image intensity level.

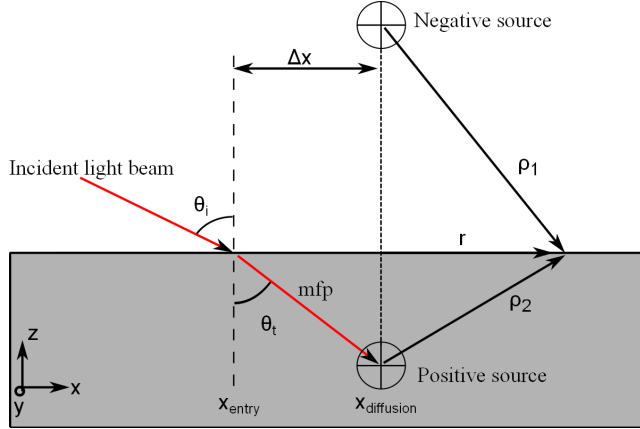


Figure 6.3: A schematic view of the quantities used in estimating μ_a and μ'_s . The incident light is initially refracted at the sample surface, x_{entry} , and travels one mean free path into the sample before it is scattered for the first time at $x_{\text{diffusion}}$. The positive and negative source are quantities introduced for the boundary conditions used in the derivation of the analytical expression given in Equation (6.3). Illustration is from Nielsen et al. (2014).

Instead, there has been greater emphasis on the extensions by Wang and Jacques (1995) and Lin et al. (1997) which is also based on the diffusion approximation but not dependent on the image intensities. They proposed to use oblique incident angle of the light and consider the intensity profile in the scattering direction. From this profile a break in symmetry can be observed near the single scattered light, as illustrated in Figure 6.2(d).

The symmetry break is further explained in Figure 6.3. Here it can be seen that the light, that is not reflected, is refracted at the surface and travels a distance into the sample before it experiences the first scattering event. This is what causes the break in symmetry. Recalling Equation (3.8), the average distance travelled is referred to as the mean free path (MFP) and, following the illustration, it can be calculated as:

$$\text{MFP} = \frac{\Delta x}{\sin(\theta_t)}, \quad (6.1)$$

where θ_t , depends on the incident angle of the light, θ_i , and the refractive index of the sample. Δx can be measured from the scattering profile as a shift in centre of mass when traversing down the intensity isocontours, as illustrated in

Figure 6.2(d). Through Monte-Carlo simulations Lin et al. (1997) empirically found that in practice the MFP for biological tissue should be expressed as (as opposed to Equation 3.8):

$$\text{MFP} = 3D = \frac{1}{(0.35\mu_a + \mu'_s)}, \quad (6.2)$$

where D is the so-called diffusion coefficient, which is related to motion of particles and thereby particle sizes. Coinciding with the original work by Farrell et al. (1992), the reflectance of the multiple scattered light, R , can be modelled as function of radius, r , however a modified expression that takes the asymmetric profile into account is applied (Wang and Jacques, 1995; Lin et al., 1997):

$$R(r) = 3D \left(\mu_{\text{eff}} + \frac{1}{\rho_1} \right) \frac{\exp(-\rho_1 \mu_{\text{eff}})}{\rho_1^2} + (3D + 4AD) \left(\mu_{\text{eff}} + \frac{1}{\rho_2} \right) \frac{\exp(-\rho_2 \mu_{\text{eff}})}{\rho_2^2}, \quad (6.3)$$

where A is the mismatch in refractive index between air and the diffusive media, which can be calculated by an empirical formulation originally given by Groenhuis et al. (1983). ρ_1 and ρ_2 are given by:

$$\rho_1 = 3D \cos \theta_t + 4AD, \quad (6.4)$$

$$\rho_2 = 3D \cos \theta_t. \quad (6.5)$$

Whereas Equation (3.4) is fitted to the image profiles, orthogonal to the scattering direction, to directly obtain values of μ_a and μ'_s , Equation (6.3) is fitted to the image profiles along the scattering direction to obtain the effective attenuation, μ_{eff} , which is defined by μ_a and μ'_s .

As both expressions are based on the diffusion approximation, the data fitting must be performed a suitable distance from the incident point of the light, in order to ensure multiple scattered light. Furthermore, both approaches are dependent on the system response, and the estimated coefficients are therefore relative quantities. However, the MFP calculated in (6.1) can ultimately be used to correct the relative estimates of μ_{eff} and provide absolute estimates of the absorption and scattering coefficients (Lin et al., 1997):

$$\mu_a = \frac{\text{MFP} \cdot \mu_{\text{eff}}^2}{3} \quad (6.6)$$

$$\mu'_s = \frac{1}{\text{MFP}} - 0.35\mu_a \quad (6.7)$$

Furthermore, as the 2DSLS technique utilises multiple wavelengths, Equation (3.7) can be applied to μ'_s in order to provide more details on the particle size distribution.

The oblique angle technique was implemented alongside the development of the 2DSLS technique, and an in-depth description of the technique is given by Nielsen et al. (2014). This description also covers a broad range of considerations and practicalities in relation to the practical implementation. The technique is not dependent on the image intensities, however some requirements are posed on the detector system. The spatial resolution needs to be small compared to Δx in order to ensure that Δx is resolved appropriately. This can get difficult for highly scattering materials, where Δx is very short. At the same time the field of view of the detector system has to be sufficiently wide, such that a reasonable amount of data can be used for fitting to the expression in Equation (6.3).

6.1.2 Intensity Based Characterisation

6.1.2.1 Loglog Model

This parameter was originally presented by Carstensen et al. (2009) and is used in a commercially available system (*VideometerSLS*, *Videometer A/S*, *Hørsholm, Denmark*), which the 2DSLS technique is originally based on.

The loglog parameter is extracted from a double logarithmically transformed intensity profile, $\log(\log(I + 2))$, where I corresponds to the profile of pixel intensities. The intensity profile is sampled orthogonal to the scattering direction through the light incident point as illustrated in Figure 6.2(a) and 6.2(b). To reduce noise an entire band of profiles is averaged. Hereafter, a linear model is fitted to one of the outer parts of the profile as illustrated in Figure 6.4. This reduces the parameterisation to a slope and an intercept. Both parameters hold information about the scattering and absorption properties. In practice we are only considering the slope parameter, as this parameter typically spans a greater dynamic range, and is less dependent on the system response compared to the intercept. This parameterisation can be seen as a simplification of the physical

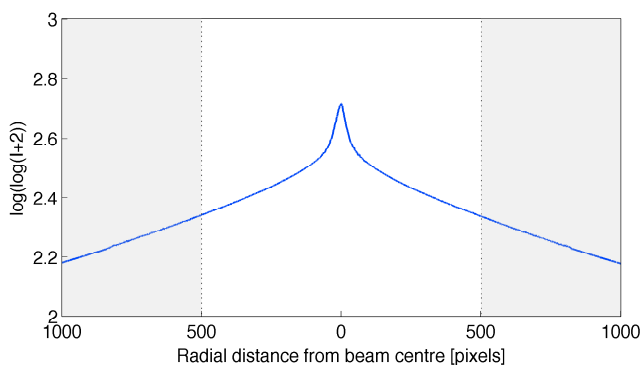


Figure 6.4: Feature extraction using the loglog model approach. A linear model is fitted to each of the grey marked intervals of the double logarithmic transformed intensity profile, and the average absolute slope parameter of the models is used as the quantification.

models covered in the previous section. The double logarithmic transformation combined with the linear model can furthermore be seen as a compromise between resistance towards noise and suppressing information.

The slope parameter of the loglog model has been found to cover the scattering regime of milk and fermented milk products well, and has been the general go-to method throughout the thesis. Furthermore, the double logarithmic transformation reduces the sensitivity toward system response variations.

6.1.2.2 Intensity Spread

Until now the quantification methods have relied on profiles extracted from the diffuse reflectance images, and thereby merely utilise a fraction of the information available. This measure, on the contrary, is based on a considerable amount of data in the images. Within a certain radius of the incident light point a histogram of the pixel intensities is considered as illustrated in Figure 6.5.

Typically intensity histograms are quantified using first order statistics, however these are very sensitive to outliers. Since the distribution of the pixel intensities is heavy tailed, robust statistics should be considered. Here, we apply a robust measure of the variability, the Median Absolute Deviation (MAD) (Hoaglin

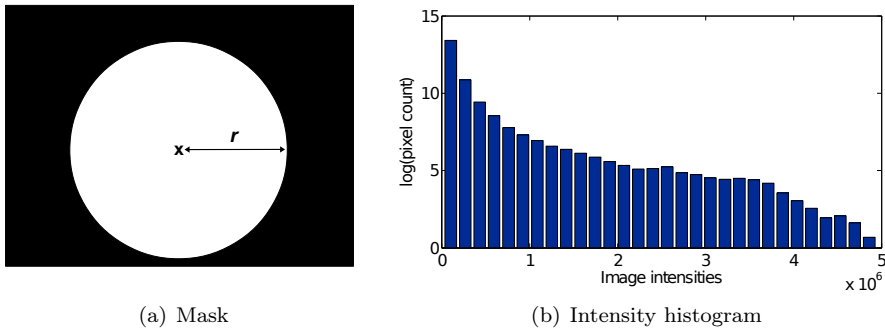


Figure 6.5: (a) presents the circular mask where the white area illustrates the data being used extracted from Figure 6.1. "x" denotes the light incident point, and r is the radius of the circular mask. (b) shows the extracted heavy-tailed intensity histogram.

et al., 1983):

$$\text{MAD} = \text{median}(|H - \text{median}(H)|), \quad (6.8)$$

where H is the pixel intensity histogram. The variability of the histogram describes how spread out the light is due to the light diffusion, and covers both single and multiple scattered light. For highly scattering samples the intensity distribution is more spread out as the light decays faster, and the variability hereby increases.

This simple scheme has been found to work consistently well for a broad scattering regime, especially when masks with large values of r are considered. However the measure is sensitive to variations in the system response.

6.1.2.3 Patch Average

This method was inspired by the methods using fibre optic probes as the shown Figure 4.12. An optical fibre can be considered a single detector with a larger field of view, whereas a CCD can be considered a 2D array of detectors, each with a narrow field of view. Thus, a patch in a diffuse reflectance image, as illustrated in Figure 6.6, can potentially approximate the signal from a fibre optic probe. The quadratic image patch is the quantified by a Gaussian weighted average.

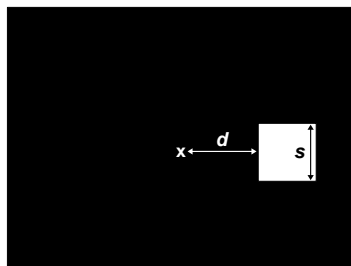


Figure 6.6: The image patch mask where the white areas illustrates the data being used extracted from Figure 6.1. "x" denotes the light incident point, while d and s denote the distance from the light incident point and side length of the quadratic image patch respectively.

This approach has been found to be extremely discriminative when d and s are chosen carefully. However, there appears to be a significant tradeoff between the discriminative power and how large a scattering regime the method is able to cover appropriately. Also, being reliant entirely on intensity averages, it is sensitive to variations in the system response.

6.1.3 Scattering Eccentricity Characterisation

In this quantification method, the effects of the phase function, cf. Equation (3.2), are investigated through the single scattered light. Joshi et al. (2006) estimated the asymmetry parameter, g , using diluted samples and Monte-Carlo simulations. This approach is not suitable in practice, in relation to fermented milk products, as dilution may disrupt the protein network. Additionally, we found that the spatial resolution of the applied detector systems of the 2DSLS technique was not adequate to perform feasible data fitting to analytical models such as the Henyey Greenstein model described in Equation (3.3).

Instead the effects of scattering eccentricity were characterised by considering the intensity isocontours in the signal, as illustrated in Figure 6.7. These isocontours approximately take the shape of ellipses for which the eccentricity can be determined as the ratio between the magnitude of the major and minor axis. For this purpose Principal Component Analysis (PCA), see Section 6.3.1, can be applied to the distribution of two-dimensional coordinate vectors for all points within the isocontour. The eccentricity, E , can hereby be described by the

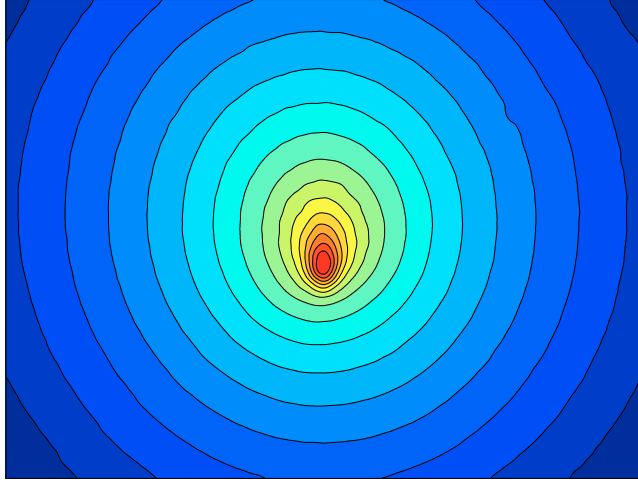


Figure 6.7: The intensity isocontours highlighted for the diffuse reflectance image in Figure 6.1.

eigenvalues, λ_{minor} and λ_{major} :

$$E = \sqrt{1 - \frac{\lambda_{\text{minor}}}{\lambda_{\text{major}}}}, \quad (6.9)$$

where E is bounded between 0 and 1. For lower values of E the isocontour is more circular, whereas for high values of E the isocontour is elliptically elongated.

If the intensity isocontour is extracted based on distances from the light incident point, this characterisation is invariant toward variations in the system response. However, the spatial resolution of the detector greatly impacts the size of isocontours that can be quantified appropriately.

6.1.4 Speckle Size Characterisation

An underlying speckle pattern can be seen when looking at a diffuse reflectance image. The effect has been found to be especially pronounced for the fermented milk products when looking at Figure 4.5 through 4.6 and concentrated around the light incident point. Figure 6.8 shows a close-up view of a diffuse reflectance

image for fermented milk, where the speckle phenomenon is clearly visible. To isolate the phenomenon a speckle image, S_f , can be extracted through a filtering which normalises with the local mean and variance at each pixel location:

$$S_f(x, y) = \frac{f(x, y) - m_f(x, y)}{\sigma_f(x, y)}, \quad (6.10)$$

where f is the original image, m_f is the estimated local mean, and σ_f is the estimated local standard deviation. Using 5×5 neighbourhoods to estimate the local quantities was found appropriate, and a result can be seen in Figure 6.8. While the speckle pattern is isolated appropriately, effects of the HDR algorithm used in the image acquisition (see Section 4.1.1) can be seen. The effects can be observed as rings with lower SNR where different HDR layers are stitched together.

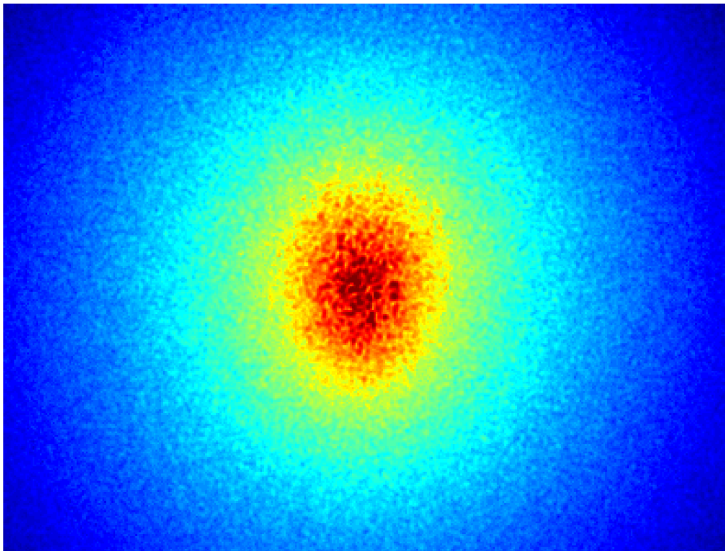
Nevertheless, the speckle size can be quantified from the image in Figure 6.8(b). Following Goodman (1975); Piederrière et al. (2004b) the average speckle size can be investigated by considering the spatial autocorrelation function. Here the width of the maximum response around lag 0 gives information on the self similarity of the local structures, and the average speckle size can be estimated by the full width at half maximum (FWHM) of the maximum response. The average speckle size estimation is illustrated in Figure 6.9

In practice the autocorrelation function and FWHM estimate is calculated for each of the lines in the image, both vertically and horizontally. Hereafter, the average FWHM response is used as an estimator for the average speckle size.

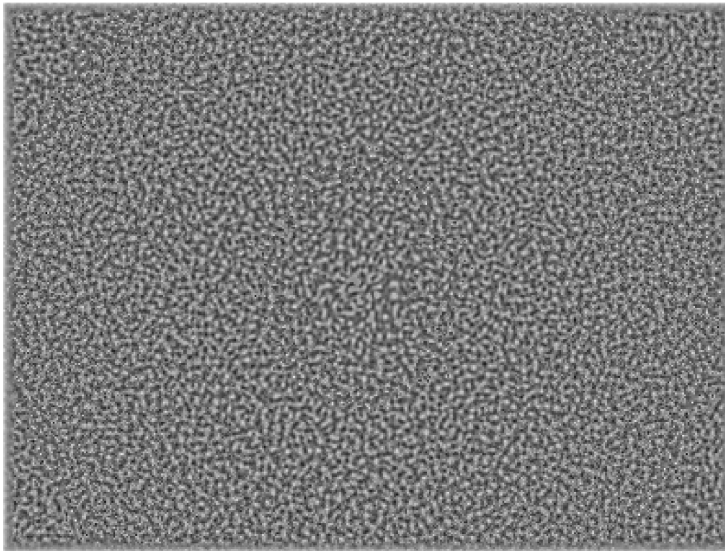
As the speckle is characterised through its size rather than intensities, it has been found to be robust towards variations in the system response.

6.1.5 Discrete Cosine Transform

Ahmed et al. (1974) introduced the Discrete Cosine Transform (DCT) in relation to image data. It is a linear transformation, in which an image can be represented in terms of its frequency components, which are uncorrelated and energy compact. Given an $n \times m$ image, f , the corresponding $n \times m$ frequency



(a) Diffuse reflectance image of fermented milk (1.5% fat) at 500nm



(b) Corresponding speckle image

Figure 6.8: (a) shows a closeup view of a diffuse reflectance image where the speckle phenomenon is clearly visible. (b) shows the underlying speckle pattern obtained when applying the local normalisation scheme in Equation (6.10).

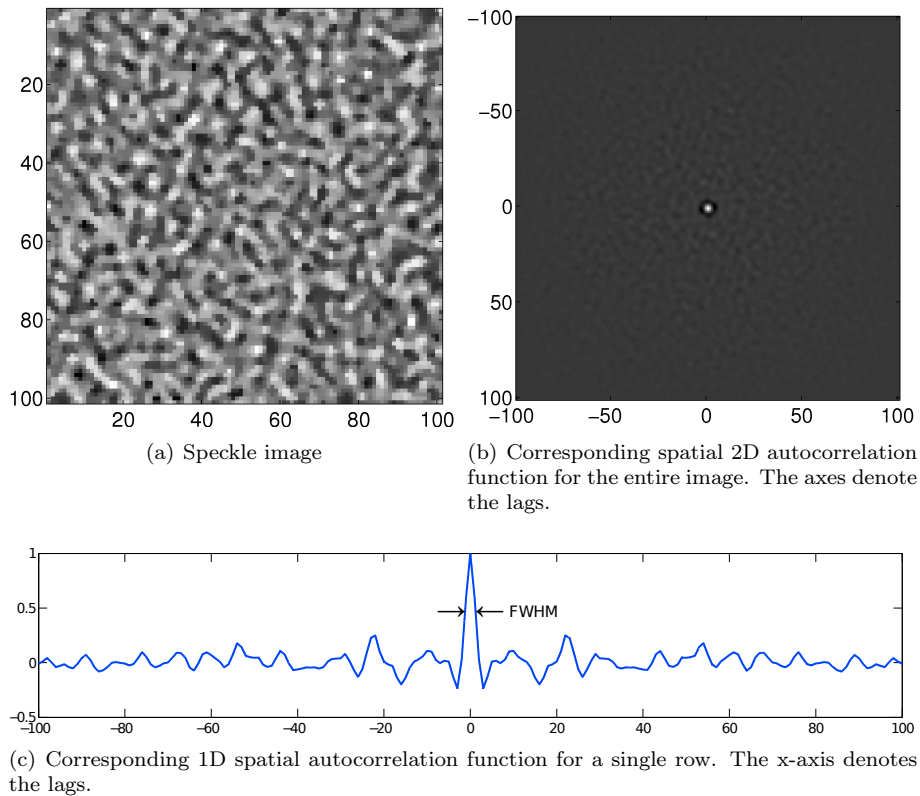


Figure 6.9: (a) shows an extracted speckle pattern, while (b) and (c) show the corresponding spatial autocorrelation functions. From the autocorrelation function the average speckle size can be estimated by the full width at half maximum of the maximum response as illustrated in (c).

map, F , can be described as:

$$F(u, v) = \frac{2}{\sqrt{nm}} c(u)c(v) \sum_{y=0}^{m-1} \sum_{x=0}^{n-1} f(x, y) \cos \frac{(2x+1)u\pi}{2n} \cos \frac{(2y+1)v\pi}{2m}, \quad (6.11)$$

where $c(0) = 1/\sqrt{2}$, $c(k) = 1$ for $k > 0$. The values $F(u, v)$ represent the importance or energy of the corresponding frequencies. Looking at the diffuse reflectance images, it is straightforward to recognise that the light diffusion can be described by the low frequencies in the image, while the speckle pattern can be described by higher frequencies. Figure 6.10 depicts how the frequency map appears when diffuse reflectance images of either milk or fermented milk are considered. A clear difference can be seen between the two milk products. While the lowest frequencies, to some degree, appear equal, the higher frequencies show more variation. When the speckle pattern is pronounced, a broader and more dense area in the frequency spectrum is covered, which makes sense considering the original images.

The diffuse reflectance images can hereby be quantified in the frequency domain rather than the spatial domain. Often when the DCT map is used as image features, the coefficients are selected from the DCT map using a zigzag or a zonal approach as illustrated in Figure 6.11 (Dabbaghchian et al., 2010). However, as we are interested in both the low and the high frequency information in the images, another approach is considered as presented in Paper C.

As the DCT utilises the image intensities, cf. Equation (6.11), the DCT coefficients are dependent on the system response. However, the frequency domain may allow for alternative formulations of shape and size features opposed to those of Section 6.1.3 and 6.1.4. At the time of writing, this has not been investigated further.

6.2 Confocal Scanning Laser Microscopy

This section introduces some of the concepts covered in Paper D. Here, confocal scanning laser microscopy (CSLM) micrographs of casein networks are treated and analysed as image textures, and the main goal is to provide a sufficient description of each network. This section first provides a general introduction to image textures, and hereafter three popular concepts, in relation to image texture description, are briefly introduced.

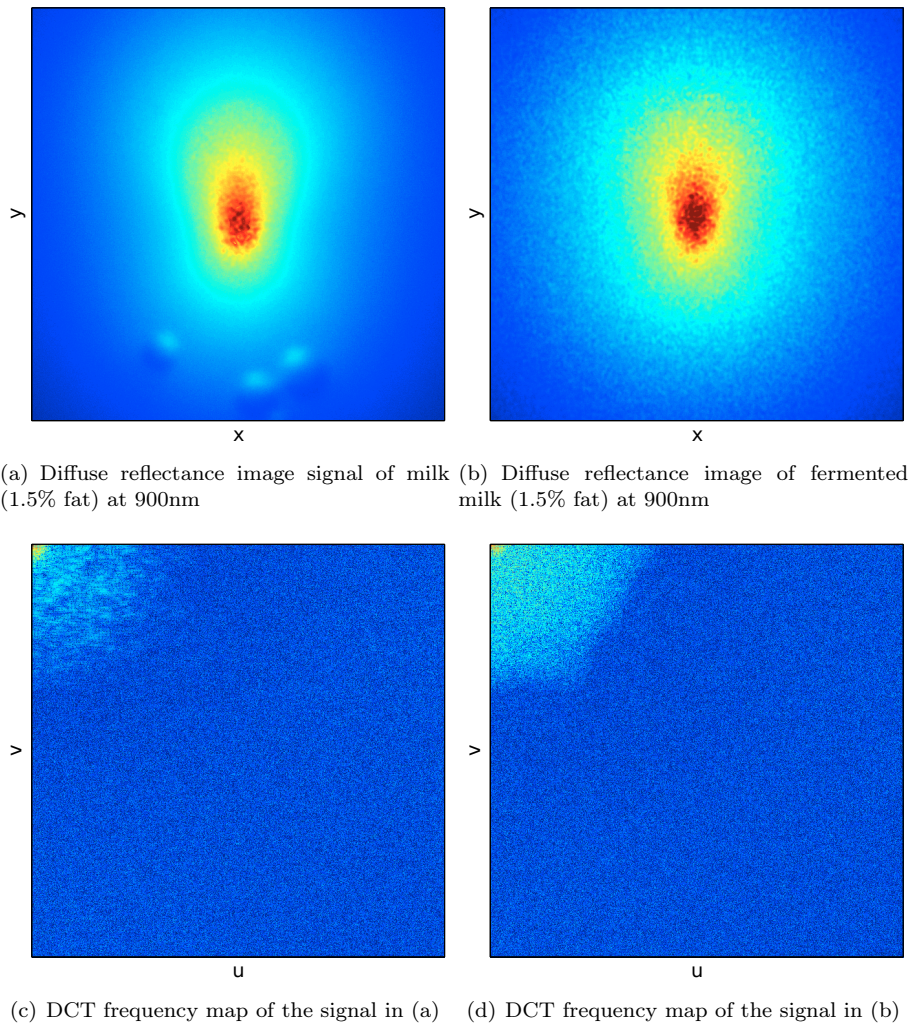


Figure 6.10: (a) and (b) show image patches extracted from the 2DSLS signal near the light incident point (the artefacts in (a) are air bubbles). (c) and (d) shows the corresponding DCT frequency maps where the lowest frequencies are located in the top left corner. The colourmap is row-wise consistent.

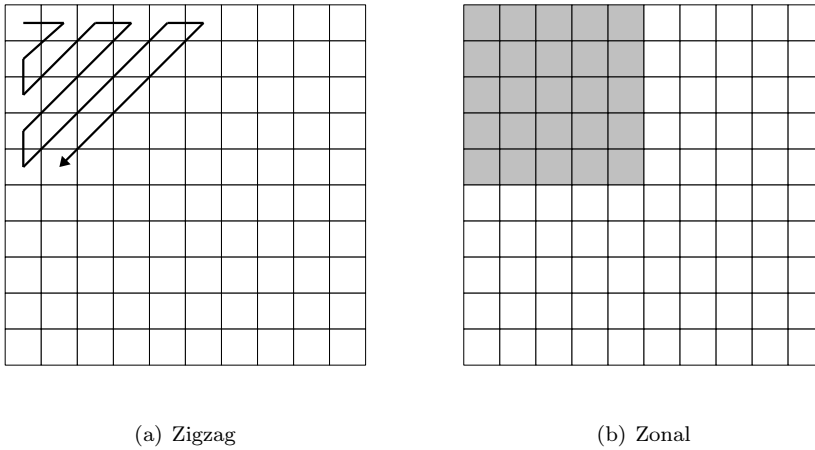


Figure 6.11: The conventional approaches to selecting image feature from the DCT map. In (b) the grey-coloured area corresponds to the selected DCT coefficients.

6.2.1 Image Textures

Authors have provided different definitions of image texture, and following Materka et al. (1998) no strict definition exists. Carstensen (1992) provides the following broad definition of an image texture: "*A texture is a region in 2D or 3D that can be perceived as being spatially homogeneous in some sense*", implying that textures contain some degree of repetitive subpattern, that appears homogeneous when considered at a certain scale.

The properties of these subpatterns have previously been described through uniformity, roughness, regularity, frequency, directionality, homogeneity, randomness, etc. (Materka et al., 1998). Some texture examples are presented in Figure 6.12. Figure 6.12(a) shows a brick wall in which every brick can be considered a regular subpattern repeated over the image. Figure 6.12(b) shows a more random texture with a high frequency structure, and no particular directionality of the subpatterns compared to the other textures. Finally Figure 6.12(c) shows an irregular texture with regular subpatterns (broad lines).

Figure 6.13 shows examples of extrema protein networks from the data set in Section 5.4. Here it can be seen that the texture of these images, to some degree, resembles that of Figure 6.12(b), which appears highly random and

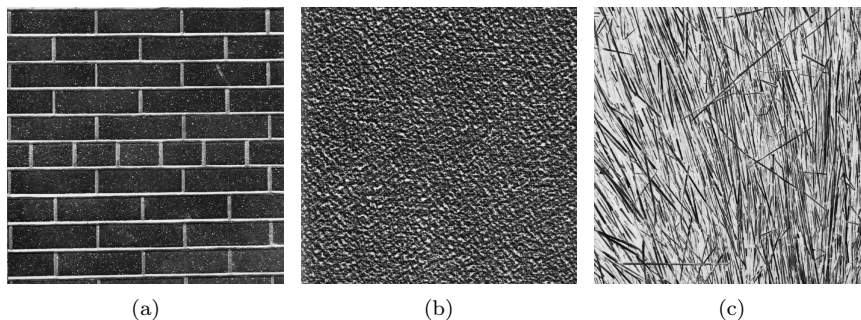


Figure 6.12: Examples of different textures from the Brodatz database (Brodatz, 1966).

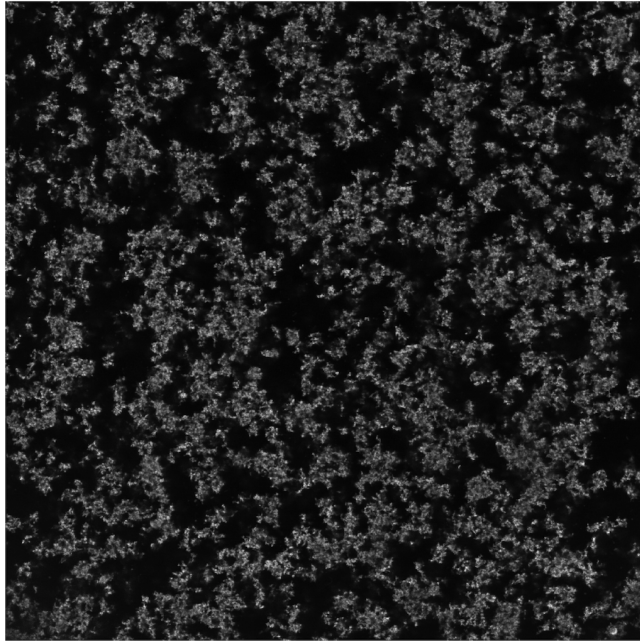
with no apparent directionality. Also, similar to the brick texture in Figure 6.12(a) that is made up by bricks and joints, the protein network is made up by two types of subpatterns: The pores (uniform black regions) and the protein network (irregular brighter regions). Comparing the loose and the dense protein network side by side, the different subpatterns seem to differ in scale. This is very apparent when considering the size of the pores, however it is much more subtle for the actual protein structures.

Our main goal in relation to the CSLM images, is to provide a suitable description of the texture that can be used to discriminate between protein networks made from different process parameter, cf. Chapter 2. Textures are often described by means of statistical methods, which can be grouped as first, second, and higher order statistics. First order statistics describe the distribution of pixel intensities; second order statistics considers pairs of pixels and thereby takes the spatial arrangement into account. Higher order considers three or more pixels at a time (Carstensen, 1992).

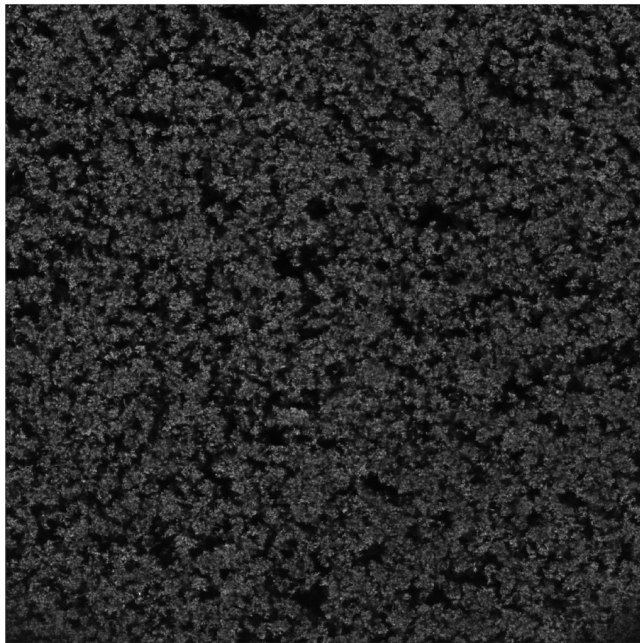
Cf. Chapter 2.2 the physical properties of the protein networks are partly defined by the amount of cross-linking between protein structures and overall density. Hereby, it is natural to believe that second- or higher order descriptors should provide the most appropriate descriptions of the gels. Therefore, these types of descriptors are the main focus in Paper D.

6.2.2 Multiscale Representation and Filter Banks

The frequency of the texture subpatterns relates to the scale of the texture, and should be considered carefully. In the case of Figure 6.12(a), the texture can



(a) Loose protein network



(b) Dense protein network

Figure 6.13: Examples of CSLM images of protein network.

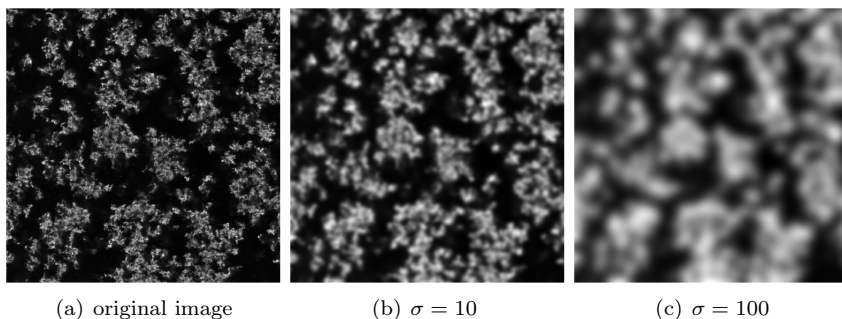


Figure 6.14: Multi scale representation using the Gaussian scale space approach. σ denotes the width of the Gaussian filter.

appear uniform at small scale (a single brick), while at a larger scale (a brick wall) the joints between the bricks break the uniformity. Moving even further up in scale (an entire brick building) the texture may appear uniform again. Thus, selecting a suitable scale has been found to be a fundamental problem in texture analysis (Lindeberg and Garding, 1993). One way to resolve this issue is to consider a multiscale representation of the texture (Lindeberg, 1994), and hereafter a texture description can be applied to each scale representation. The final texture descriptor can be considered as the joint distribution of descriptors across all scales. Most of the applied texture descriptors in Paper D utilise one of the multiscale representation covered in this section.

One of the most common approaches to multiscale representation is scale spaces. A scale space is a series of increasingly more blurred images where the blurring typically is applied by convolving the original image with Gaussian filters. An example is shown in Figure 6.14. Here it can be seen how different structures stand out at different scales. In the original image the small details of the protein network are highlighted, where at $\sigma = 100$ the overall network structure is highlighted.

A computational efficient alternative, that covers a broad range of scales, is the pyramid representations (Lindeberg, 1994). Here the different levels in the pyramid represent different scales. In the Gaussian pyramid each level is constructed by smoothing (with a Gaussian filter) and downsampling (by a factor 2) the previous level. An example is shown in Figure 6.15. In relation to Paper D, Gaussian pyramids are being used as multiscale extensions to existing texture descriptors as suggested by Qian et al. (2011); Roberti de Siqueira et al. (2013).

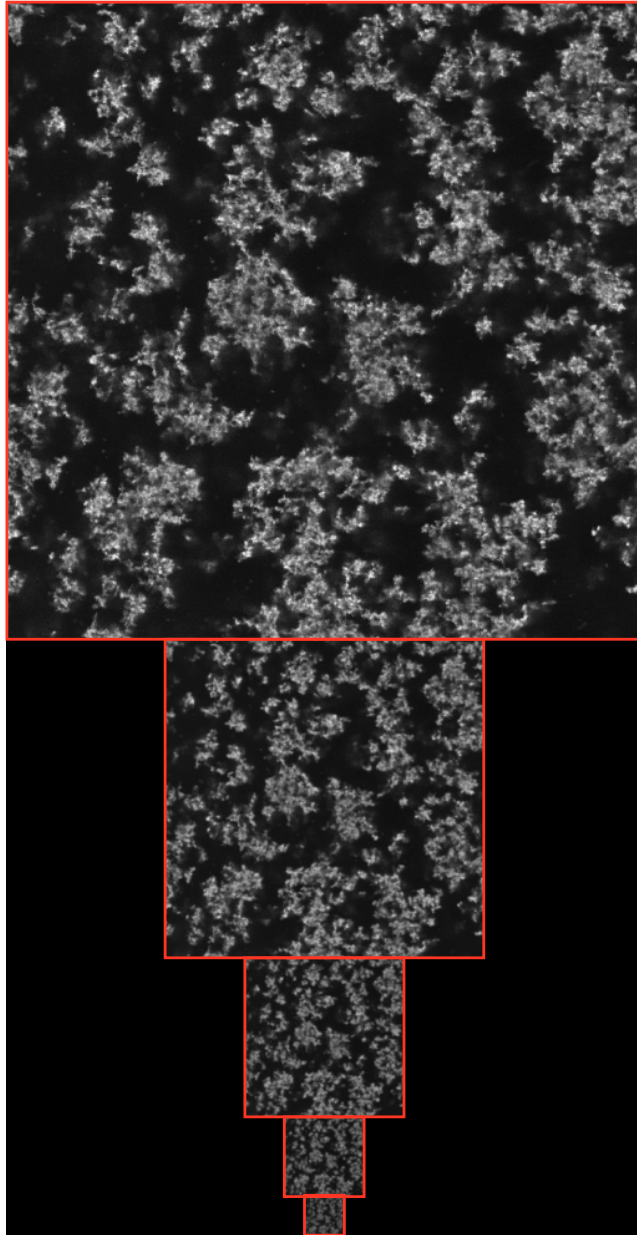


Figure 6.15: Gaussian pyramid with 5 levels, going from level 0 (top) to level 4 (bottom).

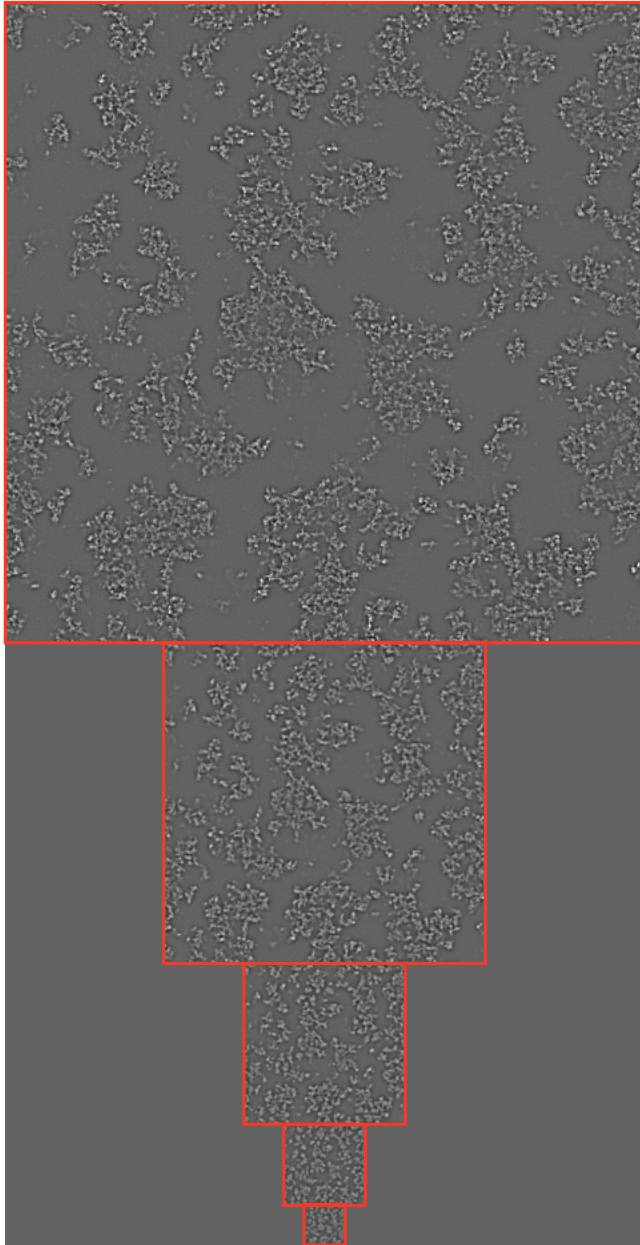


Figure 6.16: Laplacian pyramid with 5 levels, going from level 0 (top) to level 4 (bottom).

Another pyramid representation is the Laplacian pyramid, which contains the second order derivatives across multiple scales. The Laplacian pyramid can be approximated by the Difference of Gaussians approach (Marr and Hildreth, 1980), which corresponds to subtracting consecutive levels in the Gaussian pyramid. Here, an upsampling of the level above is needed. An example of a Laplacian pyramid can be seen in Figure 6.16. In relation to Paper D a variant of the Laplacian pyramid is used to detect *blobs*, which is the initial step in the Scale Invariant Feature Transform (SIFT) (Lowe, 2004). Blobs are defined as regions with large absolute second order derivatives in all directions, and by finding the local maximum blob response across multiple scales, the scale of the blob can also be estimated.

In general image derivatives can be applied in texture description to provide invariance toward pixel intensity variations. E.g. Crosier and Griffin (2008, 2010) proposed to apply a set of Gaussian derivative filters at different scales. From the filter responses each pixel location is assigned the most similar basic image feature (BIF), which covers slopes, blobs, lines, and saddle points. This is illustrated in Figure 6.17.

Here, the applied Gaussian derivative filters can be considered a filter bank. Strictly speaking the Gaussian scale space, as illustrated in Figure 6.14, can be considered a filter bank, consisting of Gaussian filters of different sizes. However, in relation to texture analysis, filter banks are typically referred to as a more focused set of filters targeting specific frequencies and patterns in the image.

While the idea of filter banks is not particularly new (Malik and Perona, 1990), remarkable results have recently motivated the use of filter banks (Leung and Malik, 2001; Cula and Dana, 2004). The filter responses present a new multivariate representation of the original image, which is commonly used in conjunction with *textons*, which will be introduced in the upcoming section. Following the results of Varma (2004) one of the most successful filter banks is the Maximum Response 8 (MR8), which is shown in Figure 6.18. It consists of 38 filters divided into edge and bar filters, each presented at three scales and six orientations, and two isotropic filters: A Gaussian and a Laplacian.

For each scale of both the edge and bar filters, only the orientation, which gives maximum response, is used. Thereby eight rotation invariant filter responses are obtained. In relation to Paper D, the MR8 filter bank is applied in conjunction with a fractal descriptor (Varma and Garg, 2007).

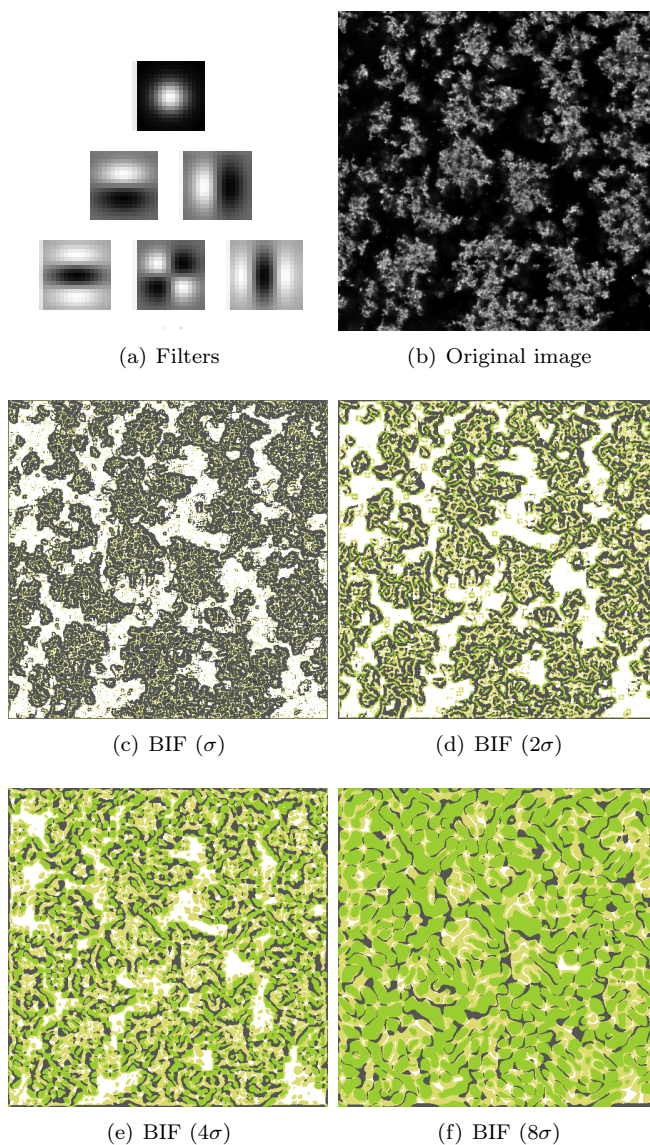


Figure 6.17: Example of Basic Image Features (BIF). (a) shows the Gaussian derivative filters (from zeroth-order to second-order) at a single scale and (b) shows the original image. (c) through (f) show the assigned BIF for four different sizes of the Gaussian derivative filters ($\sigma = 1$). These images contain slopes (grey), bright blobs (white), bright lines (yellow), and saddle points (green).

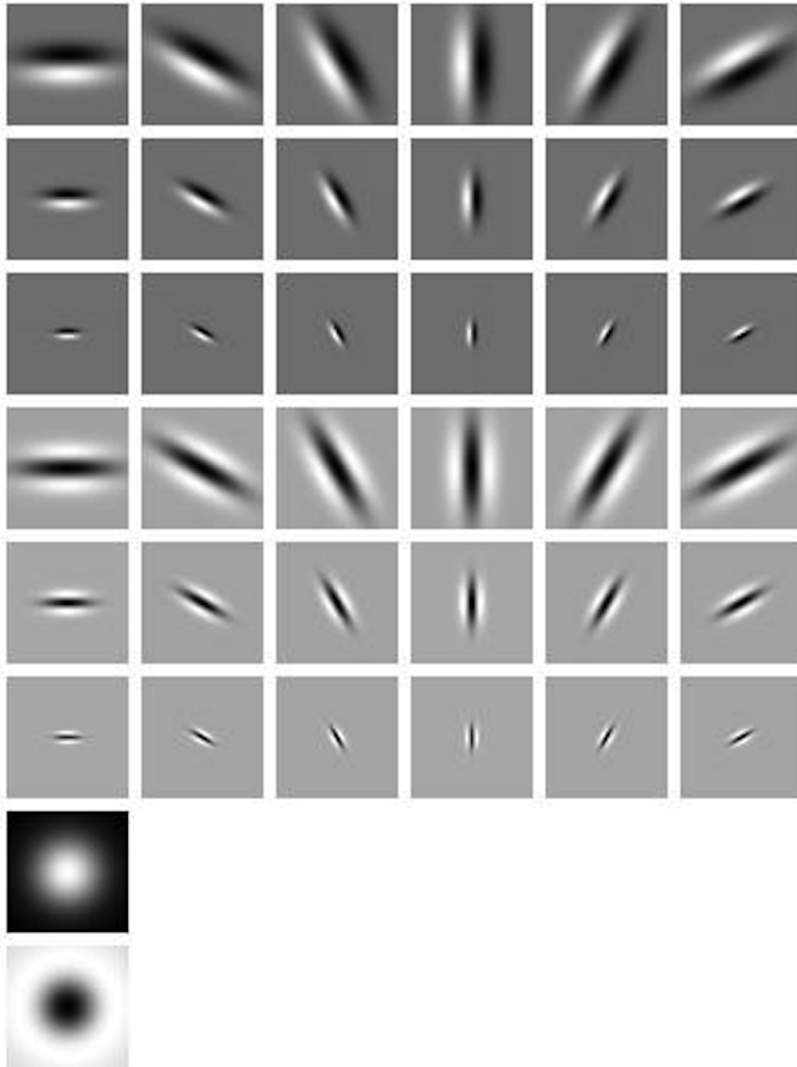


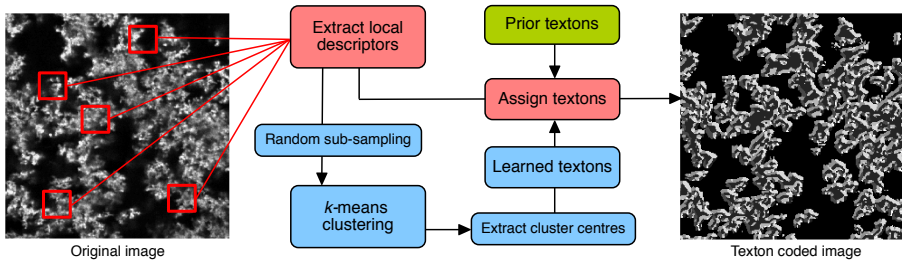
Figure 6.18: The 38 filters of the MR8 filter bank. Each filter is 49×49 pixels.

6.2.3 Textons

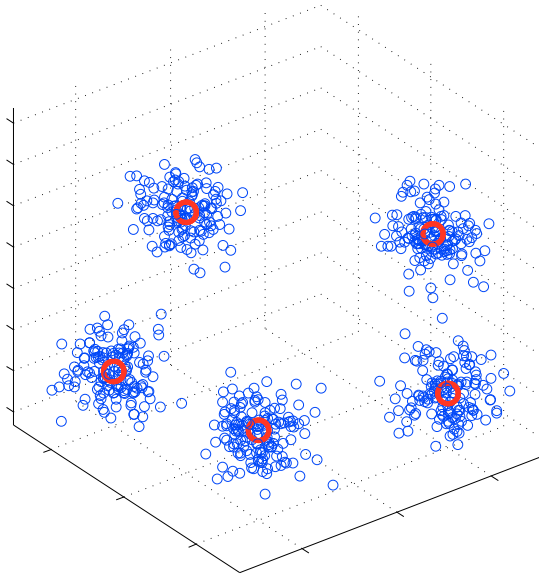
Julesz (1981) and Julesz and Bergen (1983) proposed the notion of textons, which in essence are small texture primitives, such as ellipses, rectangles, line segments, etc. Image texture was hereafter described as frequency distribution of texton occurrences. In practice, the texton approach extracts local descriptors from the texture and each descriptor is hereafter assigned the most similar texton from a predetermined texton dictionary. The texton dictionary is either defined a priori or they are learned from the data set. The BIF methodology illustrated in Figure 6.17 is an example of an a priori texton dictionary, consisting of blobs, slopes, lines, and saddle points. Learned texton sets can be created by randomly sampling local descriptors (denoted training data) from the entire data set. Hereafter a K -means clustering (see Section 6.4.1) is performed on the training data, and the K cluster centres hereafter comprise the learned texton dictionary. The general texton pipeline is shown in Figure 6.19 along with an idealised example of the clustering step.

The texton methodology has been found to be well suited for texture classification when combined with filter banks (Leung and Malik, 2001; Hayman et al., 2004; Varma and Zisserman, 2005; Caputo et al., 2005). Here the joint multivariate filter response at each pixel location is considered a local descriptor. However, a simple scheme has recently challenged this approach. Varma and Zisserman (2009) demonstrated how using small image patches ($n \times n$ pixel neighbourhoods) as local descriptors could outperform state-of-the-art filter bank methods. They, amongst other things, contributed this to the filter banks potentially smoothing away fine details.

The majority of applied texture descriptors in Paper D are based on the texton methodology, and both a priori defined- and learned texton dictionaries are considered.



(a) Texton pipeline



(b) Texton clustering

Figure 6.19: (a) shows the applied pipeline for the texton approach. Local descriptors are extracted from the texture images, and each descriptor is assigned the most similar texton from an a priori or a learned set of textons. The showed texton coded image is made from densely sampled descriptors, which have been assigned one of eight textons, corresponding to the grey level. In practice texton databases are typically much larger. (b) shows an idealised example of the clustering step in two dimensions. The clustering is performed on the training data (blue circles) from which the cluster centres (red circles) can be found and used as the texton set.

6.3 Data Transformation

This section introduces three methods for transforming data, which in essence provide new views of the data that can be exploited in further analysis, or provide easier interpretability of the data.

6.3.1 Principal Component Analysis

Considering a data matrix $\mathbf{X} \in \mathbb{R}^{N \times p}$, where N is the number of observations and p is the number of features, or the dimensionality. The essence of principal component analysis (PCA) is to reduce the dimensionality of \mathbf{X} , while retaining as much as possible of the variation present in \mathbf{X} (Jolliffe, 2005). It is a linear transformation, which rotates the original coordinate system of the data, and the new coordinate axes (principal axes) maximise the variance of the projected data (principal components) as illustrated in Figure 6.20. Furthermore, the principal axes are mutually orthogonal and ordered such that the first principal axes explains the most variation in \mathbf{X} , and for the sequential principal axes the variation explained decreases monotonically. Typically, retaining 95% of the variance in the data matrix results in a significant reduction in dimensionality.

The variance-covariance matrix, $\mathbf{\Sigma} \in \mathbb{R}^{p \times p}$, of \mathbf{X} can be expressed in terms of the eigendecomposition:

$$\mathbf{\Sigma} = \mathbf{V}\mathbf{\Lambda}\mathbf{V}^T, \quad (6.12)$$

where $\mathbf{V} = (\mathbf{v}_1, \mathbf{v}_2, \dots, \mathbf{v}_p)^T \in \mathbb{R}^{p \times p}$ is a matrix containing columns of eigenvectors and $\mathbf{\Lambda} = \text{diag}(\lambda_1, \lambda_2, \dots, \lambda_p)$ holds the corresponding eigenvalues (the variance in the direction of the corresponding eigenvector). The eigenvectors correspond to the principal axes, and thus selecting $k \leq p$ columns of \mathbf{V} can be used to project \mathbf{X} into an $n \times k$ dimensional space.

In Paper C, PCA has been used for easier visual assessment of data, however in Paper A it is used more extensively. Here it is used to reduce entire time developments into few variables, which are better suited for analysis of variance (see Section 6.6). In order to validate the dimensionality reduction, we investigated the variation explained by the projected data. For this purpose we followed the work on active shape models by Cootes et al. (1995).

Considering a 2D example, the N observations in \mathbf{X} correspond to shapes, and the p features correspond to the vectorised 2D spatial coordinates of the

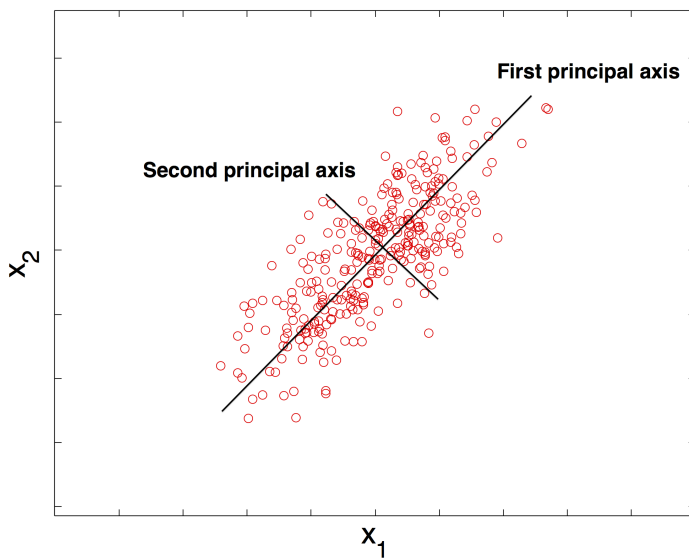


Figure 6.20: To span as much variation as possible in one direction, the original coordinate system is rotated to form a new basis, the first principal axis. The second principal axis is orthogonal to the first principal axis and spans less variance.

shapes. Thereby the i 'th observation is given by $\mathbf{x}_i = (x_{i1}, y_{i1}, \dots, x_{i\frac{p}{2}}, y_{i\frac{p}{2}})$. A mean shape, $\bar{\mathbf{x}}$, is calculated, and the shapes in \mathbf{X} are centred around it (often through Procrustes analysis (Gower, 1975)). Performing the eigendecomposition in Equation (6.12) of the corresponding covariance matrix, the variation explained by projecting the data onto the k 'th principal axis, \mathbf{v}_k can be visualised by:

$$\mathbf{x} = \bar{\mathbf{x}} + \mathbf{v}_k b_k, \quad (6.13)$$

where b_k is a weighting of the k 'th principal axis. Suitable limits for b_k are often defined by the eigenvalues: $-3\sqrt{\lambda_k} \leq b_k \leq 3\sqrt{\lambda_k}$. A 2D example is shown in Figure 6.21, where the shapes consist of facial features. Here it can be seen how the first principal axis varies the shape of the chin and placement of the nose and eyes, while the second principal axis changes the shape of the lips and the width of the chin, whereas the third axis changes the placement of the eyes and the width of the face. The figure also illustrates how the amount of variation explained decreases from the first to the third principal component.

6.3.2 Distance Matrix

Sometimes observations cannot be represented as data points, but only in the context of mutual distances between observations. In these cases we have a distance matrix, \mathbf{D} , which is a symmetric matrix with nonnegative values and a zero diagonal. Each element in the distance matrix, d_{ij} for $i \neq j$, corresponds to the pairwise distance between observations. Converting a data matrix, $\mathbf{X} \in \mathbb{R}^{N \times p}$, to a distance matrix, $\mathbf{D} \in \mathbb{R}_{\geq 0}^{N \times N}$ can also be seen as a way of reducing the dimensionality of the data.

In Paper D we use distance matrices as an approach to make fair comparisons between univariate and multivariate descriptors, and to provide the necessary input for an alternative to the conventional analysis of variance framework, which will be introduced in Section 6.6.3.

6.3.3 Multidimensional Scaling

Multidimensional scaling (MDS) can at first be seen as the inverse of creating the distance matrix introduced in the previous section. However, more commonly it can be seen as dimensionality reducing approach where the interpoint distances

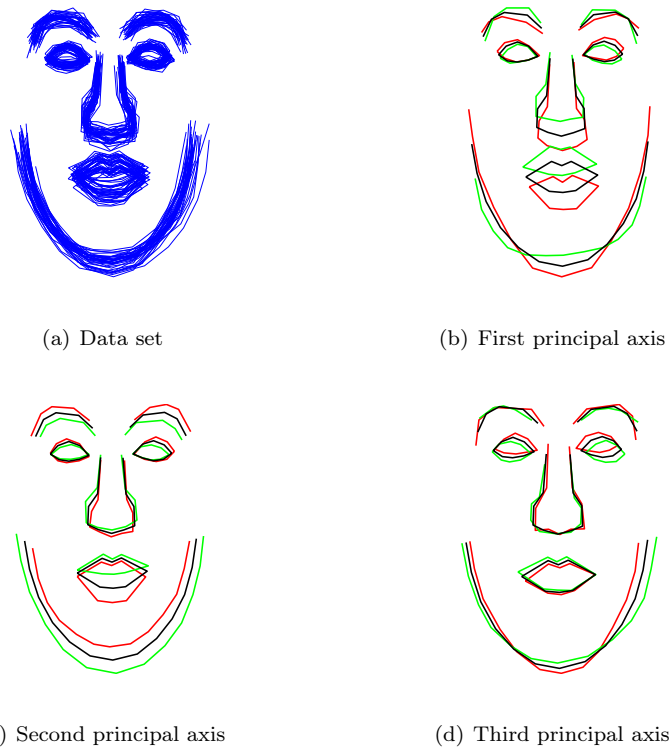


Figure 6.21: Illustration of how Equation (6.13) can be used to investigate the variation explained by projecting the data onto the k 'th principal axis. (a) shows all the shapes in the data set, while (b) through (d) shows the mean shape, $\bar{\mathbf{x}}$ (black) and the effect of varying b_k between $-3\sqrt{\lambda_k}$ (red) and $3\sqrt{\lambda_k}$ (green).

between observations are retained as well as possible. Provided a data matrix $\mathbf{X} \in \mathbb{R}^{N \times p}$ and its corresponding distance matrix, $\mathbf{D} \in \mathbb{R}_{\geq 0}^{N \times N}$, multidimensional scaling can be used to determine a lower-dimensional representation of the data where the mutual distances of \mathbf{D} are approximated. This can be done by seeking the values $\mathbf{Z} = (\mathbf{z}_1, \mathbf{z}_2, \dots, \mathbf{z}_N)^T \in \mathbb{R}^{N \times k}$ (where $k < p$) that minimises the stress function:

$$S(\mathbf{Z}) = \sum_{i=1}^N \sum_{j=1}^N (d_{ij} - \|\mathbf{z}_i - \mathbf{z}_j\|)^2, \quad (6.14)$$

where $\|\cdot\|$ is the Euclidean norm. This approach is known as *least squares scaling*. Furthermore, the stress function is commonly minimised using gradient descent algorithms (Wright and Nocedal, 1999). A slightly different formulation of the stress function is the *Sammon mapping*. Here, more emphasis is put on preserving the smaller mutual distances in the data set, and the expression is given by:

$$S_{\text{SM}}(\mathbf{Z}) = \sum_{i=1}^N \sum_{j=1}^N \frac{(d_{ij} - \|\mathbf{z}_i - \mathbf{z}_j\|)^2}{d_{ij}}. \quad (6.15)$$

The appropriate choice of stress function is dependent on the data at hand (Hastie et al., 2009). In Paper E multidimensional scaling was applied in order to compare the multidimensional texture descriptors of Section 6.2.3, with the univariate quantification of the 2DSLS signal in Section 6.1.2.1.

6.4 Clustering

In this section we consider three unsupervised clustering approaches, applied throughout the contributions. The basis of unsupervised clustering is to explore the data and find intrinsic structures. Typically the methods are initialised in terms of an $N \times p$ data matrix, where N is the number of observation, and p is the dimensionality of the data, along with the desired number of so called cluster centres.

6.4.1 K -Means Clustering

Considering a set of observations $\mathbf{X} = (\mathbf{x}_1, \mathbf{x}_2, \dots, \mathbf{x}_N)^T \in \mathbb{R}^{N \times p}$, K -means clustering attempts to perform a partition into K clusters which minimises the objective function (Bishop et al., 2006):

$$\arg \min_{r_{nk}, \boldsymbol{\mu}} \sum_{n=1}^N \sum_{k=1}^K r_{nk} \|\mathbf{x}_n - \boldsymbol{\mu}_k\|^2, \quad (6.16)$$

where $\|\cdot\|$ is the Euclidean norm, and $r_{nk} \in \{0, 1\}$ are the *responsibilities*, which take a binary variable indicating if \mathbf{x}_n is member of the k 'th cluster or not. $\boldsymbol{\mu}_k$ are the cluster centres calculated as the mean of all observations included in the k 'th cluster. The objective function can be minimised through the following iterative scheme:

1. Assign each $\boldsymbol{\mu}_k$ a random position (or initial guess) in the data set
2. For each \mathbf{x}_n :
 - Determine nearest $\boldsymbol{\mu}_k$ and update r_{nk}
3. For each cluster:
 - Recalculate $\boldsymbol{\mu}_k$ according to r_{nk}
4. If not converged go to 2.

$$n = 1, \dots, N \text{ and } k = 1, \dots, K$$

This is continued until convergence or when a minimum change in the updated cluster centres is attained. However, there is no guarantee for convergence to a global optimum, and the result may depend on the initial cluster centres. A simple clustering example is shown in Figure 6.22.

This type of clustering has been applied in relation to the textons introduced in Section 6.2.3, where it is commonly used for learning the texton set from training data (Leung and Malik, 2001; Cula and Dana, 2004; Varma and Zisserman, 2009). Thereby, it has been used to great extent in Paper D.

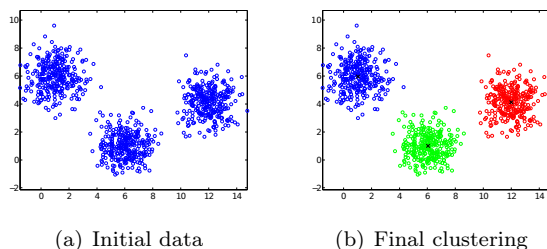


Figure 6.22: Examples of K -means clustering with three clusters. Circles denote the observation and "x" marks the cluster centres.

6.4.2 Gaussian Mixture Model

Gaussian mixture model (GMM) is a similar variant of clustering. Directly compared to K -means clustering the GMM assumes that each cluster centre is a Gaussian distribution and thereby described in terms of $\theta = \{\mu_k, \Sigma_k, \pi_k\}$ for $k = 1, \dots, K$, where μ_k is the mean, Σ_k is the covariance matrix, and π_k is the prior of the k 'th Gaussian distribution. Provided a set of observations $\mathbf{X} = (\mathbf{x}_1, \mathbf{x}_2, \dots, \mathbf{x}_N) \in \mathbb{R}^{N \times p}$ and K unknown Gaussian distributions, we seek to maximise the probability of θ given the observations. That is, we seek to maximise the likelihood function:

$$\arg \max_{\theta} p(\mathbf{X}|\theta) = \prod_{n=1}^N \sum_{k=1}^K \pi_k \mathcal{N}(\mathbf{x}_n | \mu_k, \Sigma_k). \quad (6.17)$$

A common approach to maximising this function is to apply the Expectation-Maximisation algorithm (Bishop et al., 2006; Hastie et al., 2009), which is an iterative scheme resembling that of K -means clustering. It can briefly be described in the following steps:

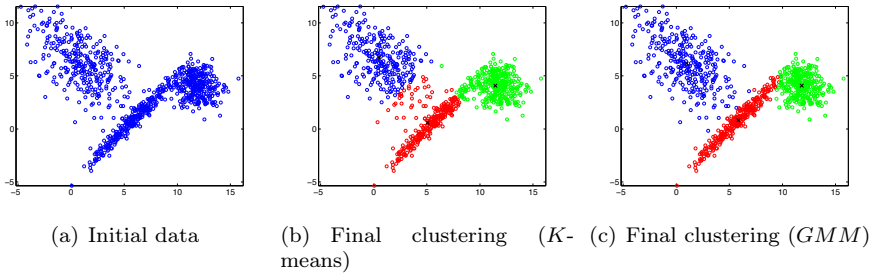


Figure 6.23: Example of applying K -means and GMM on data originating from distributions with different covariant structures. Circles denotes the observation and "x" marks the cluster centres.

1. Assign each of the K Gaussian distributions random parameters (or initial guess)
2. For each \mathbf{x}_n :
 - Assign responsibility, r_{nk} , for each cluster, based on the likelihood. A point close to the cluster centre will likely get a responsibility close to 1 for that cluster, and close to 0 for every other cluster.
3. For each cluster:
 - Recalculate $\boldsymbol{\mu}_k$, $\boldsymbol{\Sigma}_k$, and π_k weighted by r_{nk}
4. If not converged go to 2.

$$n = 1, \dots, N \text{ and } k = 1, \dots, K$$

Again, the scheme is continued until convergence or when a minimum change is attained during the updates. Directly compared to K -means clustering, the calculated responsibilities in GMM are not binary, which results in softer decision boundaries. Figure 6.23 gives an example where K -means clustering and GMM are applied to data originating from distributions with different covariant structures, highlighting the strength of the GMM. Here it can be seen that K -means have sharper decision boundaries, while GMM appears to be more adaptable to the covariant structure of the data. As with K -means clustering there is no guarantee for convergence to a global optima, and in practice GMM is very dependent on the initial clusters centres. Thus, the result of a K -means clustering is often used as initialisation for GMM.

We have applied GMM for an image segmentation task in Paper D, in which it was found to provide more satisfactory results than K -means clustering.

6.4.3 Hierarchical Clustering

Hierarchical clustering takes a slightly different approach compared to the two previous methods. Requiring neither the actual observations as input or any amount of clusters, hierarchical clustering determines the entire hierarchical structure based on the dissimilarities of the observations, e.g. in the form of the distance matrix, \mathbf{D} , introduced in Section 6.3.2.

This hierarchical structure can be determined in a bottom-up approach (agglomerative), in which every data point initially is considered one cluster. Clusters are hereafter recursively merged. Alternatively, a top-down approach (divisive) can be used, in which the entire data set initially is considered a cluster. Hereafter, a recursive splitting of the cluster is performed.

The splitting and merging of clusters is decided upon based on the chosen *linkage* function. The three following linkages are often used (Hastie et al., 2009). Given two clusters C_1 and C_2 the single linkage is described as the distance between the two most similar data points of the two clusters:

$$\ell_{single}(C_1, C_2) = \min_{\substack{i \in C_1 \\ i' \in C_2}} d_{ii'}. \quad (6.18)$$

The complete linkage measures the distance between the two most dissimilar data points:

$$\ell_{complete}(C_1, C_2) = \max_{\substack{i \in C_1 \\ i' \in C_2}} d_{ii'}. \quad (6.19)$$

And the average linkage can be seen as a compromise between single and complete linkage:

$$\ell_{average}(C_1, C_2) = \frac{1}{N_1 N_2} \sum_{i \in C_1} \sum_{i' \in C_2} d_{ii'}, \quad (6.20)$$

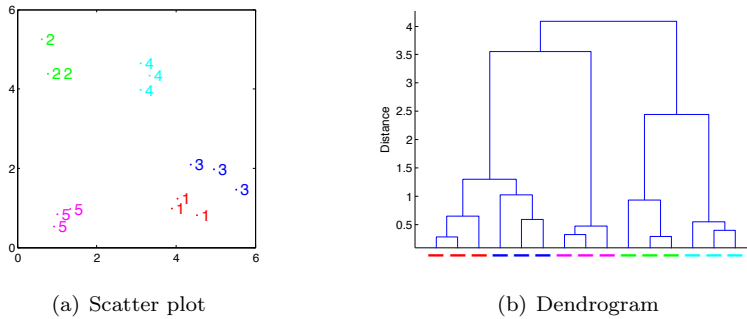


Figure 6.24: A data set (a) and its corresponding dendrogram (b) using a Euclidean distance matrix and the average linkage. The colors in the scatter plot correspond to those of the dendrogram.

where N_i corresponds to the number of data points in cluster C_i . The appropriate choice of linkage function, depends heavily on the investigated data. Figure 6.24 provides a small example using a Euclidean distance matrix and the average linkage, and the results are represented using a dendrogram. A dendrogram visualises the hierarchical structure of the data, and the vertical lines denote the distances between different cluster centres. Cutting the dendrogram horizontally results in a segmentation of the data, and the amount of intersected vertical lines corresponds to the number of clusters in the segmentation. As such, hierarchical clustering has become a popular tool for creating interpretable views of the data where a hierarchical structure exists. In Paper D we use hierarchical clustering to visualise how the protein microstructure of the 16 unique yogurts (see data set in Section 5.4) are ordered based on an image texture descriptor.

6.5 Classification

Classification is the problem of identifying to which class or label a new observation belongs. This decision is typically based on prior knowledge obtained from an initial set of observations with corresponding labels, on the base of which a classification model has been built. In other words, a classification model has been trained on the prior observations. The training is a very important part of the classification as it greatly affects the performance of the classification model. In the following sections a strategy for training classification models is briefly introduced, and hereafter two non-parametric classifiers are presented.

6.5.1 Cross Validation

Typically model training requires the selection of one or more parameters, which must be chosen carefully to ensure an appropriate generalisability. A model can be trained to perfectly classify the available training data, however it may not perform well when classifying unseen data, due to the lack of generalisability. This issue is denoted overfitting.

K -fold cross validation is a widely applied approach to counter overfitting. Here, the data set is randomly divided into K equal-sized parts, and in turn the model performance is evaluated on one part (test set), while the model is trained on the $K - 1$ remaining parts (training set). The parameters for the classification model are selected based on the average performance on the test sets.

Typical values for K are 5 or 10 (Hastie et al., 2009), however for particularly small data sets with N samples, leave-one-out cross validation (LOOCV) can be used, corresponding to ($K = N$). Most of the data sets presented in Chapter 5 are fairly limited in size, thus LOOCV has mostly been applied throughout this thesis. Furthermore LOOCV has mainly been applied in relation to support vector machines, which will be introduced in Section 6.5.3.

6.5.2 k -Nearest Neighbour

k -nearest neighbour classification is a non-parametric method which classifies a new observation by the majority vote of the k nearest neighbours in the training set. Thus, the training set simply consists of the individual observations in the training set. The measure of closeness implies a distance metric, and while the Euclidean distance is the most widely used, other metrics can be applied.

Within the field of texture classification, evaluation of texton descriptors (see Section 6.2.3) is often performed using a slight variation of k -nearest neighbour classification, combined with the χ^2 distance metric (Press et al., 2007). The performance of a texton descriptor is evaluated by isolating a number of observations from each class, and build a classification model on the remaining observations. The isolated observations are hereafter classified using the trained model. The final evaluation of each descriptor is then based on the statistical distribution of classification rates across multiple random splits of the data. Thus, cross validation is not applied as described in the previous section. This approach was initially proposed by Leung and Malik (2001) and is now commonly applied when evaluating texture descriptors (Cula and Dana, 2004; Varma and Zisserman, 2005, 2009). We also apply this approach, when evalu-

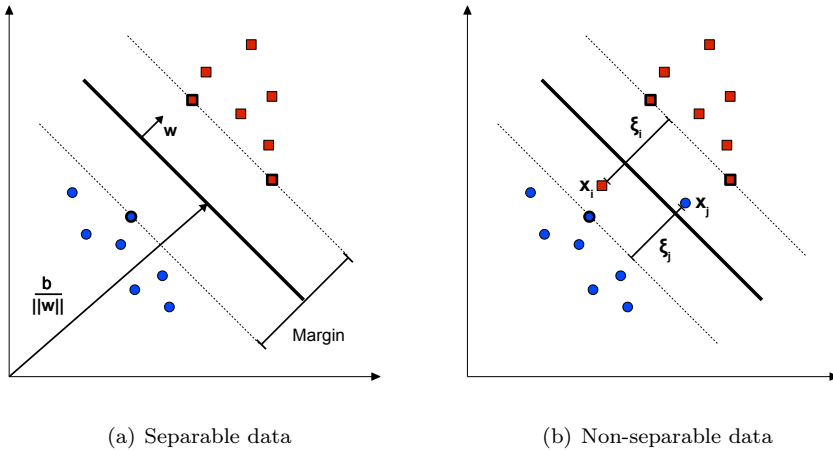


Figure 6.25: An example of the SVM classifier in two dimensions for separable data (a) and non-separable data (b). The highlighted points denotes the support vectors, which defines the hyperplane.

ating different image texture descriptors in relation to protein microstructures in Paper D.

6.5.3 Support Vector Machine

The support vector machine (SVM) classifier relies on a simple yet effective principle. Given a training set of two separable classes by the observations $(\mathbf{x}_1, \mathbf{x}_2, \dots, \mathbf{x}_N) \in \mathbb{R}^p$ and the corresponding class labels $(y_1, y_2, \dots, y_N) \in \{-1, 1\}$, the SVM classifier seeks to create a decision boundary that maximises the margin between the two classes, as illustrated in Figure 6.25(a). The separating hyperplane can be formulated as:

$$\mathbf{x}\mathbf{w} + b = 0, \quad (6.21)$$

where \mathbf{w} is the normal to the hyperplane and $\frac{b}{\|\mathbf{w}\|}$ is the perpendicular distance from the hyperplane to the origin. The two hyperplanes making up the margins can be formulated as:

$$\mathbf{x}_i \mathbf{w} + b \leq 1 \quad \text{for } y_i = -1, \quad (6.22)$$

$$\mathbf{x}_i \mathbf{w} + b \geq 1 \quad \text{for } y_i = 1. \quad (6.23)$$

Thus, the hyperplanes must lie $\frac{|1-b|}{\|\mathbf{w}\|}$ and $\frac{|-1-b|}{\|\mathbf{w}\|}$ from the origin. This results in a margin with a width of $\frac{2}{\|\mathbf{w}\|}$, and thereby maximising the margin corresponds to a minimising of $\|\mathbf{w}\|$. The minimisation must be performed such that all observations in the training set are classified correctly, thus the final objective function can be written as:

$$\min_{\mathbf{w}, b} \|\mathbf{w}\| \quad \text{subject to } y_i(\mathbf{x}_i \mathbf{w} + b) \geq 0, \quad i = 1, \dots, N. \quad (6.24)$$

However, often the data cannot be separated perfectly, and slight alterations have to be made to the objective function to accommodate for this. For this purpose a so-called slack variable, $\xi = (\xi_1, \xi_2, \dots, \xi_N)$ where $\xi_i \geq 0$, is introduced, which can be used to allow for observations in the training set to be misclassified. From Figure 6.25(b) it can be seen that an observation \mathbf{x}_i is misclassified when $\xi_i > 1$ and correctly classified when $\xi_i = 0$. Thus, bounding $\sum_{i=1}^N \xi_i$ bounds the total amount by which classifications fall on the wrong side of their margin, i.e. the total overlap. The slack variable can hereby be incorporated to the objective function in Equation (6.24) as follows:

$$\min_{\mathbf{w}, b} \|\mathbf{w}\| \quad \text{subject to } \begin{cases} y_i(\mathbf{x}_i \mathbf{w} + b) \geq \frac{1-\xi_i}{\|\mathbf{w}\|} & i = 1, \dots, N, \\ \xi_i \geq 0, \quad \sum_{i=1}^N \xi_i \leq C. \end{cases} \quad (6.25)$$

Here, the constraint measures the overlap in relative distance, which changes with the width of the margin. Thus, C , which bounds the total allowed overlap can be seen as a tuneable parameter, which controls the trade-off between error and margin. The objective functions in Equation (6.24) and (6.25) can be turned into convex quadratic optimisation problems with the use of Lagrange multipliers (Hastie et al., 2009). From the optimisation the support vectors, shown in Figure 6.25, are determined from which the hyperplane can be constructed. Thus, SVM constructs the classification model by only considering observations close to the class boundary.

A widely popular extension to SVM classifiers is to apply the *kernel trick*, which is a way of mapping data to a very high dimensional space and down to an inner product space without having to compute the mapping to the very high

dimensional space explicitly. This allows for using linear methods that will behave similar to non-linear methods in the original input space. However, for the SVM classification problems in this thesis (Paper B and C), we expected linear classification boundaries to be sufficient. Thus, we have only considered the linear kernel, which corresponds to the inner product of \mathbf{X} .

Additionally, the above-mentioned formulations only consider binary problems, however SVM classifiers can be extended to multi class problems as well. In a comparative study Hsu and Lin (2002) found the *one – against – one* methodology to be both practical and competitive. For M classes the one-against-one approach constructs $M(M - 1)/2$ binary classifiers, and a new observation is classified as the majority vote when considering all classifiers.

6.6 Analysis of Variance in Factorial Designs

Analysis of variance (ANOVA) is a class of statistical models used for understanding the sources of variability in a data set, and does so by modelling the linear relationship between a response variable and one or more independent variables. In its simplest form ANOVA provides a statistical test of whether or not the means of m groups are equal, that is the null-hypothesis $H_0 : \mu_1 = \mu_2 = \dots = \mu_m$ is tested against the alternative-hypothesis $H_1 : \exists_{i,j} \mu_i \neq \mu_j$.

Furthermore, ANOVA is commonly applied in relation to factorial designs, where the independent variables are denoted factors, which are often changed systematically within two levels (low and high). In total this yields 2^k unique factor combinations, where k is the number of factors. For the response variable, only one observation is required for each factor combination in order to perform hypothesis testing of all k factors (more observations are needed to investigate factor interactions), thus factorial designs allow for very efficient screening for significant factor effects, using a limited amount of observations. This section briefly introduces ANOVA, and variants hereof, in relation to factorial designs.

ANOVA was used in Paper A, D, and E in relation to the data sets introduced in Sections 5.1 and 5.4, which were both constructed through 2^k factorial designs. Each data set has three and four factors respectively (corresponding to milk fermentation process parameters), and the 2DSLS, CSLM, and SAOR measurements correspond to the response variables.

6.6.1 ANOVA

Figure 6.26 provides a graphic representation of a 2^2 factorial design. Here we have two factors A and B each with $a = b = 2$ levels and n univariate observations for each factor combination. Furthermore we have an interaction term AB , which describes the combined effect of A and B . Following the notation of Montgomery (2005), the ANOVA for the 2^2 factorial design can be written as the so-called *effects model*:

$$y_{ijk} = \mu + \alpha_i + \beta_j + (\alpha\beta)_{ij} + \epsilon_{ijk} \begin{cases} i = 1, 2 \\ j = 1, 2 \\ k = 1, \dots, n \end{cases} . \quad (6.26)$$

Here y_{ijk} are the measurements, μ represents the overall mean effect, and α_i , β_j , and $(\alpha\beta)_{ij}$ denote the deviations from the overall mean for factor A, factor B, and the interaction term respectively. ϵ_{ijk} is the random error assumed to be normally distributed with zero mean and variance of σ^2 . For testing whether or not the effects of factor A and B are significant the following hypotheses can be formed as

$$\begin{aligned} H_0 : \quad & \alpha_1 = \alpha_2 = 0 \quad (\text{factor effect A is absent}) \\ H_1 : \quad & \alpha_i \neq 0 \text{ for at least one } i, \end{aligned} \quad (6.27)$$

and

$$\begin{aligned} H_0 : \quad & \beta_1 = \beta_2 = 0 \quad (\text{factor effect B is absent}) \\ H_1 : \quad & \beta_i \neq 0 \text{ for at least one } i, \end{aligned} \quad (6.28)$$

and the hypothesis test for a significant interaction effects is written as

$$\begin{aligned} H_0 : \quad & (\alpha\beta)_{11} = (\alpha\beta)_{12} = (\alpha\beta)_{21} = (\alpha\beta)_{22} = 0 \\ H_1 : \quad & (\alpha\beta)_{ij} \neq 0 \text{ for at least one } ij. \end{aligned} \quad (6.29)$$

In order to test for factor significance, the total variability of the data set is partitioned into sum of squares (SS), by considering the contrast in the response

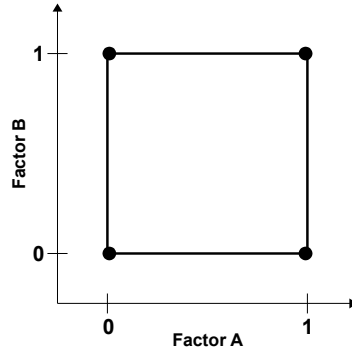


Figure 6.26: An example of a 2^2 design, with two factors A and B each with two levels. Each corner in the design contains n observations.

variable for different factor levels. Thus, the total variability in the data set, SS_T , is defined by the sum of squares of each source of variation in the design:

$$SS_T = SS_A + SS_B + SS_{AB} + SS_W, \quad (6.30)$$

where SS_W corresponds to the variability not accounted for by the main factors and interactions, that is the within-group variability or experimental error. Dividing the sum of squares by their associated degrees of freedom, df , gives the *mean squares*, from which an upper one-tailed F -test can be applied for each factor and interaction term. E.g. considering factor A we can test whether or not the variability explained by this factor exceeds the variability explained by the experimental error. Thus, the test statistic for the hypothesis (6.27) is calculated by

$$F = \frac{SS_A/df_A}{SS_W/df_W}, \quad (6.31)$$

and compared to the sample distribution F_{α, df_A, df_W} , where $df_A = (a - 1)$ and $df_W = ab(n - 1)$. If we reject the null-hypothesis the effect of factor A is considered significant within the factorial design. This approach generalises to larger factorial designs as well.

The ANOVA model assumes the data to be stochastically independent, homogeneity of variance between factor groups (homoscedasticity), and the residuals should follow a standard normal distribution. Statistical tests exist for verifying these assumptions such as the Shapiro-Wilk test (normality) and Levene's test (homoscedasticity), however model adequacy is conventionally assessed through inspection of the residuals of the underlying linear model (Montgomery, 2005).

6.6.2 MANOVA

Multivariate analysis of variance (MANOVA) is a generalisation of ANOVA, where the significance of multiple response variables can be investigated. Effects of the main factors and interactions are hereby assessed on a linear combination of the multivariate response variables. Moreover, for each investigated factor or interaction effect, the linear combination is made such that it maximises the difference between groups. Also, compared to performing an ANOVA for each of the response variables, MANOVA allows for inspection and exploitation of the covariant structures in the data. Thus, performing a MANOVA requires more degrees of freedom, as the covariances also have to be estimated. Finally, the standard F -test is not applicable for multivariate data, thus different approximations should be considered such as Wilks' Lambda and Pillai's Trace (Hand and Taylor, 1987).

6.6.3 NPMANOVA

The image texture descriptors introduced in Section 6.2.3 and applied in Paper D, are frequency histograms of texton occurrences in an image. Thus, the descriptors are expected to be multivariate, and thereby seem to fit into the scope of MANOVA. However, as will be seen in Paper D, some of the descriptors will contain as many as 1296 dimensions. Considering the number of observations in the data set used in Paper D (see Section 5.4), the covariance matrices needed for the MANOVA cannot be estimated in a feasible manner.

An alternative approach denoted non-parametric multivariate analysis of variance (NPMANOVA) has been proposed within the field of ecology (Anderson, 2001). Ecological community data typically consists of species counts (features) at a number of different sites (observations). Often the number of species greatly exceeds the number of sites, providing a similar deficit in degrees of freedom, as seen for the texture descriptors. Furthermore, for conventional distance measures for these types of data, such as Bray-Curtis dissimilarity (Bray and Curtis,

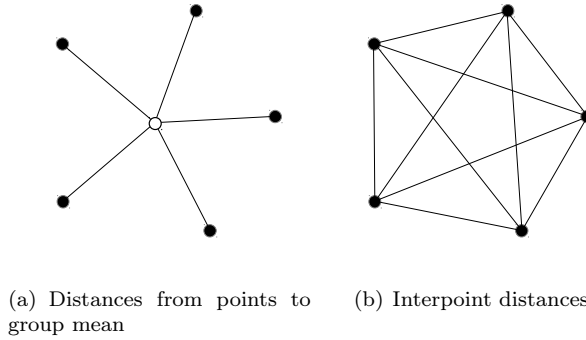


Figure 6.27: The sum of squared distances from each point to the group mean is equal to the sum of squared interpoint distances divided by the number of points.

1957), a group mean is not easily calculated. Thereby, the sum of squares cannot be calculated as for ANOVA and MANOVA.

Instead, the NPMANOVA relies on the relationship illustrated in Figure 6.27. This states that the sum of squared distances from each point to the group mean is equal to the sum of squared interpoint distances divided by the number of points. Thereby, the sum of squares can be calculated for any distance measure, provided a distance matrix (see Section 6.3.2) is available. However, it should be noted that this approach discards any information on the covariant structures in the data, which are commonly exploited in the case of MANOVA.

Thus, considering the factorial design in Figure 6.26 with two factors A and B , each with $a = b = 2$ factor levels, and n observations at each factor combination, the corresponding distance matrix, D , will be of size $N \times N$ where $N = abn$. From the elements of the distance matrix, d_{ij} , the total sum of squares can be calculated as:

$$SS_T = \frac{1}{N} \sum_{i=1}^{N-1} \sum_{j=i+1}^N d_{ij}^2, \quad (6.32)$$

which corresponds to the sum of squared distances in the upper triangular part (not including the diagonal) of the distance matrix, divided by the number of observations. In a similar fashion the sum of squares for the main factors and the residuals can be calculated, by considering the within-group variability for

the factors:

$$SS_{W(A)} = \frac{1}{bn} \sum_{i=1}^{N-1} \sum_{j=i+1}^N d_{ij}^2 \gamma_{ij}^{(A)}, \quad (6.33)$$

$$SS_{W(B)} = \frac{1}{an} \sum_{i=1}^{N-1} \sum_{j=i+1}^N d_{ij}^2 \gamma_{ij}^{(B)}, \quad (6.34)$$

$$SS_W = \frac{1}{n} \sum_{i=1}^{N-1} \sum_{j=i+1}^N d_{ij}^2 \gamma_{ij}^{(AB)}, \quad (6.35)$$

where $\gamma_{ij}^{(\cdot)}$ is an indicator function taking the value of 1 if observations i and j have the same level of the factor in the superscript. A visual interpretation of the indicator function is presented in Figure 6.28. From SS_T and the within-group variabilities the actual sum of squares for the factors, can be calculated by:

$$SS_A = SS_T - SS_{W(A)}, \quad (6.36)$$

$$SS_B = SS_T - SS_{W(B)}, \quad (6.37)$$

$$SS_{AB} = SS_T - SS_A - SS_B - SS_W. \quad (6.38)$$

Following Equation (6.31), a similar test statistic can be calculated for the factors and interactions. However, this statistic only corresponds to the F statistic of traditional ANOVA, if the distance matrix is based on Euclidean distances from univariate observations. As this is not the case for the previously mentioned texture descriptors, a different approach to hypothesis testing has to be considered.

Anderson (2001) proposes to apply permutation testing. Under the null-hypothesis, the factor "labelling" in the distance matrix can be swapped freely, relative to the investigated factor, without changing the value of the test statistic when recalculating the sum of squares. Thus, if we consider the test statistic of the original labelling, F , and the test statistic of the i 'th permutation, F_i^π , a p -value can be defined as:

$$p = \frac{\sum_{i=1}^U \Phi(F_i^\pi \geq F)}{U}, \quad (6.39)$$

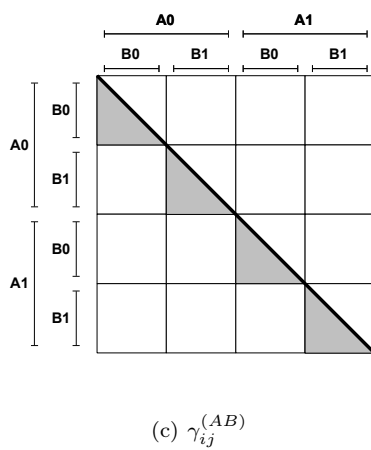
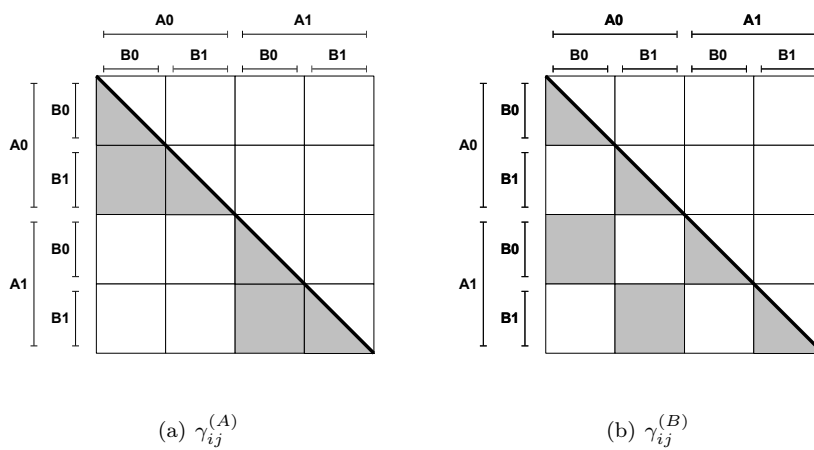


Figure 6.28: A visual interpretation of the indicator function $\gamma_{ij}^{(\cdot)}$ applied in Equation 6.33 through 6.35.

where U is the number of permutations and $\Phi(\cdot)$ is 1 when the argument is true and zero otherwise. The expression basically summarises how likely it is to obtain a permuted labelling that increases the test statistic of the original labelling. If the p -value is below the level of significance we reject the null-hypothesis as in the standard ANOVA. Testing for all possible permutations is often infeasible, and often only a predetermined number of permutations are performed for each factor and interaction effect. However, the more permutations performed the greater precision of the p -value is obtained.

Contrary to ANOVA and MANOVA, NPMANOVA only has the assumption of homoscedasticity. However, as we are performing permutation tests we do not have access to residuals, thus contrary to ANOVA and MANOVA we have to rely on statistical tests. For distance matrices Anderson (2006) proposed to use a generalised version of Levene's test. This approach applies a Levene's test to the principal coordinates of the distance matrix, obtained through an MDS technique resembling those of Section 6.3.3.

Results and Discussion

In this chapter a short summary is provided for each of the included contributions found in the appendix. The summary will mainly highlight and discuss the most significant findings and relate them to the topics of Chapter 2 through 4, as well as the other contributions.

7.1 Paper A - Monitoring Optical Changes during Milk Acidification Using Hyperspectral Diffuse Reflectance Images

In this first contribution the generalisability of the 2DSLS technique was evaluated. The 2³ milk fermentation data set (Section 5.1) was used, which consists of nine unique milk fermentations including the three repeated centre points. The three factors covered fat content, protein content, and fermentation temperature, which all are expected to affect the structure development during the fermentation in terms of microstructure and optical properties as well as the viscosity.

Both 2DSLS and SAOR were used to continuously monitor the milk fermentations. Visually, both modalities showed significant differences between the

initial condition and the final condition for each of the unique milk fermentations. Furthermore, the 2DSLS diffuse reflectance images were quantified using the loglog model (Section 6.1.2.1), and the applicability of this simple alternative to physical models was validated.

SAOR and 2DSLS showed different developments throughout the fermentations as previously reported for other optical methods in the literature. Furthermore, 2DSLS was found to correspond well to light scattering theory. The large fat globules affected the 2DSLS signal more than the smaller protein structures, and the fermentation temperature was found to affect the fermentation speed, and thereby the initial steepness of the quantified 2DSLS signal. Also, the quantified 2DSLS signal showed a wavelength dependent response, and at longer wavelengths the quantified signal resembled that of the NIR-based CoAguLite sensor described in Section 4.2.1.2.

Through ANOVA all experimental factors were found to be significant for both SAOR and 2DSLS. However, for 2DSLS the protein content was only found to be significant at the lower wavelengths. In terms of light scattering theory this makes sense, as the protein structures are small compared to the wavelength of the light, which results in rapid decay of scattering efficiency as the wavelength increases as summarised in Table 3.1.

These results encouraged the continued investigations of the 2DSLS technique. In Papers B, C, and F, different approaches to quantifying the 2DSLS signal are considered, and in Paper E the wavelength dependency of the quantified signal is investigated further in relation to protein microstructures.

7.2 Paper B - Decomposition of Diffuse Reflectance Images - Features for Monitoring Structure in Turbid Media

Following Chapter 3 the light scattering properties of a material are highly dependent on the underlying microstructure. Thereby, the characterisation of the scattering properties is of great importance. In this contribution the methods of Section 6.1.1 and 6.1.2 are used to quantify the scattering properties in the diffuse reflectance images.

Thereby, in addition to the loglog model applied and validated in Paper A, this also includes physical based models as well as empirically extracted features, which utilise more of the data available in the images. For this investigation

the Intralipid data set (Section 5.3) was used, which consists of gradually diluted Intralipid samples, which span a broad range of linearly increasing scattering properties. Classification rates, discriminative power, and linearity of the quantified scattering properties across the data set, were used to evaluate the quantification methods.

It was found that the more scattering the samples became, the harder it was for the methods to discriminate the different samples. For highly scattering samples the light decays rapidly, and in order to capture the dynamics of the decay, a suitable spatial resolution of the detector system is required. From the results it appears that the applied 2DSLS system setup could not resolve these dynamics appropriately for the entire data set. This especially holds true for the oblique model in Section 6.1.1, which relies on measuring the MFP in the diffuse reflectance images. When the scattering increases, the MFP decreases and becomes harder to resolve, which introduces noise to the estimated scattering properties.

In general the physical models were found to introduce more variance in the estimated scattering properties, which we believe can also be attributed model variance. Nevertheless, the physical models were found to maintain the expected linear increase in scattering properties across the data, even when the high scattering started to diminish the discriminative power. This was not always the case for the empirical methods, marking the strength of the physical models.

Interestingly, no method performed best across the entire data set. While the loglog model showed good performance throughout a broad range of scattering properties, the robust measure of intensity spread (Section 6.1.2.2) showed the best overall performance. However, the patch average (Section 6.1.2.3) showed better discriminative power in a limited range of scattering properties, while greatly violating the linearity in scattering properties when considering the entire data set.

We believe these results highlight both the potential of using more of the available data in the diffuse reflectance images, and the 2DSLS system as a workbench, from which more specific systems can be developed. As an example: If the optical probe in Figure 4.12 is considered in backscatter mode, the placement of the light emitting fibre and light receiving fibre can be varied freely. From the results in this contribution, the optimal offset between emitter and receiver will vary greatly depending on the scattering properties of the investigated sample. This offset corresponds to different areas in the diffuse reflectance images as illustrated in Figure 6.6, meaning that the 2DSLS system could potentially aid in determining the optimal offset between emitter and receiver for such a sensor.

7.3 Paper C - DCT-Based Characterization of Milk Products Using Diffuse Reflectance Images

In Papers A and B, the 2DSLS signal was mainly being considered in terms of multiple scattering. However, as mentioned in both Section 4.1.1 and 6.1, additional information is available in the signal. In this paper we explored the discriminative properties of the diffuse reflectance images when considering the DCT (Section 6.1.5) and the milk products data set (Section 5.2).

Hereby, the 2DSLS signals were transformed to the frequency domain using the DCT. The spatial frequency information was divided into two groups: Low and high frequencies. The low frequencies were assumed to cover the entire light diffusion in the diffuse reflectance images, and thereby both single and multiple scattered light, while the high frequencies were assumed to cover the underlying speckle pattern. The low frequencies were represented by the actual DCT coefficients, and the high frequencies were represented by entropy measures.

This approach resulted in a relatively large feature space, thus a selection of the most discriminative wavelength and features was performed sequentially. This resulted in the most discriminative wavelength being 830nm, at which both low and high frequency features were selected. The DCT description was compared directly to the loglog model, which only considers the multiple scattered light in the 2DSLS signal.

For the loglog model a slight overlap was observed for milk products with high fat content and fermented milk products with a low fat content. We have previously seen this for results based on both the loglog model and the oblique model (unpublished). However, the DCT features were found to provide a clear separation of all samples. Through visual assessment of the results this could in particular be attributed the high frequency features.

The results ultimately emphasised that considering more of the information available in 2DSLS signal, can provide additional information on the investigated sample. The effects of single scattering and speckle patterns are investigated individually and in more detail in Paper F. The most discriminative wavelength, 830nm, may seem to contradict the findings of Paper A and E. However, in these papers the preference of lower wavelengths is mainly related to the protein structures and multiple scattered light. In this paper wavelength selection is based on a broader data set and more information from the 2DSLS signals.

7.4 Paper D - Evaluation of Confocal Scanning Laser Micrographs of Stirred Yogurts Using Image Analysis

CSLM can provide close to ground truth measurements of the microstructure in protein networks. However, such microscopy images are most commonly used for subjective visual assessment. While, this is feasible for small data sets, it can become difficult when the amount of data is large or when the difference between two images has to be quantified. For this purpose objective descriptions of the microstructure are more valid.

Previously, microstructure of protein networks has mainly been quantified objectively by estimating the fractal dimension (ratio between the change in detail and change in scale) alongside morphological measures such as the average pore size in the protein network. However, in the field of image texture classification, the fractal dimension is not regarded a strong contender, as it is not a unique descriptor and it is typically calculated globally for the entire texture. Today, state-of-the-art descriptors often rely on representing texture as occurrences of textons (Section 6.2.3).

A broad range of different texture descriptors was applied to the CSLM images from the 2^4 stirred yogurt data set (Section 5.4). The descriptors covered a broad range of texton-based descriptors, as well as grey level co-occurrence matrices (GLCM) and some of the most common fractal descriptors. All descriptors were evaluated through NPANOVA and nearest neighbour classification on different partitions of the data set.

Almost all texture descriptors found the factors (fat content, protein content, pre-heat treatment, and incubation temperature) of the experimental design to be significant. Also, nearly all descriptors agreed that there was a significant variability across the three replicates of the design, which can be expected when working with lactic acid bacteria. In terms of classification rates a lot of the texton-based descriptors outperformed the descriptors based on fractal analysis and GLCM. However, due to large variation in the classification results, a best texton descriptor could not be determined.

The variation was partly found to arise from the less dense gels, which appeared more irregular in the CSLM images, compared to the dense protein networks. Furthermore, all texture descriptors were found to perform better on the denser networks. This hints that the spatial resolution applied in the image acquisition may not have been optimal for capturing representative images of the microstructure. The difference in regularity of the microstructure can also be

seen from Figure 5.6. Still, when extracting the median response for one of the best performing texture descriptors, and visualising these responses through hierarchical clustering, the result corresponded well to visual assessment. Thus, we believe an appropriate objective description of the microstructure has been achieved.

This allows for direct comparison between microstructure and the 2DSLS signal, which can aid in the investigation of the discriminative properties of the 2DSLS signal in regard to the microstructure of the protein network. This particular comparison is covered in Paper E.

7.5 Paper E - Discriminating Yogurt Microstructure Through 2D Static Light Scattering

This was a natural extension to Paper D, in which the microstructure of the protein networks in the 2⁴ stirred yogurt data set (see Section 5.4) was objectively quantified through CSLM images. CSLM can provide close to ground truth information on the actual microstructure of the protein network, whereas rheological methods such as SAOR are only partly related to the microstructure.

The 2DSLS diffuse reflectance images were quantified in terms of multiple scattered light using the loglog model, which we have found to be both discriminative and reproducible for a broad range of dairy products in Papers A, B, and C. The quantified 2DSLS signal was evaluated as in Paper D and compared directly to one of the best performing texture descriptors in Paper D.

Through ANOVA it was found that all factors in the experimental design were significant. The factors changing the chemical composition (fat content and protein content) were found to be very significant across all wavelengths. The factors that only changed the final microstructure (pre-heat treatment and incubation temperature) were typically found to be very significant for the lower wavelengths while becoming less significant when the wavelength increased. In comparison the CSLM texture descriptor found all factors to be very significant.

Looking at the general classification results, the performance of the 2DSLS signal was generally inferior to that of CSLM. However, in some cases, when only considering subsets of the entire data set, the performance was comparable. This was especially prominent for the less dense networks. As speculated in Paper D, this might be because the applied spatial resolution in the CSLM images was not particularly well suited for capturing representative views of the microstructure.

However, similar to the ANOVA, a trend was observed in which the lower wavelengths appeared better in discriminating between different microstructure. For samples with a high fat content this trend was often obscured. Following light scattering theory, this can be explained by the scattering contribution from the large fat globules entirely dominating that of the smaller protein structures in the 2DSLS signal. Thus, it appears that by quantifying multiple scattered light it is possible to distinguish different types of chemical composition and protein microstructure, especially when lower wavelengths and low fat yogurts are considered.

Looking at the correlation between the quantified 2DSLS and CSLM descriptor, the 2DSLS signal at lower wavelengths also appeared to correlate better to the objective description of the protein microstructures. These trends in wavelength dependency were also found in Paper A, where changes in protein content only significantly affected the 2DSLS signal for shorter wavelengths.

This wavelength dependency is interesting in relation to the existing commercial sensors, mentioned in Section 4.2.1.1 and 4.2.1.2, which are used for monitoring the structure formation during cheese making. These sensors are based on NIR wavelengths, as they provide the largest relative signal increase throughout the structure formation. Thereby, the existing sensor technologies may be suboptimal if discrimination between different protein microstructures is of interest.

The data material in relation to 2DSLS measurements was unfortunately limited, and as a result this report only presents preliminary results. Thereby, a natural evolutionary step to this work would be to include more optical measurements, and furthermore apply the different quantification methods of Paper F.

7.6 Paper F - Quantification of Multiple Scattered Light, Speckle Patterns, and Scattering Eccentricity in Diffuse Reflectance Images

Until now, the 2DSLS has primarily been quantified in regard to the parts of 2DSLS signal where the contribution from multiple scattered light predominates. In Paper C the entire image was decomposed into frequencies through the DCT, and a few specific frequencies were extracted based on the discriminative properties for the milk product data set (Section 5.2). While it was found

that high and low frequency information had different discriminative properties, all the extracted information was convolved and not directly interpretable.

Thus, in this paper the aim was to individually quantify the different pieces of information available in the 2DSLS signal. As mentioned in Sections 4.1.1 and 6.1 we believe, that the 2DSLS signal mainly contains information from three different types of light interaction: Multiple scattered light, single scattered light, and the underlying speckle interference pattern. The different quantification schemes were evaluated on the milk products data set (Section 5.2) and the repeated milk fermentation data set (Section 5.5).

The multiple scattered light was quantified as previously seen in Papers A, B, and E. Again, it was found that the oblique model (Section 6.1.1) produced highly interpretable results, that corresponded well to the light scattering theory of Chapter 3. However, when the investigated sample was highly scattering, a lot of variance was introduced to quantified signal as also seen in Paper B. In contrast, the loglog model (Section 6.1.2.1) was less interpretable when observed across wavelengths, due to the dependence on the combined system response (Figure 4.2). However, when considering a single wavelength, during the milk fermentation, there was a good correspondence between the oblique model and the loglog model. Albeit, the loglog model showed significantly higher SNR and reproducibility.

The speckle patterns were quantified through the average speckle size (Section 6.1.4). It was seen that the speckle size changed significantly depending on the spatial location in the 2DSLS signal, and fairly large region had to be considered in order to obtain a stable size estimate. The speckle size estimate was found to be significantly different from the signals on multiple scattered light. Most remarkable was how the average speckle size created a clear distinction between milk products and fermented milk products. This was previously hinted at in Paper C. For the milk fermentation, the average speckle size also showed a significantly different behaviour from the quantified multiple scattered light, and most of all resembled what has been reported on DWS in the literature. However, DWS indirectly measures particle mobility through dynamic speckle patterns (Section 4.2.1.3), whereas the speckle patterns in 2DSLS are static, although we believe there is a potential correlation between to two modalities.

For the scattering eccentricity (Section 6.1.3) a noteworthy wavelength dependency was observed, as periodic collapses and inflations of the quantified signal, and should be investigated further. Additionally, the eccentricity close to the light incident point was hard to resolve sufficiently, and as a consequence the eccentricity was only considered in a region border lining single scattered light and multiple scattered light. When compared directly to the signal of multiple scattered light, only a slightly different ordering of the milk products was seen. This

can be expected as scattering eccentricity quantifies effects of the asymmetry parameter g , whereas reduced scattering is defined by $\mu'_s = \mu_s(1 - g)$. Additionally, when observing the scattering eccentricity during the milk fermentation, it showed a similar behaviour to that of quantified multiple scattered light, and with a reasonable SNR.

In summary, quantifying the different pieces of information available in the 2DSLS has resulted in two major findings. First, the different types of quantified information in the images provided different information of the investigated samples. Secondly, quantifying shapes in the 2DSLS signal was verified as a viable approach, which is very relevant in relation to process control, as shape is typically invariant toward variations in the system response. However, it was also found that both the estimates of scattering eccentricity and average speckle size depended on the system setup, as well as the spatial region considered when quantifying the 2DSLS signal. This implies that more effort has to be put into determining optimal measurement and quantification conditions for each of the parameters.

Conclusion

Throughout this thesis, we have investigated the optical technique 2D Static Light Scattering (2DSLS), and investigated its applicability in relation to monitoring and discriminating microstructure during production of fermented milk products. The microstructure of these product types, and food in general, is of great importance as it relates to quality parameters such as mouthfeel and product appearance, which are critical to consumer acceptability. Briefly, 2DSLS captures images of the spatial distribution of the diffuse reflectance, when a sample is illuminated by a hyperspectral (465-1030nm) laser beam. Thereby, it is a remote sensing and non-invasive technique. This is highly desirable in relation to process control of food products.

The system applied throughout this thesis can be considered a flexible workbench with a lot of free parameters in the setup. From this workbench optimal parameters for a given problem can be determined, and a focused cost-efficient system can be designed. The workbench itself was introduced and related to existing commercially available optical instruments. The related instruments have typically been used to monitor the structure formation during cheese making in order to determine the optimal cutting time. It was found that the 2DSLS technique to some extent could be considered a generalisation of all the commercially available techniques. However, it should be stated that some related techniques utilises rapid temporal measurements, whereas 2DSLS currently utilises static measurements. To the best of our knowledge no commercially available op-

tical instruments exist for process control related to microstructure in yogurt products.

Much emphasis was put into understanding and quantifying the 2DSLS signal. Ultimately we found that the signal consists of contributions from at least three different optical phenomena: Multiple scattered light, single scattered light, as well as an underlying speckle interference pattern, that affects most of the signal.

Initially we relied on quantifying effects of the multiple scattered light, as this has been investigated in depth in the literature. We initially quantified the multiple scattered light using both physical models as well as empirically validated statistical approaches. The physical models separate the 2DSLS signal into absorption and scattering coefficients, which are primarily defined by chemical composition and microstructure, respectively. Thus, the physical models provide highly interpretable results that correspond well to light scattering theory. Also, the measures can be invariant to variations in the system response. However, the estimated parameters typically show low SNR.

In contrast, the statistical approaches provide measures that contain the convolved absorption and scattering properties, and the measures are furthermore affected by variations in the system response. In relation to dairy products, the mixing of the absorption and scattering is not a problem, as the scattering properties dominate the absorption properties in the investigated wavelength spectrum. Furthermore, the SNR is significantly higher compared to that of the physical models.

Later we considered the single scattered light and the speckle interference pattern. Our initial investigation showed that these parts of the 2DSLS signal contain both similar as well as complementary information in relation to multiple scattered light. Furthermore, the new parameters quantified in terms of shapes in the signal, which makes them invariant toward variations in the system response. Also, the initial findings showed promising SNR and reproducibility. The quantification of single scattered light and the speckle pattern is still ongoing work.

As reference measurements we initially applied rheology, which is a family of invasive measures that can provide information on the physical properties of a yogurt, e.g. the viscosity. However, rheology only provides information derived from the underlying microstructure of the investigated sample, and not the microstructure itself. Thus, we considered microscopy, which provides close to ground truth measurements on the microstructure. Especially confocal scanning laser microscopy has found its place within food science, including dairy science, as specific compounds such as the protein microstructure can be targeted. This led to the investigation of objectively quantifying micrographs

of protein microstructure. It was found that the protein microstructure resembled the periodic behaviour of general image textures, and we compared a broad range of different texture descriptors. It was found that recent approaches within the field of texture classification were especially suited for discriminating between different yogurt microstructures.

The objective description of the micrographs allowed for a comparative study of 2DSLS and microscopy. The study suggested that the 2DSLS signal (in terms of multiple scattered light) could be used to discriminate between different protein microstructures. Especially low-fat yogurts were well discriminated whereas high-fat yogurts were more problematic, due to the scattering effect from fat being significantly larger than that of protein. Furthermore, it was observed that especially shorter wavelengths were well suited for discrimination, and correlated better to quantified microscopy images as well. All observations correspond well to light scattering theory.

The study thereby also emphasised a limitation of the technique. While the current 2DSLS system setup generally covers the range of standard milks and yogurt products, the detector system cannot resolve the scattering dynamics for highly scattering samples such as high-fat products, e.g. cream cheese. However, these limitations have only been verified for the multiple scattered light (and most likely single scattered light as well) in the 2DSLS signal.

As a concluding remark we believe that our objectives have been fulfilled in such a way, that the 2DSLS technique can be brought into pilot plant scale testing in collaboration with our industrial partners. We believe we have covered a lot of the free parameters in the 2DSLS workbench, needed to design the first prototype system in relation to monitoring microstructure in low-fat yogurt products. While there is still more work to do in the laboratory, a real world in-line implementation would help us to further understand the practical limitations of the technique.

In summary, we have seen the potential for the 2DSLS technique to be a significant contribution in relation to existing technologies, both in terms scientific and practical applications. However, we also believe that we only have scratched the surface of the technique.

APPENDIX A

Monitoring Optical Changes during Milk Acidification Using Hyperspectral Diffuse Reflectance Images

Jacob L. Skytte^a, Otto H. A. Nielsen^{a,b}, Ulf Andersen^c, Flemming Møller^d, Jens M. Carstensen^a, Anders B. Dahl^a, Rasmus Larsen^a

^a DTU Compute, Department of Applied Mathematics and Computer Science, Technical University of Denmark, Matematiktorvet, Building 322, DK-2800 Kgs. Lyngby, Denmark

^b NKT Photonics A/S, Blokken 84, DK-3460 Birkerød, Denmark

^c Arla Strategic Innovation Centre, Rørdrumvej 2, DK-8220 Brabrand, Denmark

^d DuPont, Edwin Rahrs Vej 38, DK-8220 Brabrand, Denmark

^e DTU Photonics, Technical University of Denmark, Ørsteds Plads, Building 343, DK-2800 Kgs. Lyngby, Denmark

Abstract

A novel hyperspectral (480-1030nm) laser imaging system is used to monitor the optical changes during a milk acidification process. Images of diffuse reflectance are captured remotely using a tuneable laser and CCD camera, and differences in the response images between base milks and corresponding gels elucidate several interesting features. In this paper one of these features is quantified using a simple and noise resistant quantification scheme inspired by conventional light interaction models. The generalisability of the feature is investigated through a factorial design in which fat content, protein content and the fermentation temperature is changed systematically. The acidification is initialised using glucono- δ -lactone (GDL), and conventional oscillatory rheology is used to validate the gel development. Through analysis of variance the extracted image feature shows significant effects from fat and temperature throughout all wavelengths. Additionally a significant effect for protein is only seen at lower wavelengths (480-540nm).

A.1 Introduction

Simple in-line monitoring techniques for food manufacture can aid in production of high quality products with low variability. Food quality relates to factors like appearance, taste, and texture that are important for consumer acceptance, as well as chemical and microbiological composition that hold information about nutrition and food safety. For decades there has been an interest in optical methods for measuring food quality parameters, especially methods based on non-contact designs, as these methods are well suited for monitoring fragile systems and for in-line implementation in factory settings. In this paper we investigate the potential for using hyperspectral images of lights diffuse reflectance to monitor the gelation process in dairy production. The images are captured using a novel hyperspectral vision system, which is a generalisation of the commercially available product, VideometerSLS (*Videometer A/S, Hørsholm, Denmark*).

Milk gelation is a central process in the production of many products including yogurts and cheeses. These milk gels are formed by lowering the pH value of the milk, which ultimately leads to destabilization and aggregation of the suspended casein micelles. Hereby a gel network is formed by the casein. The structure formed through the gelation process is important for the consumer's experience of the final yoghurt or cheese (Bourne, 2002). Creaminess and viscosity are key factors for product quality and closely linked to the gel structure (Muir and Hunter, 1992). To optimize the product quality a control mechanism of the gel

formation is required, here a reliable monitoring system plays a key role.

The structural properties of the final gel can rely on a plethora of different parameters. Milk standardization, homogenization (Vedamuthu, 1991), pre-heat treatment (Law, 1996) and incubation temperatures (Lee and Lucey, 2004) are parameters that can be controlled (Lee and Lucey, 2010). With a precise tool to monitor the structure development these parameters can be adjusted to account for uncontrollable parameter like the natural variations in the raw milk (Tamime and Robinson, 1999).

Milk gelation is obtained by lowering the pH in the milk, and it is common to measure the temporal pH development. This is important to ensure that the product has the correct acidity, but the development of pH is not uniquely related to the structure development. Two gelation processes might have the same temporal pH development, but result in products with different viscosity or creaminess (Haque et al., 2001).

It is well known that the optical properties change throughout a milk gelation process, and these optical changes have been investigated intensively. Many methods have been suggested, which are primarily based on near infrared (NIR) transmission and reflectance (O'Callaghan et al., 2002). Especially diffuse reflectance measurements using optical probes have been investigated to a great extent. A system for estimating the optimal cutting time during cheese making was presented by Payne et al. (1993b). This system has also been investigated for a variety of different product types as well as other application areas in the milk gelation process, and multiple application studies have been published (Fagan et al., 2007).

Mezzenga et al. (2005) pays special interest to dynamic light scattering (DLS) and diffusing wave spectroscopy (DWS). These methods illuminate scattering media using a coherent laser beam. By observing the fluctuations in scattering intensity (speckle), which is caused by Brownian motion of the scattering particles, information about the size and dynamics of the particles can be derived. This can be estimated on the basis of the temporal autocorrelation function of the observed fluctuations. While DLS deals with single scattering events, DWS is an extension of DLS that deals with multiple scattering and is more suited for real world applications (Weitz et al., 1993).

Despite the abundance of optical methods, only few in-line systems are commercially available for monitoring milk coagulation (Lucey, 2002; Castillo, 2006; O'Callaghan et al., 2002). This can partly be explained by the hostile process conditions where plant vibrations and strict requirements for the implementation exist. The optical methods needs to be performed in situ, should not interfere in the production, and has to meet dairy hygiene standards. Light

transmission, light reflectance, and DWS (both transmission and backscattering), have all been used for in-line measurements (O'Callaghan et al., 2002; Castillo, 2006).

A well-documented light reflectance system is the CoAguLite (*Reflectronics, 3009 Montavesta Road, Lexington, KY 40502, USA*), which measures light reflectance ratios using optical probes. During milk coagulation it records a sigmoidal behaviour from which the time of gelation and the optimal cutting time for cheese can be predicted (Castillo et al., 2000). This particular system is installed by welding optical probes into the side of a cheese vat. While this is well-suited for large scale production, it can be uneconomical for small scale production where smaller (and perhaps several different) cheese vats are used (Craft-Jenkins, 2012).

In this paper we investigate the potential of using a hyperspectral diffuse reflectance imaging system as a tool for in-line milk gel assessment. Measurements are made by shining a tuneable laser (480-1030nm) into the sample and a CCD camera capturing an image of the spatial distribution of the diffuse reflection. Directly compared to CoAguLite, the system is also based on light reflectance, but offers increased flexibility in both system setup and analysis of data. Data can be collected non-invasively, which should alleviate in-line implementation. The system was introduced by Nielsen et al. (2011b,a), and has similarities to backscattering DWS. However, the signal output and subsequent analysis is significantly different. While DWS is based on measuring particle dynamics our measurements are influenced by the changes in the absorption and scattering properties.

We study the temporal changes in the hyperspectral diffuse reflectance images in different milk gelation processes. Protein content, fat content, and fermentation temperature are changed systematically in a factorial design to investigate the generalisability of the method. The images are quantified and through analysis of variance significance effects are determined across different wavelengths. The gelation processes are validated using small-amplitude oscillatory rheology, which can provide information about the rheological properties continuously throughout the acidification process.

A.2 Material and Methods

A.2.1 Experimental Design

The purpose of the experiment was to investigate the generalisability of the diffuse reflectance images towards three common process parameters: protein content, fermentation temperature, and fat content. These three factors were varied systematically at two levels, resulting in a full single replicated 2^3 factorial experimental design. Additionally, three replicates were added as centre points to the design. Centre points can be used to estimate the mean squared error (MSE) of the experiment from the centre points alone, and to investigate for quadratic factor effects (Montgomery, 2005). Additionally the centre points provided enough degrees of freedom to check for significance in all first and second order interactions in the experimental design.

The factor levels were chosen to ensure reasonable differences between the different gelation developments while still being relevant in the scope of commercial products. The absolute value of the fat content was ensured using commercially available UHT milk with two levels of fat; semi-skimmed (1.5%) and whole-milk (3.5%). The protein content was increased by adding 1.67% (w/w) skimmed milk powder (SMP), which results in an increase in protein content from 3.4% to 4.0%. The temperature spanned 27.5°C to 37.5°C and was controlled using water baths. The factorial design is summarised in Table A.1.

For each of the nine different process compositions, the acidification was performed by adding 2% (w/w) glucono- δ -lactone (GDL), as it is a reproducible model system for milk gelation as opposed to bacteria cultures (Lucey et al., 1998a). Each sample in the experimental design was a 5.5-hour-long series of diffuse reflectance images (taken every 6 minutes) and rheological measurements (taken every 2.5 minutes). The first measurement was made three minutes after GDL addition. The time points for image acquisition were recorded, and linear interpolation was used to obtain time correspondence between the 11 measurement series.

For the remainder of this article, the capital letters (P, T, and F for protein content, temperature, and fat content respectively) in sample names denote a high factor level, while absence of capital letters denote a low factor level. The centre points will be referred to as “centre”.

Table A.1: Factors and target levels for the 2^3 factorial experiment (plus three centre points) used for testing the generalizability of the diffuse reflectance images.

Factor	Code	Target factor levels		
		Low	Centre	High
Protein content [%]	P	3.4	3.7	4.0
Temperature [°C]	T	27.5	32.5	37.5
Fat content [%]	F	1.5	2.5	3.5

A.2.2 Milk Sample Preparation

The milk was kept at room temperature in its commercial packaging, until it was used. In preparation of the experiments, each milk sample (500ml) was initially heated for an hour in a water bath at the target temperature. It was then taken out of the water bath and the SMP was immediately dissolved (if required) in the sample using a magnetic stirrer. Hereafter GDL was added and the sample was stirred for three minutes. Three aliquots were taken from the sample. Two 200ml aliquots in open glass containers were placed back in the water bath, one for capturing diffuse reflectance images, and one for temperature measurements. One 20ml aliquot was used for rheology measurements. All experiments were carried out during a one-and-a-half-week period.

A.2.3 Milk Temperature Control

For temperature control, a shaking water bath (*SW2 ±0.2°C, Julabo Labortechnik GmbH, Seelback, Germany*) was used. The shaking function was turned off to avoid any vibrations, which would cause shifts in the sample height and interfere with the image acquisition. Using a temperature probe (*Tes-1380 Temperature Meter ±0.5°C, TES Electrical Electronic Corp., Taipei, Taiwan*) it was found that the general temperature was between 0.1 to 0.5°C lower than the target factor levels. As the milk was prepared outside the water bath the temperature dropped a few degrees before it was put back into the temperature-controlled environment.

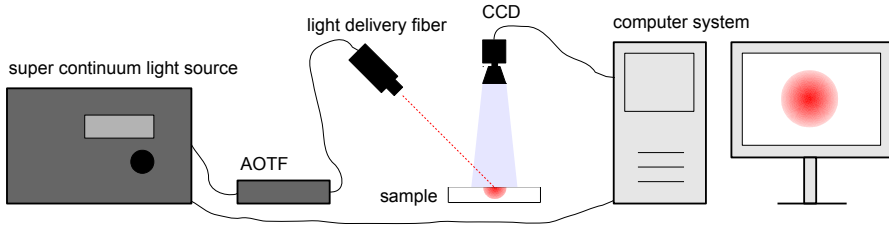


Figure A.1: A schematic view of the hyperspectral vision system. Additionally two lenses were installed, one in front of the laser beam and one in front of the camera.

A.2.4 Hyperspectral Diffuse Reflectance Images

An example of a diffuse reflectance image is shown in Figure A.2. The images are formed using a system following that of Nielsen et al. (2011b,a). A schematic view of the system set-up is shown in Figure A.1. The set-up is based on a super continuum light source (*SuperK Extreme*, NKT Photonics, Birkerød, Denmark), filtered by an acousto-optic tunable filter (*SuperK Select*, NKT Photonics, Birkerød, Denmark), and the combined system produces a collimated light beam, in the range 480-1030nm, at high spectral resolution. For each wavelength the laser is shined into the milk sample from the top down at an oblique incident angle (45°), and a CCD camera (*Grasshopper CCD Cam*, Point Grey Research Inc., Richmond, Canada) with a spatial resolution of 1200×1600 pixels, captures an high dynamic range (HDR) image of the diffuse reflectance.

Additional to the system shown, a biconvex lens (focal length: 100mm) was installed in front of the light beam. This focussed the light to a Gaussian (*transverse electromagnetic mode*₀₀) beam waist of $150\mu\text{m}$. In front of the CCD a zoom lens (*23FM50L*, Tamron Co. Ltd., Saitama, Japan) was installed with a 6.5cm spacer, which yielded a spatial pixel size of $3.2\mu\text{m}$ in the object plane. The vision system was installed around the water bath (see Section A.2.3), and the entire set-up was shielded from background light.

Both the output power of the light source and quantum efficiency of the CCD chip are wavelength dependent. For this reason we make a pre-calibration of the output power and the exposure times in the HDR algorithm, to ensure that no pixel become overexposed for short exposure times, and that an adequate signal is available for the longest exposure time. The calibration is performed on a highly scattering medium that represents the final state of the fermented milk. For these measurements whole milk was used. The camera was set to minimum exposure time and the light source power was reduced until no pixels

were saturated. Using this reduced power the maximum shutter time is set high enough to produce low noise pixel intensities far from the light entry point. A compromise was made on maximum exposure time, to avoid too long acquisition times. Thus, some averaging is performed when quantifying the images (see Section A.2.4.1).

The wavelengths were sampled in 10nm steps, which resulted in 56 different spectral samples at every time point. With a consistent acquisition time just under six minutes, approximately 60 data points were acquired throughout the 5.5-hour-long acidification process.

A.2.4.1 Parameter Extraction

Milk products are highly scattering media and following diffusion theory, the area close to the beam centre is dominated by a single or few scattering events. These events take place close to the sample surface, and do not give much information about subsurface sample properties. Further away from the beam centre, multiple scattering events begin to dominate. Here light has entered the sample and been scattered multiple times before leaving the sample again (diffuse reflectance). The appearance of this part is therefore dependent on the optical properties of a larger volume of the sample, which relates to particle sizes and volume concentration – this is where we extract the slope parameter. For simplicity we have only considered a single image feature which models the rate of light decay far away from the point of incidence. This parameter was presented by Carstensen et al. (2009) and is being used in a commercially available product (*Videometer A/S, Hørsholm, Denmark*).

The parameter is the slope of a double logarithmicly transformed profile, $\log(\log(I+2))$, where I is the pixel intensities. The profile is sampled orthogonally to the incident direction of the laser through the intensity peak. This profile is symmetric and we average the two sides. To reduce the noise further we use the average of an 11-pixel-wide band. A linear model is fitted to the latter half of the profile, i.e. the part of the profile far (400 pixels, i.e. 1.3mm) from the beam centre, which reduces the parameterisation to a slope and an intercept. The parameter extraction is visualised in Figure A.2. Both parameters hold information about the samples scattering properties and its absorption spectrum. However, the intercept parameter is also highly dependent on the amplitude of the measured signal. Thus, the slope parameter should be better suited to follow the optical changes during milk gelation.

This parameterisation can be seen as a simplification of the work by e.g. (Farrell et al., 1992; Wang and Jacques, 1995). Their work is based on physical models

where they utilise the diffusion approximation to estimate the absorption and reduced scattering coefficients. Our approach is a more statistical way of quantifying the light diffusion. The double logarithmic transformation combined with the linear model can be seen as a compromise between resistance towards noise and suppressing information.

A.2.5 Small Amplitude Oscillatory Rheology

Acidified milks are weak gel networks, thus easily damaged by deformation. In order to continuously measure on a single sample, small amplitude oscillatory rheology (SAOR) can be used. In SAOR a small sinusoidal deformation is applied, in which small deformation is defined as a relative deformation, which does not disrupt the development of the network structure (Lee and Lucey (2010)). Acidified milks are viscoelastic, meaning that they express both ideal elastic and ideal viscous behavior. These behaviors can be described by the storage (elastic) modulus (G'), which is the amount of energy stored per deformation cycle, and the loss (viscous) modulus (G''), which is the amount of energy lost as dissipation per deformation. Only the storage modulus (G') is reported when the rheological measurements are presented. Typically, during milk fermentation the storage modulus has a zero baseline until the point where casein micelles starts to aggregate (referred to as the gelation point), after which a sigmoidal behaviour can be observed (Lee and Lucey, 2010).

In this experiment a 20ml sample was used in the rheometer (*Stresstech HR* with temperature cell $\pm 0.1^\circ\text{C}$, *Reologica Instruments AB, Lund, Sweden*) with a double gap concentric cylinder measuring system.

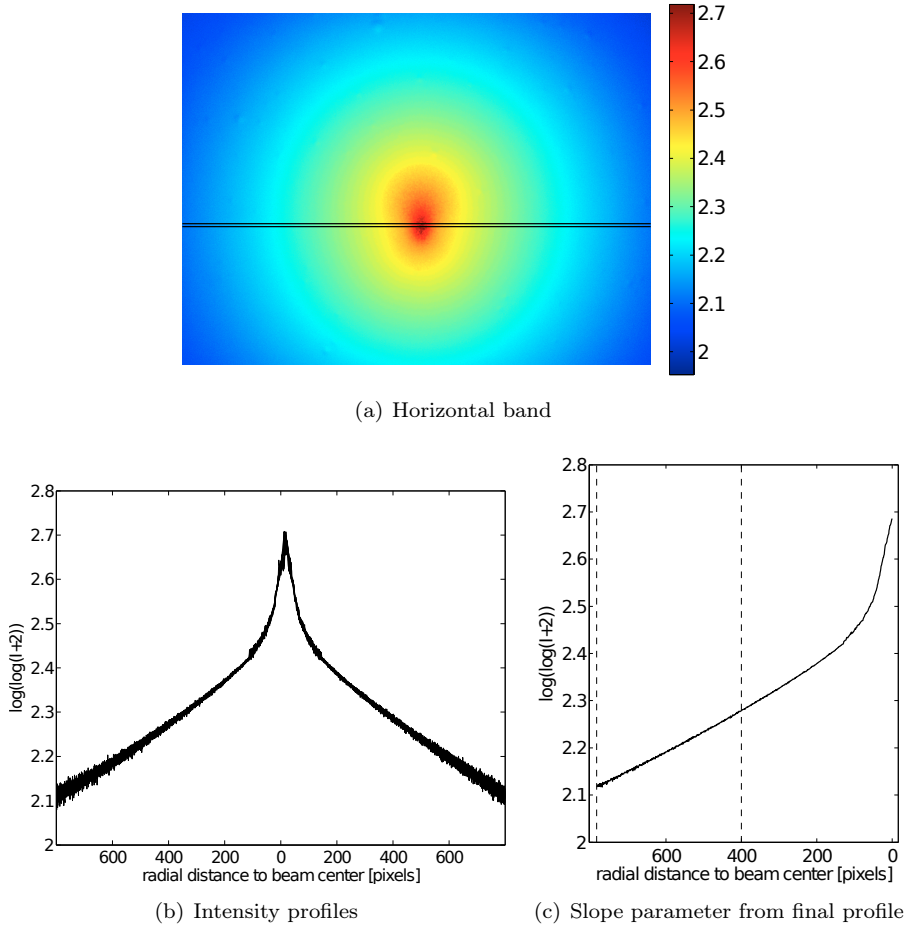


Figure A.2: Extraction of the slope parameter from a double logarithmically transformed diffuse reflectance image of whole milk at 900nm. In (a) a horizontal band of profiles is extracted from the image, and the corresponding intensity profiles can be seen in (b). (c) shows the final profile after averaging over all profiles in the band, as well as across the profile centre. The dashed lines indicate the interval where the linear model is fitted, and the slope parameter is extracted.

A.2.6 Analysis of Variance

Analysis of Variance (ANOVA) was used to determine the significant factors when considering the slope parameter or the rheology measurements as the response variable. Significance of main effects, as well as all possible interactions were investigated. Some slight modifications were made to the standard ANOVA. The mean squared error (MSE) was estimated from the centre points and the presence of quadratic effects was also included in the analysis. Also, a slightly different approach to hypothesis testing was used as the degrees of freedom in the experiment were limited. Here, the mean squares and degrees of freedom of a factor are pooled with the error, if the p -value of the corresponding F -statistic is larger than 0.25. A sequential approach to the pooling is used, starting with the higher order interactions. Thus, the error can be estimated with more degrees of freedom. These modifications to the ordinary ANOVA are suggested by Montgomery (2005).

As each acidification process is a temporal series of measurements, it is necessary to find a scalar representation for the ANOVA. Two approaches were used. The first was to record the amplitude of the signal at fixed time points, and the time points at 10, 25, 50, 75, 90, and 100% of the total time were used. The second approach utilised Principal Component Analysis (PCA) of entire signals, in which principal scores are used to make a scalar presentation of the process. To investigate the variation explained by the principal components, the approach presented by Cootes et al. (1995) can be used. Here the mean signal is calculated, and all signals are centred on it. A PCA is performed on the centred signals, and the loading vectors, scaled by their eigenvalues, are added to/subtracted from the mean shape. In this way we can investigate the variation described by each principal component.

A.2.7 Multivariate Analysis of Variance

Multivariate analysis of variance (MANOVA) was also considered. MANOVA is a generalisation of ANOVA, where multiple responses can be tested simultaneously, and linear combinations of the response variable are considered when determining factor and interaction significance. MANOVA requires more degrees of freedom, thus with this experiment we are limited to two dependent variables, if we wish to retain all factor effects from the previous ANOVA tests. The first and second principal scores are chosen as dependent variables, and Pillais trace is used as an approximation to the F -statistic (Olson, 1976). MSE calculations from centre points, and pooling of MSE and factors with a p -value, as described in Section A.2.6, was also used for the MANOVA.

A.3 Results

A.3.1 Hyperspectral Diffuse Reflectance Images

Examples of diffuse reflectance images are presented in Figure A.3. Most of the appearance of these images can be encoded by a parametric model based on the refractive index, scattering, absorption, and phase function (Joshi et al., 2006). To show the effect of the milk acidification directly in the image data, an early and late image in the time series is combined and separated by a black line. The images are presented for two different samples at three wavelengths.

For all measurements, the light attenuation is stronger by the final fermented product, as can be seen by the faster decaying signal, which corresponds to an increase in either scattering or absorption. This is remarkable, the chemical composition is the same throughout the acidification process, and yet the optical signals change significantly. This has recently been verified by Nielsen et al. (2013) where it is shown that the primarily optical difference between milk and fermented milk products is in the reduced scattering coefficient.

The elongation is caused the oblique incidence angle of the light. The specific shape is arising by a combination of the light penetration depth, which is used by Wang and Jacques (1995), and the shape of the phase function of single light scattering. As a general trend, the penetration depth increases as a function of wavelength. This makes the shape more elongated. However, it is evident that the elongation also is different between the samples with high fat or protein, where the later is more elongated across all wavelengths. The shape of the elongation is also complex, for the start point of the high protein samples at 500nm the light is forming a narrow fan-shaped shape profile rather than a simple ellipsoid. Thus it is clear that more information about the scattering process is available than what is covered by the parameterisation in Section A.2.4.1.

Additionally, the images also show differences in an underlying interference pattern, which is mostly visible close to the point of incident, and is stronger in the fully fermented samples. The effect is present over the whole image, and have been utilised in (Sharifzadeh et al., 2013) to distinguish milk and yogurt products with coinciding optical properties.

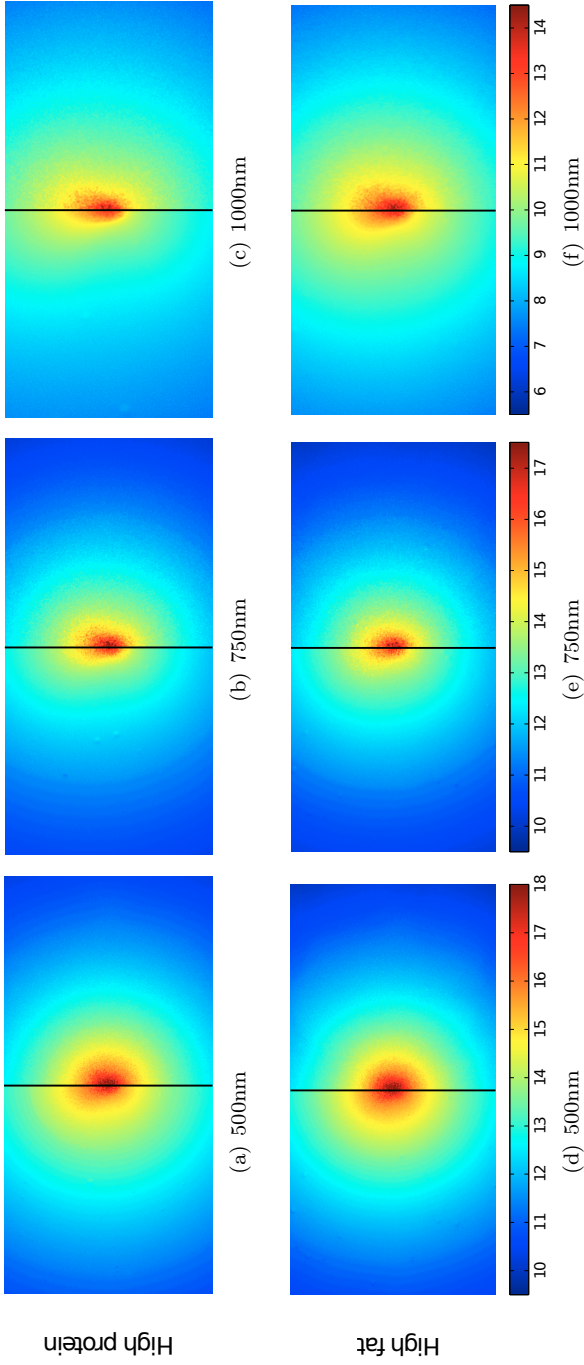


Figure A.3: False colour images of the double logarithmically transformed system responses for two extrema in the experimental design at different wavelengths. Red corresponds to high pixel intensity and blue corresponds to low pixel intensity, and the scale of the colour map is the same across wavelengths. The left hand side of each image shows the response from the milk base, and the right hand side shows the system response late in the fermentation process. The laser is shown in from the bottom of the images.

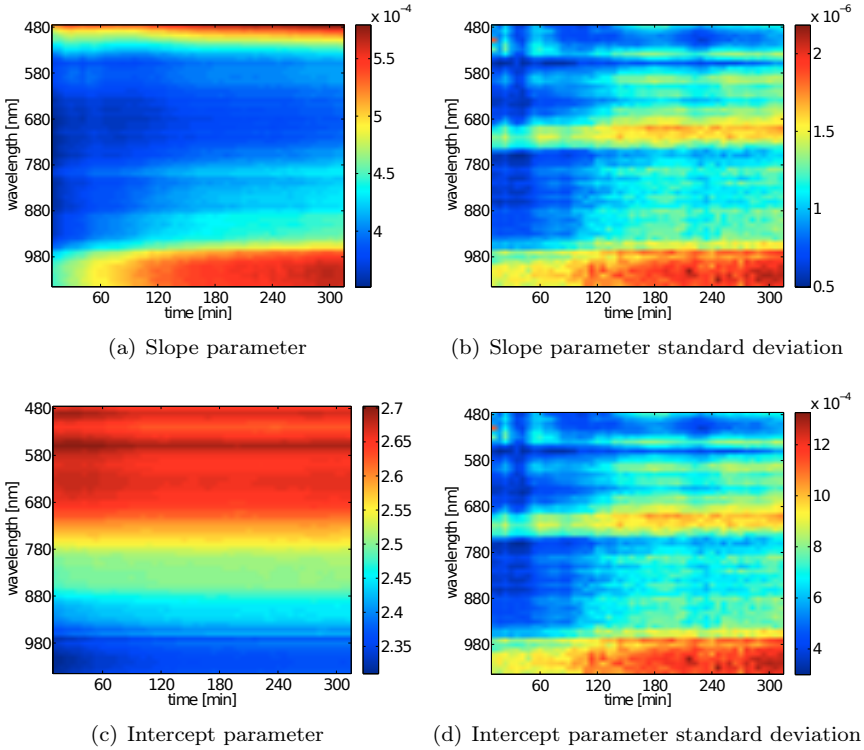


Figure A.4: Parameter and variance estimates for a centre point sample. (a) and (c) shows the parameter estimates for the slope and the intercept parameter respectively and (b) and (d) shows the corresponding variance estimates of the parameters.

A.3.1.1 Parameter Extraction

The intercept and slope parameter were extracted from the diffuse reflectance images for each time point (61 in total) and wavelength (56 in total). Figure A.4 shows the estimated parameters and their corresponding standard deviation for a centre point in the factorial experiment.

The low numerical value of the parameter variance for both the slope and intercept, combined with the smooth development of the parameters themselves, validates the applied linear model. However, the slope parameter shows clearer dynamics across time when compared to the intercept parameter. For the sake of simplicity we will only consider the slope parameter for further analysis.

Looking at the outer regions of the wavelength interval, there is a tendency towards steeper slope parameter estimates. This was the general behaviour seen throughout all experiments. Also, from Figure A.4(b) it can be seen that parameter variance is higher in two major regions. This pattern was repeated throughout all the experiments. One region is in the near-infrared area, where the low quantum efficiency of the CCD cameras results in a lower signal-to-noise ratio, and thereby larger model errors. The other region is around 700nm late in the acidification process, which is because the transformed profile starts to show more curvature inside the fitting interval. The slope parameter, averaged over three different wavelength intervals is shown alongside the rheology measurements in Figure A.5.

A.3.2 Small Amplitude Oscillatory Rheology

The rheological measurements are found in Figure A.5. According to Lucey and Singh (1997) and Sodini et al. (2004) an increase in total solids content (protein and/or fat) increase the final gel strength (storage modulus). Following Phadungath (2005) higher temperature generally increases the speed of the acidification, and lowers the final gel strength level, as a response to the increased rearrangement of the casein particles. While the increased temperature results in earlier gelation points as seen in Figure A.5, the final gel strength after 5.5 hours is also generally larger. While this contradicts Phadungath (2005), Anema (2008) notes that inconsistencies regarding this matter exist in the literature. These inconsistencies are attributed differences in the measuring conditions. Additionally, Anema (2008) presents more general results on the matter, which corresponds well to our observed values.

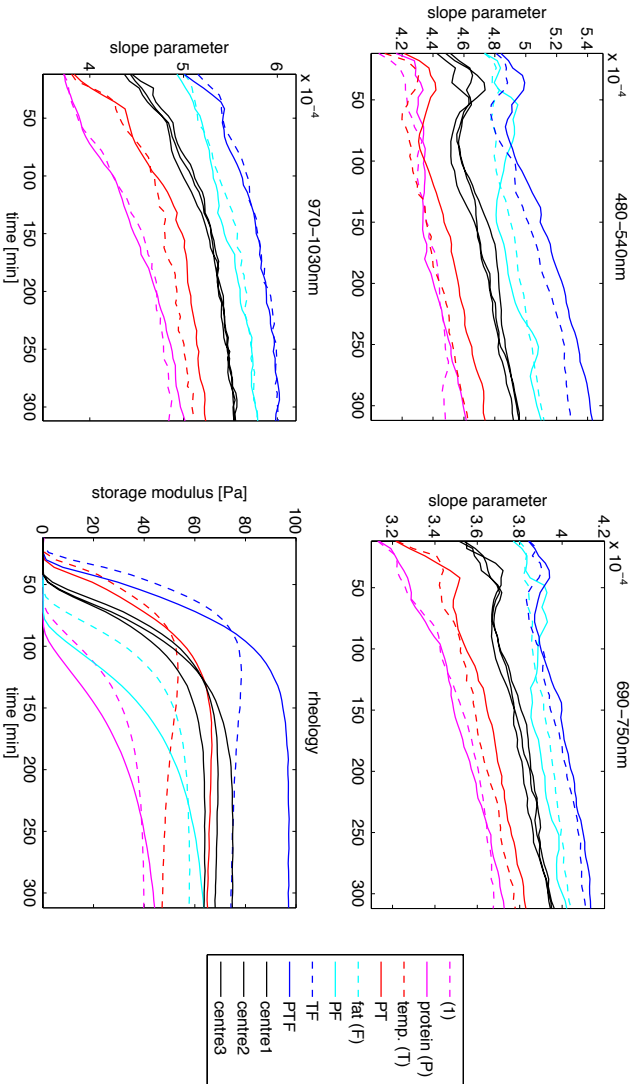


Figure A.5: The slope parameter averaged in three different wavelength interval and the rheology measurements as a function of time. Samples are coded by capital letters. A capital letter denotes a high level of that particular factor, and an absence of a capital letter denotes a low level of the factor. For sample (1) all factor levels are low. "centre" denotes the centre points.

A.3.3 Analysis of Variance

ANOVA was performed both at different time points in the measurement time series, and on the entire time series projected into one dimension, and thereby suitable for ANOVA. For the sub-space projected measurements Figure A.6 exemplifies the variation explained by the first three principal components for the slope parameter (averaged over all wavelengths) and the rheology measurements.

For the slope parameter in the lowest wavelength interval the first principal component (PC1) describes the amplitude of the signal and both PC2 and PC3 seem to cover the temporal location and amplitude of the bump located early in the process. Looking at individual spectral bands the same observation were made, however PC2 shows more pronounced effects of the bump for the lower wavelengths c.f. Figure A.5. For the rheology measurements, both PC1 and PC2 seem to incorporate the signal amplitude, steepness after the gelation point, and the overall shape of the signal, whereas PC3 was harder to interpret. In case of both slope parameter and rheology the two first components accounted for more than 95% of the total variation. It should be noted that the PCAs were applied separately for the different response variables. This means that we cannot be sure that all data is transformed in the exact same manner.

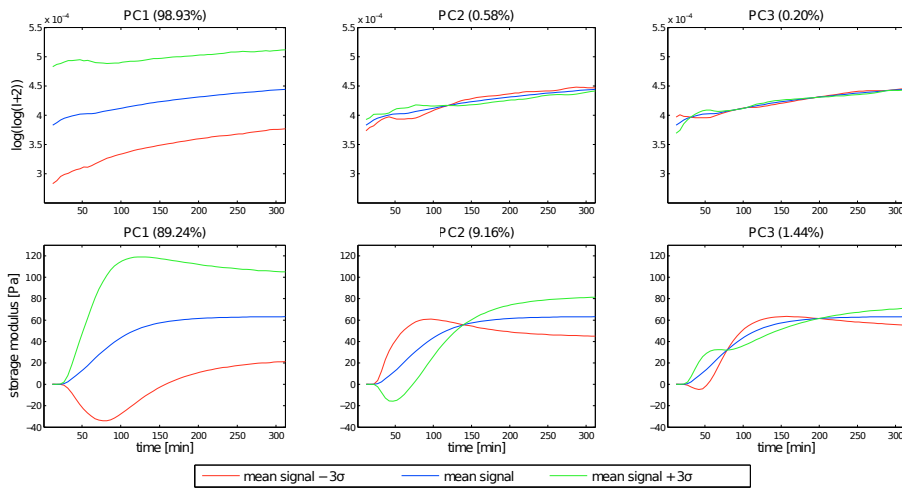


Figure A.6: The interpretation of the 1st, 2nd, and 3rd Principal Components (PC) scores used in the Analysis of Variance (ANOVA) analysis. The top row shows for the slope parameter (averaged over all wavelengths) and the bottom row shows for the rheology. The shown percentages denote the amount of variance explained by each PC.

In order to also incorporate the hyperspectral information of the slope parameter, the overall wavelength interval was uniformly divided into eight subintervals. Within these subintervals the slope parameter was averaged. Thus, in total, we effectively have 6+3 different scalar representations of the 8+1 response variables, thus a total of 81 ANOVA tests had to be performed.

Rather than presenting conventional ANOVA tables, the p -values are presented in Figure A.7. The p -values clearly show that both temperature and fat level have significant impact on both rheology and the averaged slope parameter for all wavelengths. Protein only has an effect on rheology and the averaged slope parameter in the lowest wavelength interval. Additionally, the slope parameter seems to be more sensitive to factor interactions as well as quadratic effects. These tendencies mostly appear at higher wavelengths.

Looking at the amplitudes for the rheology measurements after 10% of the total time, it can be seen that all factors are significant. This is due to the period before the gelation point in the milk acidification process, where no signal is measured for most of the experiments. Thus the centre points coincide and result in an MSE close to zero, which causes all factors to be significant. Similar trends can be observed for some slope parameter ANOVAs (550-610, 690-750, and 760-820nm). As these occur as abrupt changes compared to the neighbouring ANOVA tests, this might as well be due to nearly coinciding centre point measurements.

A.3.4 Multivariate Analysis of Variance

The MANOVA was performed on PC1 and PC2, as they accounted for more than 95% of the variance for both the slope parameter and the rheology. The results are presented in Figure A.8, and they resemble the ANOVA tests. Both fat and temperature are significant for the slope parameter and the rheology measurements, while protein is significant for the rheology measurements and the slope parameter in the 480-540nm interval. Again interactions and quadratic effects seem more prominent for the slope parameter.

A.4 Discussion

The raw image data presented in Figure A.3 show significant variation between the initial and the end states of the milk gels. This is a strong motivation for further processing of the image data. In this work we consider linear modelling

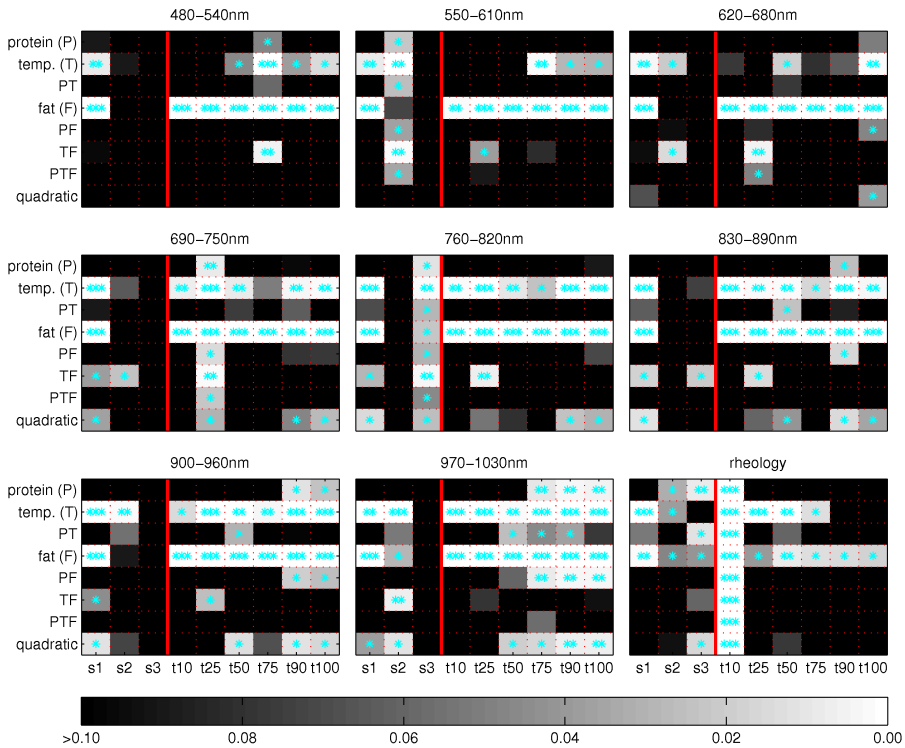


Figure A.7: Summary of the p -values in the ANOVA tests. The first eight images show the results for the averaged slope parameter in the eight different wavelength intervals, and the last image is the results for the rheology measurements. Each column in an image is one ANOVA test. $\{s1,s2,s3\}$ are the principal scores and $\{t10,t25,t50,t75,t90,t100\}$ are the slope parameter amplitudes recorded at 10, 25, 50, 75, 90, and 100% of the total time. Level of significance is denoted by asterisks (** $p < 0.001$, ** $p < 0.01$, * $p < 0.05$).

of double logarithmically transformed diffuse reflectance profiles, but it is evident from the image that other features can also be considered. Nevertheless, the linear model provides a good description of the diffused light far from the entrance point, and specifically the slope parameter show significant changes in dynamics. Furthermore, the estimated standard deviation of the slope coefficient was small compared to both the temporal changes during the milk fermentation and between the different sample compositions. This motivates it as a robust model for inspection of the diffuse reflectance images.

Through ANOVA and MANOVA we saw that all chosen factors were significant for the rheology. This was also the case for the slope parameter. However, protein content was only found significant at the lower wavelengths. Factor interactions were not predominant in either rheology or slope parameter, but quadratic effects were found to be significant for the slope parameter at the higher wavelengths. However, due to the small experimental design it is not possible to determine the source of the quadratic effects. This shows that the slope parameter was seemingly affected by both the structure development and the chemical composition of the milks. Figure A.5 also illustrates how the low wavelengths differentiate protein levels better, with the exception of samples F and PF. In general it seems harder to distinguish between protein levels in samples with a high level of fat. This is consistent with the literature, as casein micelles are known to generally scatter less light than the fat globules (Walstra et al., 2010).

As previously mentioned the slope parameter models the light decay rate, which depends on the total attenuation. Thus, increasing either scattering or absorption properties will increase the decay of light and thereby increase the slope parameter. Scattering is inversely proportional to wavelength (Martelli et al., 2010). However, Figure A.4(a) only shows a monotonous decrease in the slope parameter from 480 to 780nm hereafter it starts to increase again. A possible explanation is based on the water absorption spectra (Curcio and Petty, 1951),

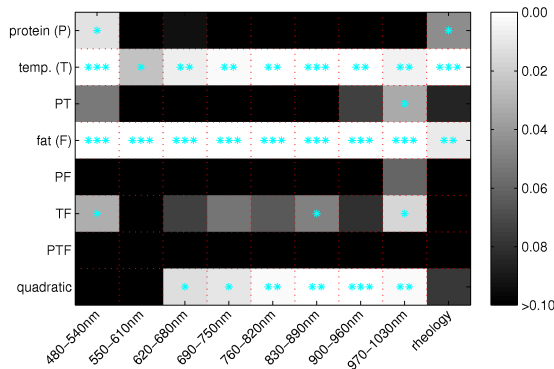


Figure A.8: Summary of the p -values in the MANOVA tests. Each column is a MANOVA test. The first eight columns are the results for the slope parameter averaged in different wavelength intervals, and the last column is the results for rheology measurements. The dependent variables are the first and second principal scores. Level of significance is denoted by asterisks (***) $p < 0.001$, ** $p < 0.01$, * $p < 0.05$).

where a small absorption peak is located between 700 and 800nm and a more dominant peak is located between 900 and 1030nm. This corresponds well to the observed behaviour of the slope parameter.

It is clear that the rheology measurements and the slope parameter describe two different developments in the milk acidification process. Contrary to the rheology measurements, the slope parameter shows a clear signal before the gelation point (the point where the casein micelles starts to aggregate), which has been observed before using optical methods (Alexander and Dalgleish, 2004; Alexander et al., 2006). Furthermore, the slope parameter has a clear ordering of the different acidification processes early on, especially when looking at the processes with different fat levels and temperature levels. However, the protein effect is clearly weak for the slope parameter. In terms of wavelength dependency the signal in the interval 480-540nm shows a clear bump in the beginning of the process, which is not present at the higher wavelengths. Especially at 970-1030nm the initial steepness of the signal seem to correspond to the fermentation temperature. The steepest initial signals are seen at high temperatures and may relate to the faster gelation processes, which are also seen for the rheology in Section A.3.2.

Also, an early ordering of the acidification processes was found when looking at the slope parameter. The ordering is kept throughout the entire acidification process and corresponds well to the final levels of G' of the rheology measurements. Lastly, the slope parameter shows a clear signal development before the gelation point. Alexander and Dalgleish (2004) and Alexander et al. (2006) also observed this phenomenon using DWS. They suggested this was due to changes in the so-called structure factor, i.e. changes to the positional correlation of the casein micelles. This may be further emphasised by a wavelength-dependent "bump", that can be found near the gelation point at lower wavelengths seen in Figure A.5. The bump is most pronounced at the lower wavelengths, which might be explained by the size of the casein micelles (50nm to 600nm (Horne and Dalgleish, 1985)). If the positional correlation of the micelles changes, it manifests itself in changes of the scattering properties for light at the lower wavelengths as casein mainly contribute as Rayleigh scatterers Martelli et al. (2010).

The analysis in this paper suggests that use of hyperspectral information can be beneficial for the use of diffuse reflectance images. Apart from the light-delivery system, the system described in Section A.2.4 consists of basic components. Thus, if all necessary information (to a given problem) can be expressed by a combination of few wavelengths (or bands of wavelengths), the light source may be replaced by laser diodes. This will allow significant shorter acquisition times and more cost-efficient vision systems. This, of course, leads to the task of determining an optimal subset of wavelengths, which will be prioritised when

larger data sets are acquired.

A.5 Conclusion

The use of hyperspectral diffuse reflectance images has provided some encouraging results for monitoring optical changes during milk acidification. The images data of the milk fermentation process show that it has a high sensitivity to both the structure formed during the fermentation process, but also the contents of both protein and fat level. A single feature from the diffuse reflectance images, the slope parameter, was found to be reproducible and enabled us to differentiate between different milk acidification processes. Some wavelength dependency was observed, in which protein content was only distinguishable at lower wavelengths. This wavelength dependency will be investigated further in the future, as it can be a key element in designing specialised multispectral vision systems. The experiment presented in this paper is limited in scope and acts as a screening of the generalisation abilities of the presented vision system. While protein, temperature, and fat were included in the experiment, these are only a few of the parameters that have been reported to influence the structure development. So it would be obvious to include other process parameters, as well as starter cultures, in addition to GDL in future experiments. Also, different quantification methods for the diffuse reflectance images will be investigated. Further, we believe the method is very applicable for diffusive media in general, and coupling the flexibility of the system set-up and data that can be recorded remotely, it may be suited for both at-line and in-line implementations.

A.6 Acknowledgements

We would like to thank The National Food Institute, Technical University of Denmark, for providing laboratory space and time during the course of our experiments. This work was (in part) financed by the Centre for Imaging Food Quality project, which is funded by the Danish Council for Strategic Research (contract no 09-067039) within the Programme Commission on Health, Food and welfare.

APPENDIX B

Decomposition of Diffuse Reflectance Images - Features for Monitoring Structure in Turbid Media

Jacob L. Skytte^a, Otto H. A. Nielsen^{a,b}, Ulf Andersen^c, Jens M. Carstensen^a, Anders L. Dahl^a, Rasmus Larsen^a, Flemming Møller^d, Faisal Kamran^e, Jeppe R. Frisvad^a

^a *DTU Compute, Department of Applied Mathematics and Computer Science, Technical University of Denmark, Matematiktorvet, Building 322, DK-2800 Kgs. Lyngby, Denmark*

^b *NKT Photonics A/S, Blokken 84, DK-3460 Birkerød, Denmark*

^c *Arla Strategic Innovation Centre, Rørdrumvej 2, DK-8220 Brabrand, Denmark*

^d *DuPont, Edwin Rahrs Vej 38, DK-8220 Brabrand, Denmark*

^e *DTU Photonics, Technical University of Denmark, Ørstedes Plads, Building 343, DK-2800 Kgs. Lyngby, Denmark*

Abstract

Light scattering in turbid media can be related to the microstructure of the media. Thus, light scattering can potentially be used for process control of products where the structure is a key component. However process control requires robust and sensitive input data to function properly. In this study we investigate different decomposition methods for extracting light scattering information from images of diffuse reflectance. Both well-established theoretical methods and data driven methods are considered and evaluated based on their robustness and sensitivity to changes in light scattering properties.

B.1 Introduction

Many food processes can be seen as controlled efforts to preserve, destroy, or transform structure (Aguilera and Stanley, 1999). According to Bourne (2002) the textural properties of foods can be derived from their structure, and is one of the most important factors concerning consumer acceptability. Microstructure in particular affects the physical properties of a material. Concerning food products the microstructure can affect a lot of the quality parameters we associate with a product, such as nutritious properties, stability, and physical properties (Aguilera, 2005). Thus, there is incentive for having improved control of the structural changes during food processing in order to ensure high and consistent quality.

In this paper we investigate the potential for process control of structural changes using a novel hyperspectral imaging modality. The method is applicable for homogenous turbid media, and incorporates elements from optics and hyperspectral imaging. Data from this modality is highly dependent on the optical properties. Typically changes in the optical properties have been characterized by looking at: changes in diffuse reflectance (Payne et al., 1993b), the transport mean free path (MFP) derived from speckle dynamics (Weitz et al., 1993; Alexander and Dalgleish, 2006), and absorption (μ_a) and reduced scattering (μ'_s) (Farrell et al., 1992; Wang and Jacques, 1995). In terms of interpretability the extraction of MFP, μ_a , and μ'_s makes it easier to relate optical properties to chemical and structural properties of turbid media. However modelling physical parameters will often introduce model variance, which can affect the robustness of the parameter estimation.

Hyperspectral imaging is a technique that integrates conventional imaging and spectroscopy. It has become increasingly popular within the field of food science

during the last two decades due to speed and also non-contact assessment (Sun, 2010). Gowen et al. (2007) gives an overview of recent publications within the hyperspectral imaging field, which exclusively covers heterogeneous materials such as vegetables and fruit. As we are dealing with homogenous turbid media, we take a different approach than conventional hyperspectral imaging. Rather than capturing images of a material in full field illumination, we shine a coherent, collimated light (laser) into the material and capture an image of the spatial distribution of the diffuse reflectance. These images make up the data used in our analysis.

Instead of using entire images for the analysis, a common step is to decompose an image into a number of features. This can reduce the computational load as well as provide higher level of interpretation of the diffuse reflectance images. Well-founded theoretical models will be considered for this decomposition step. These usually operate on one-dimensional intensity profiles. Also considered, are the data-driven methods that can be seen as empirical methods. These consider more of the information in the diffuse reflectance images.

The goal of this paper is to investigate different decomposition methods and evaluate their sensitivity towards changes in the scattering properties. The goal is also to determine how robust the decomposition schemes are. In order to use the image features for process control, a reasonable signal-to-noise ratio (SNR) must be established (MacGregor and Kourti, 1995). The turbid media considered in this paper are fat emulsions. However, we expect that the methods presented here apply to homogenous turbid media in general. In terms of structure prediction, we assume that all structural information can be related to scattering.

B.2 Material

B.2.1 Diffuse Reflectance Images

When light refracts into a turbid medium it is either scattered or absorbed when interacting with the particles in the medium. Whereas absorption is highly dependent on the chemical composition of the material, scattering is highly dependent on the size, shape, and density of the particles. Thus scattering can be correlated to the microstructural properties of a material. If light only scatters, it will eventually emerge at the surface at a point different from the point of entry. The emergent light is known as the diffuse reflectance. The spatial distribution of the diffuse reflectance will typically follow an anisotropic

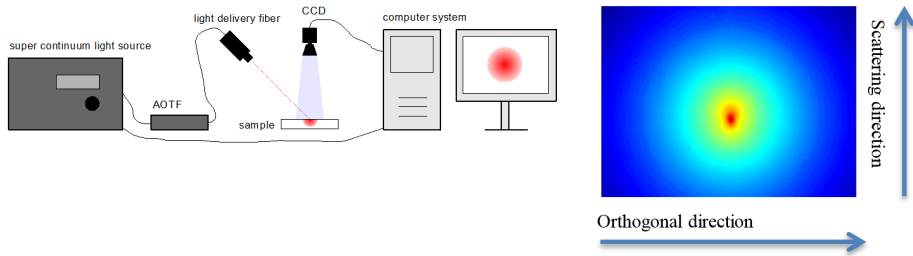


Figure B.1: Left: Schematic of the hyperspectral vision system. Right: Example of a logarithmic transformed diffuse reflectance image. The light is shone from the bottom of the image, and the point of incidence is the area with largest pixel intensity (red colour).

diffusion process, which emanates from the point where the light was incident. Light close to the point of incidence has typically scattered a few times, whereas light far away from the point of incidence has scattered multiple times.

Our aim is to extract information on the optical properties from the diffuse reflectance. The system works by shining a laser with tuneable wavelength into the sample material at an oblique incident angle (45°). High Dynamic Range (HDR) images (Mann and Picard, 1994) of the resulting diffuse reflectance are captured by a CCD camera (*Grasshopper CCD Cam, Point Grey Research Inc., Richmond, Canada*) with a zoom lens (*23FM50L, Tamron Co. Ltd., Saitama, Japan*) installed in front of the CCD with a 6.5cm spacer. The HDR images are 1200 by 1600 pixels, with a physical pixel size of $3.2\mu\text{m}$. The light delivery system is based on a super continuum light source (*SuperK Extreme, NKT Photonics, Birkerød, Denmark*), filtered by an acousto-optic tunable filter (*SuperK Select, NKT Photonics, Birkerød, Denmark*). At the moment the system potentially covers the wavelengths 450nm to 1050nm with a spectral resolution down to 5nm. As this paper is about the decomposition of the diffuse reflectance images, we will only consider a small selection of wavelengths.

A simplified schematic of the system is shown in Figure B.1 alongside an example of the diffuse reflectance images. The system is a research platform, which can be used to design cost-efficient vision systems with geometry and wavelengths optimized for a specific process. More information on the vision system is provided by Nielsen et al. (2011b).

Table B.1: The theoretically deduced scattering coefficient intervals for the three selected scattering regimes at three different wavelengths. The intervals are provided in $[\text{cm}^{-1}]$.

	Low scattering regime	Medium scattering regime	High scattering regime
500 nm	[7.2 , 31.3]	[35.0 , 63.0]	[67.5 , 87.5]
700 nm	[6.4 , 22.2]	[24.6 , 42.9]	[45.8 , 59.0]
900 nm	[6.0 , 16.9]	[18.6 , 31.3]	[33.3 , 42.4]

B.2.2 Intralipid Data Set

The data set of this paper consists of different dilutions of Intralipid (*Intralipid 20%, Fresenius Kabi, Bad Homburg, Germany*). Intralipid is a highly stable and standardized fat emulsion and approved for direct intravenous infusion for patients who are unable to get nutrition via an oral diet. It is also often used to simulate the optical properties of turbid media, as it mainly contributes as a scattering compound in the visible regime. Turbid media are generally highly scattering materials with low absorption characteristics, i.e. the reduced scattering coefficient μ'_s dominates over the absorption coefficient μ_a , and incorporates many biological samples including a wide variety of food products (fruit, vegetables, dairy products, emulsions), when considering the visible spectrum. For our experiment we made 21 graduated water dilutions of Intralipid. The dilutions were made to have linearly increasing scattering properties covering the range of milk and fermented milk products. Seven repeated measurements were made for each of the 21 dilutions, and the 21 dilutions were split into three scattering regimes of equal size, with "low", "medium", and "high" scattering properties. All dilutions were recorded at three different wavelengths (500, 700, and 900nm). The theoretical reduced scattering coefficients for the data set were calculated based on Lorenz-Mie theory (Frisvad et al., 2007; Michels et al., 2008) and are summarized in Table B.1.

B.3 Methods

It is hard to obtain information about material properties directly from the diffuse reflectance images, so the images were decomposed into compact representations (features). Two different decomposition strategies were considered. First, the theoretical models, which are commonly used for decomposing light diffusion signals into μ_a and μ'_s . These models are typically only based on what corresponds to intensity profiles in the images. Hereby they only utilise

a fraction of the data available from our images. The second strategy therefore consisted of data-driven approaches, which utilise different parts of the images. These more empirical features are typically a mixture of the absorption and scattering properties, and can therefore be harder to interpret compared to the theoretical models. We consider different approaches to both the theoretical modelling and empirical strategies in the following. All methods are implemented using Matlab (*MathWorks, Natick, Massachusetts, U.S.A.*).

B.3.1 Farrell Model Decomposition (FM)

General cases of light scattering and absorption in turbid media can be described analytically by the radiative transfer equation (Chandrasekhar, 1960). However this expression is difficult to solve and computationally inefficient for use in real time applications. For materials where scattering is dominant ($\mu'_s \ll \mu_a$), the light transport can be considered a diffusion process. By assuming that diffusion is isotropic the radiative transfer equation can be simplified significantly. While this simplification cannot accurately model the diffuse reflectance near the point of incidence, it provides an efficient way of estimating μ_a and μ'_s .

Farrell et al. (1992) derived an analytical solution for the diffusion approximation to describe the diffuse reflectance at the surface of a semi-infinite turbid medium, when illuminated by a ray of light at normal incidence. The reduced scattering coefficient was estimated by partly following the fitting routine used in the work by Lu (2004). An inherent problem with the Farrell decomposition is that it requires absolute values of the diffuse reflectance in order to estimate the actual reduced scattering coefficient. However, for some applications it should be sufficient to look at relative estimates of the reduced scattering coefficients.

B.3.2 Oblique Model Decomposition (OM)

The technique of oblique incidence angle (Wang and Jacques, 1995) is an extension of the original method by Farrell et al. (1992), in which the symmetry break between single scattered light near the entry point is measured relative to the diffuse part of the profile. The symmetry break allows an indirect measurement of the mean free path that eliminates the need for absolute intensity measurements. A major benefit to this is that it generally lowers the practical requirements of the vision system.

B.3.3 Loglog Model Decomposition (LM)

Carstensen et al. (2009) proposed the loglog model. It models the decay of the light intensity far away from the point of incidence. A double logarithmic transformed intensity profile ($\log(\log(I + 2))$, where I is the pixel intensity) is extracted orthogonal to the scattering direction and through the point of incidence. A robust linear model is fitted to this profile, and the extracted feature is the slope parameter of this model. We have previously experienced very robust results with this decomposition method (unpublished).

B.3.4 Patch Average Decomposition (PA)

A point measurement from the diffuse reflectance images resembles the measurements made by fibre optic probes, where light is sent into the sample using one fibre and the diffuse reflection is collected by another fibre some distance from the incident light. The more times the light is scattered the lower the observed intensity will be. This is the main idea behind the work by Payne et al. (1993a), which has proven itself useful in regard to determining the optimal cutting point during cheese making. As a light collecting fibre will often have a field of view, we select an image patch (50 by 50 pixels) orthogonal to the scattering direction and calculate a Gaussian weighted average of that patch. The patches will be extracted at different distances from the light incident point.

B.3.5 Intensity Spread Decomposition (IS)

A simple way to utilise a lot of the available image data is to consider histograms of the pixel intensities in the diffuse reflectance images. The histograms are created by masking out circular regions centred on the point of incidence. Typically histograms are quantified using first order statistics, however these are very sensitive to outliers. Since the distribution of the pixel intensities is heavy tailed, robust statistics should be considered. In the case of measuring the spread of the histogram we can use the median absolute deviation (MAD):

$$\text{MAD} = \text{median}(|H - \text{median}(H)|), \quad (\text{B.1})$$

which is the median of the absolute deviations from the median of the data (H). The intensity spread will give an estimate of how the diffuse reflection intensity has developed after a given distance from the incident light point. As

with the patch average decomposition, we consider different variations of the decomposition method, in this case by considering masks with different radii.

B.3.6 Feature Evaluation

The extracted features should be sensitive towards changes in scattering, such that small changes can be precisely assessed. They should also be robust with little variation within the same sample. We use the Rayleigh quotient, also known as the Fisher Criterion (Hastie et al., 2009) evaluate this property. It can be seen as an analogue to the SNR, as it evaluates the between-class variance relative to the within-class variance. In the univariate case the Rayleigh quotient can be found as B/W , where B and W are the between- and within-class variances respectively. For best discrimination between different samples we want to have a large numerator and small denominator. In addition to the Rayleigh quotient we will also report the average leave-one-out classification results using linear support vector machine (SVM) classifiers (Chang and Lin, 2011), to evaluate how well the different Intralipid dilutions can be distinguished. The Rayleigh quotient and the SVM classification rates will be reported for the three different scattering regimes in the Intralipid data set. Lastly we expect the 21 Intralipid dilutions to have linearly increasing scattering properties. To verify this we report the correlation coefficient for the features in the entire scattering regime of the data set.

B.4 Results and Discussion

The results are summarized in Table B.2. Overall the methods perform better in the low scattering regimes, and typically also at the higher wavelengths. These general observations hold true for the theoretical models (FM and OM). The two methods show similar trends both in terms of Rayleigh quotient and classification rates. They perform well in the low scattering regime, but degrade significantly when moving to the medium and high scattering regimes. The theoretical models behave well in terms of the expected linearity, and the low linearity for OM is simply because of large variance in the feature estimates. In general the theoretical models show more within class variation compared to the other methods. An example of the OM decomposition is shown in Figure B.2.

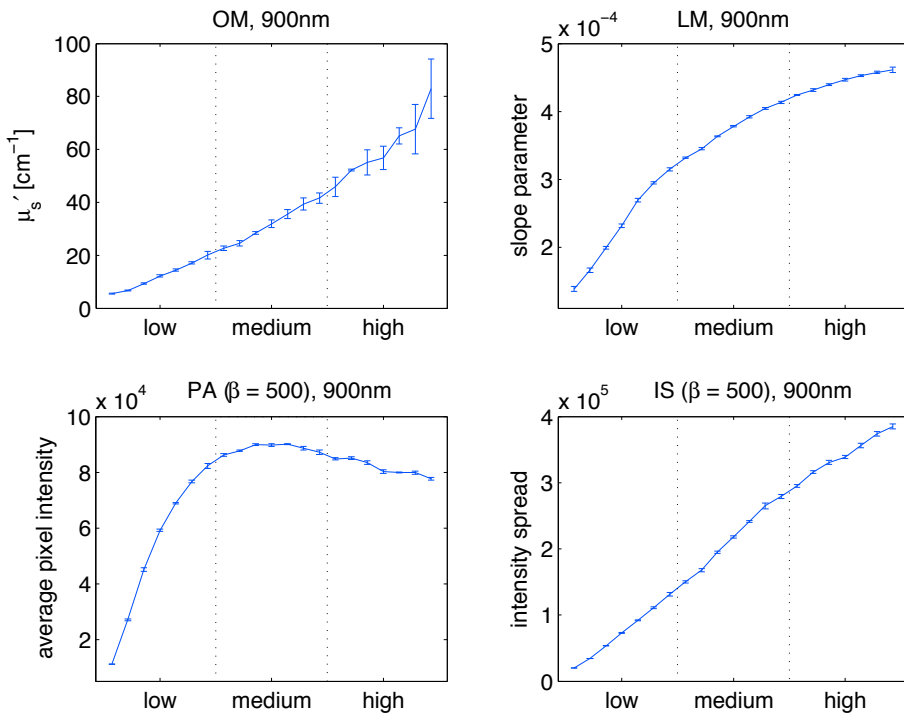


Figure B.2: Examples of how different methods perform. The bars indicate the standard deviation for the feature estimates of the seven replicates for each dilution. The dotted lines indicate the different scattering regimes.

The LM decomposition performs well overall for the low and medium scattering regime in terms of classification. There is a significant drop in the Rayleigh quotient when going from the low to the medium scattering regime, hinting that while the method is robust, the sensitivity toward scattering changes is not as pronounced compared to PA or IS. However the linearity assumptions are maintained well, as can be seen in Figure B.2.

PA decomposition works very well for the low scattering regime and has the highest Rayleigh quotients in this regime. For the medium and highly scattering regimes there is a significant drop in performance, and there seems to be a serious problem in terms of linearity. This is especially prevalent when the patch is extracted far away from the point of incident. This is most likely because if a sample is highly scattering, the majority of the diffusion dynamics happens close to the point of incidence, leaving very little variation between samples in the areas far from the point of incidence. Thus, feature estimates can reach a plateau when the scattering becomes sufficiently high. An example for PA with high discrimination (and reasonable linearity) for the low scattering regime, but bad linearity for entire regime can be found in Figure B.2.

The overall performance of the IS decomposition is good and it shows the best results throughout the entire scattering regime, while retaining the expected linear behaviour. This is especially true when looking at 900nm. The method performs best when the mask radius is large. Compared to PA the sensitivity is not as great in the low scattering regimes. The best performing IS decomposition example can be seen in Figure B.2.

From these results it is clear that no single decomposition method does not stand out as the better solution for the presented data set. It really depends on the considered scattering regime, the used wavelength, and the needed sensitivity and robustness. While the FM, OM, and LM decompositions are fairly fixed in the way they are extracted, the sampling schemes used for the PA and IS decompositions could have been done differently. Additionally two-dimensional spatial features have not been considered in this contribution.

Furthermore the geometry of the vision system can also be changed, and especially increasing the amount of zoom used for the camera should significantly enhance the performance. More zoom would allow capturing more details of the diffusion dynamics, which should increase the performance when the scattering becomes "too high". This especially holds true for the theoretical models, as their underlying models depend on modelling these dynamics.

Table B.2: Evaluation of the different decomposition method at three different wavelengths. Each cell reports three numbers, one number for each of the three different scattering regimes ("low"/"medium"/"high"). Further a parameter, β , is provided for PA and IS. For PA it denotes how far away (in pixels) from the point of incident the patch is extracted, and for IS it denotes the radius (in pixels) of the applied mask.

500 nm				
Decomposition type	β	Rayleigh quotient	Classification rates [%]	Linearity
Farrel model (FM)	–	378.1 / 11.3 / 1.6	95.5 / 55.1 / 14.3	0.97
Oblique model (OM)	–	119.6 / 1.3 / 0.1	97.8 / 64.4 / 0	0.27
loglog model (LM)	–	1397.7 / 92.5 / 0.6	100 / 95.9 / 34.7	0.92
Patch average (PA)	100	254.1 / 183.6 / 29.3	100 / 91.8 / 59.2	0.86
	300	343.4 / 10.1 / 57.7	100 / 46.9 / 81.6	0.17
	500	254.2 / 44.1 / 15.7	79.6 / 65.3 / 77.6	0.39
Intensity Spread (IS)	100	152.0 / 54.8 / 10.3	100 / 77.6 / 42.9	0.97
	300	200.3 / 207.4 / 27.5	100 / 83.7 / 53.1	0.93
	500	252.1 / 235.2 / 34.4	100 / 91.8 / 73.5	0.88

700 nm				
Farrel model (FM)	–	84.1 / 20.6 / 1.5	98.0 / 57.1 / 20.4	0.93
Oblique model (OM)	–	73.4 / 6.2 / 0.7	90.5 / 62.5 / 20.5	0.64
loglog model (LM)	–	694.6 / 254.5 / 3.4	100 / 98.0 / 57.1	0.95
Patch average (PA)	100	1127.8 / 186.6 / 119.2	100 / 98.0 / 93.4	0.91
	300	3158.2 / 24.9 / 337.3	100 / 53.1 / 67.3	0.57
	500	3325.6 / 13.6 / 36.0	100 / 30.6 / 89.8	0.08
Intensity Spread (IS)	100	156.8 / 44.6 / 12.6	100 / 85.7 / 61.22	0.95
	300	722.3 / 354.1 / 94.5	100 / 100 / 87.8	0.94
	500	1263.4 / 511.3 / 212.4	100 / 100 / 89.8	0.92

900 nm				
Farrel model (FM)	–	31.7 / 12.3 / 1.4	69.4 / 69.4 / 28.6	0.98
Oblique model (OM)	–	65.4 / 25.9 / 3.9	100 / 72.5 / 43.3	0.97
loglog model (LM)	–	632.7 / 493.5 / 43.2	100 / 100 / 93.9	0.96
Patch average (PA)	100	556.7 / 354.8 / 45.7	100 / 95.9 / 89.8	0.99
	300	2004.5 / 209.1 / 2.9	100 / 85.7 / 14.3	0.89
	500	2646.0 / 9.2 / 33.4	100 / 44.9 / 44.9	0.64
Intensity Spread (IS)	100	134.52 / 31.3 / 9.2	100 / 79.6 / 42.9	0.99
	300	564.26 / 205.3 / 69.5	100 / 100 / 93.9	0.99
	500	1042.6 / 372.8 / 113.0	100 / 100 / 96.0	0.99

B.5 Conclusions

In this paper we have demonstrated some of the potential in using diffuse reflectance images. Both theoretical and data-driven decomposition methods were demonstrated and tested in practice. It was seen that by sacrificing some of the interpretability (and some practical advantages in the case of the oblique decomposition method) provided by the theoretical methods, significant increases in both robustness and sensitivity could be achieved. While some data driven methods successfully covered the entire considered scattering range, no single decomposition method performed best in all the considered data sets. This emphasises the advantage of considering diffuse reflectance images, when designing or optimizing instruments based on light reflectance methods.

B.6 Acknowledgements

This work was (in part) financed by the Centre for Imaging Food Quality project, which is funded by the Danish Council for Strategic Research (contract no 09-067039) within the Programme Commission on Health, Food and welfare.

APPENDIX C

DCT-Based Characterisation of Milk Products Using Diffuse Reflectance Images

Sara Sharifzadeh^a, Jacob L. Skytte^a, Line K. H. Clemmensen^a, Bjarne K. Ersbøll^a

^a *DTU Compute, Department of Applied Mathematics and Computer Science,
Technical University of Denmark, Matematiktorvet, Building 322, DK-2800 Kgs.
Lyngby, Denmark*

Abstract

We propose to use the two-dimensional Discrete Cosine Transform (DCT) for decomposition of diffuse reflectance images of laser illumination on milk products at different wavelengths. Based on the prior knowledge about the characteristics of the images, the initial feature vectors are formed at each wavelength. The low

order DCT coefficients are used to quantify the optical properties. In addition, the entropy information of the higher order DCT coefficients is used to include the illumination interference effects near the incident point. The discrimination powers of the features are computed and used to do wavelength and feature selection. Using the selected features of just one band, we could characterise and discriminate eight different milk products. Comparing this result with the current characterisation method based of a fitted log-log linear model, shows that the proposed method can discriminate milk from yogurt products better.

C.1 Introduction

The Discrete Cosine Transform (DCT) is an appropriate transformation in the field of signal processing. It was first introduced in (Ahmed et al., 1974) to be used in the image processing area for the purpose of feature selection. It has excellent decorrelation properties as well as energy compaction. In addition, it decomposes the spatial frequency of an image in terms of cosine transforms. Some of its application areas are image and speech compression (Gonzalez and Woods, 2002; Ramírez and Minami, 2003), speech recognition (Bouvier et al., 2008; Sharifzadeh et al., 2012a) and medical imaging (Fu et al., 2005).

In this paper, the DCT is employed for decomposition of diffuse reflectance images. These images are obtained by illumination of a hyperspectral coherent laser (460-1000 nm) into the surface of eight different milk products. This vision system has been introduced recently for inspection of the structure of food items (Nielsen et al., 2011b,a). It is applicable for homogenous products where particle size and shape are important parameters. The main idea is to use the diffusion effects, which are known to be correlated to the microstructure, for characterisation of the structural composition of food items (Martelli et al., 2010; Mateo et al., 2010).

On the other hand, research findings in the field of food quality control have demonstrated a correlation between the texture, chemical and physical properties of food items with their microstructure characteristics (Bourne, 2002; Aguilera, 2005). Considering these sequential relationships from the optical level to the quality level, it is possible to build an automatic light-based system as a measuring tool, for monitoring the quality of dairy products along the production line and avoid microstructural artefacts during processing.

Therefore, finding an efficient method for characterisation of the hyperspectral images into key discriminative features obtained from a minimum number of bands is of special concern in this field. The reduction in the number of required

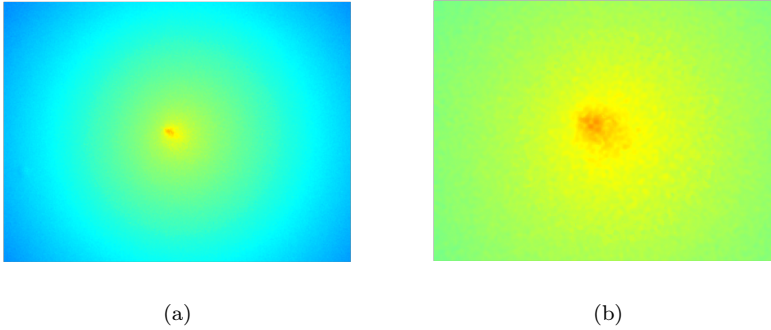


Figure C.1: (a) A log-log transformed diffuse reflectance image of yogurt showing the low frequency diffusion effect at the centre. (b) The zoomed image showing the high-frequency speckle noise around the incident point caused by the destructive interference of light to the rough surface of fermented milk.

wavelengths will assist to simplify the laser set-up and make the overall system simpler and cost effective.

According to the characteristics of the milk products e.g. fat or viscosity, we can observe different visual effects in the hyperspectral images. The main optical feature is the low frequency light diffusion emanating from the incident point that has the largest intensity in the image as can be seen in Figure C.1(a). Another important effect is a high-frequency speckle pattern caused by interference of coherent light due to surface irregularities (Goodman, 2007). It is shown in Figure C.1(b) by zooming in around the centre point. These effects vary in different products according to their molecular composition and thus reflectance and scattering properties of light.

The current characterisation technique for these images uses a narrow band of pixels of the scattering profile including the scattering centre (Nielsen et al., 2011b,a; Sharifzadeh et al., 2012b). A double logarithm transformation is applied on the original profile to form this image. Therefore, the extracted line of intensities is called the log-log model. The resulting profile includes a slope and an intercept containing with subsurface information. This method only considers the low frequency information in the image.

In this paper, we propose to apply a DCT transform on the double logarithm of the entire diffuse reflectance image to decompose the low frequency diffusion effect as well as the high-frequency speckle patterns. DCT can decorrelate the highly correlated information in these images. It decomposes the low frequency

diffusion effects and high-frequency speckle effects into low and high-order coefficients that could be quantified easier. Finally, due to the high compression level in the DCT domain, the number of discriminative features is reduced. In order to form an initial set of features for each image of each wavelength, we combine those of both low and high-frequency effects. The low order DCT coefficients are considered to characterise the optical properties. The entropy information of the high-order coefficients are used to characterise the speckle effect based on an approach that will be explained in C.3.

In the next step, the discrimination power analysis (DPA) introduced in (Dabaghchian et al., 2010), is employed as a selection criterion on the initial set of features for both wavelength and feature selection. It is a more careful method in terms of discrimination than the conventional zigzag or zonal masking for DCT coefficient selection. Especially, that is in our work, both the low and high-order features are important. Using the final selected features of one proper wavelength, we could characterise and discriminate the eight different products.

The proposed method is compared to the previous profile based characterisation method including low frequency information and the results show that in addition to the more discrimination power of the proposed method (including both the low and high-frequency information), it can separate the milk class products from the yogurt class better.

The rest of this paper is organised as follows. In section C.2, the data is described. Section C.3 presents the characterisation of the diffuse reflectance images. In section C.4, feature selection and discrimination is explained. The experimental results are shown in Section C.5. Finally, there is a conclusion for this paper.

C.2 Data Description

The data set consists of spectral diffuse reflectance images (1200×1600 pixel) of eight commercial dairy products including milk and yogurt categories. Table C.1. show their names and fat levels. L, M and H stand for low, medium and high. The CH and CU are extracted from the commercial name of the products. In each category, there are products with different fat levels and viscosities. In the yogurt category, there are two different products with similar fat levels. The yogurt products differ from each other not only in terms of the fat, but also according to the applied fermentation processes. In this paper, we are not interested in predicting product properties. Instead, we would like to characterise the products' diffuse reflectance profiles and then discriminate

Table C.1: The eight milk products and their fat levels

Product Type	Yogurt					Milk		
Short Names	L	M	H	CH	CU	L	M	H
Fat Level	0.5	1.5	3.5	0.1	1.5	0.5	1.5	3.5

them using their optical features. In fact, the optical characteristics represent the chemical, physical and structural differences between the products. For each product, there are five samples in the data set. Thus, there are 40 samples available in total. The laser was illuminated in 55 wavelengths (460-1000 nm).

C.3 Characterisation of the Images

As mentioned in section C.1 there are two important features in the diffuse reflectance images that can be used for characterisation of these images; the low frequency light diffusion effect and the high-frequency speckle effect. The light diffusion effect shows the spatial intensity distribution due to the absorption and scattering of the light. It is mostly dependent on the microstructural characteristics of the subsurface such as particle size distribution. The speckle effect is caused by the interference of light at the surface. It can be seen as a measure of surface roughness. In a fermented milk product like yogurt, the surface roughness is higher than milk due to the increase in viscosity of the material after the fermentation process. Hence, it could be used as a measure for distinguishing milk from yogurt. Figure C.2 shows in the top row, two diffusion images of a medium-fat milk sample (M-M) and a high-fat yogurt (Y-H). The images are zoomed around the incident point. The difference in both low frequency diffusion effect and the high-frequency speckle noise effect is clear between the two images.

C.3.1 DCT Transform

Two-dimensional DCT transform is applied to the diffuse reflectance images of each sample product at each wavelength. This yields 40×55 DCT matrixes of size 1200×1600 . In the second row of Figure C.2, the corresponding 400×400 DCT coefficients from the top-left DCT matrix of the above images are illustrated. The difference in the higher order DCT coefficients represents the speckle effect that was seen in the spatial domain as well. However, it is not easy to distinguish the difference in low order DCT coefficients that represent the diffusion effect.

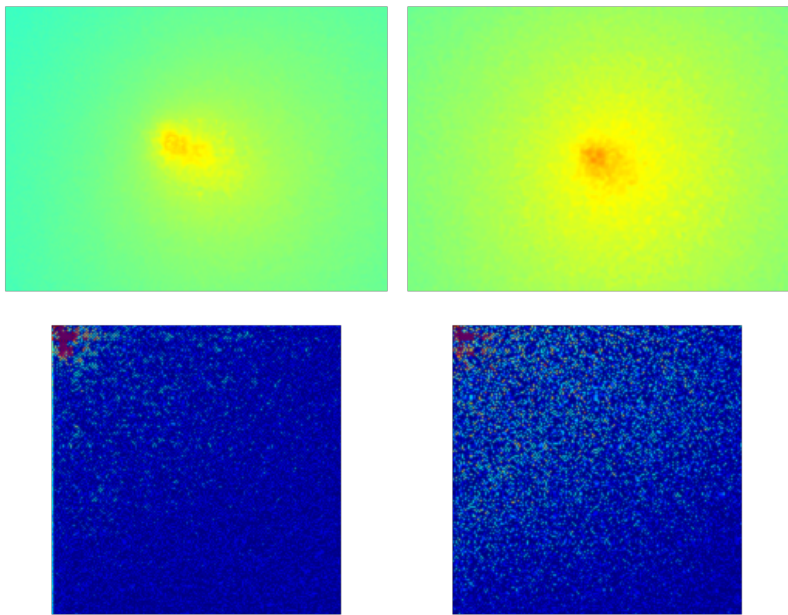


Figure C.2: (Top) left and right, the zoomed diffuse reflectance images of milk-M (1.5) and yogurt-H (3.5) respectively. (Bottom) their corresponding 400×400 top-left DCT coefficients from the DCT matrix

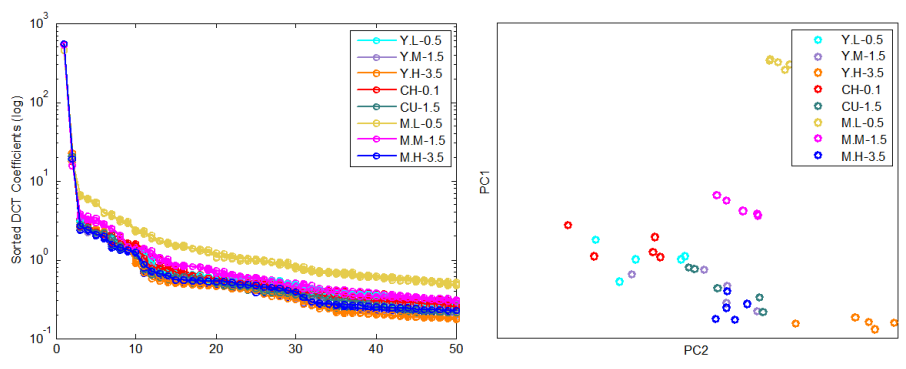


Figure C.3: The first 50 largest DCT coefficients of all the samples of the 8 products: (Left) in original domain (right) in PCA space using the first two PCs.

According to these observations, choosing the DCT coefficients in a conventional zigzag or zonal low order masking alone, is not a good choice. That is due to the large number of DCT coefficients in a wide span of low and high frequencies that describe the scattering and speckle effect. To demonstrate this issue, a 400×400 sub-volume of DCT coefficients from the top-left of the DCT matrix is considered for all the samples of all classes. For ease of visualisation, they are sorted and the logarithm of the 50 largest are illustrated in Figure C.3(a). It is difficult to distinguish all the products. In addition, they are transformed into the PCA domain and the first two PCs are shown in Figure C.3(b). In both images, just a few products can be distinguished from each other and the other classes. It is not easy to distinguish most fermented products and the high-fat milk from each other. This is because; the larger values of the DCT coefficients only carry the information about the diffusion effect and that is not enough for discrimination. In order to include the speckle effect, we propose to use the entropy of the DCT coefficients, which will be explained in the following section.

C.3.2 Entropy

The high-frequency DCT coefficients that contain information about the speckle effect result in an increase in the entropy of the sub-volumes of the DCT matrix that includes them. For example, in the two 400×400 sub-volumes that are shown at the bottom of Figure C.2, the entropies are 1.55 and 2.02 from left to right respectively. Starting from the top-left corner of a DCT matrix, we considered an $n \times m$ sub-volume and calculated the entropy repeatedly, while continuously increasing the n and m values as illustrated in Figure C.4(a). The resulting entropy profile is shown in Figure C.4(b). It shows that, as the size of the volume increases, the entropy also increases up to some point and then, decreases due to the uniform values of the DCT coefficients in higher frequencies. Since the speckle effect that characterises the surface roughness enhances the higher order DCT coefficients, the maximum entropy should describe the speckle effect for each sample. By forming such entropy profile for the eight products, we found that it can characterise their speckle effect uniquely. Therefore, the low entropies before the peak point can be considered as the diffusion effect so that, their corresponding sub-volumes include mostly the DCT coefficients describing the diffusion effect. On the other hand, the right side of the peak point includes the higher order DCT coefficients that describe the diffusion effect. To verify this further, we isolated the low order diffusion effect DCT coefficients using the index of the peak point that is 52 in Figure C.4(b). Then, an inverse DCT transform is applied to this 52×52 DCT sub-volume. Comparison of the result with the original diffuse reflectance image shows the removal of the speckle effect, as shown in Figure C.4(c, d).

C.3.3 Forming the Initial Feature Set

According to the discovered points, the right side of the entropy profile was considered for characterisation of the speckle effect. The mean, the standard deviation and the maximum value, of this part of the profile were considered as the candidate speckle effect features. By looking to the entropy profiles of the eight products, it was found that in average, the maximum entropy occurs around a 50×50 sub-volume. Regarding to its variation in different products and also considering a softer threshold for separation of the DCT coefficients of the diffusion and speckle effects, a 20×20 sub-volume of low order DCT coefficients was considered. They form a 400-length vector as the candidate feature for the light diffusion effect.

The final initial set of features for each wavelength image was formed by concatenating the three candidate features of the speckle effect with the 400 of the diffusion effect.

C.3.4 Feature Forming Based on log-log Model

In order to form the features based on log-log model, at each wavelength, a narrow diagonal band (around 10 pixels width) including the scattering center was considered in the double logarithm of the diffuse reflectance image as shown in Figure C.5(a). The orientation of the line was chosen in a way to consider as much as possible, greater number of pixels along the path through the centre. Then, it was averaged over the pixels. Since this diagonal line is approximately symmetric, just half of that was considered. The resulting averaged profile includes an intercept from the peak and a slope as shown in Figure C.5(b). These two features were used to characterise the image. For more information, we refer to (Nielsen et al., 2011b,a).

C.4 Feature Selection and Discrimination

The length of the formed initial set of features (403) per band, regarding the total number of samples of all classes (40) is quite high. Therefore, it is better to select a subset of them according to their ability for characterisation and discrimination of different products. Besides that, there are 55 bands per sample and as mentioned earlier, we are interested in reducing the number of wavelengths to simplify the laser set-up. Therefore a strategy should also be taken

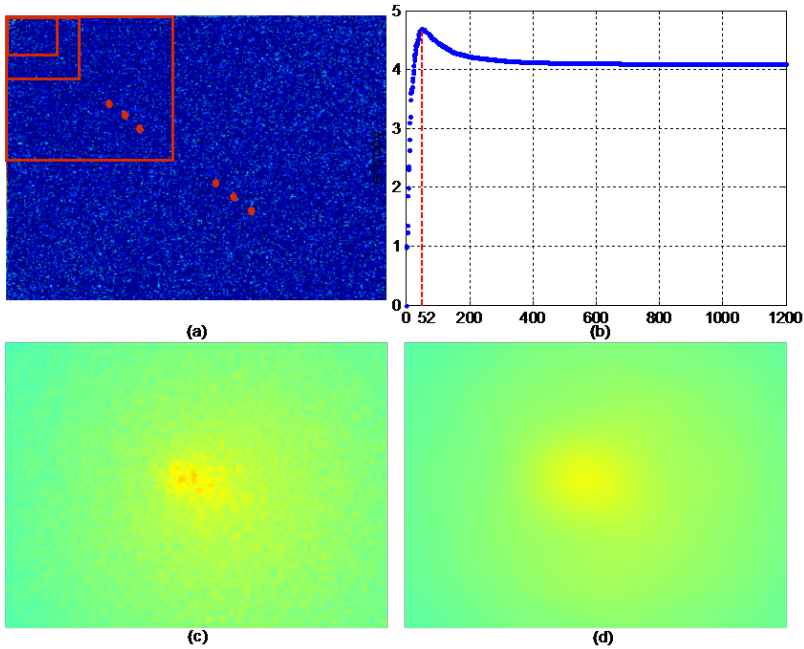


Figure C.4: (a) The sequential entropy calculation on increasing sub-volumes of the DCT matrix. (b) The resulting entropy profile. (c) The zoomed original diffusion image around the incident point. (d) The diffusion image obtained by the inverse DCT transform of the 52×52 lower order sub-volume of the DCT matrix.

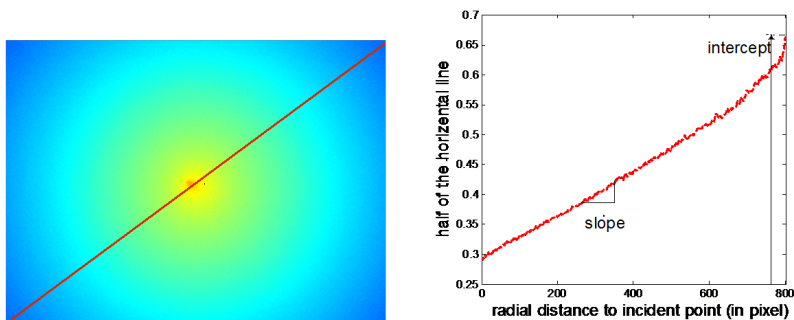


Figure C.5: (a) Symmetric narrow band of pixels crossing the incident point in the double logarithm diffuse reflectance image. (b) Half of the band is averaged and the slope and intercept from the peak are shown.

into account to sort the discrimination ability of different wavelengths and select one or few of them.

Since the majority of the features are the decorrelated DCT coefficients, it is not necessary to decorrelate them by a transformation into an orthogonal space. Inspired by the approach in (Dabbaghchian et al., 2010), we employ the DPA introduced in that work. The main idea behind this data-dependent approach is that, all of the DCT coefficients do not have the same discrimination power (DP). In other words, some of them can discriminate the classes better than the others. It is different from other similar approaches such as PCA and LDA, in the sense that it does not utilise the between- and within-class variances by a transformation to maximise the discrimination of the features in the transformed domain. It searches for the best discriminant features in the original domain. In case of decorrelated features such as DCT coefficients it is an appropriate approach for ranking the features and choosing a sub-set of them. The calculation of DPA will be explained step by step in the following.

Assuming that we have C classes with the N_c number of data points and $P = 403$ features in each class, the DP_j of each feature f_j ($j = 1, 2, \dots, 403$) is calculated as follows:

1. The mean and variance of each class is calculated for that feature

$$(f_j) : m_{jc} = \frac{1}{N} \sum_{n=1}^{N_c} f_{nj}, c = 1, 2, \dots, C,$$

$$v_{jc} = \sum_{n=1}^{N_c} (f_{nj} - m_{jc})^2, c = 1, 2, \dots, C$$

2. The variance of all classes are averaged:

$$V_j^W = \frac{1}{C} \sum_{c=1}^C v_{jc}$$

The mean and variance of all training samples are calculated for

$$f_j : M_j = \frac{1}{C \times N_c} \sum_{c=1}^C \sum_{n=1}^{N_c} f_{nj},$$

$$V_j^B = \sum_{c=1}^C \sum_{n=1}^{N_c} (f_{nj} - M_j)^2$$

3. The DP can be estimated as $DP_j = \frac{v_j^B}{v_j^W}$

It is mentioned in (Dabbaghchian et al., 2010) that DPA can be used as a stand-alone feature reduction algorithm. Since we need to do both band and feature selection, a sequential strategy is taken into account as shown in Figure C.6.

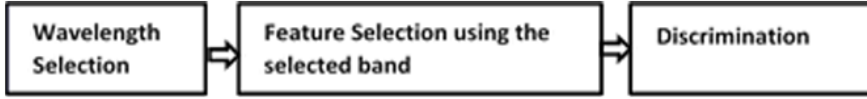


Figure C.6: The three steps of the sequential strategy

C.4.1 Preparation of Training and Test Sets

In order to maintain the training and test sets from the few data points, one sample of each class was considered as the unseen test data and the rest were assigned to the training set. Therefore, the two sets were formed as $test_{8 \times 403 \times 55}$, $train_{32 \times 403 \times 55}$. Then, leave one out cross validation (LOOCV) was used on the training data set for both wavelength selection and feature selection steps. LOOCV is used for generalisation and to avoid over-fitting as much as possible (Hastie et al., 2009). However, due to the limited training data points, this could not be achieved completely.

C.4.2 Wavelength Selection

The band selection algorithm is as follows:

1. At each iteration of LOOCV, sum of the DP's of all 403 training features are calculated at each wavelength $w = 1, 2, \dots, 55$; $SUM_{32 \times 55}$
2. The sum of DPs, $SUM_{32 \times 55}$ is averaged over the 32 iterations; $Average_SUM_{1 \times 55}$.
3. The best band is the one with the highest average discrimination power.

This algorithm was also used for wavelength selection of the log-log model.

C.4.3 Feature Selection for the Selected Band

The use of just one band is a significant reduction in the number of features, since there are 403 initial features per wavelength. In order to select the most discriminative features of the selected band, these steps are followed:

1. The DPs of the features in the selected band are sorted for each of the 32 LOOCV iterations in descending order. Then, the corresponding features to the first top five DPs at each iteration are kept in a list;
2. The densities of the unique features in this list are calculated.
3. According to these densities, the features that were among the top five features almost in all 32 LOOCV iterations are selected as the final features.

The number five in the above-explained procedure was chosen empirically by looking to the sorted features and also for the aim of selecting a limit number of features. Interestingly, we observed in all the iterations, the first three features were from distinct low frequency DCT coefficients representing the light diffusion effect and one of the last two was the mean value of the speckle effect from the entropy profile shown in Figure C.4(b).

C.4.4 Discrimination

In order to evaluate the proposed characterisation approach and compare it with the existing log-log method, the training and test data are visualised on the same plot. Besides that, the discrimination power of the two methods is numerically measured by sum of the feature's DPs as well as the maximum Rayleigh quotient term (Hastie et al., 2009):

$$max = \frac{a^T B a}{a^T W a} \tag{C.1}$$

Where, B and W are the between- and within-class covariance matrixes and a is the eigenvector of the generalised eigenvalue problem, $\det(B - \lambda W) = 0$. In order to maximise Equation (C.1), the eigenvector a_1 corresponding to the largest eigenvalue λ_1 should be used.

In addition, the support vector machine (SVM) classifier with a linear kernel is used (Chang and Lin, 2011) and the average LOOCV results and unseen test results are compared for the two methods.

C.5 Results and Discussion

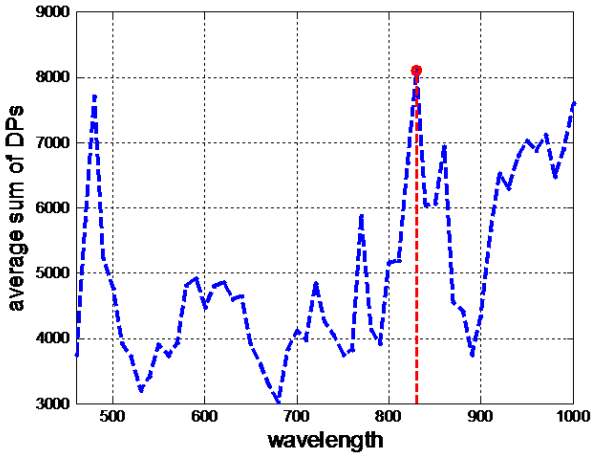
First, the results of the proposed method in DCT domain will be shown. Then, the log-log model results will be presented. Finally, there is a discussion.

C.5.1 Characterisation Results in DCT Domain

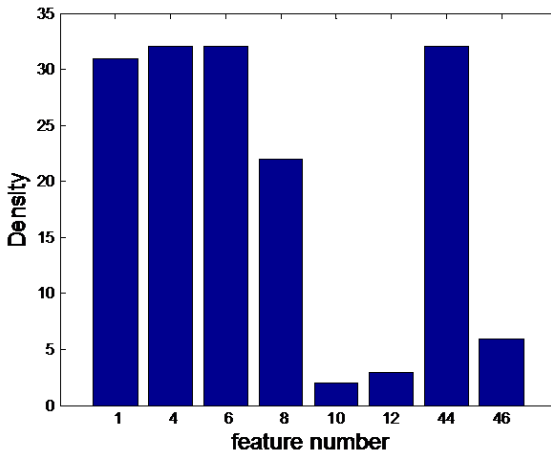
As explained in the previous section, both the band selection and feature selection were performed using LOOCV on the training data. Figure C.7(a) shows the average sum of the DPs for the 55 bands. According to this plot, the largest sum of DPs obtained for band 38 (830 nm).

By sorting the feature's DPs in this band, a list of features corresponding to the top five DPs were formed for the 32 LOOCV iterations. There were eight unique features in the list. Figure C.7(b) shows the densities of the unique features in the list. As can be seen, three features were among the top features in all 32 iterations. They are the low order DCT coefficients showing the light diffusion effect. Their location in the DCT matrix is represented in Figure C.8. In addition, the feature number one that represents the mean entropy of the speckle effect was among the top five features in 31 of the iterations. These four features were selected as the final features, for characterising the samples.

In order to visualise the ability of the speckle effect features to separate the two groups of yogurt products and milk, a 3D visualisation of the mean, standard deviation and maximum features (1, 2, 3 in Figure C.8) is represented in Figure C.9(a). The results show that these features are capable to perform the separation accurately for both training and test data. In addition to this between group separations, we can also observe a trend for within group separation according to the fat level. Fig C.9(b) shows the 3D visualisation of the three diffusion effect features (4, 6, 44 in Figure C.8). As can be seen, they fail to separate the high-fat milk sample (M-H) and the medium-fat yogurt (Y-M). Since the visualisation of the 4D selected features is impossible, three of them (1, 4, 6) are chosen and visualised in Figure C.9(c). Even in absence of one of them, we can see the successful separation of all the classes and also the two groups of milk and yogurt. Finally, the four features are transformed into the orthogonal PCA space and the first two PCs are shown in Figure C.9(d). Besides the successful discrimination, we can observe that the PC1 represents the variation from yogurt to milk group, while PC2 shows the change in fat content.



(a)



(b)

Figure C.7: (a) Average sum of DPs over the 32 LOOCV iterations for the 55 bands. (b) Density of the 8 unique features found among the top five discriminative features in the list over the 32 iterations. The horizontal axis shows the feature's number among the 403 features.

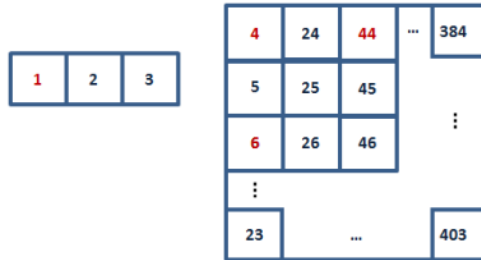


Figure C.8: The 1, 2 and 3 are the mean, standard deviation and maximum of the entropy profile of the speckle effect. The 400 low order DCT feature's numbers start from 4.

C.5.2 Characterisation Results Using the log-log Model

The same wavelength selection strategy based on sum of discrimination powers was used for band selection for log-log model dataset. Figure C.10 shows the 2D visualisation of the slope and intercepts features in original as well as PCA space. In both spaces, the two features group the samples only according to their fat level, while there is no trend to separate the milk group from the yogurt group. For example the high-fat milk (M-H) and the medium fat yogurt (Y-M) have close overlap which may make the discrimination difficult.

C.5.3 Discussion

According to the visualised results, the combination of the speckle effect (high frequency) and diffusion effect (low frequency) features in DCT domain shows to be a promising way of characterising the diffuse reflectance images. The statistical analyses results are presented in Table C.2. Although both methods could discriminate the single test samples of all classes, the average LOOCV classification performance shows that the proposed method can work better. However, the statistical models suffer from the over-fitting due to the limited number of samples. The table results show that, the DCT domain features are capable to characterise the images better in terms of discrimination power and Rayleigh criteria than the log-log model features. Besides that, considering the plots in Figure C.9 and Figure C.10, they are capable to reduce the overlap between classes and separate the products not only according to their fat level, but also according to their category (milk-yogurt). That is obtained by employing the ability of DCT transform in frequency decomposition and combining the high and low frequency information of the images. When only the analysis of the

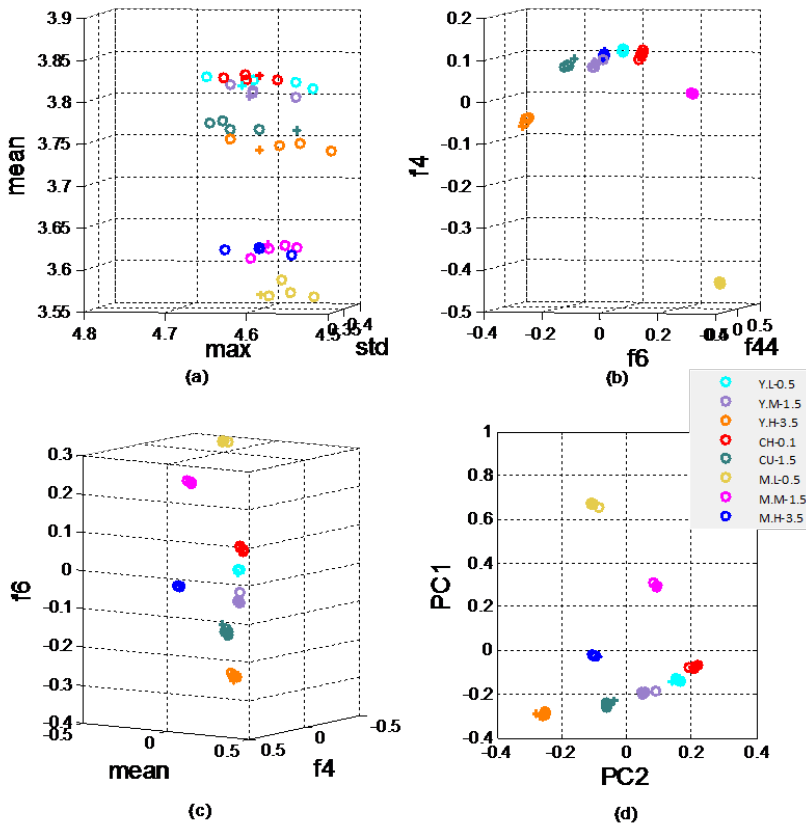


Figure C.9: (a) 3D visualisation of speckle effect features (b) 3D visualisation of the three diffusion effect selected features (c) 3D visualisation of speckle and diffusion selected features (d) 2D plot in PCA space using the first two PCs. The 'o' shows a training sample and '+' shows a test sample.

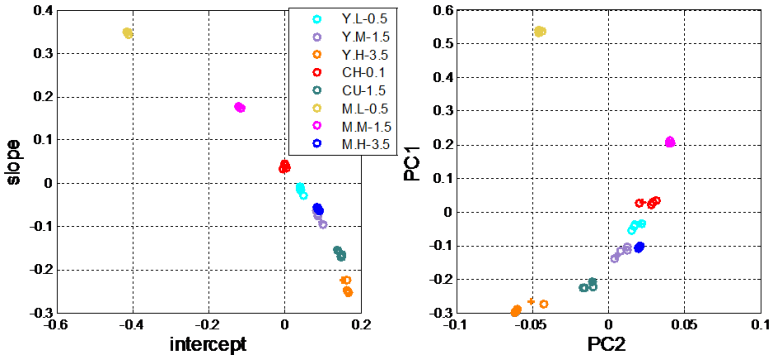


Figure C.10: 2D visualisation of the log-log model features (a) in original space (b) in PCA space.

Table C.2: The discrimination results

	Av. SVM Perf. of LOOCV	SVM Test Perf.	Sum of DPs of the selected features	Rayleigh criteria
DCT	100%	100%	2460.3	5850.6
Log-Log Model	96.87%	100%	1815.1	79.60

diffusion effect is needed, this frequency-decomposed information can be used to exclude the speckle effect as shown in Figure C.4(d), using the inverse DCT transform.

C.6 Conclusion

In this paper, a DCT-based characterisation method is introduced for diffuse reflectance images. These images result from illumination of a narrow laser beam in different wavelengths into eight different dairies. They were milks and yogurts of different types and fat levels. The low order DCT coefficient was used to characterise the low frequency light diffusion effect and the entropy information of higher order DCT coefficients were used to characterise the speckle effect in the images. The discrimination power criterion was used to reduce the number of wavelength and to select the features. The existing characterisation method based on a linear log-log model can only separate the products according to their fat levels, but the proposed method can discriminate them based on both their category (milk-yogurt) and fat level. It also improves the discrimination and removes the overlap between the classes.

APPENDIX D

Evaluation of Confocal Laser Scanning Micrographs of Stirred Yogurts Using Image Analysis

Jacob L. Skytte^a, Ovidiu Ghita^b, Paul F. Whelan^b, Ulf Andersen^c, Flemming Møller^d, Anders B. Dahl^a, Rasmus Larsen^a

^a *DTU Compute, Department of Applied Mathematics and Computer Science, Technical University of Denmark, Matematiktorvet, Building 322, DK-2800 Kgs. Lyngby, Denmark*

^b *Centre for Image Processing & Analysis, Dublin City University, Faculty of Engineering and Computing, Dublin 9, Ireland*

^c *Arla Strategic Innovation Centre, Rørdrumvej 2, DK-8220 Brabrand, Denmark*

^d *DuPont, Edwin Rahrs Vej 38, DK-8220 Brabrand, Denmark*

^e *DTU Photonics, Technical University of Denmark, Ørsteds Plads, Building 343, DK-2800 Kgs. Lyngby, Denmark*

Abstract

The microstructure of protein networks in yogurts defines important physical properties of the yogurt and hereby partly its quality. Imaging this protein network using Confocal Scanning Laser Microscopy (CSLM) has shown good results, and CSLM has become a standard measuring technique for fermented dairy products. When studying such networks, hundreds of images can be obtained, and here image analysis methods are essential for quantitative assessments. There is no standard image analysis method for CSLM images, but methods including grey level co-occurrence matrix analysis and fractal analysis have been used with success. However, a range of other image texture characterisation methods exists. Our contribution is an investigation of the choice of image analysis methods, by performing a comparative study of nine different methods. Here CSLM images from a yogurt fermentation study are investigated, where production factors including fat content, protein content, heat treatment, and incubation temperature are varied. Method evaluation is conducted by analysis of variance, classification, and cluster analysis, and our investigation reveals that there is a significant effect in choosing image texture descriptors based on frequency distribution of predefined image features (textons). Texton based methods were found to have superior performance over both grey level co-occurrence matrix descriptors and variants of fractal analysis.

D.1 Introduction

Interpretation of a large body of images requires automated image analysis techniques to ensure a quantitative assessment. In this paper we investigate the choice of the image analysis technique for studying Confocal Scanning Laser Microscopy (CSLM) images of protein networks in fermented yogurts. The CSLM image depicts a small sample area, typically of less than 1mm^2 , just under the surface of the sample. Two sampling steps are involved in the analysis. First a sample is taken from a larger yogurt container and placed on a microscope slice and then a suitable set of imaging sites are chosen. A very small part of the actual yogurt is hereby measured, and we have experienced that a relatively large variation between images can be observed. This must be accounted for in the choice of image analysis method.

CSLM has become popular in the field of dairy science within the last two decades. It has been used for studying both milk gels made from bacteria culture or glucono- δ -lactone (Lucey and Singh, 1997; Lucey et al., 1998b,a). CSLM is well suited for microstructure studies of milk gel because little sample prepa-

ration is needed. Moreover, one can use fluorescent probes to target specific compounds of interest such as bacteria, fat, and protein – here we study protein networks of casein, which is of special interest for analysing milk gels.

The main constituents of milk are protein (mainly casein), water, and fat. Through fermentation, the casein aggregates and forms a network (the gel) in which water and fat are embedded. The microstructure of this network affects the general functionality of the gel as well as the textural properties and the appearance of the gel (Lee and Lucey, 2010), which are important quality factors (Muir and Hunter, 1992).

Process parameters, such as processing temperatures and ingredient composition, can affect the microstructure of the casein network. Such effects can be seen as appearance changes in the CSLM images, like difference in interconnectivity, pore size distribution, strand thickness, and tortuosity. These characteristics are often used for describing the appearance of milk gels; see e.g. (Lucey et al., 1998a). However, such qualitative characterisations are not operational for large data sets. Instead we propose using an automated analysis technique where the micrographs are characterised using so called image descriptors. These descriptors should preferably correlate with the physical properties of the milk gel, i.e. how the consumer experiences it. In addition it should be robust to the variance introduced by the measurement procedure, while being sensitive to changes in structure.

CSLM images of casein networks can be described as image textures, which typically can be described as repetitive patterns with some degree of structure. It is therefore natural to choose image analysis methods for texture characterisation. A common texture descriptor is the fractal dimension, which describes complexity of irregular objects as a ratio of the change in detail by the change in scale (Mandelbrot, 1983). Previously there has been much emphasis on fractal analysis in regard to food structure (Barrett and Peleg, 1995). This also applies to milk gels, where fractal models have been suggested to mathematically model the kinetic behaviour of the gel formation (Horne, 1999). Fractal analysis has successfully been used to study the properties for a range of different protein gels (Hagiwara et al., 1998; Pugnali et al., 2005; Dàvila et al., 2007; Dàvila and Parés, 2007; Kuhn et al., 2010; Torres et al., 2012). Nonetheless, Pugnali et al. (2005) recognised that while the fractal dimension can be a sensitive descriptor it is not unique. Consequently clearly different structures can have same fractal dimension, making the validity of fractal analysis problem dependent. Thus, Pugnali et al. (2005), Dàvila et al. (2007), and Dàvila and Parés (2007) applies fractal analysis in conjunction with other morphological measures such as pore size distribution and lacunarity. The latter can be seen as a measure of inhomogeneity.

In the wake of the popularity of fractal analysis, a lot of methods for estimating the fractal dimension have been proposed. Soille and Rivest (1996) and Lopes and Betrouni (2009) provide insightful overviews of fractal analysis for images, and Lopes and Betrouni (2009) also covers the field of multi fractal analysis. This is a generalisation of fractal analysis where a single fractal dimension is not sufficient to describe the dynamics of the system; hence a spectrum of fractal dimensions is estimated.

In terms of texture classification, fractals have some nice properties like invariance towards affine and perspective transformations, which was illustrated in Xu et al. (2006). Nevertheless, Varma and Garg (2007) state that while both fractal and multi-fractal analysis have been investigated for texture classification, they are often lagging behind the state-of-the-art classifiers primarily for two reasons. Firstly to the non-uniqueness of the fractal dimension, and secondly that fractal dimension is often computed globally for an image. Multiple studies in material classification (Leung and Malik, 2001; Hayman et al., 2004; Varma and Zisserman, 2005; Caputo et al., 2005) suggest that such image textures are best discriminated using statistical distributions of textons. Textons are prototypical image features found throughout an entire data set. For an image all features are individually assigned to the most similar texton, and the image descriptor is then defined by the frequency distribution of texton occurrences. Another widely used texture characterisation is the grey level co-occurrence matrix, which has been used for texture characterisation including food analysis (Zheng et al., 2006).

With the aim of quantifying the microstructure of milk gels, we compare a set of image descriptors, originating from general texture classification, but based on different design principles. These are compared to common fractal analysis as well as a state-of-the-art fractal based image descriptor. Our investigation is based on a fermentation study where we have varied the fat and protein content and heat treatment and incubation temperatures – factors that are expected to influence the formation of the casein network. Furthermore, the study was repeated over three consecutive days. Our expectation is that a well-behaved image descriptor will enable a classification of the micrograms to the categories defined by our experiment. There might, however, be some misclassifications if the treatment does not result in pronounced structural changes.

We also aim at using the image descriptors to determine the significance of the experimental factors. Stand-alone fractal analysis can easily be carried over to an analysis of variance framework, as it outputs a single numerical value. However, this is not usually the case for the other investigated image descriptors, where the output is often a multi-dimensional vector. If the number of observations is small compared to the vector dimensionality, this can potentially lead to a lack of degrees of freedom in a multivariate analysis of variance framework.

Instead we represent the image descriptors by mutual distances. Thus, we can transfer the image descriptors to a similar, albeit non-parametric framework (Anderson, 2001). Also, data with a high order of dimensionality is typically difficult to interpret in its original form. Therefore, we also use the distance representation to form a hierarchical representation of the data, which is well suited for visual interpretation.

D.2 Materials and Methods

D.2.1 Experimental Design

A triple replicated 2^4 experimental design was used to create the different milk gel formulas. The four factors spanned fat and protein content, and pre-heat treatment and incubation temperature. An overview of the experimental design and the factor levels is shown in Table D.1. All formulas were prepared in 1 litre batches, and the three replicates were created on three consecutive days. Systematic day-to-day variation was expected, and this nuisance factor was eliminated by incorporating the days as a block in the experimental design (Montgomery, 2005).

The fat content was varied using homogenised UHT semi-skimmed and whole milk for the low and high level respectively. Protein content was changed by adding 3% (w/w) skimmed-milk powder (*Lactalis Ingredients, Bourgbarré, France*) in the high factor level. Pre-heat treatment was performed using an autoclave (Systec V-Series, Holm & Halby, Brøndby, Denmark). Immediately after pre-heat treatment the samples were put into a cold-water bath until next day. The following day the samples were heated to their target incubation temperature in water baths (*Lauda Ecoline E100, Lauda Dr. R. Wobser GmbH & Co. Kg, Lauda-Königshofen, Germany*), and hereafter inoculated with a yogurt bacterial culture (*YO-MIX 863, DuPont Danisco Range, Copenhagen, Denmark*). The pH development was measured every 5 minutes (*CINAC pH Controller, Ysebaert Dairy Division, Frepillon, France*). When a sample reached pH 4.6 it was stirred and stored at 5°C in a plastic container for a week.

D.2.2 Confocal Laser Scanning Microscopy

All micrographs were captured using a Leica DM IRE2 confocal scanning laser microscope (*Leica Microsystems, Heidelberg, Germany*). Before microscopy the

Table D.1: The 2^4 experimental design. Minus and plus denote low and high factor levels respectively. The actual factor level values are given in the left most column. The entire design is replicated across three days. The subsets will be referred to in Section D.3.

	Subset 1				Subset 2				Subset 3				Subset 4			
	1	2	3	4	5	6	7	8	9	10	11	12	13	14	15	16
Fat content [1.5/3.5 g/100g]	-	-	-	-	-	-	-	-	+	+	+	+	+	+	+	+
Protein content [3.4/4.4 g/100g]	-	-	-	-	+	+	+	+	-	-	-	-	+	+	+	+
Pre-heat treat. [75/90 °C/15min]	-	-	+	+	-	-	+	+	-	-	+	+	-	-	+	+
Incubation temp. [39/43 °C]	-	+	-	+	-	+	-	+	-	+	-	+	-	+	-	+

yogurts were stirred gently. Protein was stained using a FITC (fluorescein-5-isothiocyanate) solution (2g/litre) in acetone, which was applied to a microscope slide. The slide rested until the acetone had evaporated, and yogurt was applied to the slide, and rested for 15 minutes at room temperature. Sample micrographs were captured using a 40× oil immersion objective (40× *HXC PL Apo 1.25 Oil*), and FITC was excited at 488nm using an Ar/Kr laser, and the emitted signal was collected from 503 to 533nm at a depth of 7µm into the sample. To eliminate bias in the data acquisition the CSLM images were randomly sampled, however major artefacts such as air pockets were avoided. The images were captured at resolution 1024 × 1024 pixels, and each images covered an area of 375 × 375µm. The pixel intensities are mainly affected by the focus and the amount of protein present at the given pixel. During recording each image line was captured four times and averaged to reduce noise. 10 images were recorded for each yogurt sample, making a total of 480 micrographs.

Examples of micrographs from each of the samples in Table D.1 can be seen in Figure D.1. These examples have been chosen as the median image from each sample defined by the best overall performing method in Section D.3.3. The examples in Figure D.1 indicate that an increase in both protein and fat content generally increases the coverage of the protein network. The influence from fat is due to the homogenised fat globules being covered by a layer of casein (Yildiz, 2010). This way they become an integral part of protein network. The influence of changing the protein content is straightforward.

Changes to pre-heat treatment and incubation temperature results in more subtle changes to the images. Higher pre-heat treatment temperatures results in more willing casein fusions, leading to more interconnected and dense gel net-

works (Lucey et al., 1999). Incubation temperature affects the speed of the gel formation. Lower temperatures result in lower gel formation speeds, which again produce more interconnected and dense gels (Lee and Lucey, 2004).

D.2.3 Image Pre-Processing

D.2.3.1 Image Normalisation

The pixel intensities in the micrographs correspond to the combined response from the local protein content, dye concentration, and focus. Thus, comparisons between pixel intensities across the entire data set may not be meaningful unless we apply image normalisation. We normalise the images to have zero mean and unit variance.

D.2.3.2 Gel Segmentation

A typical pre-processing step when assessing protein gel micrographs is to segment out the gel structures. In this paper this gel segmentation is used for the box counting method in Section D.2.4.2. However, the segmentation could also be used to extract morphological descriptors. We will not consider such descriptors in this paper.

As seen in Figure D.1, the CSLM images contain two major region types: regions with in-focus light (the gel) and regions with out-of-focus light (the pores). Naturally the out-of-focus light produces areas with low intensity and low signal-to-noise ratio. Usually, the gel network and pores are segmented by applying a threshold on the pixel intensities. However, the pixel intensities in CSLM images of protein gels are typically not of bimodal type (Mellema et al., 2000; Pugnali et al., 2005), which complicates the identification of a suitable threshold.

Looking at Figure D.1, three major regions can be identified in the images: the internal pore structure, the casein gel, and the transitions between these regions. We propose to use three convolutions that capture the uniqueness of the three different regions. A mean filter and a local entropy estimate is used to distinguish between the intensity and uniformity of the gel and pore regions respectively, and a local skewness estimate is used to detect region transitions. In order to segment out the different regions, the three-dimensional image representation was used as input for a Gaussian Mixture Model (Hastie et al., 2009) with three clusters (one for each image region).

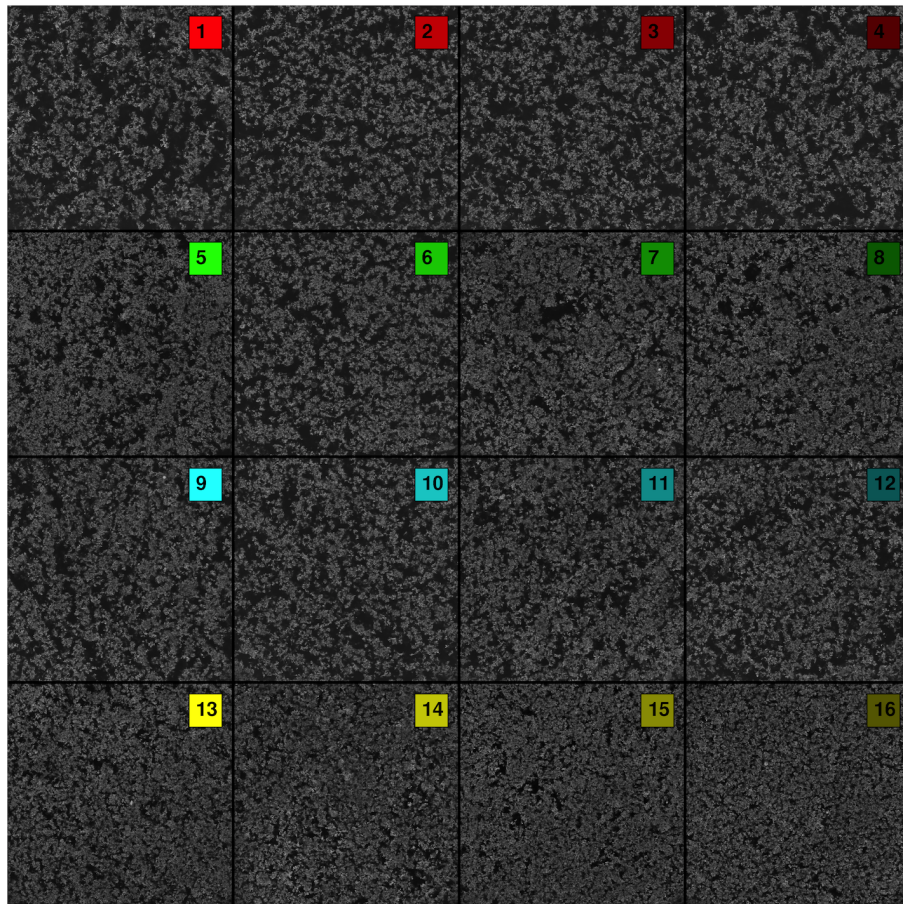


Figure D.1: Examples of the 16 different yogurt samples from a single replicate. The numbering corresponds to that of Table D.1.

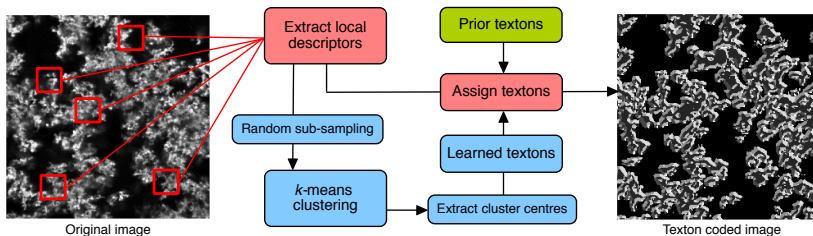


Figure D.2: The applied pipeline for the texton approach. Local descriptors are extracted from the original images, and can be extracted densely or at specific key points. Each descriptor is assigned a texton from a prior or a learned set of textons. The texton coded image is made from densely sampled descriptors, which have been assigned one of eight textons.

D.2.4 Image Descriptors

A broad range of image descriptors are presented below. In Sections D.2.4.1 through D.2.4.3 we consider some classical image descriptors and in D.2.4.4 through D.2.4.8 we consider the image descriptors based on the texton approach, which is well suited for classifying image textures (Leung and Malik, 2001; Hayman et al., 2004; Varma and Zisserman, 2005; Caputo et al., 2005). The texton approach was initially proposed by Julesz (1981) and the main idea is to extract local descriptors from each image and assign each descriptor to a set of predetermined descriptors (denoted textons). The final image descriptor is a normalised frequency histogram of the textons. Furthermore, local descriptors can be extracted from all pixel locations (dense sampling), or only at specific key points of interest. In summary, textons can be seen as a dictionary of reoccurring image structures. Assigning each local descriptor to a texton can also be seen as a way of suppressing potential noise in the local descriptors.

For the methods in Sections D.2.4.4 and D.2.4.5 the textons are defined a priori by the method, but for the methods in Sections D.2.4.6 through D.2.4.8 the textons have to be learned from the data set. This can be done by randomly sampling local descriptors from the entire data set (denoted training data), and perform a k -means clustering on the training data. The k cluster centres hereafter comprises the textons. The texton pipeline is illustrated in Figure D.2.

Looking at the microstructure in Figure D.1, no distinct orientation of the structures can be seen. Thus, the image descriptor should preferably not be dependent on the direction of a given feature; that is, it should be rotation invariant. Furthermore, as suggested by Møller et al. (2013) the protein gels should also be

considered at different scales for a more complete description. Table D.2 gives an overview of the investigated image descriptors and their general features.

All methods mentioned in this section have one or more free parameters that can be chosen by the user. In most cases these parameters greatly affects the performance of the method and must be chosen carefully. Specifically for the methods following the texton approach (without prior textons), the amount of training data and the number of desired textons should be decided.

D.2.4.1 Intensity Histogram

This image descriptor is a histogram where each bin corresponds to a pixel intensity in the image. The number of histogram bins can be varied by uniformly downsampling the dynamic range of the pixel intensities.

D.2.4.2 Fractal Dimension

While there are many approaches to fractal analysis, most methods follows the same basic approach (Lopes and Betrouni, 2009). First some image quantity, $N(r)$, is measured at different scales or step sizes, r . For true fractal scaling these quantities can be related by a power law behaviour:

$$N(r) \propto c \cdot r^D, \tag{D.1}$$

where D is the fractal dimension and c is a constant. This expression is then linearised through a log-transformation:

$$\log(N(r)) = D \log(r) + \log(c), \tag{D.2}$$

and the fractal dimension can be estimated by the slope. For real world data, the log-transformed response may not show perfect fractal scaling (linear behaviour) across all values of r . Thus, it is important to select the appropriate fractal range of r for estimating D . (Varma and Garg, 2007) suggested to also include the intercept in Equation (D.2) as discriminative property, to alleviate the problem of the non-uniqueness of the fractal dimension. They denote it the *fractal length*. We will present results for using the fractal dimension alone and with the fractal length as well. The fractal length is also used for the method in Section D.2.4.8.

Table D.2: Overview of investigated image texture descriptors.

Descriptor name	Texoton approach	Dense	Rotational invariant	Multi scale
Intensity histograms	yes (w. prior set)	yes	yes	no
Fractal (box count)	no	yes	yes	no
Fractal (variogram)	no	yes	yes	no
GLCM	no	yes	yes	Gaussian pyramid
LBP	yes (w. prior set)	yes	yes	Gaussian pyramid
BIF	yes (w. prior set)	yes	yes	Gaussian derivative filters
SIFT	yes (w. training)	no	yes	Laplacian pyramid
Image patches	yes (w. training)	yes	no	no
Local fractal features	yes (w. training)	yes	yes	MR8 filter bank

GLCM = Grey Level Co-occurrence Matrices, **LBP** = Local Binary Pattern, **BIF** = Basic Image Features, **SIFT** = Scale Invariant Feature Transform

In this paper we apply two different approaches to fractal analysis. First is the box counting method, which is the most popular and frequently used type of fractal analysis (Lopes and Betrouni, 2009). Following the notations in Equation (D.1) and (D.2), boxes with side length r are placed on a binary image, and $N(r)$ corresponds to the number of boxes that sample the gel structure. In the second approach we look at the spatial autocorrelation modelled through semivariograms. For an image the semivariogram is estimated by

$$\gamma(h) = \frac{1}{2}E [(I(\mathbf{x}) - I(\mathbf{x} + h))^2], \quad (\text{D.3})$$

where $I(\mathbf{x})$ is the pixel intensity at image coordinate \mathbf{x} , and h is a displacement. Again, we can relate back to power law behaviour of equation (D.1) such that $\gamma(h)$ and h correspond to $N(r)$ and r respectively. A similar approach was used by Pugnali et al. (2005). It should be clarified that we are estimating a fractal parameter for the image and not the actual fractal dimension of the protein gel itself.

D.2.4.3 Grey Level Co-occurrence Matrices

Grey Level Co-occurrence Matrix (GLCM) is a well-established method introduced by Haralick et al. (1973). The GLCM expresses the probability of a given grey level intensity change between two pixels distanced by a displacement, h , and an angle ϕ . Let (i, j) denote the pixel intensities, then a GLCM, c is defined by $c = P((i, j)|h, \phi)$. An example is given in Figure D.3. Thereby, the number of grey level intensities in the image defines the dimensionality of a GLCM. Typically the image intensities are downsampled. We use a uniform downsampling of the grey level intensities, but other schemes may also be considered (Soh and Tsatsoulis, 1999). The properties of the GLCM are commonly quantified by statistical measures, and Haralick et al. (1973) propose 14 different of such measures, which we also apply.

When creating the GLCM, multiple angles and displacements can be considered. Due to the lack of direction of the protein structures, we pool the directional information by averaging the GLCM over multiple angles ($0, 45, 90, 135^\circ$) as done in (Soh and Tsatsoulis, 1999). In terms of selecting appropriate displacements, Møller et al. (2013) suggest using a single displacement at different scale representations of the image following the work by Roberti de Siqueira et al. (2013). To generate different scale representations Gaussian pyramids are created by sequentially smoothing and downsampling (by a factor 2) in the original image for each level of the pyramid (Lindeberg, 1994). Level 0 in the pyramid

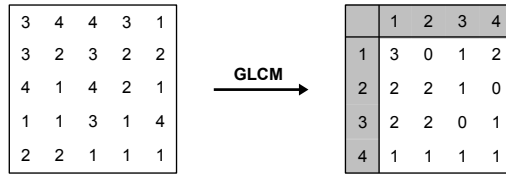


Figure D.3: The Grey Level Co-occurrence Matrix (GLCM) calculated for a 5×5 image with four grey level intensities. $h = 1$ and $\phi = 0^\circ$.

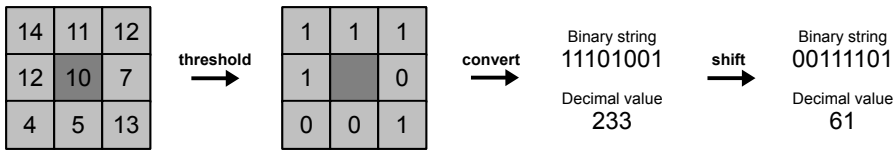


Figure D.4: Local binary pattern (LBP) calculated for 3×3 neighbourhood ($R = 1$, $P = 8$). First the neighbourhood is thresholded according to the centre value, and hereafter the thresholded neighbourhood is converted to a binary string. To obtain a rotation invariant description of the neighbourhood, the binary string is shifted to obtain the smallest possible decimal value.

corresponds to the original image. Thus, the GLCM can be created at different image scales, and the final image descriptor is the joint distribution of the quantified GLCM across multiple scales.

D.2.4.4 Local Binary Patterns

Ojala et al. (2002) introduced the Local Binary Patterns (LBP) for texture analysis. Here a circular neighbourhood of radius, R , and P pixels is investigated for each pixel in the image. A local descriptor is defined by measuring the intensity difference between a pixel and its neighbourhood. Negative differences are assigned 0, and positive differences are assigned 1. This results in a binary string (or pattern) with a length equal to the amount of pixels in the neighbourhood. Rotational invariance is obtained by shifting each binary pattern to get the minimum value. An example of the LBP descriptor is shown in Figure D.4. Ojala et al. (2002) note that some pattern occurrences are generally more discriminative and they proposed only considering a subset of so-called uniform

patterns. The LBP image descriptor is a histogram over the occurrences of all binary patterns in the image. As with the GLCM in Section D.2.4.3 a similar multi scale approach using Gaussian pyramids is adopted (Qian et al., 2011). Thus, the final image descriptor is the joint distribution of LBP histograms across multiple scales.

D.2.4.5 Basic Image Features

The Basic Image Features (BIF) descriptor was introduced by Crosier and Griffin (2008). This descriptor detects how local image structures change across scales. At first, six Gaussian derivative filters (from zeroth-order to second-order) are applied to the image. From the filter responses each pixel is assigned one of six BIFs corresponding to *bright/dark blobs*, *slopes*, *bright/dark lines*, and *saddle points*. The BIFs are then assigned across multiple scales defined by the width of the Gaussian derivative filters. An example is shown in Figure D.5. Crosier and Griffin (2008) empirically found that four logarithmic distributed scales were appropriate. That is σ , 2σ , 4σ , and 8σ , where σ is the standard deviation of the Gaussian filters. The final image descriptor is constructed by considering how the BIF of each pixel changes across the four scales. This results in a frequency histogram with $6^4 = 1296$ bins.

D.2.4.6 Scale Invariant Feature Transform

After being introduced by Lowe (1999), the Scale Invariant Feature Transform (SIFT) has become a popular tool in the field of object recognition. This method detects stable key points in an image and provides a local description of the surrounding area for each key point. The key points of interest are bright/dark blobs found across multiple scales using a difference of Gaussian pyramid (Lindeberg, 1994). Thresholds can be applied to remove weak contrast blobs and blobs located on edges. For each key point a local descriptor is defined on a 4×4 grid of locations (based on the orientation and scale in which the key point was found), where each location contains a histogram of the local gradient magnitudes in 8 orientations. This makes for a local key point description of $4 \times 4 \times 8 = 128$ dimensions, that is both scale and rotation invariant.

The method and all parameters are adopted directly from Lowe (2004). This results in between 6000-8000 key points being found in each micrograph (denser gels have more key points). The texton approach with training is used to make the final image descriptor.

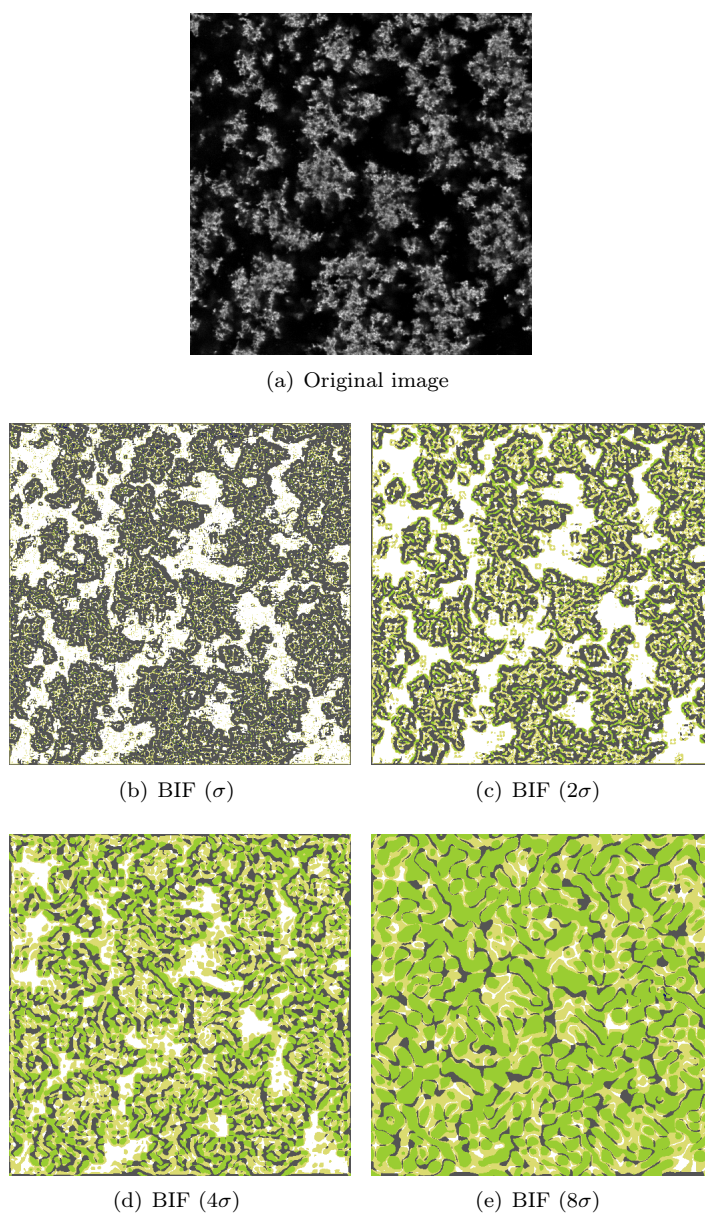


Figure D.5: The Basic Image Features (BIF) extracted at four different scales. The BIFs extracted from the original image are slopes (grey), bright blobs (white), bright lines (yellow), and saddle points (green). $\sigma = 1$ was used for the width of the Gaussian derivative filters.

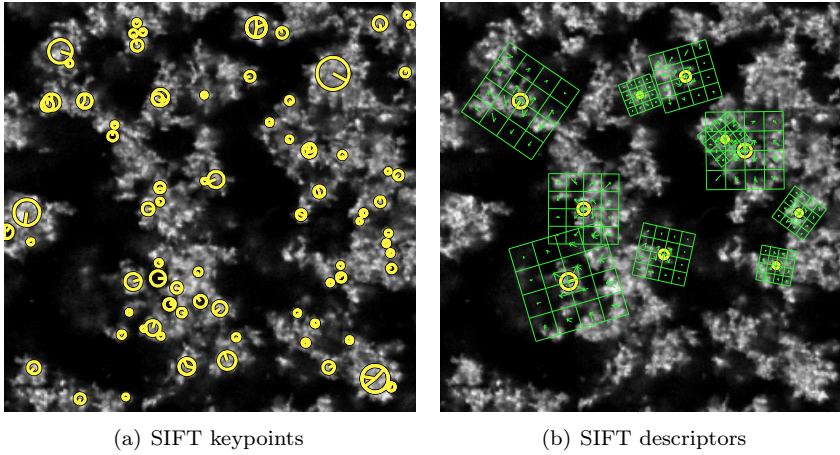


Figure D.6: Two steps from Scale Invariant Feature Transform (SIFT). (a) shows 100 random key points (corresponding to blobs) found in the image. The size of the circle corresponds to the scale of the blob and the pin shows the orientation. (b) shows descriptors for ten of the random key points in (a). As depicted, the descriptor is made from a 4×4 grid, and for each grid space the gradient magnitude is calculated for eight orientations. The size of the grid is determined by the blob scale.

D.2.4.7 Image Patches

Varma and Zisserman (2009) showed that the use of image patches, as local features for the texton approach, can be an efficient way of discriminating different materials. Image patches are extracted at each pixel location. From a patch of size $n \times n$ pixels, a n^2 -dimensional local descriptor is defined as the joint distribution of pixels intensities. Each descriptor is contrast normalised by: $p \leftarrow p[\log(1 + L(p)/0.03)]/L(p)$, where p is the local descriptor and $L(p) = \|p\|_2$ is the Euclidean norm of p , which has empirically been determined to give better discrimination. The texton approach with training is used for creating the final image descriptor. An example of a texton dictionary based on image patches is shown in Figure D.7.

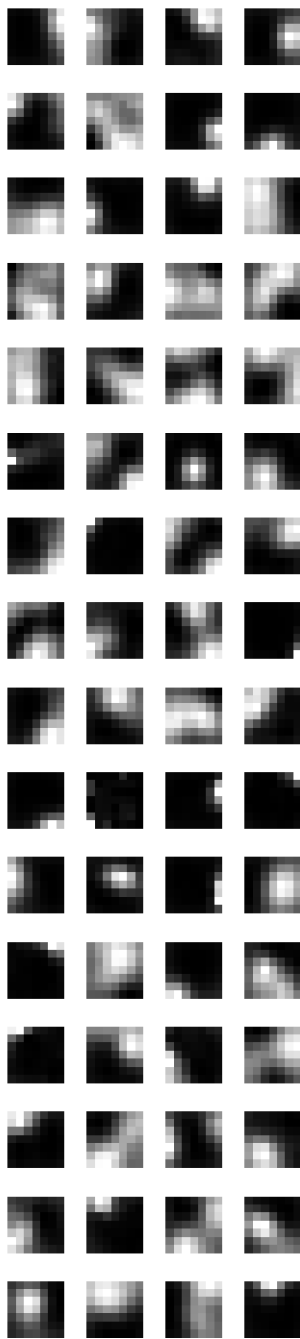


Figure D.7: An example of texton dictionary for 7×7 image patches. The 64 textons are learned from the entire data set where 1000 random descriptors were extracted from each image.

D.2.4.8 Local Fractal Features

Rather than estimating the fractal dimension for the entire image, Varma and Garg (2007) proposed to estimate the fractal dimension locally. Let $N(x, r) = \sum I(\mathbf{x}, r)$, where $I(\mathbf{x}, r)$ are the pixel intensities within a closed disc of radius, r , at image coordinate, \mathbf{x} . Varma and Garg (2007) hypothesised that $N(x, r)$ follows the power behaviour of Equation (D.1), from which the fractal dimension can be estimated from the slope in Equation (D.2). Furthermore, they also add the intercept to the image descriptor and denotes it the fractal length. As discussed in Section D.2.4.2 the fractal range in which the fractal parameters are estimated has to be determined. To accommodate rotation invariance and a multi scale representation, the MR8 filter bank (Varma and Zisserman, 2005) is applied to the image. This results in eight representations of the original image. For each representation the fractal dimension and fractal length are estimated at each pixel location, thus a 16-dimensional local descriptor is obtained. As in section D.2.4.7, each descriptor is contrast normalised. The texton approach with a training step is used for creating the final image descriptor.

D.2.5 Method Evaluation

This section describes three ways of evaluating and interpreting the image descriptors presented in Section D.2.4. The dimensionality of the image descriptor for each method and details about each descriptor will be provided in Section D.3.2. A fair way of comparing descriptors of different dimensionality is to make comparisons based on the distances between image descriptors. When comparing histograms, a suitable distance measure is the χ^2 distance (Malik et al., 1999; Press et al., 2007):

$$\chi^2(H^1, H^2) = \sum_i \frac{(H_i^1 - H_i^2)^2}{(H_i^1 + H_i^2)}, \quad (\text{D.4})$$

where H^i are the histograms, and i denotes the bin. This way the pairwise difference between each bin is weighed by the numerical size of the bins. As a result, large and small bins are treated more equally. This distance measure is commonly used for texton frequency histograms in general (Malik et al., 1999; Leung and Malik, 2001; Varma and Zisserman, 2005). We also found this distance measure suitable for the non-histogram image descriptors used by fractal analysis and GLCM. Thus, all methods in this section evaluate and compare the image descriptors based on the χ^2 distance.

D.2.5.1 Nearest Neighbour Classification

The nearest neighbourhood classifier is a popular evaluation method within the field of texture classification (Leung and Malik, 2001; Cula and Dana, 2004; Varma and Zisserman, 2005, 2009). First the data is randomly split into training and test data (9 training samples, and 1 test sample in each each class). Hereafter, each observation in the test data is classified as the distance-wise closest observation in the training data. Multiple random splits of the data set are performed to give a statistical distribution of the classification rates.

D.2.5.2 Non-Parametric Multivariate Analysis of Variance

Within the analysis of variance (ANOVA) framework, multidimensional response variables (image descriptors in this case) are typically handled using multivariate analysis of variance (MANOVA). As will be seen in Table D.3, the dimensionality of the image descriptors will be as large as 1296. Considering the data set presented in Section D.2.1, this means that there is too few observations in order for the covariance matrices to be estimated in a feasible manner and an alternative approach is needed. Such an alternative, denoted non-parametric multivariate analysis of variance (NPMANOVA), was proposed by Anderson (2001).

Here, the high dimensionality is handled by representing the multidimensional response vectors as a $N \times N$ distance matrix containing the pairwise mutual distances between observations. As a trade-off this distance representation discards any information regarding the covariant structures in the data. From the distance matrix the total variability can be partitioned by considering the mutual distances between observations rather than using the traditional sum of squares. A pseudo F-statistic can hereafter be calculated through permutation tests.

Contrary to ANOVA, NPMANOVA does not assume normality and is not necessarily based on Euclidean distances. However, similar to ANOVA, a major assumption for the NPMANOVA is equal variance across groups in the experimental design. This can be validated through a generalised version of Levene's test (Anderson, 2006).

D.2.5.3 Hierarchical Clustering

Hierarchical clustering is an unsupervised clustering method, which uses the interpoint distances to define a hierarchical ordering of the data. The clustering is typically done in a bottom-up fashion, meaning that each data point initially comprises a cluster and hereafter most similar clusters are greedily merged. Similarity is defined in terms of a link function (Hastie et al., 2009). We use the group average link function in which similarity is determined by the average similarity between all members in the considered clusters. The final hierarchical structure can be presented as dendrograms.

D.3 Results

D.3.1 Gel Segmentation

For the gel segmentation, we found filter sizes of 5×5 to be appropriate, for the mean, skewness, and entropy filters. Segmentation results for two of the samples are shown in Figure D.8. The segmentations successfully segment out the protein, the pores, and the transitions between the two regions. Additionally the segmentations are found to be smooth. However, there seem to be a tendency of overestimating the transitions between pore and protein regions, resulting in transitions being favoured more than the pores. This is most likely related to the deepness of the pores. Some pores are deep and thereby is represented by out-of-focus light, whereas some less deep pores will have light that is more in focus, thus creating structures similar to transitions. However, we found this to be of little importance, as we are only concerned with the segmentation of the protein, used for the box counting method in Section D.2.4.2.

D.3.2 Parameter Selection

The parameters for the methods in Section D.2.4 were chosen such that the method achieved the best possible correct classification in the nearest neighbour classifier. To limit the parameter space substantially, the parameter search in some cases was only considered for dyadic intervals. The rest of the parameters have been investigated in a fairly dense manner. Table D.3 summarises the chosen parameters.

A couple of observation can be made. In general most methods favour low

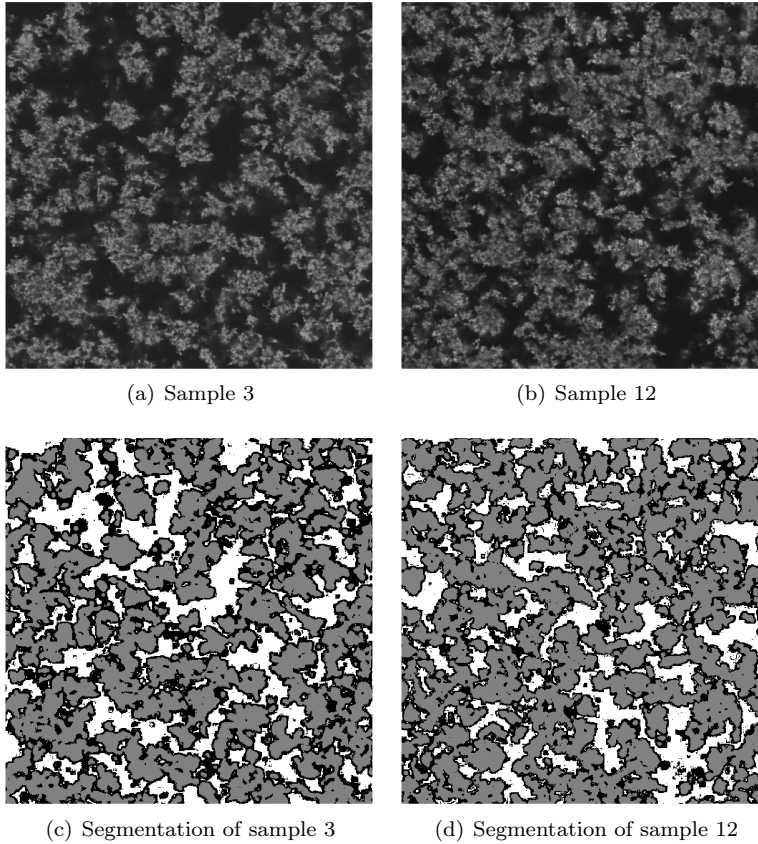


Figure D.8: Segmentation examples. White denotes pores, grey denotes protein, and black denotes transitions between pores and protein. These examples correspond to closeup views of sample 3 and 12 from Figure D.1.

spatial support, e.g. the best displacement for the variogram in fractal analysis was 6 pixels and the optimal patch size for image patch exemplars was 7×7 pixels. However, both LBP and GLCM successfully utilise multiple levels in the Gaussian pyramid, which can be seen as an increase in spatial support. LBP consistently favoured one or more levels in the Gaussian pyramid in addition to the original image. Also, while the chosen standard deviation for the basic image features seems small, the largest scale at 8σ corresponds to Gaussian filters with relative large support ($\approx 40 \times 40$ pixels). Thereby, both LBP and basic image features successfully exploit greater spatial support when describing the micrographs.

Looking at the texton approaches where textons are learned through training, only a limited amount of textons are needed in order to provide a feasible description. This makes sense considering both the inter and intra similarity between the images of different casein gel. However, image patch exemplars use twice as many textons compared to the methods with SIFT and local fractal features. This may be explained by the lack of rotation invariance of the image patches, i.e. multiple patches are needed to describe multiple rotations of the same structure. The limited amount of unique image structures is further emphasised when looking at the methods covering intensity histograms or GLCM. Here a uniform down sampling of the pixel intensity range is performed, and down sampled intensity ranges gave better discrimination of the casein gels.

Table D.3: Summary of the considered tuning parameters for each of the image descriptors. It is not a complete list of the parameters associated with each method. Some parameters have been selected a priori c.f. Section D.2.4. * denotes that the parameter search has been performed in a dyadic interval. ¹Only the estimate of the fractal dimension is considered. ²Both estimates of fractal dimension and fractal length are considered.

Descriptor name	Parameter descriptions	Parameter values	Dimensionality
Intensity histograms	Number of histogram bins*	16	16
Fractal (box count) ¹	Fractal range, box side lengths (r)*	[1, 16] pixels	1
Fractal (box count) ²	Fractal range, box side lengths (r)*	[1, 4] pixels	2
Fractal (variogram) ¹	Fractal range, variogram displacement (h)	[1, 4] pixels	1
Fractal (variogram) ²	Fractal range, variogram displacement (h)	[1, 6] pixels	2
GLCM	Levels in Gaussian pyramid	[0, 6]	154
	Number of grey level intensities*	32	
	Displacement (h)	1 pixel	
LBP	Levels in the Gaussian pyramid	[0, 3]	144
	Binary pattern type	rotation invariant	
	Radius (R)	2 pixels	
	Number of sample points (P)	8	
BIF	Gaussian filter standard deviation (σ)	0.8	1296
SIFT	Training data from each image*	≈ 7000	64
	Number of textons*	64	
Image patches	Patch size	7×7 pixels	128
	Training data from each image*	1000	
	Number of textons*	128	
Local fractal features	Fractal range, disc radius (r)	[1, 5] pixels	64
	Training data from each image*	1000	
	Number of textons*	64	

GLCM = Grey Level Co-occurrence Matrices, **LBP** = Local Binary Pattern, **BIF** = Basic Image Features, **SIFT** = Scale Invariant Feature Transform

D.3.3 Nearest Neighbour Classification

The results for the nearest neighbour classification are presented in Table D.4. They are calculated based on 1000 random splits of the data, and averaged over the three blocks in the experimental design. Overall correct classification rates using all 16 samples are presented as well as smaller experiments using only subsets of the data set. Finally, classification rates are also given in an experiment where we create supersets of the previous subsets, i.e. sample 1-4 comprises one class etc. The subsets are used to closely investigate the discrimination of the subtle changes made by pre-heat treatment and incubation temperature. The supersets are used to investigate discrimination between different fat and protein compositions.

Looking at the overall classification rates, the image patch method is the best performer closely followed by the basic image features. In general the texton methods appears to be the best performers. Also, it can be seen that adding the fractal length to the fractal analysis increases the discriminative power in case of both the box counting and the variogram method. One important issue to note is the standard deviations are high, immediately suggesting that the methods are not performing significantly different. However, the standard deviations are often comparable in size across the methods hinting that they, at least to some degree, can be explained by data variation. Referring to Figure D.1 this can be further emphasised due to the potential appearance overlap of the different image samples. The standard deviations are even higher when considering the subsets or grouped subsets, likely due to misclassifications having higher impact on each random split, when fewer groups are considered.

From the subsets it can be seen that the subtle changes to the gel are easier to detect when the gel structure is dense. Subset 1 has the lowest correct classification rates, whereas subsets 2 and 3 have higher classification rates and are generally comparable. The highest classification rates are found at subset 4 where the gel is most dense. Also, differences in classification rates between non-texton and texton methods become more pronounced as the gel density increases. SIFT has the greatest increase in classification rates when going from subset 2 and 3 to subset 4. Again this can probably be contributed to the density of the gels, as SIFT finds more key points in the dense gels. The decrease in performance for sparser gels can also be explained by the fact that the textures in these gel structures are more inhomogeneous than the textures in denser gels (see images in Figure D.1). This can be a problem as a single image may not contain a representative description of the sample, and two images of the same sample can potentially be very different.

When considering the superset, where each sample is classified into subset 1

through 4, we see large performance increases for all methods. This is especially noticeable in the classification results for intensity histograms, which see a large performance increase as the amount of protein is the main changing factor across the subsets, which directly affects the pixel intensity distribution. In summary the texton approaches seem to be well suited for discriminating between the microstructure of the different samples, with the best performer being the image patch approach. While fractal analysis is outperformed by the texton methods it is still a strong competitor to the more complex GLCM approach, which additionally utilises the multiple scales.

Table D.4: The average correct classification rates plus/minus one standard deviation for the different image descriptors. Classification rates are given for the entire data set, for subsets, and for a superset in which the subsets have been grouped. ¹Only the estimate of the fractal dimension is considered. ²Both estimates of fractal dimension and fractal length are considered.

Descriptor name	Entire data set	Subset 1 sample 1-4	Subset 2 sample 5-8	Subset 3 sample 9-12	Subset 4 sample 13-16	Superset subset 1-4
Intensity histogram	39.0 ± 10.8	44.3 ± 22.7	51.8 ± 22.4	50.6 ± 21.0	59.0 ± 22.1	74.5 ± 20.7
Fractal (box count) ¹	22.1 ± 09.2	28.5 ± 18.4	43.9 ± 23.1	50.5 ± 22.5	55.7 ± 21.6	54.0 ± 22.8
Fractal (box count) ²	35.9 ± 10.4	38.0 ± 21.1	56.0 ± 22.6	51.5 ± 21.4	66.5 ± 20.8	68.8 ± 21.9
Fractal (variogram) ¹	36.4 ± 10.4	53.6 ± 20.6	76.5 ± 17.4	56.5 ± 20.0	73.1 ± 19.2	50.7 ± 24.6
Fractal (variogram) ²	44.2 ± 10.7	57.5 ± 20.9	69.3 ± 20.4	65.5 ± 20.3	78.6 ± 18.2	62.5 ± 22.5
GLCM	48.8 ± 11.0	50.1 ± 22.4	58.4 ± 22.1	64.2 ± 21.1	76.6 ± 19.1	76.1 ± 19.8
LBP	58.1 ± 10.4	50.0 ± 21.5	71.5 ± 20.2	74.1 ± 20.2	89.8 ± 13.4	80.3 ± 18.6
BIF	69.5 ± 10.4	61.6 ± 22.3	73.3 ± 19.9	72.8 ± 20.1	90.2 ± 14.4	92.0 ± 12.9
SIFT	56.9 ± 10.7	47.8 ± 21.5	62.5 ± 21.9	64.7 ± 21.3	85.2 ± 16.5	83.6 ± 17.8
Image patch	71.7 ± 10.3	60.9 ± 22.3	76.7 ± 19.4	82.5 ± 18.4	94.0 ± 10.8	90.8 ± 13.9
Local fractal features	65.3 ± 10.6	60.4 ± 21.9	73.4 ± 20.1	76.9 ± 17.8	81.4 ± 18.2	88.5 ± 14.8

GLCM = Grey Level Co-occurrence Matrices, LBP = Local Binary Pattern, BIF = Basic Image Features,
SIFT = Scale Invariant Feature Transform

D.3.4 Non-Parametric Multivariate Analysis of Variance

Table D.5 presents the results for the NPMANOVA. The blocking of the replicates was also included in the analysis as the factor *Day*. The test for equal variance among samples within each of the three replicates is also included. For both analyses a square root transformation of the data was used to suppress some of the data variance.

It can be seen that all methods agree that each of the factors in the experimental design are significantly changing the appearance of the protein network in the micrographs. Also, most image descriptors find "day" to be significant, meaning there is a significant day-to-day variation between the samples, which can be expected when working with bacteria cultures. Looking at the test for equal variances, most methods show significant differences in variance across factor groups within one or two of the replicates. This can be a problem as a difference in group variance can lead to falsely detecting significant changes in group means (Anderson, 2001). Thus, the results from the NPMANOVA should be treated with some degree of caution, when considering the methods that show significant differences in variance between factor groups.

Table D.5: The p -values for the NPMANOVA, the blocking of the three replicates is included as the factor *Day*. The table also includes the tests for equal variance within each replicate. * denotes a significance on a 0.05 level.

Descriptor name	Day	Fat			Protein			Pre-heat			Incubation			Equal variance		
		content	content	content	content	content	content	treatment	treatment	treatment	temperature	temperature	temperature	Day 1	Day 2	Day 3
Intensity histogram	0.016*	<.001*	<.001*	<.001*	<.001*	<.001*	<.001*	<.001*	<.001*	<.001*	<.001*	<.001*	0.137	0.078	0.080	
Fractal (box count) ¹	0.513	<.001*	<.001*	<.001*	<.001*	<.001*	<.001*	<.001*	<.001*	<.001*	<.001*	<.001*	0.349	0.021*	<.001*	
Fractal (box count) ²	0.735	<.001*	<.001*	<.001*	<.001*	<.001*	<.001*	<.001*	<.001*	<.001*	<.001*	<.001*	0.255	0.115	<.001*	
Fractal (variogram) ¹	<.001*	<.001*	<.001*	<.001*	<.001*	<.001*	<.001*	<.001*	<.001*	<.001*	<.001*	<.001*	0.484	0.266	0.029*	
Fractal (variogram) ²	0.005*	<.001*	<.001*	<.001*	<.001*	<.001*	<.001*	<.001*	<.001*	<.001*	<.001*	<.001*	0.381	0.233	0.009*	
GLCM	0.010*	<.001*	<.001*	<.001*	<.001*	<.001*	<.001*	<.001*	<.001*	<.001*	0.002*	<.001*	0.359	0.249	0.160	
LBP	0.044*	<.001*	<.001*	<.001*	<.001*	<.001*	<.001*	<.001*	<.001*	<.001*	<.001*	<.001*	0.194	0.002*	0.161	
BIF	0.040*	<.001*	<.001*	<.001*	<.001*	<.001*	<.001*	<.001*	<.001*	<.001*	<.001*	<.001*	0.204	0.008*	0.054	
SIFT	0.031*	<.001*	<.001*	<.001*	<.001*	<.001*	<.001*	<.001*	<.001*	<.001*	<.001*	<.001*	0.152	0.022*	0.021*	
Image patches	0.011*	<.001*	<.001*	<.001*	<.001*	<.001*	<.001*	<.001*	<.001*	<.001*	<.001*	<.001*	0.180	0.114	0.071	
Local fractal features	0.005*	<.001*	<.001*	<.001*	<.001*	<.001*	<.001*	<.001*	<.001*	<.001*	<.001*	<.001*	0.146	0.144	0.089	

GLCM = Grey Level Co-occurrence Matrices, LBP = Local Binary Pattern, BIF = Basic Image Features,
SIFT = Scale Invariant Feature Transform

D.3.5 Hierarchical Clustering

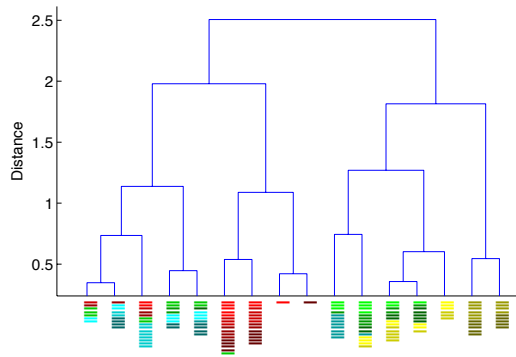
Hierarchical clusterings are frequently presented using dendrograms. Figure D.9 presents dendrograms from two different clusterings using the image patch descriptor from Section D.2.4.7. For comparison, the clustering is based on the same replicate, in the experimental design, from which the examples in Figure D.1 were extracted.

In Figure D.9(a) the hierarchical clustering is based on all data in this replicate. It can be seen that there is a lot of overlap between the different samples, which can be attributed to the potential overlap of the samples and the within sample variation. It can be seen that subset 1 (red) is rather isolated from the other samples. There is a large overlap between subset 2 and subset 4 (yellow). This can be expected as both subset 2 and 4 have high protein content, which visually contributes most to the changes in the images in Figure D.1. High fat content also changes the appearance but to a less degree than protein. This leads to subset 2 slightly overlapping with subset 3. By analysing Figure D.9 in greater detail it can be seen that the densest sample in subset 2 (sample 6) favours subset 3, and the least dense sample in subset 3 (sample 11) favours subset 3.

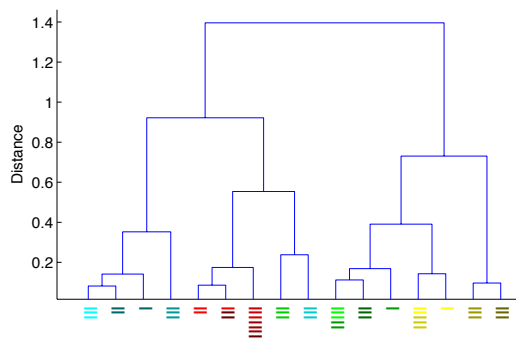
While Figure D.9(a) gives an overview of the major changes in the data, the more subtle changes from different pre-heat treatments and incubation temperatures can be difficult to assess. To get a clearer view, we can filter out some of image descriptors points. We do this by only selecting the median image descriptor and its two closest neighbours for each of the samples. The sample median is found as the image descriptor that is closest to all other image descriptors within the same sample. The result is shown in Figure D.9(b), and comparing directly to Figure D.1 there is a good visual correspondence between the images and the hierarchical representation.

D.4 Discussion

This paper has provided a comparative study between some of the methods typically associated with analysis of protein gels, and different methods from the field of material classification. Common for all methods is that they have free parameters that need to be chosen carefully. We have considered and covered a broad range of these free parameters, but our objective was not to exhaustively evaluate their impact on the performance of each method. In this study the parameters were chosen based on the best classification rates on the entire data set, but tuning parameters on the subsets of the data could also be considered.



(a) Clustering using all data



(b) Clustering using a subset of the data

Figure D.9: Hierarchical clusterings presented by dendrograms. The colours correspond to the sample colours in Figure D.1, and each coloured bar represents a sample image. In (a) the hierarchical clustering is performed on all data in a single replicate. In (b) the clustering is performed using only three selected observations from each class in a single replicate.

As previously mentioned, fractal analysis can be performed in several ways (Soille and Rivest, 1996; Lopes and Betrouni, 2009), and we have just considered two of the most widely used approaches. For other methods like GLCM and LBP, multiple extensions exist (Roberti de Siqueira et al., 2013; Huang et al., 2011). We have only considered a single extension of each method; a multi scale representation using Gaussian pyramids. However, several other multi scale or filter bank representations can be considered (Lindeberg, 1994; Varma and Zisserman, 2005). Similarly, while image descriptors like BIF and local fractal features are more convolved and self-contained methods, both rely on multi

scale or filter bank representations. These can, to some degree, be considered as parameter-free methods.

The SIFT image descriptor locates blobs in the images, and creates a local descriptor for each blob. Compared to the other methods, SIFT only considers 6000-8000 key points rather than the entire image, which actually lead to reasonably classification rates, when the gels were dense. Other image key points could be considered such as corners or branch points, depending on the appearance of the gel network.

Looking at the classification rates, the image patch method appears to be the overall best performing method. It utilises small patches of the raw image data, which can outperform state-of-the-art filter bank based methods. Varma and Zisserman (2009) discuss this in detail, and they also suggest to investigate rotational invariance and dimensional reduction of the patches.

It was found that other methods also favoured low spatial support, when the parameters were chosen. However, for the methods that utilised multi scale representation, multiple scales were actually chosen. This might suggest that unions of image descriptors across different scales should be further investigated. This is emphasised in Figure D.1, where it can be seen that structures appear to be smaller the denser the gel network is.

In general, the texton methods seem to significantly outperform fractal analysis and GLCM, however, due to the large standard deviations in classification rates, it is hard to determine the best texton method. As mentioned earlier the less dense gels appear more inhomogeneous, and this contributes to the large variations in the data set. Less zoom during image acquisition could be a potential solution to generate more representative images of the gel network. Also, concatenation of several images could be employed to reduce the variation.

D.5 Conclusion

A broad range of image descriptors has been investigated for discriminating between the protein networks of stirred yogurts made with different compositions and processing temperatures. The experiment was replicated on three consecutive days. Conventional image descriptors, such as fractal analysis and grey level co-occurrence matrices, were investigated alongside more recent approaches to image description. The recent approaches rely on using textons, which was found to increase the discrimination between different yogurt microstructures. Also, while non-texton approaches performed similarly on the entire data set,

the texton methods performed better when denser gel networks were considered. However, due to large within sample variation and overlap between samples, the best texton method cannot be determined without further testing. For the non-parametric multivariate analysis of variance, all methods agreed that all factors in the experimental design were significant. Also a significant day-to-day variation was observed by most of the methods. However, some of the methods did not have equal sample variation within all of the replicates. Hierarchical clustering was applied to one of the best performing image descriptors and showed a hierarchy of the data, which was consistent with our own visual interpretation of structure and density of the gel networks.

D.6 Acknowledgements

This work was (in part) financed by the Centre for Imaging Food Quality project, which is funded by the Danish Council for Strategic Research (contract no 09-067039) within the Programme Commission on Health, Food and welfare. We would like to thank the laboratory staff at DuPont for being incredible helpful throughout the course of the experiments. Part of this work was undertaken by the lead author, as a visiting researcher at the Centre for Image Processing and Analysis, at Dublin City University.

APPENDIX E

Discriminating Yogurt Microstructure Through 2D Static Light Scattering

Jacob L. Skytte

Abstract

Previously there has been much emphasis on studying the milk fermentation process in relation to cheese making. Especially optical methods have been applied to a great extent due to the convenience explicitly defined by their non-invasive nature. However, studies concerning discrimination of microstructure in yogurt products using optical methods are limited. This report presents preliminary results for an explorative study of a novel hyperspectral (460-900nm) optical technique denoted 2D Statics Light Scattering (2DSLS). Comparisons were made to objective measures of the yogurt microstructure observed by confocal scanning laser microscopy (CSLM). The output signal from both measuring techniques was evaluated for 16 different yogurts, created through a 2^4 factorial design, covering four common production parameters, that changes the final microstructure of the yogurt. Both methods detected significant changes for

all factors, and it was also observed that 2DSLS is more sensitive to changes in microstructure when shorter wavelengths are considered. This corresponds well to Mie theory. Additionally, the shorter wavelengths also resulted in higher correlation coefficients between CSLM and 2DSLS.

E.1 Introduction

The quality perception of fermented milk products is partly defined by the microstructure of the network formed during protein aggregation (Muir and Hunter, 1992; Folkenberg et al., 2005). To investigate the microstructure of the protein network, confocal scanning laser microscopy (CSLM) has become a popular imaging modality, as little sample preparation is required. Along with the relative easy data collection, this also reduces the risk damaging the investigated sample (Lee and Lucey, 2010).

Typically, the microstructure in the CSLM images is evaluated subjectively, and the protein networks are often described by the interconnectivity and tortuosity (Lucey et al., 1998a). However, for large data sets or comparative studies, subjective evaluation becomes problematic. A human inspector can, in most cases, easily distinguish two different microstructures, whereas it is very difficult to quantify difference in an objective manner.

Therefore, in Skytte et al. (2014a) we investigated different approaches to quantify the microstructure in protein network of stirred yogurts in an objective manner. We found that popular image descriptors, from the field of material classification, could discriminate well between 16 unique types of stirred yogurt made in a 2^4 factorial design. Two factors, fat and protein content, were related to the chemical composition of the base milk, and two factors, pre-heat treatment and incubation temperature, were process parameters that primarily affected the formation of the microstructure. All four treatments were expected to change the final microstructure and through analysis of variance this was verified by the image descriptors. Additionally, the hierarchical ordering of the objective measurements corresponded well to what was observed visually. The objective description allows us to use CSLM images directly as reference measures, and comparisons to other objective methods can be made. Thus, in this report we compare the microstructure of the protein networks to a signal output from a novel hyperspectral optical method: 2D Static Light Scattering (2DSLS).

From light scattering theory it is known that the main scatterer in milk and yogurt are the fat globules, due to their size (Walstra et al., 2010; Martelli et al., 2010). However, the significantly smaller protein structures are also contributing

to the overall scattering properties, and hereby the aggregation of the protein structures during fermentation can be observed by optical measurements. Milk fermentations have previously been investigated to great extent in relation to cheese making, where the initial structure formation is followed in order to predict the optimal cutting time (Lucey, 2002; O’Callaghan et al., 2002; Castillo, 2006). In Skytte et al. (2014b) we applied 2DSLS in relation to milk fermentations and saw signals similar to those of other optical methods (O’Callaghan et al., 2002). Comparing CSLM and optical method directly, there is a difference in the scale at which a sample is observed. CSLM images are captured on microscopic scale, whereas light scattering measurements are typically performed on a macroscopic scale. Thereby it can potentially be easier to perform measurements that are representative of the entire sample, when using light scattering techniques.

Best to our knowledge little has been published in regard to discrimination of different microstructures in fermented milk products using optical methods. Hereby, we investigate how well 2DSLS can differentiate between the 16 unique stirred yogurts previously used in Skytte et al. (2014a). Additionally, comparisons will be made to one of the objective measures of the microstructure observed through CSLM. If the 2DSLS method is sensitive to different microstructures it can potentially be used for process control in the making of dairy products, but also act as a screening tool when developing new dairy products in addition to conventional rheological measurements (Lee and Lucey, 2010).

It should be noted that due to the small amount of optical measurements this study is considered preliminary, and the presented results should be seen as encouraging rather than concluding.

E.2 Materials and Methods

In this section the experimental design is initially introduced, and hereafter the 2DSLS technique is presented alongside a way of characterising its signal. Finally, the multidimensional CSLM image descriptor, used for making the comparisons to 2DSLS, is briefly introduced alongside an approach to map this multidimensional descriptor into a one-dimensional space.

E.2.1 Experimental Design

The data was collected in a 2^4 factorial design. The four factors were common process parameters found in yogurt making, and covered fat content, protein content, pre-heat treatment temperature, and incubation temperature. The fat and protein content naturally affects the chemical composition of the yogurt, while the two latter factors define the amount of protein cross-linking that will be made when the protein structures start to aggregate (Lucey et al., 1999; Lee and Lucey, 2010). All factors were expected to significantly affect the final microstructure, however the heat-treatment and incubation temperature were only expected to show subtle differences.

Initially, the base milk was adjusted to the right fat and protein content, and hereafter the milk was heat treated for 15min at the target factor temperature level. After heat treatment the milk was rapidly cooled in a cold-water bath. Finally, the milks were heated to the target incubation temperature, lactic acid bacteria were added to the milk, and the fermentation was initialised. The fermentation was continued until a pH of 4.6 was reached. Hereafter, the milks (now yogurts) were stirred and stored in a refrigerator for a week prior to measurements. Three replicates of the experiment were performed on three consecutive days, resulting in a total of $3 \cdot 16 = 48$ yogurts.

For each yogurt sample we had three optical measurements, and 10 CSLM images of the protein microstructure. As some day-to-day variation was expected due to the use of bacteria culture, each replicate was included as a block in the factorial design. Thus, the day-to-day variation will be isolated in the analysis (Montgomery, 2005). The block will be referred to as *day*. The experimental design is summarised in Table E.1, and Figure E.1 shows example images of the different microstructures for one of the replicates. For specific details on the experiment, and the data collection in relation to CSLM, please refer to Skytte et al. (2014a).

E.2.2 2D Static Light Scattering

We have recently introduced the novel optical method, 2D Static Light Scattering (2DSLS) (Nielsen et al., 2011a,b; Skytte et al., 2014b). The system setup consists of a hyperspectral light delivery system (460-900nm), from which the light beam is focused on the sample surface at an oblique angle. Using a CCD orthogonal to the sample surface, the spatial distribution of the diffuse reflectance is captured. In front of the CCD a 6.5cm spacer and an objective lens was installed. A simplified schematic of the setup is shown in Figure E.2 and Figure

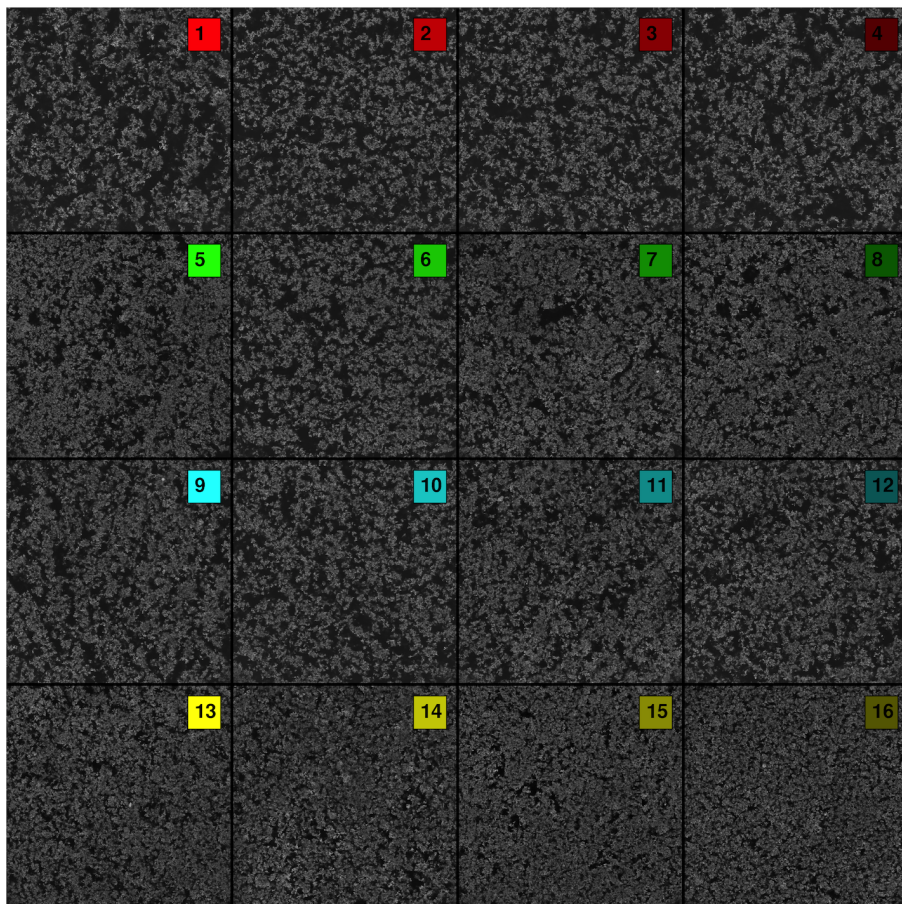


Figure E.1: Examples of the 16 different yogurt samples from a single replicate. The numbering corresponds to that of Table E.1.

Table E.1: The 2^4 experimental design. Minus and plus denotes low and high factor levels respectively. The actual factor level values are given in the left most column. The entire design is replicated across three days. The subsets used in Section E.3.

	Subset 1				Subset 2				Subset 3				Subset 4			
	1	2	3	4	5	6	7	8	9	10	11	12	13	14	15	16
Fat content [1.5/3.5 g/100g]	-	-	-	-	-	-	-	-	+	+	+	+	+	+	+	+
Protein content [3.4/4.4 g/100g]	-	-	-	-	+	+	+	+	-	-	-	-	+	+	+	+
Pre-heat treat. [75/90 °C/15min]	-	-	+	+	-	-	+	+	-	-	+	+	-	-	+	+
Incubation temp. [39/43 °C]	-	+	-	+	-	+	-	+	-	+	-	+	-	+	-	+

E.3(a) shows a data example for semi-skimmed milk at 600nm. Three measurements were taken for each of the prepared stirred yogurts.

E.2.2.1 Diffuse Reflectance Image Quantification

An example of the captured diffuse reflectance images can be seen in Figure E.3(a). In order to quantify the diffuse reflectance images we consider the loglog model, an approach applied and validated in Skytte et al. (2014b). It models the intensity decay of the multiple scattered light, i.e. the light far away from the light incident point.

The quantification scheme is illustrated in Figure E.3. Here, the diffuse reflectance image is log-transformed twice and a intensity profile is extracted orthogonal to the scattering direction. A linear model is fitted to the outer part at both ends of the extracted profile, and the average slope of the two models (denoted the slope parameter from here on) describes the combined contribution of the absorption and scattering properties. However, milk and fermented milk products are diffusive materials, meaning that the scattering properties greatly dominate the absorption properties (Martelli et al., 2010). Thus, the combined contribution mainly reflects the scattering properties.

The quantification only considers a small amount of the data available in the images. A multivariate description, which considered frequencies of the entire image, was presented in Sharifzadeh et al. (2013). However, for this comparative study we preferred the one-dimensional representation for simplicity.

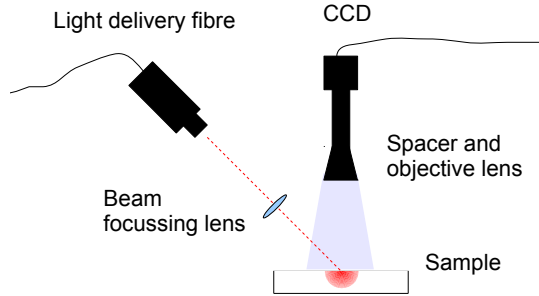


Figure E.2: Simplified schematic of the 2DSLS system setup.

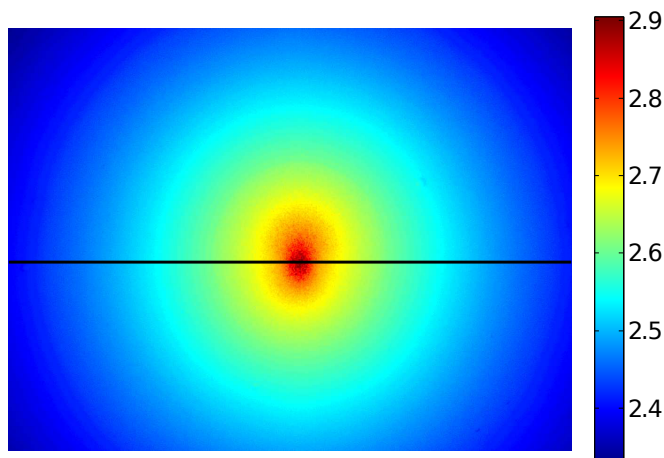
E.2.3 CSLM Image Descriptor

Alongside the slope parameter extracted from the diffuse reflectance images, we present the results for one of the image descriptors used to describe the protein microstructure in the CSLM images. This particular descriptor was found to be one of the overall best performers in Skytte et al. (2014a). It represents the microstructure as a frequency distribution of reoccurring structures, defined by small image patches (7×7 pixels) (Varma and Zisserman, 2009).

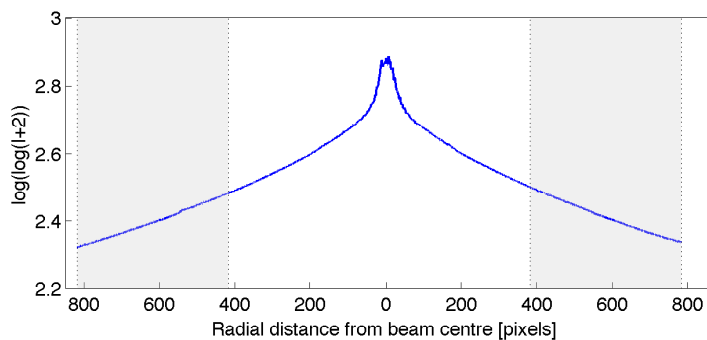
E.2.4 Multidimensional Scaling

The CSLM image descriptor described in the previous section is of high dimensionality. Thus, in order to compare it directly to the slope parameter, the observations are mapped to a one-dimensional space. This can be done through multidimensional scaling, where the observations are considered in a distance space. Thus, rather than representing the image descriptors using the actual p -dimensional space with N observations, the descriptors are represented as the mutual distances between all pairs of observations. Thus, the observations are represented as an $N \times N$ dissimilarity matrix, \mathbf{D} .

Multidimensional scaling can hereafter be used to determine a low-dimensional representation of the data, where the mutual distances of \mathbf{D} are approximately retained. This can be done by seeking the values $\mathbf{Z} = (\mathbf{z}_1, \mathbf{z}_2, \dots, \mathbf{z}_N)^T \in \mathbb{R}^{N \times k}$



(a) Diffuse reflectance image



(b) Corresponding intensity profile

Figure E.3: Illustration of the diffuse reflectance image quantification. (a) shows the double logarithmic transformed 2DSLS signal, and the black line denotes the corresponding intensity profile seen in (b). A linear model is fitted to both of the grey intervals in (b) and the average value of the slope parameter comprises the quantified signal.

(where $k < p$) that minimises the stress function:

$$S_{\text{SM}}(\mathbf{Z}) = \sum_{i=1}^N \sum_{j=1}^N \frac{(d_{ij} - \|\mathbf{z}_i - \mathbf{z}_j\|)^2}{d_{ij}}, \quad (\text{E.1})$$

where d_{ij} is an element of \mathbf{D} and $\|\cdot\|$ is the Euclidean norm. The expression is a slightly modified version of the least squares formulation and denoted *Sammon mapping* (Hastie et al., 2009). The modification puts more emphasis on preserving the smaller mutual distances (Hastie et al., 2009). This was motivated by the fact that some factors in the experimental design were expected to only make subtle differences to the microstructure. For $k = 1$ a one-dimensional representation of the observations is obtained. Hereby the CSLM image descriptor and the slope parameter from the 2DSLS signal can be compared in a one-to-one manner.

E.2.5 Statistical Analysis

To make the best possible comparison between the CSLM image descriptor and the slope parameter, we apply the majority of evaluation techniques used in Skytte et al. (2014a). This includes performing ANOVA to determine the factor significance in the experimental design, and applying nearest neighbour classification on the entire data set as well as different subsets of the data set. Additionally, we present the correlations between the one-dimensional representation of the CSLM image descriptor and the slope parameter from the 2DSLS signal.

E.3 Results

E.3.1 Multidimensional Scaling

Multidimensional scaling was performed on the CSLM image descriptors, in order to make a one-dimensional representation. The average approximation error for the mapping was found to be 10.9%, when using the Sammon mapping. Using a least squares mapping the average approximation error was found to be 17.4%, thus validating the choice of the Sammon mapping. This one-dimensional representation of the CSLM image descriptor is used for the correlation analysis in Section E.3.2.3.

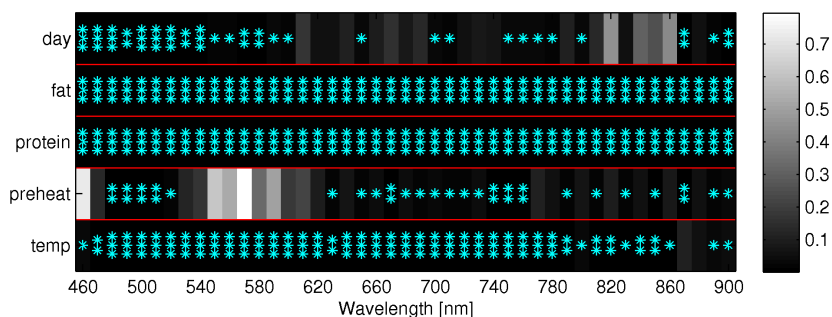


Figure E.4: Factor significance for the 2DSLS technique across all wavelengths through analysis of variance. *day* denotes the day-to-day variation between the three replicates. The greyscale values correspond to the p -values, and the level of significance is denoted by asterisks (*** $p < 0.001$, ** $p < 0.01$, * $p < 0.05$)

E.3.2 Statistical Analysis

E.3.2.1 ANOVA

The results for the slope parameter from the ANOVA are shown in Figure E.4. As expected, the changes in chemical composition (fat and protein) are very significant across all wavelengths. The incubation temperature was also found to be nearly as significant, however a slight trend can be found after 800nm where the level of significance starts to decrease as the wavelength increases. A similar trend can be noted for both day and pre-heat treatment across the entire wavelength interval. However, both day and pre-heat treatment are found to be less significant than the other factors.

In comparison, the chosen CSLM image descriptor found all factors to be very significant ($p < 0.001$), and day-to-day variation was found to be slightly less significant ($p = 0.011$).

E.3.2.2 Nearest Neighbour Classification

Nearest neighbour classification was performed on different partitions of the data set. This was done in order to highlight the specific capabilities of the two methods:

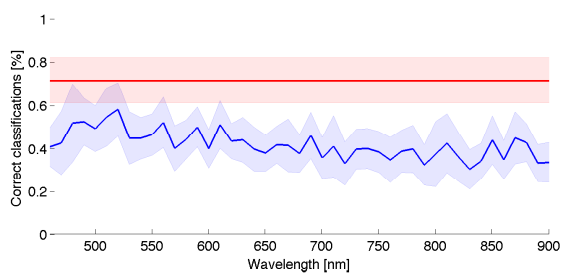
- **Entire data set (sixteen classes).** The overall performance on the entire data set was evaluated.
- **Superset (four classes).** Here, each of the subsets, defined in Table E.1, constitutes a single class, and reflects how well different chemical compositions can be discriminated.
- **Subsets 1-4 (each subset has four classes).** The subsets defined in Table E.1 were used to evaluate how well the subtle microstructural changes are reflected in the measurements, when the chemical composition of the yogurt changes.

For each class, a single observation was isolated (the test data), and the nearest neighbour classification model was build on the remaining data (the training data). The presented test classification rates are based on the average over 1000 random splits of the data set, and further averaged across the three replicates of the experimental design. The classification results for all partitions are summarised in Figures E.5 and E.6. Here the blue curves represent the classification rates of the slope parameter at different wavelengths, and the red curves represent the classification rates of the CSLM image descriptor obtained in Skytte et al. (2014a). Furthermore, Figure E.7 provides the corresponding confusion matrices for the CSLM image descriptor and the 2DSLS slope parameter at three different wavelengths.

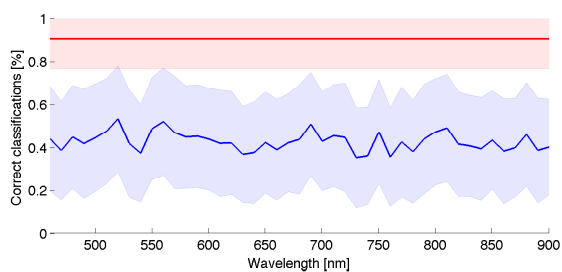
Looking at the classification rates for the entire data set and the superset (Figure E.5), 2DSLS appears to perform significantly worse than the CSLM image descriptor. When considering the entire data, the classification rates for the 2DSLS slope parameter tends to decrease as the wavelength increases, and for the shortest wavelengths there is even a slight overlap in performance with the CSLM descriptor. This corresponds well to the presented confusion matrices in Figure E.7.

The same tendency is not seen for the classification rates of the superset. Here the performance generally appears to be lower, with larger standard deviations, and virtually no wavelength dependency. We found this was due to the samples with a high level of fat (samples 9 through 16), in which the effect of protein content seemed to be obscured. This can also be seen in the confusion matrices. This confounding, combined with only four classes, is likely to cause the lower performance.

Moving on to subsets 1 and 2, it can be seen that the performance actually appears similar for CSLM and 2DSLS especially at the lower wavelengths. Considering the subsets 3 and 4, which have a high fat content, the performance is a bit lower for 2DSLS and a wavelength dependency is only seen for subset



(a) Entire data set



(b) Superset

Figure E.5: Classification rates for the CSLM image descriptor (red) and the 2DSLS slope parameter for all wavelengths on different partitions of the data set. The margins denotes one standard deviation.

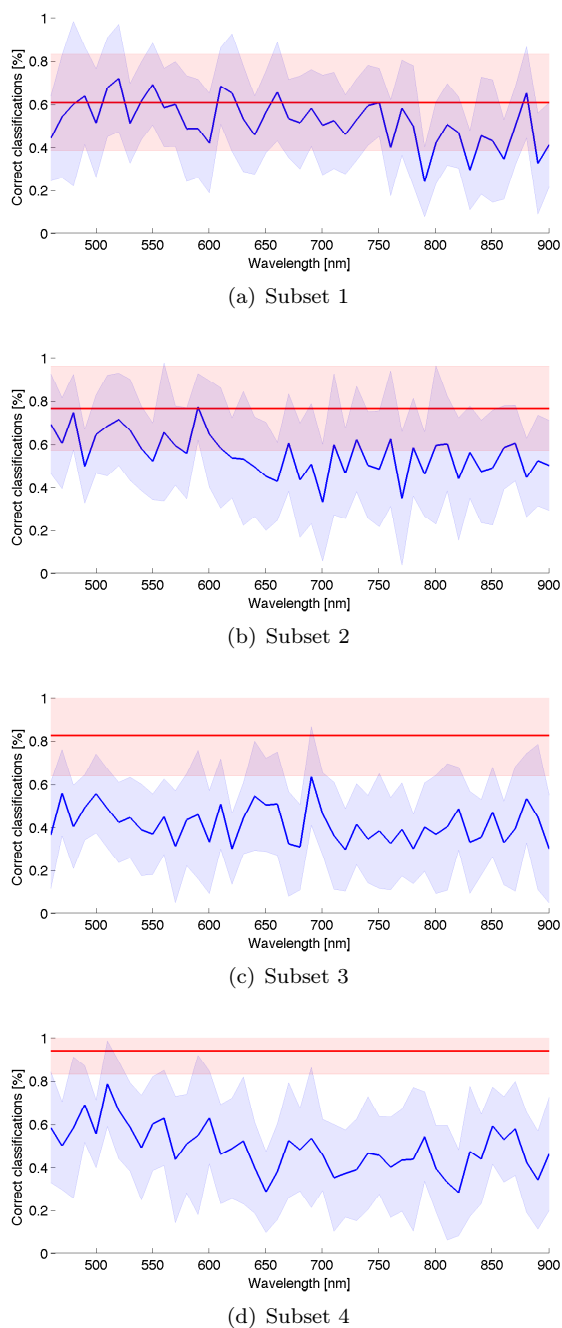


Figure E.6: Classification rates for the CSLM image descriptor (red) and the 2DSLS slope parameter for all wavelengths on different partitions of the data set. The margins denote one standard deviation.

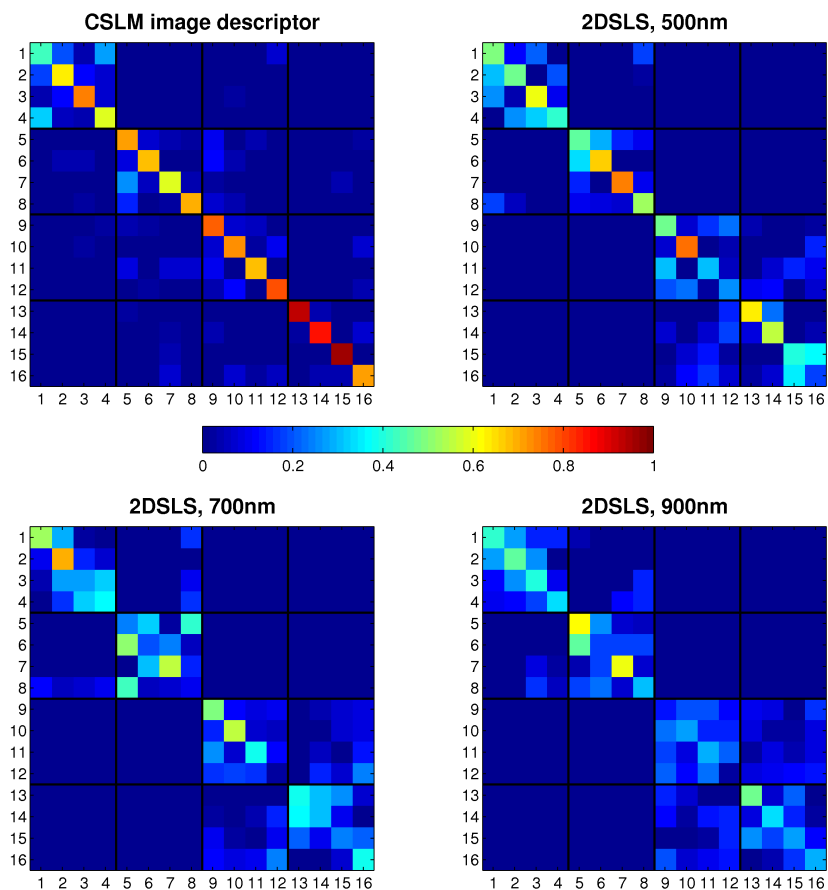


Figure E.7: Confusion matrices for the classification on the entire data set. The sample numbers corresponds to those of Table E.1, and furthermore the grid highlights the four defined subsets.

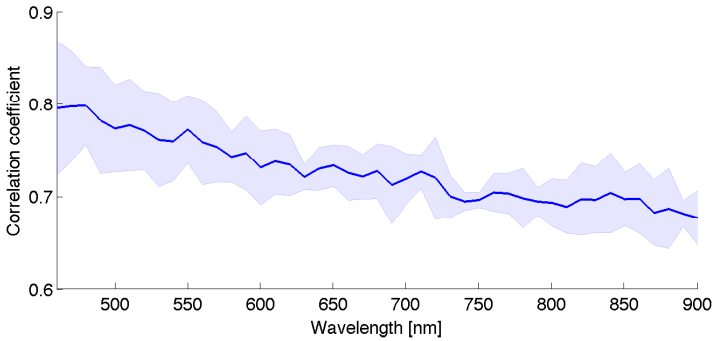


Figure E.8: The average correlation between the average CSLM descriptor and 2DSLS slope parameter as a function of wavelength. The correlation is averaged across the three replicates and the margins denotes the standard deviation.

4, which has a high protein content. The results for the subsets also seem to correspond well to the confusion matrices.

E.3.2.3 Correlation

Correlations could be calculated between the 2DSLS slope parameter and the one-dimensional representation of the CSLM image descriptor obtained through multidimensional scaling in Section E.3.1. The correlation coefficients presented in Figure E.8 are based on the average responses from the two modalities, and averaged across the three replicates. Again, a wavelength dependency can be seen, and in this case it is even more prominent than for the classification rates.

In Figure E.9 we have plotted the average responses, for a single replicate, against each other, at three different wavelengths. When comparing across wavelengths it quite clear to see how the signal at 500nm is affected more by changes to protein content and the protein network microstructure compared to the higher wavelengths. Especially for the samples with low fat content (sample 1 through 8) the effects of pre-heat treatment and incubation temperature are pronounced. Contrary, at 900nm there is a clear separation between low fat and high fat samples, while there is only a small effect from the protein content. Looking at the effects of pre-heat treatment and incubation temperature they are more or less collapsed into a single point, making them hard to distinguish.

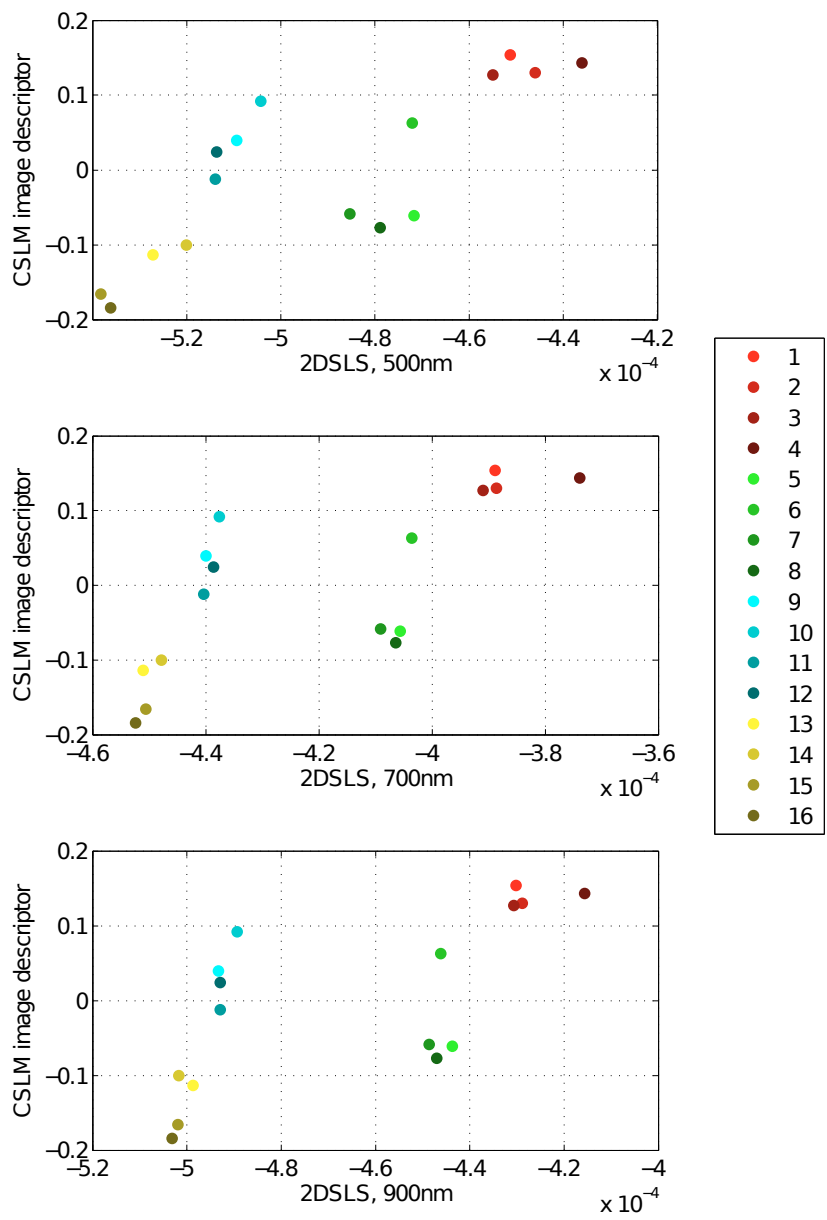


Figure E.9: The average CSLM image descriptor and the average 2DSLS slope parameter plotted against each other at different wavelengths. The sample numbers and colours corresponds to those of Table E.1 and Figure E.1.

E.4 Discussion and Conclusion

A comparative study has been made between the 2DSLS signal and an CSLM image descriptor, and several interesting observations can be made. All of the applied evaluation techniques generally showed a wavelength dependency, in which lower wavelengths were better at discriminating between different protein microstructures. However, when fat is added to the system, the effects of protein content, pre-heat treatment and incubation temperature diminishes.

These findings corresponds well to Mie theory (Mie, 1908) as the scattering efficiency of milk fat is significantly larger than that of milk protein due to the difference in structure size (fat lies within the range 100-10000nm while protein lies within 20-400nm) (Walstra et al., 2010). Additionally, the scattering effect decays faster across wavelengths when considering small structures compared to the wavelength of the light.

For the applied wavelength interval (460-900nm) this means that the scattering contribution from the fat structure remains fairly constant across the interval, whereas the contribution from the protein structures decays significantly across the interval. Thus, the effect of protein content and different protein microstructures should be more visible at lower wavelengths. This corresponds well to the observations from all evaluation techniques.

In general the CSLM image descriptor showed more sensitivity towards the experimental factors compared to the 2DSLS slope parameter, however in a few cases classification performance was comparable. This was especially clear for the samples 1 to 4 with low fat and protein content. Here it should be noted that the CSLM have just been captured at a single level of zoom, and from Figure E.1 it can be seen that the less dense microstructure also appears more irregular. This suggests that the applied zoom level does not necessarily yield a representative view of the less dense microstructures and other zoom levels should be considered (Skytte et al., 2014a). A similar, albeit inverted, problem was observed in relation to the 2DSLS slope parameter, where the high fat content seemingly confounded the effects from the other experimental factors. Here a higher spatial resolution might be able capture the appropriate dynamics in the decay of the light diffusion.

In relation to commercially available optical sensors, the observations of this report are interesting. As mentioned in the introduction, optical methods have most commonly been investigated in relation to the initial structure formation during cheese making. A comparative study by O'Callaghan et al. (1999) considered commercially available modalities for monitoring this structure formation. All the applied optical sensors were based on near-infrared (NIR) light. Claesson

and Nitschmann (1957) initially recommended NIR light as these wavelengths showed a larger relative increase in the signal output, compared to lower wavelengths, during the structure formation.

Thereby, for assessing the microstructure of protein networks, the preliminary results of this report suggests that new optical sensors should be developed, rather than relying on the already commercially available sensors used in cheese making. Future work will consist of validating these findings on a larger data set, where more data is available for each sample in the factorial design. Additionally, other quantification schemes for the 2DSLs signal will also be considered in future analysis.

APPENDIX F

Quantification of Multiple Scattered Light, Speckle Patterns, and Scattering Eccentricity in Diffuse Reflectance Images

Jacob L. Skytte

Abstract

2D static light scattering (2DSLS), is a recently introduced optical technique, that captures images of the spatial distribution of the diffuse reflectance from a sample illuminated by a laser beam. The signal of this modality includes information from several different light interaction phenomena, thus throughout this report we seek out to quantify and compare the individual parts of the signal. This includes light attenuation by scattering, directionality of the scattering properties, and finally an underlying speckle interference pattern. Preliminary

results will be shown for quantifying fixed regions of the 2DSLS signal. The individual quantifications are visually assessed for two different data sets, in relation to discriminative properties and reproducibility. One data set covers different commercial milk products, and the other covers a milk fermentation.

F.1 Introduction

Nielsen et al. (2011b,a) introduced the optical technique, 2D Static Light Scattering (2DSLS), which potentially can be well suited for process control. The method is based on capturing images of the spatial distribution of the diffuse reflectance when illuminating a sample with an oblique laser beam. Investigating the distribution of the diffuse reflectance can reveal both chemical and microstructural properties of the illuminated sample (Martelli et al., 2010).

In Skytte et al. (2014b) we applied the technique in regard to milk fermentations, and found that it was possible to follow the protein aggregation during the structure development. However, only a small part of the 2DSLS signal was quantified. Furthermore, 2DSLS was applied to different commercial dairy products in Sharifzadeh et al. (2013), and here the entire signal was considered in the frequency domain by means of the discrete cosine transformation (Ahmed et al., 1974). It was found that the low and high frequency parts of the signal discriminated the products differently and furthermore complimented one another.

In this report we specifically try to quantify individual types of information in the 2DSLS signal, which are found at spatially different locations. Figure F.1(a) shows an example of the 2DSLS signal. It is a complex signal containing contributions from at least three different phenomena: Multiple scattered light, single scattered light, and speckle, all of which will be explored in this report. Multiple scattered light is located "far" from the incident point where the intensity isocontour is approximately circular and isotropic scattering dominates. Single scattered light is located "close" to the light incident point where the intensity isocontours are asymmetric and effects of the so-called phase function dominates. This is illustrated in Figure F.1(b). Speckle is present as an underlying inference pattern and will be visualised more clearly in Section F.2.1.2. Figure F.1(c) shows a conceptual cross-section of the 2DSLS signal, which consists of the reflected Gaussian beam (red), single scattered light (green), and multiple scattered light (blue). All three parts contain an underlying interference pattern denoted speckle.

Multiple scattered light can be described by physical models which rely on the

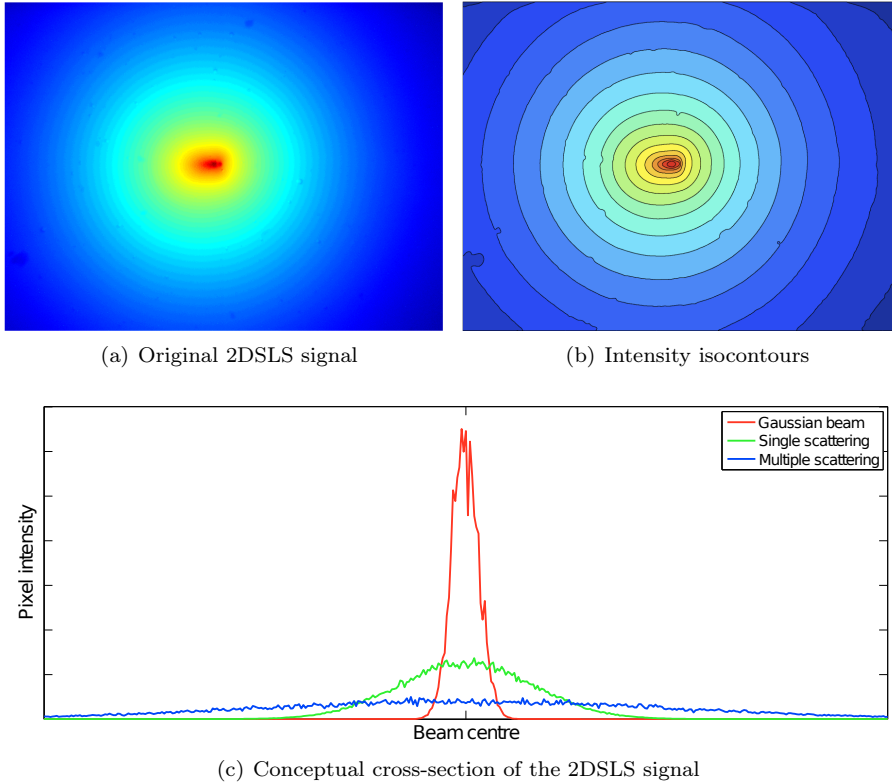


Figure F.1: (a) shows the 2DSLS signal (diffuse reflectance image) of milk (1.5 % fat) at 900nm. (b) shows the corresponding intensity isocontours (artefacts arise from bubbles in the measured sample). The laser beam comes in from the righthand side of the image at an oblique angle, and the light incident point is located around the highest pixel intensities (coloured red). (c) shows a conceptual cross-section of the 2DSLS signal orthogonal to the light incident direction.

diffusion approximation. The models are defined in terms of the absorption coefficient, μ_a and the reduced scattering coefficient, $\mu'_s = \mu_s(1 - g)$, where $-1 < g < 1$ is the asymmetry parameter (Farrell et al., 1992; Wang and Jacques, 1995; Lin et al., 1997). Through Mie theory (Mie, 1908), both μ_s and g can be related to the shape and size distribution of the suspended particles.

The single scattered light provides information on the directionality of the scattering process; that is the scattering phase function, which is often described by

g (Martelli et al., 2010). For milk, the scattering directionality is forward lobed as can be seen in Figure F.1(b). This is especially clear near the light incident point, where the intensity isocontours are elongated.

The final phenomenon is the underlying speckle pattern, which in addition can be attributed several different phenomena. First of all speckle is an interference phenomenon that arises when illuminating a material with a coherent light source (such as a laser). Constructive or destructive interference arises when the light gets out of phase due to Doppler shifts caused by Brownian motion (Alexander and Dalgleish, 2006), or when light travels different path lengths before reaching the detector (Piederrière et al., 2004a). As 2DSLS employs static measures, the speckle effects due to Doppler shifts should not be directly visible in the signal. In contrast, effects due to differences in path lengths should be visible. These path length differences are often attributed surface irregularities (as many surfaces appear rough when observed at the scale of an optical wavelength) (Goodman, 1976) or when light is scattered in random media in general (Piederrière et al., 2004b). However, these two phenomena can be hard to distinguish (Guyot et al., 2004)

As will be seen in Section F.2.1 most of the investigated quantification methods in this paper rely on shapes and distances, rather than pixel intensities. In relation to process control this poses a significant advantage as the quantification of the signal hereby becomes independent of variations in the system response (light intensity, detector sensitivity, etc.), which is desirable (Chen and Sun, 1991). Furthermore, the quantification methods will be subjectively evaluated on two data sets.

The first data set consists of commercially available dairy products, and is used to investigate what kinds of information the different 2DSLS quantification can be related to (chemical composition or microstructure). The second data set is a milk fermentation, which is used to investigate how each of the quantification methods develops throughout the protein aggregation, in which the characteristic structure of fermented milk products is formed. Optical changes throughout milk fermentations have been studied thoroughly in relation to cheese making (O'Callaghan et al., 1999, 2002; Lucey, 2002; Castillo, 2006).

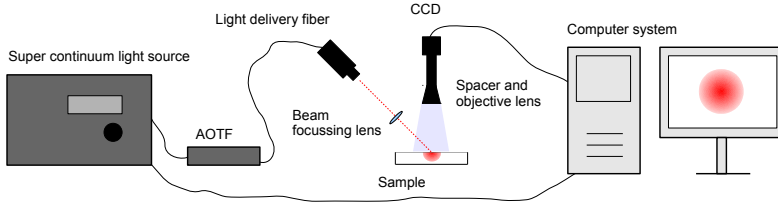


Figure F.2: A schematic view of the 2DSLS system setup.

F.2 Materials and Methods

F.2.1 2D Static Light Scattering

A schematic view of the 2DSLS system is shown in Figure F.2, and an example of the 2DSLS signal was shown in Figure F.1. The system setup consists of a super continuum light source (*SuperK Extreme*, NKT Photonics, Birkerød, Denmark), filtered by an acousto-optic tunable filter (*SuperK Select*, NKT Photonics, Birkerød, Denmark), and the combined system produces a polarised laser beam, in the range 470-1000nm, at high spectral resolution.

The laser is focused on the sample surface using a beam-focusing lens (focal length = 40mm) at an oblique incident angle (45°), which results in a Gaussian beam with a wavelength dependent beam waist ranging from 100-200 μm . For each selected wavelength images are captured using a CCD camera (*AM-800GE*, JAI, Yokohama, Japan) with a 6.5cm spacer and an objective lens (*LM50XC*, Kowa Co. Ltd., Nagoya, Japan). The resolution of the images is 2472×3296 pixels with a spatial pixel size of $3.2 \times 3.2\mu\text{m}$. High dynamic range imaging is applied in order to ensure an appropriate signal-to-noise ratio (SNR) (Mann and Picard, 1994).

As previously mentioned, the 2DSLS signal contains contributions from a lot of different phenomena, and Sections F.2.1.1 through F.2.1.2 describe different approaches to quantify these individually.

F.2.1.1 Multiple Scattered Light

Figure F.3 presents typical pixel intensity profiles that can be extracted from the diffuse reflectance images. Previously we have quantified such intensity

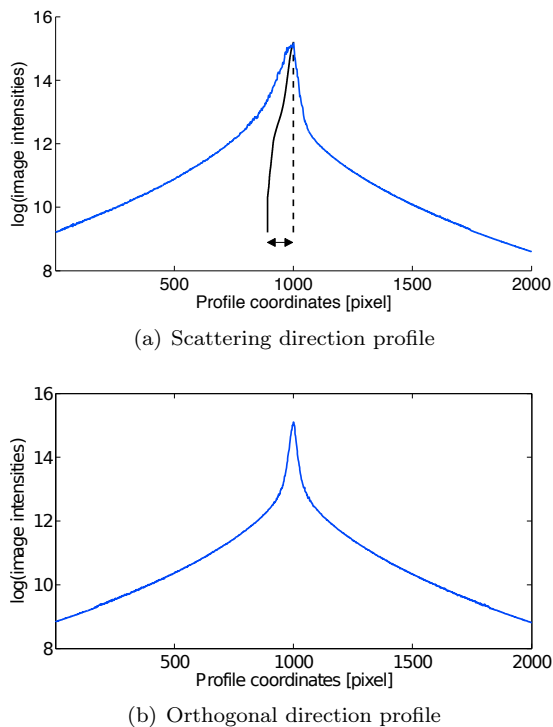


Figure F.3: Examples of pixel intensity profiles that can be extracted from the diffuse reflectance images. (a) is extracted through the light incident point and along the scattering direction, while (b) is extracted orthogonal to the scattering direction. Additionally for (a) the symmetry break due to the oblique incident angle of the light is visualised.

profiles in the 2DSLS signal through physical models (Nielsen et al., 2014) and a similar, yet simplified approach in (Skytte et al., 2014b). We will shortly summarise both approaches in this section.

Multiple scattered light can be quantified by means of the intensity profile in the scattering direction, by fitting it to an analytical expression determined by the combined contribution of μ'_s and μ_a . The symmetry break in the applied intensity profile is dependent on the mean free path (MFP) and thereby the absolute values of μ'_s and μ_a . The MFP can therefore be used together with the analytical expression to obtain absolute estimates of μ'_s and μ_a , which are invariant toward variations in the system response (Wang and Jacques, 1995; Lin et al., 1997; Nielsen et al., 2014). Moreover, the wavelength dependency

of μ'_s can be used to obtain additional information on particle size and particle density of the investigated sample (Graaff et al., 1992). This is done by fitting μ'_s to a power function

$$\mu'_s = \alpha \lambda^{-\beta}, \quad (\text{F.1})$$

where λ is the wavelength, and α and β relate to the particle concentration and average particle size respectively. Large values of α correspond to high particle density, while low values of β corresponds to a rapid scattering decay across wavelengths, and thereby a small average particle size as explained by Mie theory (Mie, 1908).

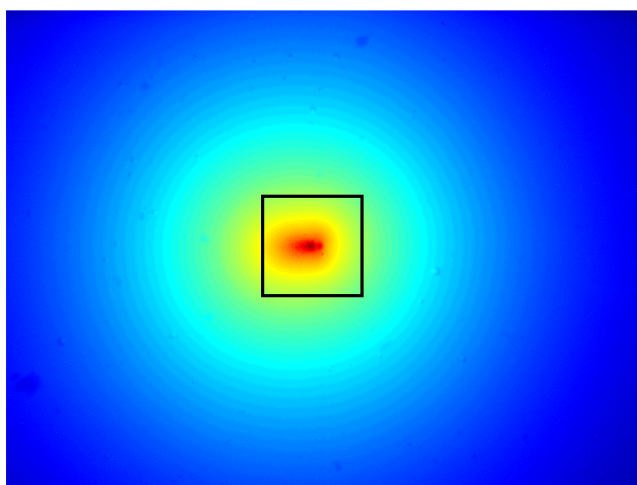
Alternatively, a simplified approach to quantifying the multiple scattered light is also considered. Here, the intensity profile orthogonal to the scattering direction is considered. By applying a logarithmic transform to the profile twice, the outer parts become approximately linear and can hereby be described by a linear model. From these models average absolute estimates of the slope and intercept can be extracted, which are both affected by the absorption and scattering properties of the sample. Both parameters are furthermore affected by variations in the system response. The approach was validated in (Skytte et al., 2014b), where it was also found that the slope parameter is more discriminative than the intercept parameter. Thus, in the following we will only consider the slope parameter.

In summary the quantified multiple scattered light will be presented in terms of μ'_s , α , β , and the slope parameter of the loglog model. Values for μ_a will not be presented as they primarily reflect water absorption in the investigated wavelength interval (Martelli et al., 2010).

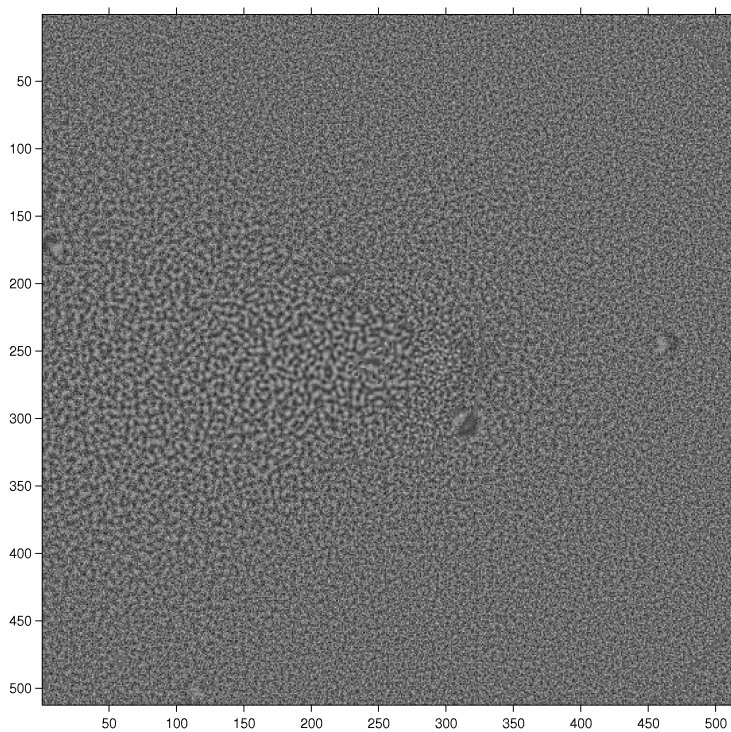
F.2.1.2 Speckle

The underlying speckle pattern can be extracted by performing a local normalisation for all pixel in the image. Thus, each pixel is normalised to zero mean unit and variance through estimates from the local $n \times n$ neighbourhood. Using 5×5 neighbourhoods was found to be appropriate, and examples for the extracted speckle pattern can be seen in Figure F.4 and F.5. From here it can be seen that depending on the sample, both speckle size and SNR varies quite significantly depending on the spatial location in the image.

The average speckle size can be estimated through the full width at half maximum (FWHM) of the maximum response in the spatial autocorrelation function

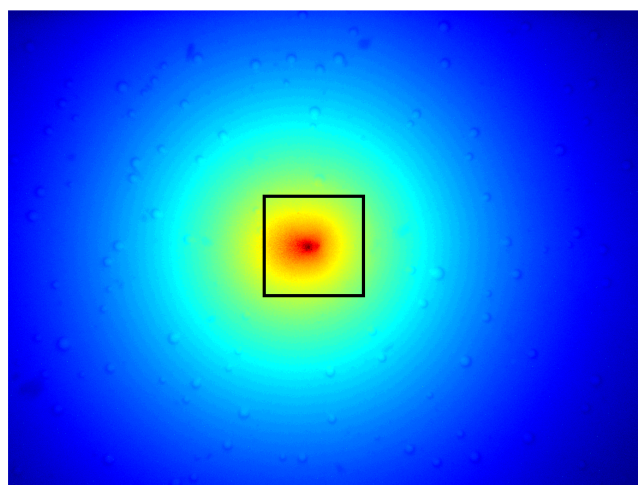


(a) 2DSL signal

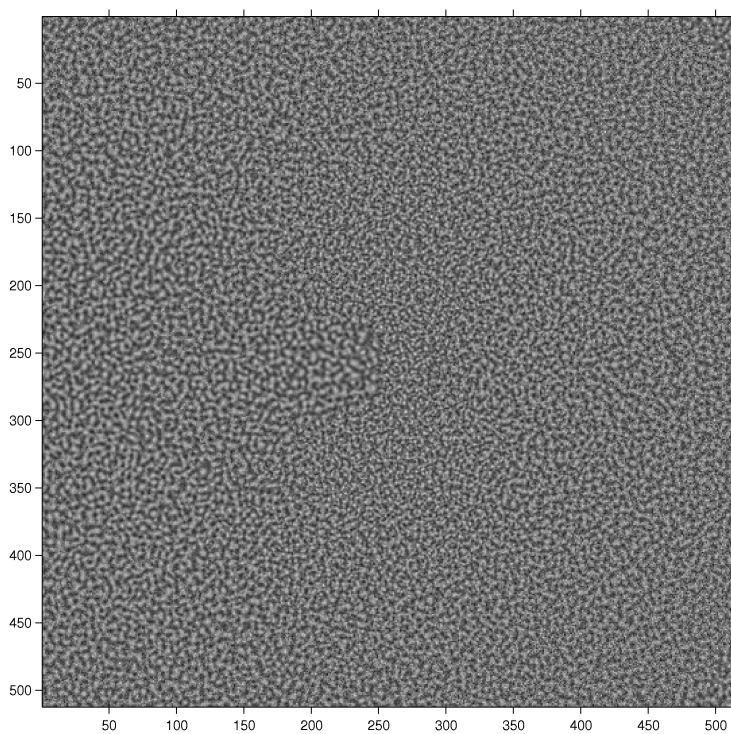


(b) Speckle

Figure F.4: Milk (1.5%) at 900nm. (a) shows the 2DSL signal while (b) shows the speckle pattern extracted at the 512×512 pixels region marked by the black square in (a).



(a) 2DSLS signal



(b) Speckle

Figure F.5: Fermented milk (1.5%) at 900nm. (a) shows the 2DSLS signal while (b) shows the speckle pattern extracted at the 512×512 pixels region marked by the black square in (a).

(Goodman, 1975). For simplicity we will present the average speckle size for three different sized regions centred on the light incident point.

F.2.1.3 Scattering Eccentricity

Effects of the phase function, or g , can be quantified by extracting intensity isocontours (see Figure F.1(b)) at specific distances from the light incident point. By comparing the magnitude of the minor and major axis, the eccentricity of the isocontour can be estimated. One approach to quantifying the eccentricity, is to perform a principal component analysis (PCA) on the spatial coordinates of all pixels lying within a given intensity isocontour. From the PCA, the ratio between the two eigenvalues can be used to describe the eccentricity. The scattering eccentricity will be measured for isocontours extracted at three different distances from the light incident point, along the scattering direction. The eccentricity is bounded between 0 and 1, and for low values the isocontour is almost circular, while larger values denote a more elongated isocontour.

F.2.2 Data

This section introduces the two dairy based data sets used in this report, and very briefly how the data sets were collected.

F.2.2.1 Commercial Dairy Products

This data set consists of six commercially available milk products, three milks and three fermented milks, summarised in Table F.1. All products are homogenised, and the fermented milks are based on lactic acid bacteria. Thus, both ingredient composition and microstructure differs throughout the data set, and the products are expected to span a broad range of scattering properties. This allows for a meaningful interpretation of the quantified 2DSLS signal in relation to chemical composition and microstructure. For each product five repeated measurements were performed using the 2DSLS technique.

F.2.2.2 Milk Fermentation

For the milk fermentation we used commercial UHT milk (1.5% fat, 3.4% protein), and 2% (w/w) Glucono- δ -lactone (GDL) was used as acidifier. The actual

Table F.1: Product information for the six commercial dairy products. The reference name will be used for the remainder of this report. All products are homogenised. The first three products are milks and the next three products are fermented milks, and all fermented milks are based on lactic acid bacteria.

Product name	Reference name	Fat (g/100g)	Protein (g/100g)
Arla Lærkevang Sødmælk	milk (3.5%)	3.5	3.5
Arla Lærkevang Letmælk	milk (1.5%)	1.5	3.5
Arla Lærkevang Minimælk	milk (0.5%)	0.5	3.5
Arla A38 Naturel 3.5%	A38 (3.5%)	3.5	3.5
Arla A38 Naturel 1.5%	A38 (1.5%)	1.5	4.0
Arla A38 Naturel 0.5%	A38 (0.5%)	0.5	4.5

milk fermentation was performed at 25°C, and the temperature was kept constant using a water bath ($SW2 \pm 0.2^\circ C$, *Julabo Labortechnik GmbH, Seelback, Germany*). Before fermentation the milk sample (2000ml) was heated to 25°C in the water bath. During heating, the milk was kept in a sealed container to avoid evaporation of water. When the target temperature was reached, GDL was added and the sample was stirred with a magnetic mixer for three minutes. Hereafter 20ml of the sample was extracted and used for small amplitude oscillatory rheology (*Stresstech HR* with temperature cell $\pm 0.1^\circ C$, *Reologica Instruments AB, Lund, Sweden*) (Bohlin et al., 1984), and 1800ml was used for the 2DSLS measurements, which were performed through a 1.5cm soda lime sight glass (*Lumiglas, F.H.Papenmeier GmbH & Co., Schwerte, Germany*). The sight glass rested on a custom made pedestal, which ensured that the glass was in full contact with the sample surface.

Rheological measurements were performed every three minutes, and 2DSLS measurements were performed every two minutes. In order to ensure time consistency between 2DSLS and rheology, linear interpolation was used. Additionally, the 2DSLS signal at lower wavelengths was found to be corrupted and not feasible for analysis, thus for the milk fermentations the quantified 2DSLS signal is only presented for some of the higher wavelengths. The source of error remains unknown at the time of writing.

F.3 Results

F.3.1 Dairy Products

In this section the results of applying the quantification schemes from Section F.2.1.1 through F.2.1.2 are presented and discussed for the dairy product data set.

F.3.1.1 Multiple Scattered Light

The reduced scattering coefficient, μ'_s , presented in Figure F.6(a), follows a monotonically decreasing behaviour, which corresponds well to light scattering theory (Mie, 1908). The ordering of the products corresponds well to what we saw in Nielsen et al. (2013). Furthermore, the error bars increase as the estimated μ'_s increases, and some of the products (milk (3.5%), A38 (0.5%), and A38 (1.5%)) are not separable for the majority of the investigated spectrum. The primary reason for the larger error bars is that the MFP becomes short and hard to resolve, for highly scattering samples, using the current detector system. This directly introduces measuring noise to the final estimates of μ'_s .

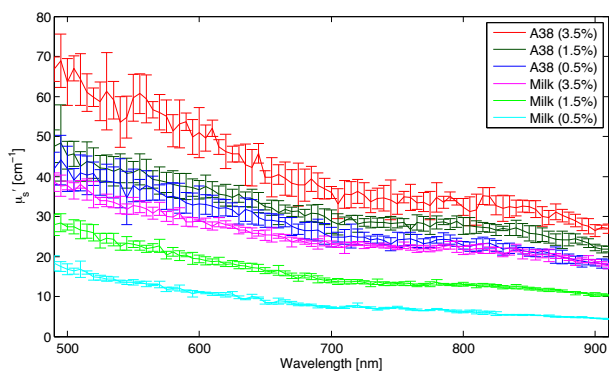
In Table F.2 values for α and β of Equation (F.1) are provided. As previously mentioned, α relates to particle concentration and β relates to the average particle size. For milk, the interpretation is straightforward. As the protein content is equal for all milks, cf. Table F.1, only the fat content changes, which means that the particle concentration decreases as the fat content is lowered. This corresponds well to the decrease in α . Additionally, the average particle size decreases, as the protein structures (20-400nm) are significantly smaller than the fat structures (100-10000nm) (Walstra et al., 2010), which correspond well to the decreases in β . For A38, the behaviour is more complex, as the protein content increases while the fat content decreases, cf. Table F.1. Where α decreases as expected when looking at the total amount of fat and protein, the behaviour of β does not follow the trend seen for the milk products. Also, the β value for A38 (3.5%) is significantly different from that of a similar product reported in Nielsen et al. (2013), for this we have no final explanation.

Moving on to the slope parameter in Figure F.6(b), a very different behaviour can be found when compared to μ'_s . The general near-convex behaviour of the slope parameter can most likely be contributed the combination of the light delivery system and the sensitivity of the CCD detector setup. The output power of the light decreases when approaching the lower wavelengths, and the quantum

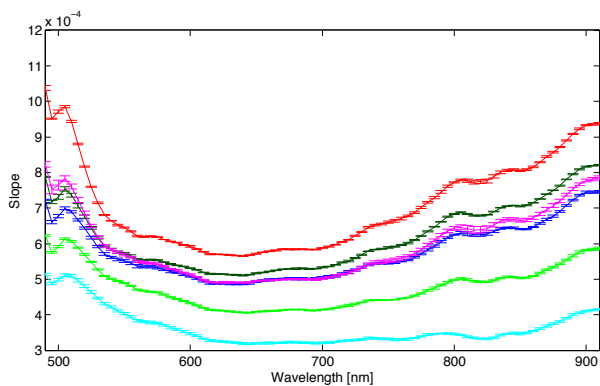
Table F.2: Estimates of α and β , cf. Equation (F.1), for the milk product data set.

Reference name	α	β
milk (3.5%)	36.1 ± 0.345	-1.11 ± 0.038
milk (1.5%)	26.9 ± 0.185	-1.68 ± 0.0379
milk (0.5%)	16.0 ± 0.0967	-2.13 ± 0.0421
A38 (3.5%)	64.0 ± 0.874	-1.52 ± 0.0614
A38 (1.5%)	44.6 ± 0.268	-1.08 ± 0.024
A38 (0.5%)	42.3 ± 0.253	-1.36 ± 0.0269

efficiency of the CDD decreases when approaching the higher wavelengths. This implies the expected dependence on the system response when using the slope parameter. On the other hand, the ordering of the products corresponds well to that of μ'_s and the slope parameter appears more reproducible and with a higher SNR. Furthermore, the parameters for all products are separated for large parts of the investigated wavelength spectrum. Thus, while the slope parameter is not as interpretable as μ'_s , it can still be a feasible way of quantifying the 2DSLs signal. This was also concluded in Skytte et al. (2014b).



(a) Reduced scattering



(b) Slope parameter

Figure F.6: Multiple scattered light quantified for the dairy products data set.

F.3.1.2 Speckle

Moving on to the speckle part of the signal, we have estimated the average speckle size for different $n \times n$ regions ($n \in \{100, 300, 500\}$) centred on the light incident point. For $n = 100$ in Figure F.7(a), the average speckle size does not seem to be very reproducible. The reason for the large error bars for $n = 100$ may be found in Figure F.5(b). Here it can be seen that the speckle size is not very well defined near the centre of the signal and there appears to be a lot of different speckle contributions. This can potentially result in very different estimates of the average speckle size in a 100×100 region. However, the problem appears to be alleviated when considering larger regions.

Thus, for $n = 300$ in Figure F.7(b) the error bars, for most products, become significantly smaller and the discriminative properties of using the average speckle size becomes clearer. Contrary to the results for multiple scattered light, an entirely different ordering of the products is seen. Most remarkable is the distinction between milk products and fermented milk products, which becomes very clear for the longer wavelengths. This suggests that the speckle is related to a different phenomenon than multiple scattered light.

For the dense samples, the speckle size seems to be estimated reproducibly for most wavelengths, however for the less dense samples, milk (0.5%) and milk (1.5%), the reproducibility appears significantly worse. This could be explained by Figure F.4(b), from which it appears that the speckle is not well defined for the milk products. Similar results are seen for $n = 500$ in Figure F.7(c), however A38 (3.5%) is suddenly distinguished from A38 (0.5%) and A38 (1.5%), while the milk products appears less separated. Also, the reproducibility and SNR appears slightly better.

Contrary to the results of multiple scattered light, there is no distinct monotony found across wavelengths. Instead there actually appears to be some slow reproducible fluctuations in the average speckle size across certain wavelength intervals, e.g. 500-650nm for A38 (0.5%) and A38 (1.5%). In general, the trend across wavelengths seems very different for all of the investigated region sizes. These differences between the applied region sizes and wavelengths, suggest that several different sources are contributing to the observed speckle patterns.

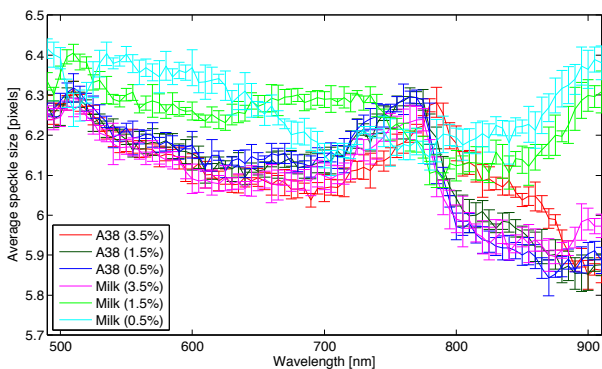
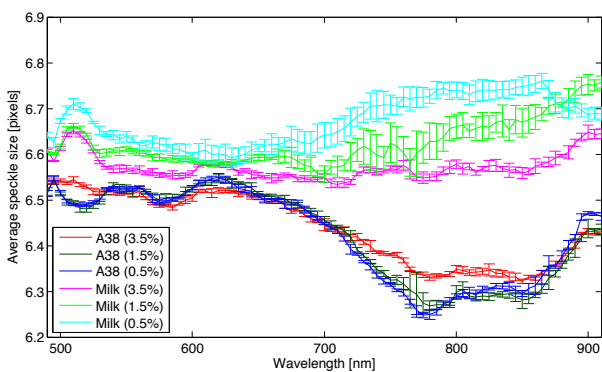
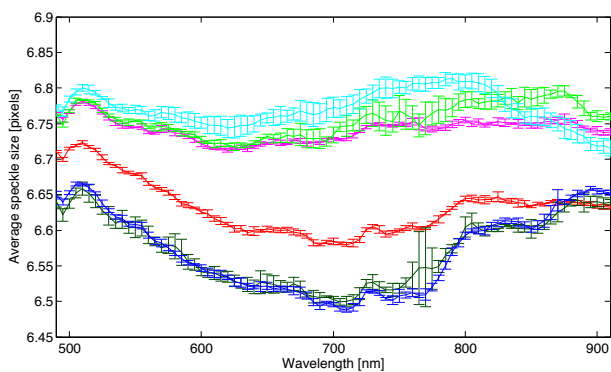
(a) Speckle size, $n = 100$ (b) Speckle size, $n = 300$ (c) Speckle size, $n = 500$

Figure F.7: Average speckle size estimated for the dairy products data set. n refers to the size of the region ($n \times n$) in which the average speckle size has been estimated. The region is centred upon the light incident point.

F.3.1.3 Scattering Eccentricity

Finally, the quantified scattering eccentricity was estimated for the intensity isocontours located m pixels away ($m \in \{100, 300, 500\}$) from the light incident point in the scattering direction. The general behaviour of the eccentricity is repeated for all values of m as can be seen in Figure F.8(a) through F.8(c). For $m = 100$ the reproducibility of the parameter estimate is worse than for $m = 300$ and $m = 500$. This is not particularly surprising since isocontours extracted close to the centre of the 2DSLS signal are smaller and harder to resolve appropriately. Thereby the reproducibility and SNR of the parameter estimate increases as larger isocontours are considered. Furthermore, when considering the higher wavelengths the products become well separated. Also, highly scattering products, cf. Figure F.6(a), have values closer to zero, meaning that the extracted isocontour is more circular. This is expected as highly scattering samples the light scattering becomes completely random (and thereby isotropic) closer to the light incident point.

Looking at the actual eccentricity estimates, a slightly different ordering of the products can be seen when compared to the results of multiple scattered light. The main difference is found at the high fat products milk (3.5%) and A38 (3.5%), which are now grouped together. This makes sense as fat should be the primary scatterer in high fat milk products, even for fermented milk products with the dense protein structures. It should be restated that the reduced scattering coefficient is formulated as $\mu'_s = \mu_s(1 - g)$, and scattering eccentricity is primarily related to g , thus some relation between the parameters can be expected.

However, the most pronounced effect of the eccentricity is the wavelength dependency, seen as sudden collapses and inflations of the eccentricity. Furthermore, the wavelength dependency is not equal for all products. At the time of writing, we have three hypotheses on this prominent wavelength dependency. Our first hypothesis is that it is an effect of the polarisation of the laser. We know this polarisation is wavelength dependent, thus this may be what is affecting the scattering eccentricity. Our second hypothesis concerns the water absorption peaks located between 700 and 800nm and between 900 and 1000nm (Curcio and Petty, 1951). An increase in absorption would decrease the MFP, and the measured scattering eccentricity would thereby become more circular. The third hypothesis is that the wavelength dependent behaviour reflects particle sizes present in the milk products. Protein structures naturally exist as differently sized structures, and while the milk products are homogenised (which results in standardised fat particle size), it has been shown that homogenisation can lead to multilobed size distributions of the fat particles (Olson et al., 2004). These hypotheses will be investigated in the future.

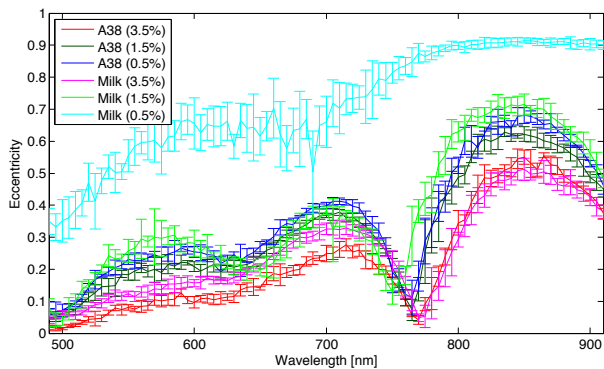
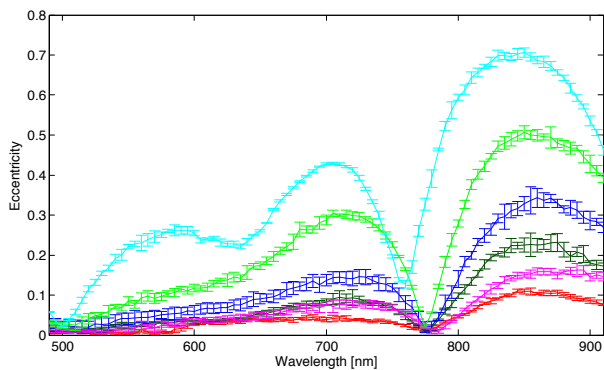
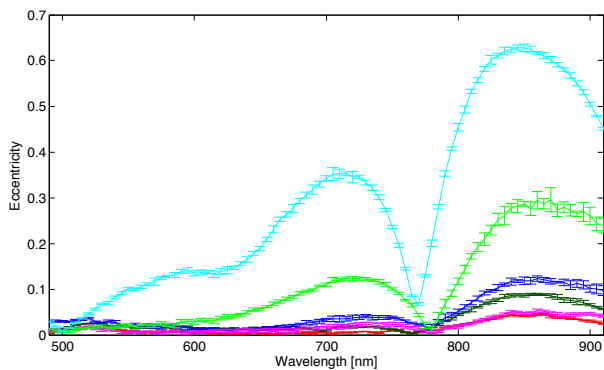
(a) Isocontour eccentricity, $m = 100$ (b) Isocontour eccentricity, $m = 300$ (c) Isocontour eccentricity, $m = 500$

Figure F.8: Intensity isocontour eccentricity estimated for the dairy products data set. m denotes the distance away from the light incident point, along the light direction, that the isocontour is extracted.

F.3.2 Milk Fermentation Data

Based on the observed results for the dairy product data set, the results presented for the milk fermentation will be narrowed down. Thus, the following sections only present a subset of the quantified parameters for the milk fermentations. Furthermore, as the milk fermentation presents a time development, results will only be shown for three wavelengths to maintain a clear overview of the presented results. The selected wavelengths are 700, 780, and 860nm, which corresponds to the local minima and maxima from Figure F.8(b). The wavelengths were also found to be appropriate for the other quantification methods.

The initial condition of the milk fermentation should approximately correspond to milk (1.5%), however the end condition is expected to be a bit different from A38 (1.5%). This is expected as different heat treatments have been used, and furthermore this milk fermentation is performed using GDL, whereas the commercial products have been created using lactic acid bacteria.

F.3.2.1 Rheology

Figure F.9 shows the rheological measurements. Here it can be seen how the viscosity (G') develops throughout the milk fermentation. The rapid increase in viscosity denotes the gelation point, on which all protein structures have aggregated. Using the measurements of G' , we will highlight the approximate gelation point in the following plots of the quantified 2DSLs signal.

F.3.2.2 Multiple Scattered Light

Looking at μ'_s in Figure F.10(a), a clear development is seen before any change in viscosity is detected. This has also been reported previously in the literature and most likely corresponds to early rearrangements of the protein structures (Alexander and Dalgleish, 2006; Payne and Castillo, 2007). The signal amplitude corresponds well to that seen in Figure F.6(a), and higher wavelengths seem to span a greater dynamic range as originally reported by Claesson and Nitschmann (1957).

Looking at α and β in Figure F.10(b) and F.10(c) respectively, they correspond very well to the underlying mechanics of milk fermentations. Throughout the fermentation, there should not be changes to the chemical composition or particle density, which corresponds well to the approximate constant level of α .

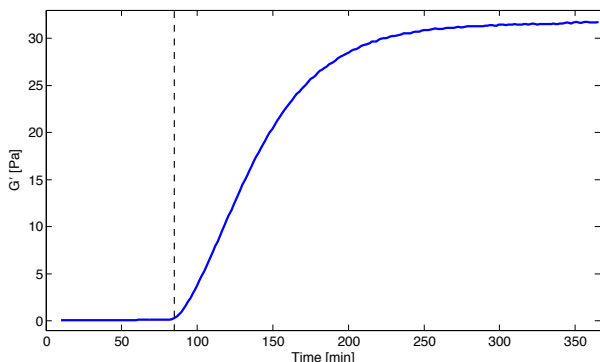


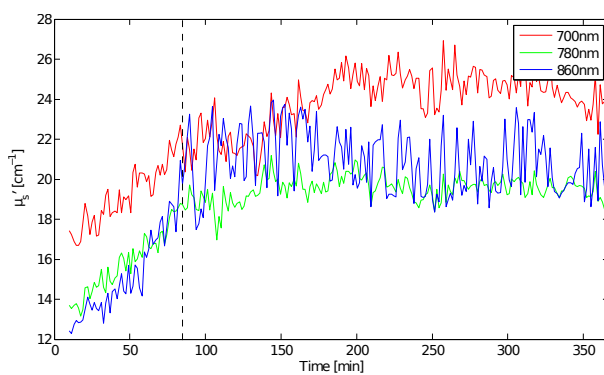
Figure F.9: The rheological development for the milk fermentation. The point where the curve rapidly increases is denoted the gelation point. The dashed line denotes the approximate gelation point.

On the other hand the average particle size is expected to increase as the protein structures starts to aggregate. This is reflected well in the β parameter. Furthermore, the SNR appears higher for β .

The slope parameter in Figure F.11(a) generally behaves similar to μ'_s , however parameter estimates show significantly higher SNR. Thus, while the wavelength dependency is different between the two methods as seen in Figure F.6(a) and F.6(b), the actual time development observed at a single wavelength appears similar. Furthermore, the behaviour corresponds well to what has been presented for related modalities (O'Callaghan et al., 1999; Payne and Castillo, 2007).

F.3.2.3 Speckle

The development of the average speckle size for $n = 500$ can be seen in Figure F.11(b). It clearly behaves differently from the quantified multiple scattered light, and the rapid signal increase resembles that of the rheological measurements. Contrary to the results for the dairy data set in Figure F.7(c), there is not much difference found in the signals across wavelengths. Thereby, as the two data sets were not made under the same measuring conditions, this indicates the observed speckle patterns are very dependent on the system setup. This corresponds well to what has been reported in relation to other speckle modalities (Viasnoff et al., 2002; Guyot et al., 2004; Piederrière et al., 2005). Here, the wavelength, as well as aperture size and working distance of the detector



(a) Reduced scattering

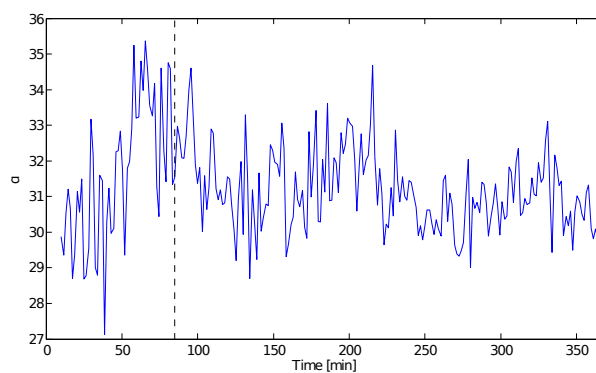
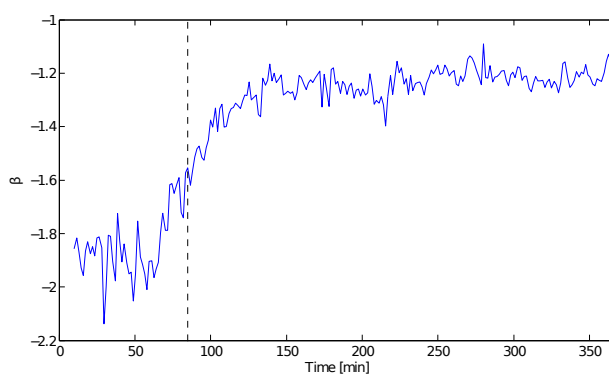
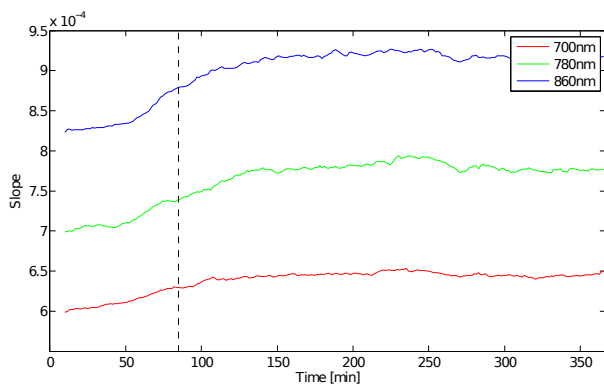
(b) α -parameter(c) β -parameter

Figure F.10: Parameter estimates for quantified multiple scattered light for the milk fermentation data set. The dashed line denotes the approximate gelation point.



(a) Slope parameter

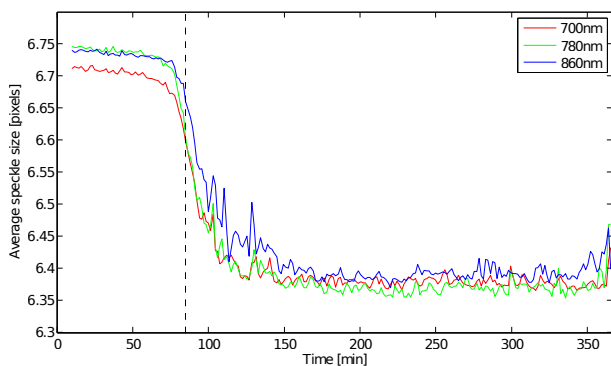
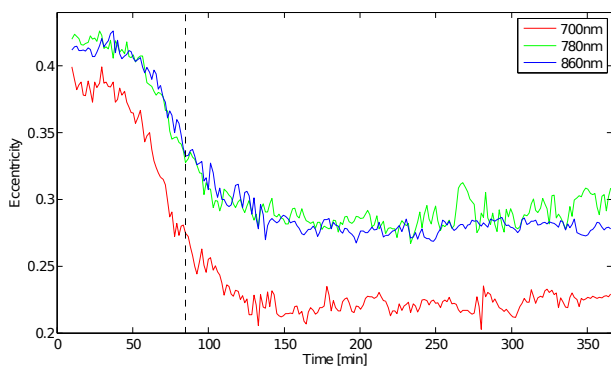
(b) Speckle size, $n = 500$ (c) Isocontour eccentricity, $m = 300$

Figure F.11: Parameter estimates for quantified multiple scattered light, speckle size, and single scattered light for the milk fermentation data set. The dashed line denotes the approximate gelation point.

systems, have been reported to affect the speckle pattern.

Looking at the time development of the average speckle size, a sharp signal increase is seen just before the gelation point. The behaviour is significantly different from what was observed through multiple scattered light. Actually, the signal resembles that of diffusing wave spectroscopy (although inverted), which measures particle mobility through dynamic speckle patterns (Alexander and Dalglish, 2004, 2006). In contrast, the speckle patterns in the 2DSLS signal are measured statically. However, as the protein aggregates the sample becomes denser, which likely affects the degree of light interference, and thereby the speckle patterns. Thus, static speckle patterns in the 2DSLS signal may potentially be an alternative approach to observing the phenomenon investigated through diffusing wave spectroscopy.

F.3.2.4 Scattering Eccentricity

Finally, the time development for the eccentricity parameter at $m = 300$ is shown in Figure F.11(c). Looking at the ordering of the wavelengths it does not correspond well to the local minima and maxima seen in Figure F.8(b). As with the speckle measure in the previous section, this suggests that the eccentricity parameter may very well also be dependent on the system setup.

When considering the time development of the eccentricity, the signal actually resembles that of the quantified multiple scattered light (especially the slope parameter) in Figure F.6(b). This may verify the relation between the eccentricity and μ'_s previously mentioned in Section F.3.1.3.

F.4 Discussion and Conclusion

In this report three different light phenomena: Multiple scattered light, speckle interference pattern, and single scattered light, were identified in the 2DSLS signal, and further quantified.

Multiple scattered light has previously been investigated in detail, and physical models have previously been developed (Wang and Jacques, 1995; Lin et al., 1997). We applied the physical model which relies on resolving the MFP in the signal, and thereby providing an absolute estimate μ'_s , and furthermore α and β . The physical modelling provided interpretable coefficients, which, for the most part, corresponded well to theory. To the best of our knowledge,

μ'_s , α , and β have not been reported for entire milk fermentations previously. A simplified approach was also applied in form of the loglog slope parameter. While this parameter is dependent on the system response, it was found to be significantly more reproducible than the physical model. However, it is not nearly as interpretable and does not provide an analysis across wavelength as the α and β coefficients. Nevertheless, it was found to show similar dynamics in the time development for the milk fermentation.

For the speckle pattern, the average speckle size was estimated. Here it was seen that this resulted in a clear distinction between the milk products and fermented milk products. The reasoning for this being that the denser samples produces more light interference. Furthermore, it was found that the time development of the estimated average speckle size during milk fermentation resembled the signal previously seen for diffusing wave spectroscopy (Alexander and Dagleish, 2004, 2006). However, it was also seen that the speckle size is dependent on both the applied system setup, as well as the spatial region in the 2DSLS signal in which the speckle size is estimated.

Single scattered light and effects of the phase function was investigated by the eccentricity of the intensity isocontours. Some remarkable wavelength dependencies were discovered which should be investigated further. The isocontours close to the light incident point were found hard to resolve, with the current detector system. Thus, isocontour eccentricity was estimated "far" away from the light incident point, in a region possibly border lining single scattered light and multiple scattered light. As with the quantified speckle, the eccentricity was found to be dependent on the system setup.

The eccentricity and speckle size measures are both interesting in relation to process control. They appeared reproducible and with a good SNR. Furthermore, they rely on shape rather than image intensities, and are thereby potentially invariant toward variations in the system response. Thus, in the future optimal system setup configurations should be investigated further for both the scattering eccentricity and speckle size parameters. Likewise, suitable regions in the 2DSLS signal should be determined for both parameters. These regions should preferably change dynamically according to the scattering of the sample, such that the same "optical regions" are found in both images. E.g. the eccentricity is measured two or three MFPs from the light incident point, instead of a fixed spatial distance, away from the light incident point.

Bibliography

- Abdelgawad, A. R., Guamis, B., and Castillo, M. (2014). Using a fiber optic sensor for cutting time prediction in cheese manufacture from a mixture of cow, sheep and goat milk. *Journal of Food Engineering*, 125:157–168.
- Aguilera, J. M. (2005). Why food microstructure? *Journal of Food Engineering*, 67(1):3–11.
- Aguilera, J. M. and Stanley, D. W. (1999). *Microstructural principles of food processing and engineering*. Springer.
- Ahmed, N., Natarajan, T., and Rao, K. R. (1974). Discrete cosine transform. *IEEE Transactions on Computers*, 100(1):90–93.
- Alexander, M., Corredig, M., and Dalgleish, D. G. (2006). Diffusing wave spectroscopy of gelling food systems: The importance of the photon transport mean free path (l^*) parameter. *Food Hydrocolloids*, 20(2):325–331.
- Alexander, M. and Dalgleish, D. G. (2004). Application of transmission diffusing wave spectroscopy to the study of gelation of milk by acidification and rennet. *Colloids and Surfaces B: Biointerfaces*, 38(1):83–90.
- Alexander, M. and Dalgleish, D. G. (2006). Dynamic light scattering techniques and their applications in food science. *Food Biophysics*, 1(1):2–13.
- Anderson, M. J. (2001). A new method for non-parametric multivariate analysis of variance. *Austral Ecology*, 26(1):32–46.
- Anderson, M. J. (2006). Distance-based tests for homogeneity of multivariate dispersions. *Biometrics*, 62(1):245–253.

- Anema, S. G. (2008). Effect of temperature and rate of acidification on the rheological properties of acid skim milk gels. *Journal of Food Processing and Preservation*, 32(6):1016–1033.
- Anema, S. G. and Li, Y. (2003). Association of denatured whey proteins with casein micelles in heated reconstituted skim milk and its effect on casein micelle size. *Journal of Dairy Research*, 70(01):73–83.
- Barrett, A. H. and Peleg, M. (1995). Applications of fractal analysis to food structure. *LWT-Food Science and Technology*, 28(6):553–563.
- Berne, B. J. (1976). *Dynamic light scattering: with applications to chemistry, biology and physics*. Dover Publications.
- Berridge, N. (1952). Some observations on the determination of the activity of rennet. *Analyst*, 77(911):57b–62.
- Bishop, C. M. et al. (2006). *Pattern recognition and machine learning, volume 1*. Springer.
- Bohlin, L., Hegg, P.-O., and Ljusberg-Wahren, H. (1984). Viscoelastic properties of coagulating milk. *Journal of Dairy Science*, 67(4):729–734.
- Bourne, M. (2002). *Food texture and viscosity: concept and measurement, 2nd Edition*. Academic Press.
- Bouvier, J., Ezzat, T., and Poggio, T. (2008). Localized spectro-temporal cepstral analysis of speech. In *IEEE International Conference on Acoustics, Speech and Signal Processing*, pages 4733–4736.
- Bray, J. R. and Curtis, J. T. (1957). An ordination of the upland forest communities of southern wisconsin. *Ecological Monographs*, 27(4):325–349.
- Briers, J. D. and Webster, S. (1996). Laser speckle contrast analysis (lasca): a non-scanning, full-field technique for monitoring capillary blood flow. *Journal of Biomedical Optics*, 1(2):174–179.
- Brodatz, P. (1966). *Textures: a photographic album for artists and designers, volume 66*. Dover Publications.
- Caputo, B., Hayman, E., and Mallikarjuna, P. (2005). Class-specific material categorisation. In *IEEE International Conference on Computer Vision*, volume 2, pages 1597–1604.
- Carstensen, J. M. (1992). *Description and simulation of visual texture*. PhD thesis, Technical University of Denmark, Department of Informatics and Mathematical Modeling.

- Carstensen, J. M., Møller, F., and Frisvad, J. (2009). Online monitoring of food processes using subsurface laser scattering. *Advances in Process Analytics and Control Technologies*, pages 5–7.
- Castillo, M. (2006). Cutting time prediction methods in cheese making. *Encyclopedia of Agricultural, Food, and Biological Engineering*, pages 1–7.
- Castillo, M., González, R., Payne, E., Laencina, J., and Lopez, M. (2005). Optical monitoring of milk coagulation and inline cutting time prediction in murcian al vino cheese. *Appl. Eng. Agric*, 21(3):465–471.
- Castillo, M., Payne, F., Hicks, C., and Lopez, M. (2000). Predicting cutting and clotting time of coagulating goat’s milk using diffuse reflectance: effect of ph, temperature and enzyme concentration. *International Dairy Journal*, 10(8):551–562.
- Chandan, R. C. and Kilara, A. (2013). *Manufacturing yogurt and fermented milks*. Wiley.
- Chandley, P. (1976). Surface roughness measurements from coherent light scattering. *Optical and Quantum Electronics*, 8(4):323–327.
- Chandrasekhar, S. (1960). *Radiative transfer*. Dover Publications.
- Chang, C. C. and Lin, C.-J. (2011). Libsvm: a library for support vector machines. *ACM Transactions on Intelligent Systems and Technology*, 2(3):27.
- Chen, P. and Sun, Z. (1991). A review of non-destructive methods for quality evaluation and sorting of agricultural products. *Journal of Agricultural Engineering Research*, 49:85–98.
- Cho, Y. J. and Han, Y. J. (1999). Nondestructive characterization of apple firmness by quantitation of laser scatter. *Journal of Texture Studies*, 30(6):625–638.
- Claesson, O. and Nitschmann, H. (1957). Optical investigation of the rennet clotting of milk. *Acta Agriculturae Scandinavica*, 7(4):341–360.
- Cootes, T., Taylor, C., Cooper, D., Graham, J., et al. (1995). Active shape models-their training and application. *Computer Vision and Image Understanding*, 61(1):38–59.
- Craft-Jenkins, M. (2012). Development of a noncontact sensor for monitoring milk coagulation and cutting time prediction in cheese making. Master’s thesis, University of Kentucky.
- Crosier, M. and Griffin, L. D. (2008). Texture classification with a dictionary of basic image features. In *IEEE Conference on Computer Vision and Pattern Recognition*, pages 1–7.

- Crosier, M. and Griffin, L. D. (2010). Using basic image features for texture classification. *International Journal of Computer Vision*, 88(3):447–460.
- Cula, O. G. and Dana, K. J. (2004). 3d texture recognition using bidirectional feature histograms. *International Journal of Computer Vision*, 59(1):33–60.
- Curcio, J. and Petty, C. (1951). The near infrared absorption spectrum of liquid water. *Journal of the Optical Society of America*, 41(5):302–302.
- Dabbaghchian, S., Ghaemmaghami, M. P., and Aghagolzadeh, A. (2010). Feature extraction using discrete cosine transform and discrimination power analysis with a face recognition technology. *Pattern Recognition*, 43(4):1431–1440.
- Dalgleish, D. G. (2011). On the structural models of bovine casein micelles: review and possible improvements. *Soft Matter*, 7(6):2265–2272.
- Dalgleish, D. G. and Corredig, M. (2012). The structure of the casein micelle of milk and its changes during processing. *Annual Review of Food Science and Technology*, 3:449–467.
- Dàvila, E. and Parés, D. (2007). Structure of heat-induced plasma protein gels studied by fractal and lacunarity analysis. *Food hydrocolloids*, 21(2):147–153.
- Dàvila, E., Toldrà, M., Sagner, E., Carretero, C., and Parés, D. (2007). Characterization of plasma protein gels by means of image analysis. *LWT-Food Science and Technology*, 40(8):1321–1329.
- Desobry-Banon, S., Vetier, N., and Hardy, J. (1999). Health benefits of yogurt consumption. a review. *International Journal of Food Properties*, 2(1):1–12.
- Fagan, C., Leedy, M., Castillo, M., Payne, F., O'Donnell, C., and O'Callaghan, D. (2007). Development of a light scatter sensor technology for on-line monitoring of milk coagulation and whey separation. *Journal of Food Engineering*, 83(1):61–67.
- Farrell, T. J., Patterson, M. S., and Wilson, B. (1992). A diffusion theory model of spatially resolved, steady-state diffuse reflectance for the noninvasive determination of tissue optical properties in vivo. *Medical Physics*, 19:879.
- Folkenberg, D., Dejmek, P., Skriver, A., and Ipsen, R. (2005). Relation between sensory texture properties and exopolysaccharide distribution in set and in stirred yoghurts produced with different starter cultures. *Journal of Texture Studies*, 36(2):174–189.
- Frisvad, J. R., Christensen, N. J., and Jensen, H. W. (2007). Computing the scattering properties of participating media using lorenz-mie theory. *ACM Transactions on Graphics*, 26(3):60.

- Fu, J., Lee, S.-K., Wong, S. T., Yeh, J.-Y., Wang, A.-H., and Wu, H. (2005). Image segmentation feature selection and pattern classification for mammographic microcalcifications. *Computerized Medical Imaging and Graphics*, 29(6):419–429.
- Gonzalez, R. C. and Woods, R. E. (2002). *Digital image processing*. Prentice Hall.
- Goodman, J. W. (1975). Statistical properties of laser speckle patterns. In *Laser speckle and related phenomena*, pages 9–75. Springer.
- Goodman, J. W. (1976). Some fundamental properties of speckle. *Journal of the Optical Society of America*, 66(11):1145–1150.
- Goodman, J. W. (2007). *Speckle phenomena in optics: theory and applications*. Roberts and Company Publishers.
- Gowen, A., O'Donnell, C., Cullen, P., Downey, G., and Frias, J. (2007). Hyperspectral imaging – an emerging process analytical tool for food quality and safety control. *Trends in Food Science & Technology*, 18(12):590–598.
- Gower, J. C. (1975). Generalized procrustes analysis. *Psychometrika*, 40(1):33–51.
- Graaff, R., Aarnoudse, J., Zijp, J. R., Sloot, P., De Mul, F., Greve, J., and Koelink, M. (1992). Reduced light-scattering properties for mixtures of spherical particles: a simple approximation derived from mie calculations. *Applied Optics*, 31(10):1370–1376.
- Groenhuis, R., Ferwerda, H. A., and Bosch, J. T. (1983). Scattering and absorption of turbid materials determined from reflection measurements. 1: Theory. *Applied Optics*, 22(16):2456–2462.
- Gunasekaran, S. and Ay, C. (1994). Evaluation milk coagulation with ultrasonics. *Food Technology*, 48.
- Guyot, S., Péron, M.-C., and Deléchelle, E. (2004). Spatial speckle characterization by brownian motion analysis. *Physical Review E*, 70(4):046618.
- Hagiwara, T., Kumagai, H., and Nakamura, K. (1998). Fractal analysis of aggregates in heat-induced bsa gels. *Food Hydrocolloids*, 12(1):29–36.
- Hand, D. J. and Taylor, C. C. (1987). *Multivariate analysis of variance and repeated measures: a practical approach for behavioural scientists, volume 5*. CRC Press.
- Haque, A., Richardson, R., and Morris, E. (2001). Effect of fermentation temperature on the rheology of set and stirred yogurt. *Food Hydrocolloids*, 15(4):593–602.

- Haralick, R. M., Shanmugam, K., and Dinstein, I. H. (1973). Textural features for image classification. *IEEE Transactions on Systems, Man and Cybernetics*, SMC-3(6):610–621.
- Hardy, J. and Fanni, J. (1981). Application of reflection photometry to the measurement of milk coagulation. *Journal of Food Science*, 46(6):1956–1957.
- Hastie, T., Tibshirani, R., Friedman, J., Hastie, T., Friedman, J., and Tibshirani, R. (2009). *The elements of statistical learning, 2nd edition*. Springer.
- Hayman, E., Caputo, B., Fritz, M., and Eklundh, J.-O. (2004). On the significance of real-world conditions for material classification. In *Computer Vision – ECCV 2004*, pages 253–266. Springer.
- Heney, L. G. and Greenstein, J. L. (1941). Diffuse radiation in the galaxy. *The Astrophysical Journal*, 93:70–83.
- Herremans, E., Bongaers, E., Estrade, P., Gondek, E., Hertog, M., Jakubczyk, E., Trong, N. N. D., Rizzolo, A., Saeys, W., Spinelli, L., et al. (2013). Microstructure-texture relationships of aerated sugar gels: novel measurement techniques for analysis and control. *Innovative Food Science & Emerging Technologies*.
- Hoaglin, D. C., Mosteller, F., and Tukey, J. W. (1983). *Understanding robust and exploratory data analysis, volume 3*. Wiley.
- Horne, D. (1999). Formation and structure of acidified milk gels. *International Dairy Journal*, 9(3):261–268.
- Horne, D. and Dalgleish, D. (1985). A photon correlation spectroscopy study of size distributions of casein micelle suspensions. *European Biophysics Journal*, 11(4):249–258.
- Hsu, C.-W. and Lin, C.-J. (2002). A comparison of methods for multiclass support vector machines. *IEEE Transactions on Neural Networks*, 13(2):415–425.
- Huang, D., Shan, C., Ardabilian, M., Wang, Y., and Chen, L. (2011). Local binary patterns and its application to facial image analysis: a survey. *IEEE Transactions on Systems, Man, and Cybernetics, Part C: Applications and Reviews*, 41(6):765–781.
- Huang, H., Yu, H., Xu, H., and Ying, Y. (2008). Near infrared spectroscopy for on/in-line monitoring of quality in foods and beverages: A review. *Journal of Food Engineering*, 87(3):303–313.
- Janhøj, T., Petersen, C. B., Frøst, M. B., and Ipsen, R. (2006). Sensory and rheological characterization of low-fat stirred yogurt. *Journal of Texture Studies*, 37(3):276–299.

- Jolliffe, I. (2005). *Principal component analysis, 2nd edition*. Springer.
- Jonasz, M. and Fournier, G. (2011). *Light Scattering by Particles in Water: Theoretical and Experimental Foundations: Theoretical and Experimental Foundations*. Academic Press.
- Joshi, N., Donner, C., and Jensen, H. W. (2006). Noninvasive measurement of scattering anisotropy in turbid materials by nonnormal incident illumination. *Optics Letters*, 31(7):936–938.
- Julesz, B. (1981). Textons, the elements of texture perception, and their interactions. *Nature*, 290:91–97.
- Julesz, B. and Bergen, J. R. (1983). Textons, the fundamental elements in preattentive vision and perception of textures. *Bell System Technical Journal*.
- Kalab, M. (1981). Electron microscopy of milk products: a review of techniques. *Scanning Electron Microscope*, pages 453–472.
- Kalab, M. (2010). The beauty of milk at high magnification. *Infocus Magazine*, pages 4–37.
- Kuhn, K. R., Cavallieri, Â. L. F., and Da Cunha, R. L. (2010). Cold-set whey protein gels induced by calcium or sodium salt addition. *International Journal of Food Science & Technology*, 45(2):348–357.
- Larsson, S. C., Andersson, S.-O., Johansson, J.-E., and Wolk, A. (2008). Cultured milk, yogurt, and dairy intake in relation to bladder cancer risk in a prospective study of swedish women and men. *The American journal of clinical nutrition*, 88(4):1083–1087.
- Law, A. (1996). Effects of heat treatment and acidification on the dissociation of bovine casein micelles. *Journal of Dairy Research*, 63:35–48.
- Lee, W. and Lucey, J. (2004). Structure and physical properties of yogurt gels: Effect of inoculation rate and incubation temperature. *Journal of Dairy Science*, 87(10):3153–3164.
- Lee, W. and Lucey, J. (2010). Formation and physical properties of yogurt. *Asian-Australasian Journal of Animal Sciences*, 23(9):1127–1136.
- Leung, T. and Malik, J. (2001). Representing and recognizing the visual appearance of materials using three-dimensional textons. *International Journal of Computer Vision*, 43(1):29–44.
- Lin, S.-P., Wang, L., Jacques, S. L., and Tittel, F. K. (1997). Measurement of tissue optical properties by the use of oblique-incidence optical fiber reflectometry. *Applied Optics*, 36(1):136–143.

- Lindeberg, T. (1994). Scale-space theory: A basic tool for analyzing structures at different scales. *Journal of Applied Statistics*, 21(1-2):225–270.
- Lindeberg, T. and Garding, J. (1993). Shape from texture from a multi-scale perspective. In *The Proceedings of the IEEE International Conference on Computer Vision*, pages 683–691.
- Lopes, R. and Betrouni, N. (2009). Fractal and multifractal analysis: a review. *Medical Image Analysis*, 13(4):634–649.
- Lowe, D. G. (1999). Object recognition from local scale-invariant features. In *The proceedings of the IEEE international conference on Computer vision*, volume 2, pages 1150–1157.
- Lowe, D. G. (2004). Distinctive image features from scale-invariant keypoints. *International Journal of Computer Vision*, 60(2):91–110.
- Lu, R. (2004). Multispectral imaging for predicting firmness and soluble solids content of apple fruit. *Postharvest Biology and Technology*, 31(2):147–157.
- Lucey, J. (2002). Formation and physical properties of milk protein gels. *Journal of Dairy Science*, 85(2):281–294.
- Lucey, J., Munro, P., and Singh, H. (1999). Effects of heat treatment and whey protein addition on the rheological properties and structure of acid skim milk gels. *International Dairy Journal*, 9(3):275–279.
- Lucey, J. and Singh, H. (1997). Formation and physical properties of acid milk gels: a review. *Food Research International*, 30(7):529–542.
- Lucey, J., Tamehana, M., Singh, H., and Munro, P. (1998a). A comparison of the formation, rheological properties and microstructure of acid skim milk gels made with a bacterial culture or glucono- δ -lactone. *Food Research International*, 31(2):147–155.
- Lucey, J., Teo, C. T., Munro, P. A., and Singh, H. (1998b). Microstructure, permeability and appearance of acid gels made from heated skim milk. *Food Hydrocolloids*, 12(2):159–165.
- Lucey, J. A. (2004). Cultured dairy products: an overview of their gelation and texture properties. *International Journal of Dairy Technology*, 57(2-3):77–84.
- MacGregor, J. and Kourti, T. (1995). Statistical process control of multivariate processes. *Control Engineering Practice*, 3(3):403–414.
- Malik, J., Belongie, S., Shi, J., and Leung, T. (1999). Textons, contours and regions: Cue integration in image segmentation. In *The Proceedings of the IEEE International Conference on Computer Vision*, volume 2, pages 918–925.

- Malik, J. and Perona, P. (1990). Preattentive texture discrimination with early vision mechanisms. *Journal of the Optical Society of America*, 7(5):923–932.
- Mandelbrot, B. B. (1983). *The fractal geometry of nature*. Henry Holt and Company.
- Mann, S. and Picard, R. W. (1994). Being undigital with digital cameras: Extending dynamic range by combining differently exposed pictures. Technical Report 323, MIT Media Lab Perceptual Computing Section, Boston, Massachusetts.
- Marr, D. and Hildreth, E. (1980). Theory of edge detection. *Proceedings of the Royal Society of London. Series B. Biological Sciences*, 207(1167):187–217.
- Martelli, F., Del Bianco, S., Ismaelli, A., and Zaccanti, G. (2010). *Light propagation through biological tissue and other diffusive media: theory, solutions, and software*. SPIE Press.
- Mateo, M. J., O’Callaghan, D. J., Everard, C. D., Castillo, M., Payne, F. A., and O’Donnell, C. P. (2010). Evaluation of on-line optical sensing techniques for monitoring curd moisture content and solids in whey during syneresis. *Food Research International*, 43(1):177–182.
- Materka, A., Strzelecki, M., et al. (1998). Texture analysis methods—a review. *Technical University of Lodz, Institute of Electronics, COST B11 report, Brussels*, pages 9–11.
- McMahon, D. J., Brown, R., Richardson, G., and Ernstrom, C. (1984). Effects of calcium, phosphate, and bulk culture media on milk coagulation properties. *Journal of Dairy Science*, 67(5):930–938.
- Mellema, M., Heesakkers, J., Van Opheusden, J., and Van Vliet, T. (2000). Structure and scaling behavior of aging rennet-induced casein gels examined by confocal microscopy and permeametry. *Langmuir*, 16(17):6847–6854.
- Mezzenga, R., Schurtenberger, P., Burbidge, A., and Michel, M. (2005). Understanding foods as soft materials. *Nature Materials*, 4(10):729–740.
- Michels, R., Foschum, F., and Kienle, A. (2008). Optical properties of fat emulsions. *Optics Express*, 16(8):5907–5925.
- Mie, G. (1908). Contribution to the optical properties of turbid media, in particular of colloidal suspensions of metals. *Ann. Phys. (Leipzig)*, 25:377–452.
- Møller, F., Larsen, R., and Carstensen, J. M. (2013). *Imaging Food Quality*. PhD thesis, Technical University of Denmark, Department of Informatics and Mathematical Modeling.

- Montgomery, D. C. (2005). *Design and analysis of experiments, 6th Edition*. Wiley.
- Mozaffarian, D., Hao, T., Rimm, E. B., Willett, W. C., and Hu, F. B. (2011). Changes in diet and lifestyle and long-term weight gain in women and men. *New England Journal of Medicine*, 364(25):2392–2404.
- Muir, D. D. and Hunter, E. A. (1992). Sensory evaluation of fermented milks: vocabulary development and the relations between sensory properties and composition and between acceptability and sensory properties. *International Journal of Dairy Technology*, 45(3):73–80.
- Nielsen, O. H. A. (2014). *Broadband optical characterization of material properties*. PhD thesis, Technical University of Denmark, DTU Compute.
- Nielsen, O. H. A., Dahl, A. L., Larsen, R., Møller, F., Nielsen, F. D., Thomsen, C. L., Aanæs, H., and Carstensen, J. M. (2011a). In depth analysis of food structures: Hyperspectral subsurface laser scattering. In *Scandinavian Workshop on Imaging Food Quality*. Ystad, Sweden.
- Nielsen, O. H. A., Dahl, A. L., Larsen, R., Møller, F., Nielsen, F. D., Thomsen, C. L., Aanæs, H., and Carstensen, J. M. (2011b). Supercontinuum light sources for hyperspectral subsurface laser scattering. In *The Scandinavian Conference on Image Analysis*, pages 327–337. Ystad, Sweden.
- Nielsen, O. H. A., Kamran, F., Dahl, A. B., Skytte, J. L., Nielsen, F. D., Thomsen, C. L., Andersen, P. E., Larsen, R., and Frisvad, J. R. (2014). Non-invasive assessment of dairy products using spatially resolved diffuse reflectance spectroscopy. *Submitted*.
- Nielsen, O. H. A., Subash, A. A., Nielsen, F. D., Dahl, A. B., Skytte, J. L., Andersson-Engels, S., and Khoptyar, D. (2013). Spectral characterisation of dairy products using photon time-of-flight spectroscopy. *Journal of Near Infrared Spectroscopy*, 21(5):375–383.
- O’Callaghan, D. J., O’Donnell, C., and Payne, F. (1999). A comparison of on-line techniques for determination of curd setting time using cheesemilks under different rates of coagulation. *Journal of Food Engineering*, 41(1):43–54.
- O’Callaghan, D. J., O’Donnell, C., and Payne, F. (2002). Review of systems for monitoring curd setting during cheesemaking. *International Journal of Dairy Technology*, 55(2):65–74.
- Ojala, T., Pietikainen, M., and Maenpaa, T. (2002). Multiresolution gray-scale and rotation invariant texture classification with local binary patterns. *IEEE Transactions on Pattern Analysis and Machine Intelligence*, 24(7):971–987.

- Olson, C. (1976). On choosing a test statistic in multivariate analysis of variance. *Psychological Bulletin*, 83(4):579.
- Olson, D., White, C., and Richter, R. (2004). Effect of pressure and fat content on particle sizes in microfluidized milk. *Journal of Dairy Science*, 87(10):3217–3223.
- Palmer, K. F. and Williams, D. (1974). Optical properties of water in the near infrared. *Journal of the Optical Society of America*, 64(8):1107–1110.
- Pasephol, T., Small, D. M., and Sherkat, F. (2008). Rheology and texture of set yogurt as affected by inulin addition. *Journal of Texture Studies*, 39(6):617–634.
- Payne, F. and Castillo, M. (2007). Light backscatter sensor applications in milk coagulation. In *Encyclopedia of Agricultural, Food, and Biological Engineering*, pages 1–5. Taylor & Francis.
- Payne, F., Hicks, C., Madangopal, S., and Shearer, S. (1993a). Fiber optic sensor predicting the cutting time of coagulating milk for cheese production. *Transactions of the ASAE*, 36.
- Payne, F., Hicks, C., and Shen, P.-S. (1993b). Predicting optimal cutting time of coagulating milk using diffuse reflectance. *Journal of Dairy Science*, 76(1):48–61.
- Payne, F., Madangopal, S., Hicks, C., and Shearer, S. (1990). Fiber optic milk coagulation sensor for cut-time detection. In *Food Processing Automation Conference*, pages 02–90. American Society of Agricultural Engineers St. Joseph, Michigan.
- Peng, Y. and Lu, R. (2007). Prediction of apple fruit firmness and soluble solids content using characteristics of multispectral scattering images. *Journal of Food Engineering*, 82(2):142–152.
- Phadungath, C. (2005). The mechanism and properties of acid-coagulated milk gels. *Songklanakarinn Journal of Science and Technology*, 27(2):433–448.
- Piederrière, Y., Boulvert, F., Cariou, J., Le Jeune, B., Guern, Y., and Le Brun, G. (2005). Backscattered speckle size as a function of polarization: influence of particle-size and-concentration. *Optics Express*, 13(13):5030–5039.
- Piederrière, Y., Cariou, J., Guern, Y., Le Jeune, B., Le Brun, G., and Lortrian, J. (2004a). Scattering through fluids: speckle size measurement and monte carlo simulations close to and into the multiple scattering. *Optics Express*, 12(1):176–188.

- Piederrière, Y., Le Meur, J., Cariou, J., Abgrall, J., and Blouch, M. (2004b). Particle aggregation monitoring by speckle size measurement; application to blood platelets aggregation. *Optics Express*, 12(19):4596–4601.
- Pine, D., Weitz, D., Chaikin, P., and Herbolzheimer, E. (1988). Diffusing wave spectroscopy. *Physical Review Letters*, 60(12):1134.
- PM Food & Dairy Consulting (2012). World yoghurt market report: 2000-2020.
- Press, W. H., Teukolsky, S. A., Vetterling, W. T., and Flannery, B. P. (2007). *Numerical recipes 3rd edition: The art of scientific computing*. Cambridge University Press.
- Pugnali, L. A., Matia-Merino, L., and Dickinson, E. (2005). Microstructure of acid-induced caseinate gels containing sucrose: quantification from confocal microscopy and image analysis. *Colloids and Surfaces B: Biointerfaces*, 42(3):211–217.
- Pusey, P. (1999). Suppression of multiple scattering by photon cross-correlation techniques. *Current Opinion in Colloid & Interface Science*, 4(3):177–185.
- Qian, X., Hua, X.-S., Chen, P., and Ke, L. (2011). Plbp: An effective local binary patterns texture descriptor with pyramid representation. *Pattern Recognition*, 44(10):2502–2515.
- Qin, J. and Lu, R. (2007). Measurement of the absorption and scattering properties of turbid liquid foods using hyperspectral imaging. *Applied Spectroscopy*, 61(4):388–396.
- Qin, J. and Lu, R. (2008). Measurement of the optical properties of fruits and vegetables using spatially resolved hyperspectral diffuse reflectance imaging technique. *Postharvest Biology and Technology*, 49(3):355–365.
- Qing, Z., Ji, B., and Zude, M. (2008). Non-destructive analyses of apple quality parameters by means of laser-induced light backscattering imaging. *Postharvest Biology and Technology*, 48(2):215–222.
- Ramírez, M. A. and Minami, M. (2003). Low-bit-rate speech coding. *Encyclopedia of Telecommunications*.
- Rayleigh, L. (1899). On the transmission of light through an atmosphere containing small particles in suspension, and on the origin of the blue of the sky. *The London, Edinburgh, and Dublin Philosophical Magazine and Journal of Science*, 47(287):375–384.
- Research and Markets (2012). Dairy products - global strategic business report.

- Roberti de Siqueira, F., Robson Schwartz, W., and Pedrini, H. (2013). Multi-scale gray level co-occurrence matrices for texture description. *Neurocomputing*, 120:336–345.
- Roggo, Y., Chalus, P., Maurer, L., Lema-Martinez, C., Edmond, A., and Jent, N. (2007). A review of near infrared spectroscopy and chemometrics in pharmaceutical technologies. *Journal of Pharmaceutical and Biomedical Analysis*, 44(3):683–700.
- Romano, G., Nagle, M., Argyropoulos, D., and Müller, J. (2011). Laser light backscattering to monitor moisture content, soluble solid content and hardness of apple tissue during drying. *Journal of Food Engineering*, 104(4):657–662.
- Sandoval-Castilla, O., Lobato-Calleros, C., Aguirre-Mandujano, E., and Vernon-Carter, E. (2004). Microstructure and texture of yogurt as influenced by fat replacers. *International Dairy Journal*, 14(2):151–159.
- Schneck, A. (1928). Dispersoid-chemische methoden zur untersuchung der milch. *Milchwirtschaftl Forschungen*, 7.
- Serra, M., Trujillo, A., Quevedo, J., Guamis, B., and Ferragut, V. (2007). Acid coagulation properties and suitability for yogurt production of cows milk treated by high-pressure homogenisation. *International Dairy Journal*, 17(7):782–790.
- Sharifzadeh, S., Serrano, J., and Carrabina, J. (2012a). Spectro-temporal analysis of speech for spanish phoneme recognition. In *IEEE International Conference on Systems, Signals and Image Processing*, pages 548–551.
- Sharifzadeh, S., Skytte, J. L., Clemmensen, L. H., and Ersboll, B. K. (2013). Dct-based characterization of milk products using diffuse reflectance images. In *IEEE International Conference on Digital Signal Processing*, pages 1–6.
- Sharifzadeh, S., Skytte, J. L., Nielsen, O. H. A., Ersboll, B., and Clemmensen, L. H. (2012b). Regression and sparse regression methods for viscosity estimation of acid milk from its sls features. In *IEEE International Conference on Systems, Signals and Image Processing*, pages 52–55.
- Siesler, H. W., Ozaki, Y., Kawata, S., and Heise, H. M. (2008). *Near-infrared spectroscopy: principles, instruments, applications*. Wiley.
- Skriver, A. (1995). *Characterization of stirred yoghurt by rheology, microscopy and sensory analysis*. PhD thesis, Royal Veterinary and Agricultural University, Institute of Dairy Research.
- Skriver, A., Holstborg, J., and Qvist, K. B. (1999). Relation between sensory texture analysis and rheological properties of stirred yogurt. *Journal of Dairy Research*, 66(04):609–618.

- Skytte, J. L., Ghita, O., Whelan, P. F., Andersen, U., Iler, F. M., Dahl, A. B., and Larsen, R. (2014a). Evaluation of confocal scanning laser micrographs of stirred yogurts using image analysis. *Submitted*.
- Skytte, J. L., Nielsen, O. H. A., Andersen, U., Møller, F., Carstensen, J. M., Dahl, A. B., and Larsen, R. (2014b). Monitoring optical changes during milk acidification using hyperspectral diffuse reflectance images. *Submitted*.
- Sodini, I., Remeuf, F., Haddad, S., and Corrieu, G. (2004). The relative effect of milk base, starter, and process on yogurt texture: a review. *Critical Reviews in Food Science and Nutrition*, 44(2):113–137.
- Soh, L. K. and Tsatsoulis, C. (1999). Texture analysis of sar sea ice imagery using gray level co-occurrence matrices. *IEEE Transactions on Geoscience and Remote Sensing*, 37(2):780–795.
- Soille, P. and Rivest, J.-F. (1996). On the validity of fractal dimension measurements in image analysis. *Journal of Visual Communication and Image Representation*, 7(3):217–229.
- Steffe, J. F. (1996). *Rheological methods in food process engineering*. Freeman Press.
- Sun, D. W. (2010). *Hyperspectral imaging for food quality analysis and control*. Academic Press.
- Tamime, A. and Robinson, R. (1999). *Yoghurt: science and technology*. Woodhead Publishing.
- Torres, I. C., Amigo Rubio, J. M., and Ipsen, R. (2012). Using fractal image analysis to characterize microstructure of low-fat stirred yoghurt manufactured with microparticulated whey protein. *Journal of Food Engineering*, 109(4):721–729.
- Vallas, M., Bovenhuis, H., Kaart, T., Pärna, K., Kiiman, H., and Pärna, E. (2010). Genetic parameters for milk coagulation properties in estonian holstein cows. *Journal of Dairy Science*, 93(8):3789–3796.
- Van de Water, J., Keen, C. L., and Gershwin, M. E. (1999). The influence of chronic yogurt consumption on immunity. *The Journal of Nutrition*, 129(7):1492–1495.
- Varma, M. (2004). *Statistical Approaches to texture classification*. PhD thesis, University of Oxford, Department of Engineering Science.
- Varma, M. and Garg, R. (2007). Locally invariant fractal features for statistical texture classification. In *IEEE International Conference on Computer Vision*, pages 1–8.

- Varma, M. and Zisserman, A. (2005). A statistical approach to texture classification from single images. *International Journal of Computer Vision*, 62(1-2):61–81.
- Varma, M. and Zisserman, A. (2009). A statistical approach to material classification using image patch exemplars. *IEEE Transactions on Pattern Analysis and Machine Intelligence*, 31(11):2032–2047.
- Vedamuthu, E. R. (1991). The yogurt story: past, present and future. iv. *Dairy, food and Environmental Sanitation*, 11(7):371–374.
- Viasnoff, V., Lequeux, F., and Pine, D. (2002). Multispeckle diffusing-wave spectroscopy: a tool to study slow relaxation and time-dependent dynamics. *Review of Scientific Instruments*, 73(6):2336–2344.
- Walstra, P., Walstra, P., Wouters, J. T., and Geurts, T. J. (2010). *Dairy science and technology, 2nd edition*. CRC press.
- Wang, L. and Jacques, S. L. (1995). Use of a laser beam with an oblique angle of incidence to measure the reduced scattering coefficient of a turbid medium. *Applied Optics*, 34(13):2362–2366.
- Weitz, D., Zhu, J., Durian, D., Gang, H., and Pine, D. (1993). Diffusing-wave spectroscopy: The technique and some applications. *Physica Scripta*, 1993(T49B):610.
- Wright, S. and Nocedal, J. (1999). *Numerical optimization, 2nd edition*. Springer.
- Xu, Y., Ji, H., and Fermuller, C. (2006). A projective invariant for textures. In *IEEE Computer Society Conference on Computer Vision and Pattern Recognition*, volume 2, pages 1932–1939.
- Yildiz, F. (2010). *Development and manufacture of yogurt and other functional dairy products*. CRC Press.
- Young, H. D. and Freedman, R. A. (2008). *Sears and Zemansky's University Physics: Modern Physics, 11th edition*. Pearson Education.
- Zheng, C., Sun, D.-W., and Zheng, L. (2006). Recent applications of image texture for evaluation of food qualities - a review. *Trends in Food Science & Technology*, 17(3):113–128.